

DOTTORATO DI RICERCA IN
SCIENZA E TECNOLOGIA DEI MATERIALI



Multifunctional Ni-Mn-based Heusler compounds from bulk to nanoparticles by ball-milling techniques

Greta Cavazzini



UNIVERSITÀ
DI PARMA



UNIVERSITÀ DI PARMA

UNIVERSITA' DEGLI STUDI DI PARMA

DOTTORATO DI RICERCA IN
SCIENZA E TECNOLOGIA DEI MATERIALI
CICLO XXXIII

Multifunctional Ni-Mn-based Heusler compounds from bulk to nanoparticles by ball-milling techniques

COORDINATORE:

Chiar.mo Prof. Enrico Dalcanale

TUTORE:

Chiar.mo Prof. Massimo Solzi

CO-TUTORI:

Chiar.mo Prof. Oliver Gutfleisch

Chiar.ma Dr. Franca Albertini

DOTTORANDA: Greta Cavazzini

A.A. 2017/2018-2019/2020

To my beloved family and friends

“The most beautiful experience we can have is the mysterious. It is the fundamental emotion that stands at the cradle of true art and true science.”

Albert Einstein (1879-1955)
“The World as I See It” (1934)

ABSTRACT

Attractive for the extraordinary coupling between different degrees of freedom (magnetic-elastic-caloric) and for the peculiar structural and microstructural rearrangement under application of external stresses, the large class of Heusler compounds, among which the family of Ni-Mn-based Heusler compounds, are multifunctional smart materials offering a wide range of exploration, from both the fundamental and technological perspective. The outstanding properties of the bulk material, such as the magnetic shape memory effect and the magnetocaloric effect, are based on the onset of a diffusion-less first order thermoelastic martensitic transformation, which gives rise to a complex interaction between magnetic and elastic domains from the micro- to the nanoscale. Determining the characteristic length scales underlying the formation of the martensite phase and its twinned martensitic microstructure, and investigating the role of sample/grain-size on the thermal hysteresis of the transformation are the key issues to better understand and possibly control the magneto-thermal, magneto-structural, and magneto-mechanical properties of these compounds. The large interest in nanotechnology and magnetic nanoparticles, for potential applications and advantages over the bulk-counterpart, and the relatively new and controversial field of research in the framework of Ni-Mn-based Heusler materials, have motivated the current study on the preparation and characterization of Heusler particles, at the micro- and sub-microscale. It has been chosen to investigate three specific off-stoichiometric Heusler systems, namely $\text{Ni}_{50}\text{Mn}_{30}\text{Ga}_{20}$, $\text{Ni}_{50}\text{Mn}_{18.5}\text{Cu}_{6.5}\text{Ga}_{25}$, $\text{Ni}_{45}\text{Co}_5\text{Mn}_{37}\text{In}_{13}$, since in the bulk form are benchmark materials for their peculiar magnetic and magneto-structural phase transitions, hence interesting to explore also at a lower dimensionality, to reveal any change, tunability or even improvement of the associated multifunctional properties. The synthesis strategy adopted is the top-down method based on the ball-milling technique. With the purpose to assess and optimize its effectiveness, different ball-milling types and several milling parameters have been tested and varied. For each Heusler system, the effects of size-reduction and mechanically induced lattice defects and deformations on the as-milled particles have been studied through morphological, structural and thermomagnetic characterizations, highlighting the differences by varying the milling-energy and milling procedure. Then, a fundamental part of this work has been dedicated to the optimization of the annealing conditions to recover the original magnetic properties and peculiar martensitic transformation, by discussing the role of kinetic and thermodynamic aspects in relation to the achieved particle's

size and degree of atomic disorder. The results of the different ball-milled batches have been compared among each other and with respect to the starting bulk and hand-grinded counterparts. Moreover, a comparison between the behaviours of the three Heusler systems upon the same milling conditions, as well as between the evolutions upon heating to recover the original configuration, has been carried out. The whole investigation, on the one hand, has permitted to understand the possibility to obtain via ball-milling sub-micron or nanoparticles able to recover the desired magneto-structural coupling and magneto-thermal properties after a suitable annealing treatment. On the other hand, there have been highlighted the size-dependent phenomena and the structural and compositional phase stability that characterize and differentiate the selected Heusler compounds.

CONTENTS

<i>Abstract</i>	1
CONTENTS	3
1 Introduction	5
1.1 State of Art	5
1.2 Motivation and Summary of the Work	8
1.3 Structure of the Thesis	10
2 Fundamentals	12
2.1 Magnetocaloric Effect	12
2.1.1 Second-order phase transitions	15
2.1.2 First-order phase transitions	18
2.2 Heusler Compounds	24
2.2.1 Systems under investigation	36
2.3 Magnetic Hyperthermia	39
3 Experimental Techniques	41
3.1 Sample Preparation	41
3.1.1 Arc-Melting furnace	41
3.1.2 Ball-milling technique	43
3.2 Structural and Morphological Characterizations	48
3.2.1 Structural analysis	48
3.2.2 Morphological & Compositional analysis	48
3.2.3 Dynamic Light scattering Analysis	49
3.2.4 Transmission Electron Microscope analysis	50
3.3 Magnetic Characterization	50
3.3.1 Thermo-Magnetic analysis	50
3.3.2 Extraction Magnetometer	52
3.3.3 Vibrating sample Magnetometer	53
3.3.4 SQUID Magnetometer	53
3.4 Mechanical compressive test	54
3.5 Magnetic hyperthermia measurements	54
4 Results	56
4.1 Analysis of Bulk Materials	56
4.2 Analysis of the Hand-grinded Powders	65
4.2.1 Mechanical Characterization	66
4.2.2 Ni _{49.4} Mn _{30.3} Ga _{20.3} : a comparison between hand-grinded and bulk samples	69

4.2.3	Ni _{49.7} Mn _{18.7} Cu _{6.4} Ga _{25.2} : a comparison between hand-grinded and bulk samples	75
4.2.4	Ni ₄₅ Mn ₃₇ In ₁₃ Co ₅ : a comparison between hand-grinded and bulk samples	81
4.2.5	Summary of the Hand-grinded powders' preparation	104
4.3	Ball-Milling of Ni-Mn-Ga Compound	106
4.3.1	High-Energy Ball-milling	106
4.3.2	Cryo-milling	113
4.4	Ball-Milling of Ni-Mn-Cu-Ga Compound	118
4.4.1	Cryo-milling	119
4.4.2	Planetary Ball-milling	124
4.4.3	Test of Magnetic Hyperthermia	134
4.5	Ball-milling of Ni-Mn-In-Co Compound	140
4.5.1	High-Energy Ball-milling	141
4.5.2	Planetary Ball-milling	145
4.5.3	Cryo-milling	159
4.5.4	Summary of results for cryo-milled and wet planetary ball-milled powders	181
4.5.5	A two-steps process: Cryo-milling + wet Planetary ball-milling	193
5	Summary & Comparison of the Main Results	201
6	Conclusions and Perspectives	207
7	Appendix	211
7.1	Ni _{49.4} Mn _{30.3} Ga _{20.3} Compound	211
7.2	Ni _{49.7} Mn _{18.7} Cu _{6.4} Ga _{25.2} Compound	211
7.3	Ni _{44.5} Mn _{37.9} In _{12.6} Co ₅ Compound	212
7.3.1	Planetary ball-milling	213
7.4	Ni _{45.7} Mn _{36.9} In _{13.2} Co _{4.2} Compound	218
8	List of Publications	222
9	Bibliography	223
	Acknowledgements	237

1 INTRODUCTION

1.1 STATE OF ART

Nowadays, the search for functional, sustainable, non-critical materials is the active target of research in Materials Science and Technology, for the development of low-carbon, energy efficient and eco-friendly technological devices.

Among the most used applications, the refrigeration systems, for food preservation and air-conditioning, play a fundamental role in everyday life. Yet they sadly represent the largest power consumer in human household activities, with an ever-increasing demand, leading to an alarming ecological footprint. [1–4].

The conventional cooling principle is based on the old and never-changed mechanism of vapour-compression and expansion, that presents many drawbacks on the level of energy inefficiency and environmentally harmful effects, caused by the use of ozone-depleting chemicals (chlorofluorocarbons (CFCs)) and greenhouse gases (hydrochlorofluorocarbons (HCFCs) and hydrofluorocarbons (HFCs)) [2,4,5].

These problems have driven the research towards new cooling strategies, and, since the discovery by Pecharsky and Gschneidner in 1997 of the giant magnetocaloric effect close to room temperature [6], and the realization of the first magnetic refrigerator prototype by Zimm et al. in 1998 [7], the development of solid-state magnetic refrigeration, close to ambient conditions, has seen a great acceleration.

The exponential interest on this topic, during the last twenty years, have permitted the development of several tens of magnetic refrigerator prototypes, that demonstrate great potentialities for an environmentally friendly and more efficient cooling alternative [8].

Based on the magnetocaloric effect (MCE), an intrinsic property of any magnetic material, a thermo-magnetic cycle can be built by the alternated adiabatic magnetization and demagnetization of a magnetic material, with application and removal of an external magnetic field enabling a temperature change ΔT_{ad} , conventionally heating and cooling in the respective two processes. This can be exploited in a regenerative thermal cycle through a heat exchanger fluid [3,4].

Being the core of the refrigerator, a lot of study has been devoted to identifying the best magnetocaloric materials, which should exhibit large and reversible induced effects around room-temperature, by application of a moderate external field. Moreover, they should be based on non-critical, non-strategic and abundant elements, for the potential cost-effectiveness and scale-up production, that would make the magnetic refrigeration technology a competitive commercial solution [3,8].

Up to now the class of Heusler compounds, especially the Ni-Mn-based Heusler family, with generic formula $\text{Ni}_{50}\text{Mn}_{25}\text{Z}_{25}$, have shown appealing magnetocaloric properties, in rare-earth-free compositions, with highly tuneable magnetic phase transitions [9]. Since their early discovery, at the beginning of the last century, they have been attracting a lot of interest, from both the fundamental and the technological point of view, thanks to the exhibition of several multi-functionalities and multi-caloric responses to the application of an external stimulus or combined ones (temperature, magnetic field, mechanical loading) [9,10].

For instance, Ni-Mn-Ga and Ni-Mn-In-Co systems are well-known in the bulk form for large magneto-elastic effects, like the ferromagnetic shape memory effect, and outstanding inverse magneto-caloric effect near room temperature, which make them promising materials in the field of sensing/actuation and magnetic refrigeration technology, respectively [11].

The peculiar strong coupling between structural, magnetic and elastic degrees of freedom derives from a first order diffusion-less martensitic transformation (MT), taking place between a high temperature cubic austenitic phase and a low temperature, low symmetry, martensitic phase, which are characterized by different magnetic ordered states [12,13].

Besides the martensitic transformation, a second-order Curie transition (T_C) of the austenite and/or martensite phase can be observed, determining the range of stability of their corresponding ferromagnetic behaviours.

Depending on the specific temperature-composition phase diagram of the compound, the Curie transition and the martensitic transformation can occur at well separated temperatures, or be tuned, by compositional changes and/or substitutions, to coincide in a single magneto-structural phase transition [14].

This is the case of specific compositions of Ni-Mn-(Cu)-Ga systems, where the coupling leads to a magneto-structural transition from a ferromagnetic martensitic phase, at low temperature, to a paramagnetic austenitic phase, at high temperature, giving rise to enhanced direct magnetocaloric and magnetoelastic effects, by applying a magnetic field [14,15]. For different compositions, instead, i.e., Ni-Mn-In-Co Heusler compounds, the martensite is weak-magnetic (paramagnetic or anti-ferromagnetic) while the austenite is ferromagnetic and the application of an external

magnetic field shifts the martensitic transformation to a lower temperature, favouring energetically the most ferromagnetic phase (austenite), and an inverse magneto-caloric effect can be measured [16].

The abrupt change of magnetization during the structural transition is the key-feature driving giant magnetocaloric effects and magnetic-field induced transformation, even for low-applied fields [16,17]. On the other hand, the large magneto-crystalline anisotropy of the martensite phase enables, during the application of an external magnetic field, the twin-boundary motion and the reorientation of the martensitic variants, leading to large recoverable magnetic-induced strains. This effect, called “magnetic shape memory effect”, is additional to the conventional shape memory effect, observed upon application of mechanical stress and heating afterwards [13,17,18].

The unique martensite-related multi-functional properties characterize all the shape memory materials and they have recently been the subject of great interest and investigation in order to reduce the sample size towards the nanoscale, since new potentialities and advantages over the bulk in several fields of application could be obtained [19,20]. Indeed, it is known that the preparation of single crystals is challenging and that both single- and poly-crystalline bulk materials present very poor mechanical integrity and large irreversible energy losses, due to the first-order character, that prevent their efficient use in magnetic-refrigeration cycles across the martensitic transition [11,16].

As an alternative, the development of new shapes, like thin films, ribbons, wires, foams or smart composites, have demonstrated, instead, to bring good formability, fast heat exchange and low eddy current losses [19,21,22].

The most investigated shape-memory materials are the Ni-Ti alloys and the ferromagnetic Ni-Mn-Ga Heusler compounds, for biomedical applications and sensing/actuation, respectively, and they have been successfully manufactured at the micro- and sub-microscale by severe plastic deformation methods or by epitaxial growth [23–29].

From the experimental observations and 1D modelling [20,30,31], it has emerged that, by decreasing the size towards the nanoscale, the size-effects, due to the increase of the surface-to-volume ratio and the grain-size reduction drastically affect and modify the martensitic transformation behaviour and eventually cause the phase transformation suppression [19,24,30]. Nevertheless, some studies on Ni-Ti microwires also reveal the possibility to recover the martensitic transformation and the functional properties, by optimizing both the heat treatments, after cold-working [23,27], and the sample’s microstructure [26,30].

It is worth noting that, among the nanoscale functional materials, the magnetic and magnetocaloric nanoparticles could be widespread employed in new potential applications, such as in biotechnology, where, depending on the specific chemical and physical properties, could be used for therapeutic, drug delivery or diagnostic purposes [32]. However, lot of experimental work and tests are still required before their actual application, first of all the synthesis optimization.

For what concerns the ferromagnetic Heusler nanoparticles, their preparation represents a quite novel and challenging field of research, because several difficulties, connected with the synthesis procedure, prevent obtaining the desired stoichiometry control, size uniformity and/or reliable physical properties.

In literature, only a few thorough works on Heusler nanoparticles are reported. Basically, they deal with the synthesis by a bottom-up approach, using different chemical methods [33–37], which, however, are limited to the preparation of only specific stoichiometric Heusler compositions, i.e., $\text{Co}_{50}\text{Fe}_{25}\text{Ga}_{25}$, $\text{Co}_{50}\text{Ni}_{25}\text{Ga}_{25}$, $\text{Co}_{50}\text{Ni}_{25}\text{Al}_{25}$.

Recently, some authors have applied a physical top-down approach based on the ball-milling technique to obtain powder of both near-stoichiometric Ni-Mn-Ga and off-stoichiometric Ni-Mn-In Heusler compounds [38–46]. This technique, indeed, is one of the most employed methods to synthesize nanostructured metals and alloys of different typology, thanks to its versatility, high productivity and cost-effectiveness [47,48]. However, it requires the selection of several different milling parameters to achieve the final desired morphological and structural characteristics, and, so far, it has not been extensively investigated for the preparation of nanosized Heusler particles. Therefore, the use of ball-milling method for obtaining Heusler nanoparticles is still under debate, as well as the understanding of the magneto-structural phase transitions at the nanoscale with respect to the well-known bulk properties.

1.2 MOTIVATION AND SUMMARY OF THE WORK

The need to assess limitations and potentialities of the use of the ball-milling technique to prepare Ni-Mn-based Heusler sub-micron and/or nanoparticles, with properties similar to those of the bulk, for potential applications in energy-conversion technology and biomedicine, has motivated the research activity of this Ph.D. thesis.

In this work, different types of Ni-Mn-X Heusler compounds, with X= Ga/Ga-Cu and In-Co, were prepared in the bulk form, with specific off-stoichiometric

compositions, already studied in literature. Indeed, Ni-Mn-(Cu)-Ga and Ni-Mn-In-Co are benchmark materials for the direct [15] and inverse [16] magnetocaloric effects, respectively. The former one is measured in correspondence of a coupled magneto-structural martensitic-Curie transition, tuneable near room-temperature, with the proper substitution of Mn by Cu. The latter one, instead, is observed across a metamagnetic martensitic transformation, characterized by a large magnetization change between austenite and martensite, close to room-temperature.

Apart from the associated MCE properties, little is already understood about the possibility to recover and observe the peculiar magneto-structural coupling at different length scales and the stability of the metamagnetic martensitic transformation by decreasing the sample size towards the micro and sub-microscale.

These facts have driven the interest and the investigation on the role of particle size and microstructural features on the martensitic phase transformation and related properties, to deepen the experimental observation on the size-dependent phenomena and gain a better understanding of the evolution of the magneto-thermal and magneto-structural properties by changing the bulk configuration.

For the mentioned purposes, the systems were subjected to several ball-milling methods, namely ball-milling at cryogenic temperatures (cryo-milling), high energy ball-milling, planetary ball-milling in dry conditions or with surfactant-assistance, in order to study the microstructural variation, the particle size reduction, and the change of structural and magnetic behaviours, under different severe plastic deformation conditions. This was aimed at optimizing the strategy of preparation of sub-micron and/or nanoparticles, avoiding agglomeration and keeping unvaried the original composition.

The study was carried out by systematic analyses of morphology, composition, crystal structure and thermo-magnetic behaviour, after ball-milling, which pointed out the necessity to perform thermal treatments. Hence, different annealing conditions were tested and adjusted to possibly optimize the release of the internal mechanical stresses and the recovery of the magnetic and martensitic phase transformations of the starting bulk material.

The results of the mechanical and structural response of each Heusler system, after different milling energy and dry/wet conditions, were investigated and were put in relation to the microstructural and magnetic evolution upon heating.

For each batch of powders, the restoration of long-range ferromagnetic order and of the martensitic phase transformation was studied and discussed with reference to the results obtained on similar ball-milled systems found in literature.

Then, the transition temperatures and the magnetic properties, at low dimensionality, were compared to the bulk-counterpart ones to understand and highlight changes and differences.

Finally, for the same milling conditions, the results of size-reduction and recovery processes of the three Heusler compounds were analysed and compared between each other to gain an insight of their characteristic structural stability, recovery mechanisms and size-dependent phenomena.

1.3 STRUCTURE OF THE THESIS

The thesis is organized as follows.

The *Chapter 2 of Fundamentals* provides the thermodynamic explanation of the magnetocaloric effect, in the vicinity of a second order and first-order magnetic phase transition, a general overview of the class of Heusler compounds, with a detailed presentation of the selected Heusler systems, and a brief introduction to the use of magnetic nanoparticles for the magnetic hyperthermia biomedical application.

The *Chapter 3 of Experimental Techniques* includes the description of all the methods employed for the sample preparation, such as the arc-melting technique for the bulk material and the different ball-milling techniques adopted for the preparation of the Heusler particles, and it provides the description of the instrumental tools employed for the structural, morphological, magneto-thermal, mechanical, and magnetic hyperthermia analyses.

The *Chapter 4 of Results* is based on the illustration of the magneto-structural properties of the obtained bulk materials and the crystallographic characterization of the powders prepared by hand-grinding process and post-annealing, with comparison between their magnetic properties and the bulk ones.

Thereafter, for each system, the outcomes of each ball-milling procedure are described with respect to the morphological, compositional, and structural features of the achieved particles, and a detailed description of the process of optimization of the annealing conditions, for the recovery of the original Heusler ferromagnetic phase and martensitic transformation, is provided.

This is followed by the *Chapter 5 of Summary & Comparison of the Main Results* for the ball-milled and annealed particles of the three examined compounds, with a discussion and cross-reference between the systems on the influence of the microstructural and morphological features of the obtained particles in the recovery

of the martensitic transformation. Hereafter, the best preparation strategies, for the different compounds, are identified and commented.

Finally, in *Chapter 6 of Conclusions and Perspectives*, the highlights of the overall research activity are summarized, with the conclusive remarks on the most significant obtained results. Potential applications at the micro- and nanoscale of the achieved ball-milled and post-annealed powders, as well as the most relevant implications from the fundamental point of view are briefly suggested.

2 FUNDAMENTALS

2.1 MAGNETOCALORIC EFFECT

All magnetic materials are characterized by a strict interdependence between thermal and magnetic properties that allows the exhibition of interesting phenomena by application of external fields, such as the Magnetocaloric Effect (MCE).

Discovered in 1881 by Warburg in iron, the magnetocaloric effect has been later exploited, over the last century, to reach ultralow temperatures, through the adiabatic demagnetization of paramagnetic salts [17]. Nowadays, this intrinsic property is particularly studied in soft magnetic materials for the development of new efficient energy-conversion applications, such as the solid-state magnetic refrigeration technology, near room-temperature [13].

In order to fully analyse and understand the nature of this effect, the thermodynamic concept of the total entropy of a magnetic system must be introduced.

Generally, at constant pressure, it can be represented as:

$$S_{tot}(T, H) = S_{el}(T, H) + S_{lat}(T, H) + S_m(T, H) \quad (2.1)$$

where the $S_{el}(T, H)$, $S_{lat}(T, H)$, $S_m(T, H)$ are the electronic, lattice and magnetic contributions to the total entropy, respectively, for a specific temperature and magnetic field.

While all three contributions strongly depend on the temperature, only the magnetic one changes significantly by applying a magnetic field. Therefore, the relation (2.1) can be re-written as:

$$S_{tot}(T, H) = S_{el}(T) + S_{lat}(T) + S_m(T, H) \quad (2.2)$$

where the electronic and lattice contributions are basically independent on the magnetic field. When the latter is varied in an isothermal (and isobaric) process, of an amount $\Delta H = H_1 - H_0$, the total entropy change of the system is equal to the sole magnetic entropy change:

$$\begin{aligned} \Delta S_{tot}(T, \Delta H)|_{T,p} &= [S_{tot}(T, H_1) - S_{tot}(T, H_0)]_{T,p} \\ &= [S_m(T, H_1) - S_m(T, H_0)]_{T,p}. \end{aligned} \quad (2.3)$$

Due to the coupling between the magnetic subsystem and the external magnetic field, the magnetic moments of the material tend to re-orientate themselves along the direction of the applied magnetic field resulting in a decrease of the magnetic entropy, from a random to an ordered state.

In adiabatic conditions, the perturbation of the magnetic state must be compensated by an increase of the combined electronic and lattice entropies, in accord to:

$$\Delta(S_{el} + S_{lat}) = -\Delta S_m \quad (2.4)$$

to fulfil the condition that

$$\Delta S_{tot} = \Delta S_{el} + \Delta S_{lat} + \Delta S_m = 0. \quad (2.5)$$

The energy (entropy) transfer from the magnetic to the lattice subsystem leads to an adiabatic temperature change in the material:

$$\Delta T_{ad}(T, \Delta H)|_{S,p} = [T(S, H_1) - T(S, H_0)]_{S,p}. \quad (2.6)$$

According to the relations (2.3) and (2.6), when the entropy behaviour of the magnetic material is known, as a function of both temperature and magnetic field, the magnetocaloric effect is completely characterized [49]. In the S-T diagram of Fig. 2.1, the MCE can be visualized as the adiabatic temperature change $\Delta T_{ad}(T, \Delta H)$ (following the horizontal arrow), or alternatively, as the isothermal entropy change $\Delta S_{iso}(T, \Delta H)$ (following the vertical arrow), of a magnetic material upon variation of an external magnetic field (ΔH).

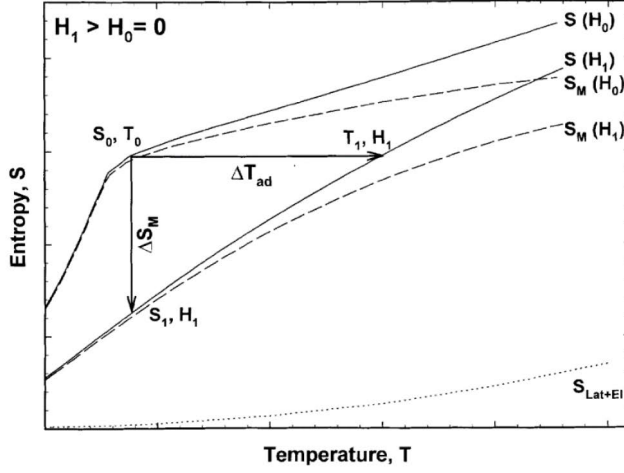


Figure 2.1: Schematic representation of the $S(T)$ curves for two different values of the applied magnetic field (H_0, H_1). The horizontal arrow defines the adiabatic temperature change ΔT_{ad} , while the vertical one shows the isothermal entropy variation ΔS_{iso} (adapted from Ref: [50]).

Using the Maxwell formalism, it is possible to relate the ΔS_{iso} to the variation of magnetization $M(T, H)$ of the material with respect to the temperature [50]:

$$\Delta S_{iso}(T, H) = \mu_0 \int_{H_i}^{H_f} \left(\frac{\partial M(T, H)}{\partial T} \right)_{H'} dH' \quad (2.7)$$

Otherwise, it can be estimated by measuring the heat capacity at constant pressure c_p , as a function of temperature and magnetic field, taking into account the second law of the thermodynamics [51]:

$$dS(T)_{H,p} = \frac{C(T)_{H,p}}{T} dT \quad (2.8)$$

$$\Delta S(T, \Delta H)_p = \Delta S_m(T, \Delta H)_p = \int_0^T \frac{[c(T)_{H_2} - c(T)_{H_1}]_p}{T'} dT' \quad (2.9)$$

Likewise, it is obtained the expression of the ΔT_{ad} by inserting in Eq. (2.7) the specific heat capacity under constant pressure [49]:

$$\Delta T_{ad}(T, H) = -\mu_0 \int_{H_i}^{H_f} \frac{T}{c_p} \left(\frac{\partial M}{\partial T} \right)_{H,p} dH' \quad (2.10)$$

From the three relations (2.7), (2.9) and (2.10) some important remarks are easily deduced: since both quantities ΔS_{iso} and ΔT_{ad} depend on the magnetization variation as a function of temperature and/or on the change of heat capacity by varying the magnetic field, the MCE is expected to be enhanced in correspondence of a magnetic phase transition. Moreover, since in the calculation of $\Delta T_{ad}(T, H)$ (2.10) the heat capacity c_p appears at denominator, for the same entropy variation, a much higher adiabatic temperature change is observed at low temperatures where the total heat capacity tends towards zero.

It is then understood that in a typical ferromagnet where the magnetization, at constant magnetic field, decreases with increasing temperature ($\left(\frac{\partial M}{\partial T}\right)_{H,p} < 0$), the isothermal entropy change is expected to be negative, while the adiabatic temperature change to be positive (heating effect, conventional MCE). By contrast, in the case of an increase of magnetization with temperature an inverse MCE is observed, characterized by a negative ΔT_{ad} (cooling effect) for a positive magnetic field variation [52,53].

In the following, the study of the magnetocaloric effect in proximity of a second order and first-order magnetic phase transition is described, presenting both the direct and inverse MCE.

2.1.1 Second-order phase transitions

A pure magnetic phase transition, of the second-order type, takes place in a ferromagnet at the Curie point T_C , while in an antiferromagnet at the Néel temperature T_N , without discontinuities in the first derivatives of the Gibbs free energy, with respect to the intensive thermodynamic variables, e.g., T, p, H .

In general, a second order magnetic phase transition is also defined as a continuous transition, since the entropy, the volume and the magnetization are continuous functions in all the temperature range. Moreover, it is neither accompanied by a latent heat of transformation ($\Delta Q = T\Delta S = 0$), nor by hysteresis losses, enabling a fully reversible magnetocaloric effect.

The second derivatives of the thermodynamic potential, such as the magnetic susceptibility χ_m and the heat capacity at constant pressure c_p , present an anomaly, divergence and discontinuity, at the transition temperature, respectively.

In the case of a ferromagnet, the spontaneous magnetization behaviour, in absence of an external magnetic field, which is displayed in Fig. 2.1-1 by the red line, gradually

decreases $\left(\frac{\partial M}{\partial T}\right)_{H,p} < 0$) while approaching the Curie point T_C , due to the effect of the thermal agitation that disorders the configuration of the magnetic moments and gives rise to a paramagnetic randomized state. When an external magnetic field is applied, the ferromagnetic order is stabilized against thermal fluctuations and the magnetization curve as a function of temperature becomes smoother in the vicinity of the Curie transition, as shown in Fig. 2.1-1 by the blue and green curves (referred to a simulated magnetic field of 1 and 2 T, respectively).

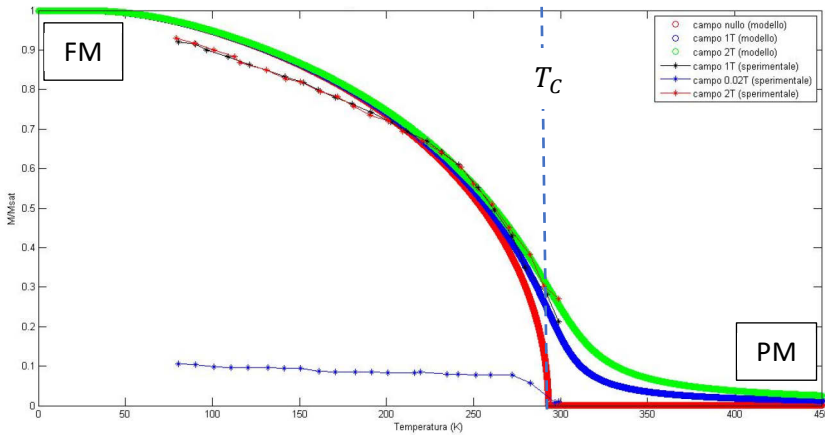


Figure 2.1-1: Comparison between the experimental results and the mean-field model prediction of the magnetization behaviour (M/M_0) as a function of temperature (T), for Gd, characterized by a second-order magnetic transition (T_C).

This is due to the alignment of the magnetic moments in the direction of the applied external magnetic field, resulting in an increase of magnetic order, thus lowering of the magnetic entropy term. The result is a direct (or conventional) magnetocaloric effect, as displayed, in the S-T diagram of Fig. 2.1-2, by the heating of the material $\Delta T_{ad}(T, \Delta H) > 0$, in adiabatic conditions, between the zero-field entropy curve (pink line) and the field-induced entropy curve (green colour), and by a decrease of the total entropy, in isothermal conditions, upon application of an external magnetic field.

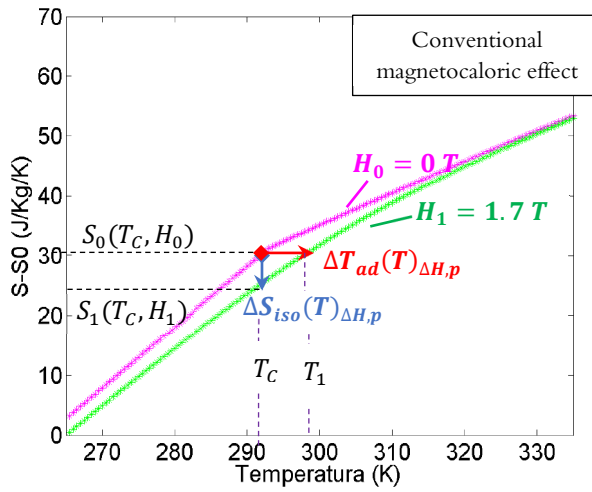


Figure 2.1-2: Modelling of the thermal dependence of the total entropy under H_0 and H_1 applied magnetic field, of a magnetic material with second-order Ferro-Para magnetic transition.

An opposite effect, named inverse magnetocaloric effect (IMCE) is, instead, observed in an antiferromagnetic material, below the Néel Temperature, when the application of a magnetic field, in an adiabatic process, leads the sample to cool down ($\Delta S_{iso} > 0$ and $\Delta T_{ad} < 0$) [53].

If, for instance, the external magnetic field is applied along the direction of the magnetic moments of one of the two sublattices, it drives the rotation of the magnetic moments of the other one toward the direction of the magnetic moments' ions of the first sublattice, with an increase of the net magnetization with temperature ($\frac{\partial M}{\partial x} > 0$) until reaching T_N , as displayed in Fig. 2.1-3(a). This leads to an increase in the magnetic part of the entropy of the second sublattice. In adiabatic conditions, since the magnetic entropy of the first sublattice remains unaltered, a decrease of the lattice entropy results in a cooling of the system, i.e., *inverse* MCE, as schematically shown in Fig. 2.1-3(b).

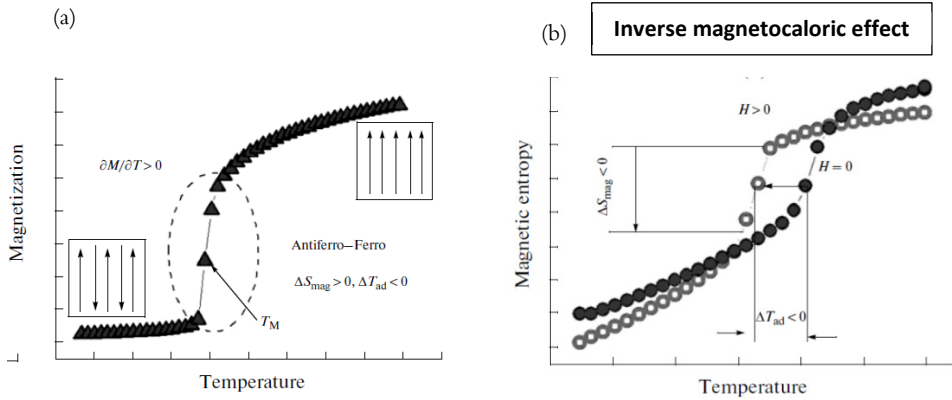


Figure 2.1-3: (a) Schematic temperature dependence of the magnetization of an antiferromagnet under an applied magnetic field H . (b) S - T diagram showing the inverse magnetocaloric effect as a negative adiabatic temperature change ($\Delta T_{\text{ad}} < 0$) by applying the magnetic field H adiabatically [52].

Historically, the direct MCE associated with a ferromagnetic to paramagnetic second-order Curie transition has been the first and most studied one for the practical application, thanks to the advantage of the non-hysteretic behaviour.

The prototype material of the second order magnetocaloric effect for the room-temperature magnetic refrigeration is the Gd lanthanide metal, a rare-earth element, which undergoes a continuous magnetic transition, from the ferromagnetic (ordered) to the paramagnetic (disordered) state, at $T_C \approx 293 \text{ K}$, showing a fully reversible MCE, with values of $\Delta S_{\text{iso}} \sim 3 \text{ J/Kg K}$ and $\Delta T_{\text{ad}} \sim 2.5 \text{ K}$ under 1 T [2,5,51].

2.1.2 First-order phase transitions

The magnetic materials undergoing a transition of a first-order type present a jump-like discontinuity at the point of transition in the first derivatives of the thermodynamic potential, such as the magnetization, the entropy and the volume, and, in addition, the divergence of the second derivatives, as the heat capacity.

The first-order transition, between two physically different phases, proceeds through a non-equilibrium two-phase state and is accompanied by a latent heat of transformation ($\Delta Q = T\Delta S$), linked to the entropy change between the two phases, and an enthalpy variation, depending on the equilibrium condition of the total Gibbs free energy of the system at the transition: $\Delta G = \Delta E - T\Delta S = 0$.

Since the discovery, at the end of last century, of the giant magnetocaloric effect GMCE in FeRh [54] and GdSiGe materials [6], the first order magnetocaloric material has been largely investigated: indeed, due to the absence of short-range order and spin fluctuations, which, instead, characterized the order-disorder transitions, the sharpness of the magnetization change at the first-order transition temperature and the additional entropic contribution of latent heat enable notably larger magnetocaloric effects, with respect to the best second-order type materials, as Gd. However, the intrinsic irreversibility of the effect, due to the thermal and magnetic hysteresis, the slow kinetic or the narrow temperature range, prevent their implementation as active magnetic refrigeration materials.

Interestingly, by using the phenomenological model of Bean and Rodbell, which was primarily introduced to describe the first-order magnetic transition in MnAs [55,56], and by minimizing the Gibbs free energy with respect to the magnetization and the volume, it is possible to obtain the evolution of a magnetic phase transition, from the second to the first order type, as a function of the η parameter, which controls the magneto-volume coupling. With reference to Fig. 2.1-4, it is observed that, in absence of any external magnetic field, by only varying η , from zero to the value of $\eta_c = 1$, a second-order transition, with the typical continuous Brillouin function, occurs, whereas for $\eta > \eta_c$, a first-order transition takes place. It is clearly seen that, differently from the former, the latter presents a sharp transition with a large magnetization jump, indicated with ΔM in figure, and that, between the heating and the cooling branches, a thermal hysteresis ΔT_{hyst} appears and becomes larger for increasing η values.

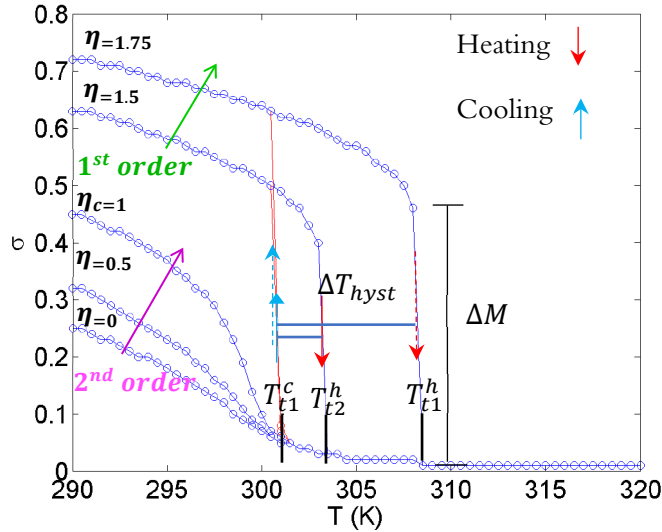


Figure 2.1-4: Temperature dependence of the relative magnetization σ ($\sigma = \frac{M}{g\mu_B J N}$) of $\text{MnFeP}_{1-x}\text{As}_x$ calculated in zero-field with different values of parameter η .

When a magnetic field is applied in proximity of a first-order magnetic phase transition not only a spin reordering, as the case for the second-order magnetic transitions, but also a shift of the transition temperature, $\frac{dT_t}{dH}$, occurs, on the basis of the difference in the Zeeman energy between the low temperature and high temperature magnetic phases ($\Delta E_{\text{Zeeman}} = -\mu_0 \Delta M H$). If the low-temperature phase possesses the highest magnetization, by applying an external magnetic field $H_1 > 0$, the transition is shifted to higher temperature, $\frac{dT_t}{dH} > 0$, as shown in Fig. 2.1-5(a) and a direct magnetocaloric effect, characterized by the heating of the system in adiabatic conditions, is detected. In fig. 2.1-5(b) it is shown a schematic example of the S-T diagram with an ideal parallelogram shape, due to the discontinuity of the entropy at the transition temperature and the shift of the latter with the magnetic field. As for the case of the Curie transition, keeping constant the temperature, the isothermal entropy decreases (vertical arrow) when the field is applied, while in adiabatic conditions, the temperature of the material increases (horizontal arrow).

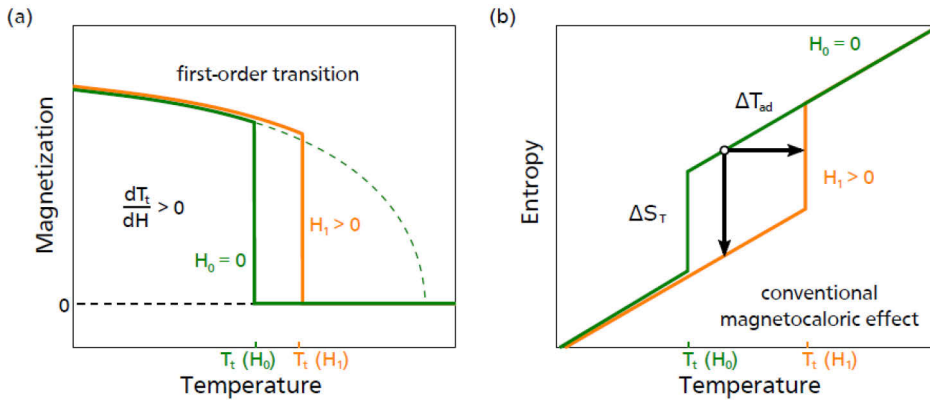


Figure 2.1-5: Schematic illustration of (a) a first-order magnetic transition, from a low temperature magnetic phase to a high temperature paramagnetic phase at $T_t(H_0)$ in zero-field (green curve), which is shifted to a higher temperature $T_t(H_1)$ when an external magnetic field $H_1 > 0$ is applied ($\frac{dT_t}{dH} > 0$). (b) Corresponding behaviour of the temperature dependent total entropy in two different magnetic fields with evidence of the direct (or conventional) magnetocaloric effect ($\Delta T_{ad} > 0$ and $\Delta S_{iso} < 0$) [57].

A different but equally important example of first-order magnetic transition is the metamagnetic transition (Fig. 2.1-6(a)), around which an inverse magnetocaloric effect (Fig. 2.1-6(b)) is observed under positive magnetic field variations. Being more ferromagnetic than the low temperature phase (paramagnetic or anti-ferromagnetic), the high-temperature phase is energetically favoured when a magnetic field is applied, hence the transition temperature is decreased, and, in adiabatic conditions, a negative temperature change is detected ($\Delta T_{ad} < 0$).

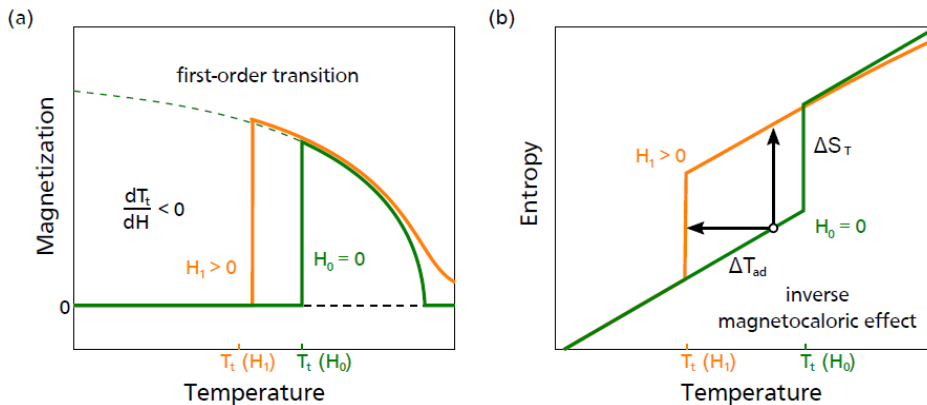


Figure 2.1-6: Schematic illustration of (a) a first order metamagnetic transition, from a low-temperature non-magnetic phase to a high temperature ferromagnetic phase, where the application of a magnetic field $H_1 > 0$ tends to stabilize the high temperature phase, shifting the transition to a lower temperature ($\frac{dT_t}{dH} < 0$). (b) Associated inverse magnetocaloric effect under a positive field variation, characterized by a negative temperature change, in adiabatic conditions, and, at constant temperature, by an increase of the total entropy of the system [57].

The analysis of the magnetocaloric effect in proximity of a first-order magnetic phase transition is not straightforward and it is still matter of heated debates and controversies, concerning the possibility to extend and properly use the Maxwell equations (2.7) and (2.10) also in the case of discontinuities in the first derivatives [58–62]. It seems, then, way better the use of the Clausius-Clapeyron relation.

The magnetic formulation of the Clausius-Clapeyron equation is given by the following expression [63]:

$$\Delta S_t = -\mu_0 \Delta M \frac{\Delta H}{\Delta T_t} \quad (2.11)$$

which, for infinitesimal field variation ($\Delta H \rightarrow 0$) and by introducing the latent heat of transformation ($L = \Delta E = T \Delta S_t$) between the two transforming phases, assumes the following form:

$$\Delta E = -T \mu_0 \Delta M \frac{dH}{dT_t} \quad (2.11)$$

The Clausius-Clapeyron relation (2.11) relates the transition entropy change to the shift of the transition temperature in magnetic fields and to the magnetization difference between the two phases; strictly speaking, the relation is correct only if the entire system is completely transformed.

Interestingly, the reformulation of Eq. (2.11) as follows:

$$\frac{dT_t}{\mu_0 dH} = -\frac{\Delta M}{\Delta S_t} \quad (2.12)$$

permits to recognize and analyse the driving force of the magnetocaloric effect [64]. Since the entropy change between the two phases, in a first-order phase transition, is always a positive quantity (second law of thermodynamics), in order to minimize the total Gibbs free energy, only the sign of ΔM , between the high and low temperature phases, plays the fundamental role in determining the direction of the transition temperature shift when a magnetic field is applied, thus the typology of

magnetocaloric effect. Accordingly, if the magnetic moment of the high-temperature phase is larger than that of the low-temperature phase, a positive ΔM triggers the shift of the transition to lower temperature by applying a magnetic field (which always stabilizes the phase with the highest total magnetic moment), and an inverse magnetocaloric effect is obtained.

When, instead, the low temperature phase has the largest magnetization, $\Delta M < 0$, the magnetic field stabilizes it to a higher temperature, and gives rise to a conventional magnetocaloric effect with a net heating of the system, due to the decrease of both the structural and magnetic entropy contributions, in isothermal conditions.

During the above-mentioned explanation of the magnetocaloric effect in correspondence of a first-order transformation, the presence of the thermal hysteresis, between the heating and cooling branches of the temperature dependent magnetization curves (Fig. 2.1-4), has been completely neglected, but it represents a crucial issue from the operational point of view, due to the drastic reduction of reversibility of the “giant” effect after the first thermo-magnetic cycle [64]. Indeed, after the switching of the magnetic field, the system cannot reach the initial state, because the entropy curves, in heating and cooling runs, do not coincide. This is highlighted, in the S-T diagrams of Figs. 2.1-7(a)-(b), by the small reversible adiabatic temperature change obtained under cycling (dashed area) as compared to the larger first field-induced one, for both direct and inverse magnetocaloric effects.

It is worth stressing that the presence of thermal hysteresis not only limits the reversible magnetocaloric performance of the material, but also imposes the selection of an adequate thermal protocol for the correct evaluation of ΔS_{iso} and ΔT_{ad} parameters [2,49,65–69].

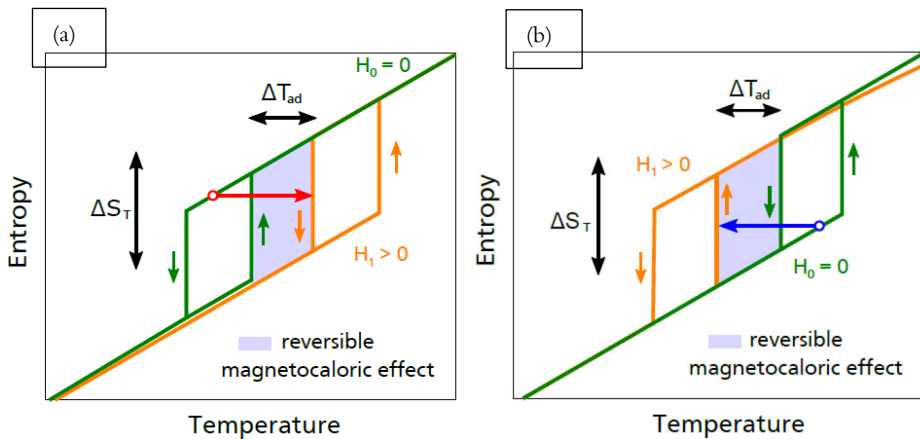


Figure 2.1-7: Representation of the real reversible (a) direct magnetocaloric effect and (b) inverse magnetocaloric effect, for first-order type magnetocaloric materials characterized by the onset of thermal hysteresis between the cooling and heating runs of the $S(T)$ curves [57].

2.2 HEUSLER COMPOUNDS

The Heusler compounds are named after the German chemist and metallurgist Friedrich Heusler, who, in 1903, discovered that an alloy with chemical composition $Cu_{50}Mn_{25}Al_{25}$ could exhibit ferromagnetism, even though none of its constituent is magnetic by itself [52]. From the early discovery of this material, many Heusler compounds, with general stoichiometric formula $X_{50}Y_{25}Z_{25}$, have been found out and investigated, over the last century, with great interest for the unique magnetic, electronic and multifunctional properties they show, by changing the number of valence electrons per formula unit (e/a) [9,70]. Today, the Heusler compounds constitute a wide class of intermetallic materials, with more than 1000 members, thanks to different possible combinations of elements, according to the colour scheme shown in the Periodic Table of fig. 2.2-1, where, usually, the X and Y are transition metals, like Ni, Co, Fe , and the Z elements belong to the III-V groups, as for instance In, Ga, Sn or Sb .

These intermetallic materials crystallize in the cubic $L2_1$ superstructure, with space group $Fm\bar{3}m$ (no. 225), consisting of four interpenetrating fcc sublattices, two of which are equally occupied by X atoms, at the Wyckoff positions $8c$ $(\frac{1}{4}, \frac{1}{4}, \frac{1}{4})$ and $(\frac{3}{4}, \frac{3}{4}, \frac{3}{4})$, while Y and Z atoms are located at $4a$ $(0, 0, 0)$ and $4b$ $(\frac{1}{2}, \frac{1}{2}, \frac{1}{2})$ sites, respectively [17], as shown in the schematic picture of Fig. 2.2-2.

X_2YZ Heusler compounds

H 2.20																	He	
Li 0.98	Be 1.57											B 2.04	C 2.55	N 3.04	O 3.44	F 3.98	Ne	
Na 0.93	Mg 1.31											Al 1.61	Si 1.90	P 2.19	S 2.58	Cl 3.16	Ar	
K 0.82	Ca 1.00	Sc 1.36	Ti 1.54	V 1.63	Cr 1.66	Mn 1.55	Fe 1.83	Co 1.88	Ni 1.91	Cu 1.90	Zn 1.65	Ga 1.81	Ge 2.01	As 2.18	Se 2.55	Br 2.96	Kr 3.00	
Rb 0.82	Sr 0.95	Y 1.22	Zr 1.33	Nb 1.60	Mo 2.16	Tc 1.90	Ru 2.20	Rh 2.28	Pd 2.20	Ag 1.93	Cd 1.69	In 1.78	Sn 1.96	Sb 2.05	Te 2.10	I 2.66	Xe 2.60	
Cs 0.79	Ba 0.89	Hf 1.30	Ta 1.50	W 1.70	Re 1.90	Os 2.20	Ir 2.20	Pt 2.20	Au 2.40	Hg 1.90	Tl 1.80	Pb 1.80	Bi 1.90	Po 2.00	At 2.20	Rn		
Fr 0.70	Ra 0.90																	
		La 1.10	Ce 1.12	Pr 1.13	Nd 1.14	Pm 1.13	Sm 1.17	Eu 1.20	Gd 1.20	Tb 1.10	Dy 1.22	Ho 1.23	Er 1.24	Tm 1.25	Yb 1.10	Lu 1.27		
		Ac 1.10	Th 1.30	Pa 1.50	U 1.70	Np 1.30	Pu 1.28	Am 1.13	Cm 1.28	Bk 1.30	Cf 1.30	Es 1.30	Fm 1.30	Md 1.30	No 1.30	Lr 1.30		

Figure 2.2-1: Periodic Table of Elements, in which are highlighted, according to the colour scheme, all the different possible combinations of elements forming an Heusler compound [9].

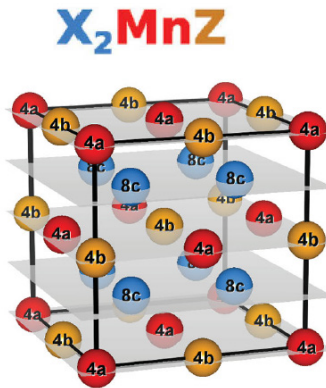


Figure 2.2-2: Unit cell of the Heusler $L2_1$ structure, corresponding to the $X_{50}Mn_{25}Z_{25}$ (or equivalently X_2MnZ) composition, where the Wyckoff positions 4a, 4b and 8c of Mn, Z and X atoms are marked with red, yellow and blue colours, respectively [71].

The cubic $L2_1$ superstructure is normally the Heusler crystal structure of the resulting phase after cooling (quenching or slow cooling rate) from high temperature, known as Austenite. Indeed, the compounds do not solidify directly from the melt to the Heusler structure and an annealing treatment, at high temperature, is always performed, in order to enhance homogenization, thanks to atomic diffusion [72]. On cooling, the austenitic $L2_1$ phase, characterized by next-nearest neighbour atomic

order, is reached through a disorder-order $B2 - L2_1$ phase transition, taking place at different temperatures depending on both composition and Z element [73]. In fig. 2.2-3(b), the disordered $B2$ structure, characterizing the high temperature phase above the transition temperature $T_t^{B2-L2_1}$, is presented beside the full ordered $L2_1$ one (Fig. 2.2-3(a)), and, by their comparison, it emerges that, due to the high atomic mobility at high temperature, the Y and Z atoms are equivalently distributed on both $4a$ and $4b$ sites and the unit cell can be regarded as a bcc crystal structure [70].

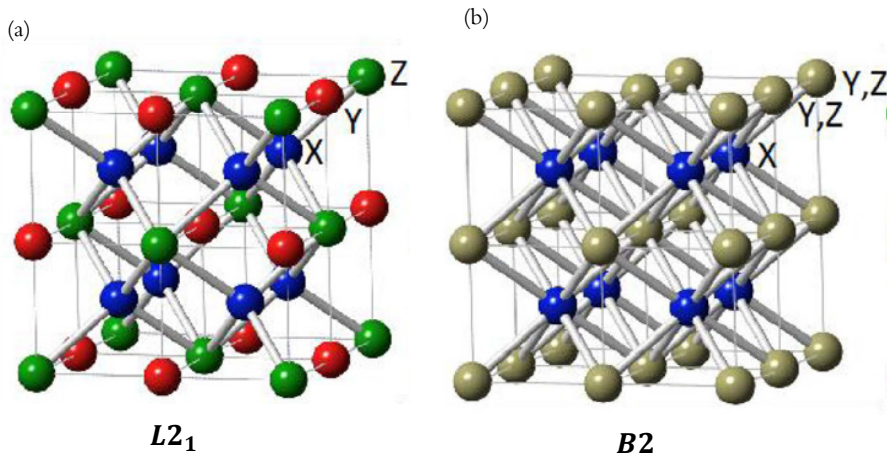


Figure 2.2-3: Comparison between the ordered Heusler $L2_1$ structure (a) and the disordered cubic structure $B2$ (b), where Y and Z elements are equivalently distributed on both $4a$ and $4b$ sites and cannot be distinguished [70].

When the Heusler compound is off-stoichiometry, such as for Mn -rich or X (= Ni)-rich compositions, the next-nearest neighbours atomic ordering is not well-established, due to the formation of anti-site disorder, and the retained $B2$ -like disorder (nearest-neighbours), after quenching, has significant consequences on both the magnetic properties and the structural phase transitions of the compound, especially in ferromagnetic Ni-Mn-based Heusler compounds, that undergo a first-order magneto-structural martensitic transformation [74,75].

In fact, in off-stoichiometric compositions and/or quaternary compounds of Ni-Mn-Z-W ($Z=In, Ga, Sn, Sb, Al$; $W=Co, Fe, Cu$), with the only exception of the stoichiometric $Ni_{50}Mn_{25}Ga_{25}$ system, the cubic Heusler Austenitic phase, stable at

high temperature, which can exhibit either ferromagnetic or paramagnetic behaviours, undergoes a tetragonal distortion, called ‘Le Bain deformation’, on cooling, transforming into a low symmetry Martensitic phase [76] (as shown in Fig. 2.2-4), where a different and often complex magnetic ordering is observed, depending on the composition [17,77].

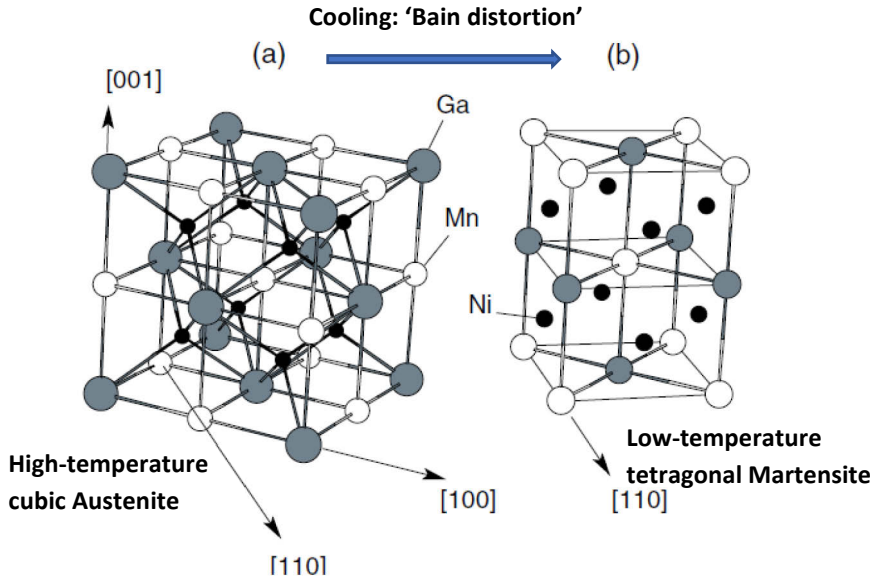


Figure 2.2-4: Schematic representation of the structural martensitic transformation, from the cubic Austenite, stable at high temperature, to the low symmetry (tetragonal) martensite, at low temperature, through the so-called Bain lattice distortion [75].

This first-order martensitic transformation has a diffusion-less character: the atoms of the austenite phase collectively shift a fraction of interatomic distances along the same direction (habit plane), through a shear-dominated mechanism, resulting in a macroscopic shape change [12]. As a result, interesting phenomena, such as the shape memory effect and the super-elasticity, are to it associated. Moreover, due to the decrease of crystal symmetry, the martensite is highly degenerate and forms multiple energetically equivalent variants, which, in absence of an external field breaking the degeneracy, are self-accommodated with twin related boundaries, in order to minimize the elastic strain energies [17,78]. Hence, a complex twinned

microstructure is generated, as schematically illustrated in Fig. 2.2-5 and experimentally observed by optical microscopy as in Fig. 2.2-6.

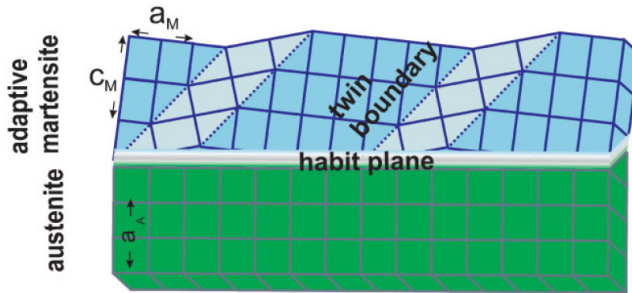


Figure 2.2-5: Schematic illustration of the formation of twinned martensite at the interface (habit-plane) with the parent austenitic phase [78].

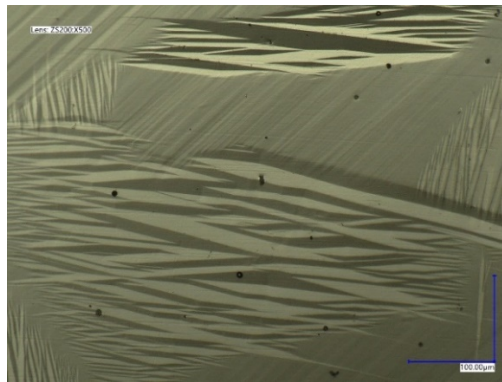


Figure 2.2-6: Experimental observation, with optical-microscopy, of the martensite microstructure of the $Ni_{45.7}Mn_{36.6}In_{13.3}Co_{4.2}$ compound [3], in which are visible regions of parallel stripes, characterizing the twin-related martensitic variants.

The thermoelastic martensitic transformation can be explained with reference to the difference in the total Gibbs free energy, between austenite and martensite, as a function of temperature [24,79,80], as schematically illustrated in fig. 2.2-7. The formation of the initial martensite embryos inside the parent austenite phase (forward transformation) starts below the equilibrium position T_0 , when the system is undercooled at the martensite start temperature M_s . Nuclei with radius and semi-

thickness above critical values spontaneously grow at constant radius and temperature, if they are not hindered by grain-boundaries and other energy barriers, thanks to the gain in the Gibbs free energy, with respect to the austenite phase, with the martensite volume increase, below M_s [80]. Further growth requires that the temperature be lowered in order to increase the available driving force; the full transformation from austenite to martensite is then achieved at the martensite finish temperature M_f . The chemical forces ΔG_{ch}^{P-M} are not the only ones acting and driving the process of transformation, but other two main non-chemical forces play a crucial role [79]. The accommodation of shape and volume changes takes place elastically, with elastic-energy storage ΔG_{el}^{P-M} , of internal stresses and strains, in form of microstructural defects, such as twinning and dislocations, that are reversibly released during the reverse transformation in heating. This is, indeed, the necessary and sufficient condition for thermoelastic behaviour. Upon heating, the reverse martensitic transformation requires an over-heating to the austenite start temperature A_s to be initiated and is accomplished above the austenite finish temperature A_f . The second contribution of the non-chemical energy arises from the energy dissipated as heat during the transformation, caused by the frictional resistance to the interface motion, either during growth or shrinkage of the martensite plates. Hence, the irreversible part of the energy supplied E_{irr}^{P-M} , in form of undercooling during the forward martensitic transformation or over-heating, during the reverse one, is responsible for the thermal hysteresis.

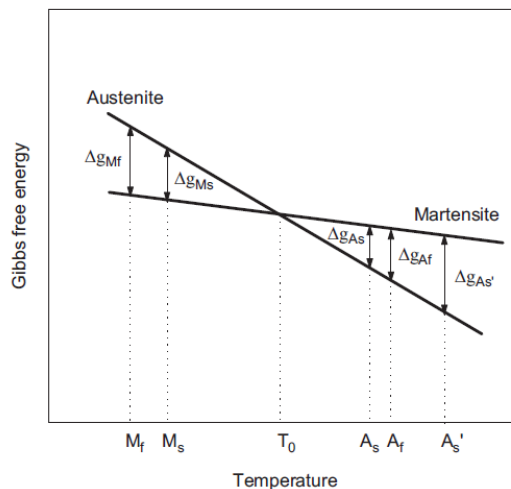


Figure 2.2-7: Schematic of the Gibbs free energy as a function of temperature, at a constant pressure, during the martensitic transformation. At the cross-section temperature T_0 the two phases are in equilibrium. The transformation from austenite to martensite (and vice-versa) initiates only with undercooling to M_s (and overheating to A_s) and proceeds till the martensite finish temperature M_f (and austenite finish temperature A_f)[81].

The latter, defined as $\Delta T_{hyst} = \frac{[(A_s + A_f) - (M_s + M_f)]}{2}$, is detected as the temperature difference between the heating and cooling branches, of the magnetization and/or calorimetric measurements as a function of temperature, across the martensitic transformation [82]. Indeed, in Ni-Mn-based Heusler compounds the martensitic transformation, apart from the structural change, is accompanied by a magnetization change, as it will be described below in this section. In fig. 2.2-8, it is shown, for instance, the behaviour of the magnetic susceptibility across the martensitic and Curie transition of Ni-Mn-In-Co compound. Following the cooling branch, indicated by the blue arrow, the austenitic phase, stable at high temperature and ferromagnetic below the magnetic Curie transition (T_C^A), undergoes a magneto-structural martensitic transformation (forward transformation T_{fwd}) by decreasing the temperature, below the martensitic start temperature (M_s), transforming into a weak-magnetic martensitic phase, below M_f . Upon heating, the reverse martensitic transformation, from the weak magnetic martensite to the ferromagnetic austenite, takes place between A_s and A_f , as indicated by the orange arrows, after a sufficient over-heating to $A_s > M_f$, because of the energy barriers (lattice mismatch) that need to be overcome. Therefore, the forward and reverse transformations do not overlap and a thermal hysteresis, indicated by the double-sided arrow, is observed.

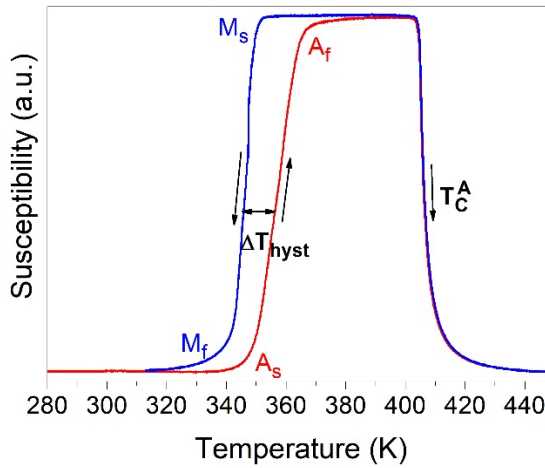


Figure 2.2-8: Temperature-dependent magnetic susceptibility for a bulk sample of Ni-Mn-In-Co Heusler compound. The metamagnetic martensitic transformation, characterized by a thermal hysteresis between heating and cooling branches, and the second-order magnetic Curie transition have been highlighted.

Depending on the Z element concentration, in Heusler compounds $Ni-Mn-Z$, the martensite phase can appear in a tetragonal $L1_0$ structure ($c/a > 1$), named non-modulated (NM), for low Z concentrations, or in its related modulated structures, 10M and 14M, also denoted as 5M and 7M, ($c/a < 1$), for higher Z concentrations. Here, ‘M’ refers to the monoclinicity resulting from the distortion, associated with the modulation [17,74,76,83]. Since the compounds with the martensitic modulated structures have shown outstanding properties, such as the largest recoverable strains, the lower twinning stress and the narrower thermal hysteresis, making them favourable for energy-conversion applications [11,19,21], a great effort has been spent to investigate and understand the origin of such modulation. The investigation of this mechanism, by neutron and X-ray diffraction measurements, have brought about two different competing explanations: according to Webster *et al.* [84], the modulation can be interpreted as an independent incommensurate modulated superstructure, that origins from a periodic shuffling of $(110)_A$ planes, due to the instability of the cubic austenitic phase, approaching the martensite start temperature on cooling. Conversely, in the framework of the adaptive concept introduced by Khachatryan *et al.* [85], the modulation consists of twinning at the nano-scale (nano-twinning) of the tetragonal martensite, in order to adapt and minimize the lattice strain along the invariant plane, and it is not regarded as a distinct structural phase but rather like a nano-scaled microstructure [78]. Beyond the origin’s explanation, it is worth stressing

that, for specific off-stoichiometric compositions, the NM tetragonal martensite and the modulated structure, mainly 10M and 14M, are observed to coexist in the low temperature phase, as, for instance, in the two selected Heusler compositions of Ni-Mn-Ga and Ni-Mn-In-Co, matter of study of the current Ph.D. research activity.

The magnetic properties of the ferromagnetic Ni-Mn-based Heusler compounds are strongly influenced by the degree of the long-range $L2_1$ atomic order and abruptly modify with the occurrence of the martensitic transformation, as displayed in fig. 2.2-8, due to the distance-dependence of the magnetic exchange interactions. Indeed, it has been found out by neutron scattering spectroscopy, that, for most of the Mn-based Heusler compounds, the magnetic moments, of nearly $4\mu_B$, are mainly localized on Mn atoms, and that, because of the large interatomic distances between nearest neighbours, do not interact directly but rather via an indirect Ruderman-Kittel-Kasuya-Yosida (RKKY) oscillatory exchange, mediated by the conduction sp electrons [86,87]. In the case of Co-doped Heusler compounds, also Co atoms carry a magnetic moment and contribute to the overall magnetization. However, the stabilization of the ferromagnetic ground state of both austenite and martensite phases depends on the overlap of different magnetic interactions (also Mn-Ni and Ni-Ni exchange interactions) [88]. Generally, a long-range ferromagnetic order can be established only for near-stoichiometric compositions, with high-degree of $L2_1$ atomic order, which results in a high Curie transition temperature of the Austenitic phase (T_C^A). By contrast, in presence of $B2$ atomic disorder, which can be induced by off-stoichiometric compositions, for example, with Mn-excess atoms, the magnetic moments of Mn on the sites of the Z element couple antiferromagnetically with the ones on the regular Mn sublattice, resulting in competing ferro- and antiferromagnetic interactions. This fact reduces the T_C^A value and gives rise to a magnetization drop across the martensitic transformation, due to the different interatomic distances and redistribution of the electronic structure in the tetragonally distorted lattice [77]. Hence, for the same typology of compound (i.e., Z element), different types of magnetic behaviours can be found for austenite and martensite phases, by simply changing the valence electron concentration per atom (e/a) and/or the degree of long-range atomic order. Indeed, peculiar phase diagrams Temperature vs Concentration are reported in literature [75]. With reference to the ones depicted in Fig. 2.2-9, in which, for each type of Heusler compound Ni-Mn- Z (Z =Ga, In, Sn, Sb), the *ab initio* calculations (blue and black lines and circles) have been compared with the experimental data (orange lines and circles), it can be seen that the martensitic transformation temperature M_s rapidly increases with increasing the e/a number, and the martensitic structure evolves in $10M \rightarrow 14M \rightarrow L1_0$, showing different magnetic ordering depending on the intersection with the line of T_C^M , which

instead decreases and it is expected to vanish for $e/a > 8$. Differently, T_C^A shows only little variation (decrease or increase depending on Z element) with e/a value [74,77,89]. Furthermore, it has been predicted and experimentally observed that the increase of atomic disorder and lattice strain, caused by the presence of Co-impurities, in addition to Mn-excess (i.e. Ni-Co-Mn-In, Ni-Co-Mn-Sn, Ni-Co-Mn-Ga-In, Ni-Co-Mn-Ga), leads to the formation of frustrated short-range and long-range magnetic interactions and complex spin configurations, such as noncollinear magnetism and super spin-glass behaviour, below the martensitic transformation temperature [90], which are responsible for structural instability and eventually phase decomposition [91].

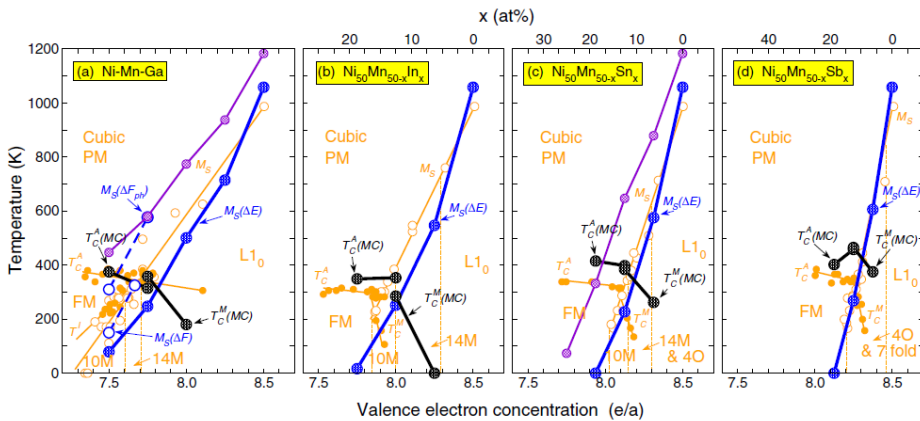


Figure 2.2-9: Phase diagrams of Ni-Mn-Z ($Z=Ga, In, Sn, Sb$) Heusler compounds, respectively, in which the orange lines and circle represent the experimental data obtained by structural and magnetic measurements, while the black and blues curves refer to the theoretical calculations [77].

The metamagnetic Ni-Mn-based Heusler compounds (i.e., $Ni_{45}Co_5Mn_{36.6}In_{13.4}$, $Ni_{50}Mn_{34}In_{16}$, $Ni_{43}Co_{12}Mn_{20}Ga_{25}$, $Ni_{50-x}Co_xMn_{39}Sn_{11}$) exhibit a martensitic transformation from a high temperature ferromagnetic austenite to a low temperature weak magnetic martensite, as shown in Fig.2.2-10(a) for Ni-Co-Mn-In compound, and they have been largely investigated for the characteristic magneto-structural and magneto-thermal properties, as for instance the giant inverse magnetocaloric effects and the giant magnetoresistance, observed by application of external fields. More recently, they have acquired a great interest for the possibility to modify their magnetic and structural properties through secondary annealing treatments, microstructural changes and crystallographic re-ordering [72,82,92–97]. Such

behaviour, on the one hand, points out the presence of different external tools for controlling and tuning the transition temperatures, and, on the other one, it highlights the complexity and richness of magnetic properties to investigate for the same metamagnetic compound, as for the Ni-Co-Mn-In one, whose phase diagram is shown in Fig.2.2-10(b).

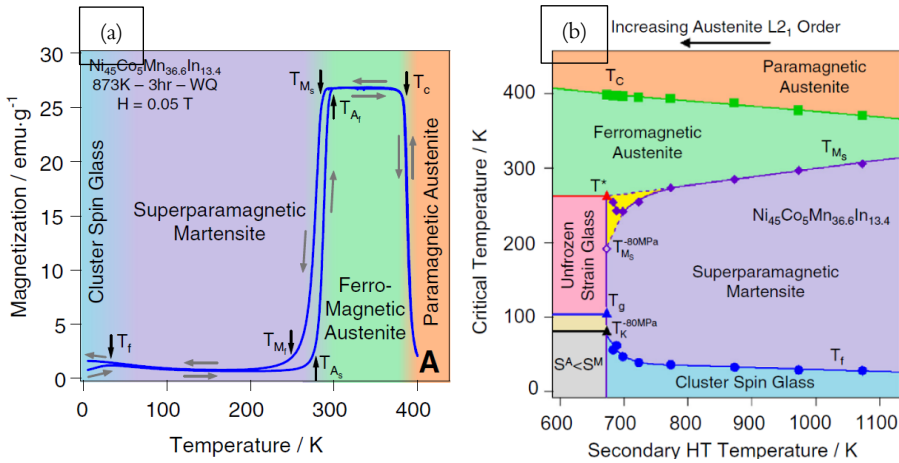


Figure 2.2-10: (a) Low-field temperature-dependent magnetization curve of $Ni_{45}Co_5Mn_{36.6}In_{13.4}$ bulk compound subjected to a secondary heat treatment (adapted from [97]). (b) Phase diagram of the corresponding sample showing the critical temperatures as a function of the temperature of the secondary annealing treatment and of the degree of $L2_1$ atomic order [97].

Conversely, Ni-Mn-Ga compound shows a ferromagnetic martensite with a high magnetic anisotropy, which enables an external magnetic field to drive outstanding magneto-mechanical effects at the meso-scale, such as the re-orientation of the martensitic variants and the magnetic shape memory effect [17], as schematically displayed in Fig.2.2-11.

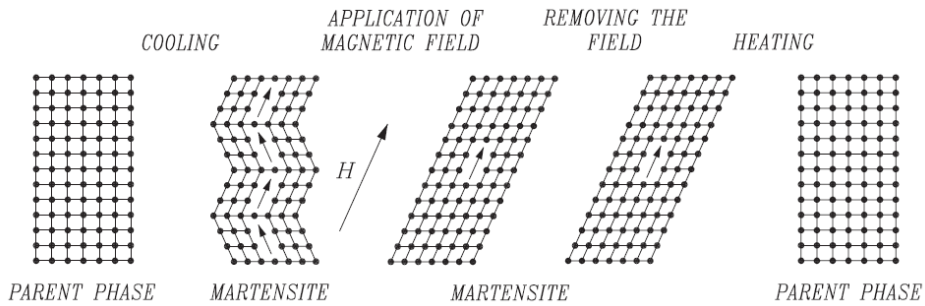


Figure 2.2-11: Schematic illustration of the magnetic shape memory effect taking place in a Ni-Mn-based Heusler shape memory compound. The application of the magnetic field leads to twin boundary motion and reorientation promoting the variants aligned in the field direction. After removal of the magnetic field, upon heating, the original austenite cubic phase is recovered [17].

Its peculiar phase diagram has been the first and most investigated one in the family of the magnetic shape memory Heusler compounds, during the last fifteen years. Such studies have brought about an exceptional high tunability of the magnetic and magneto-structural transition temperatures by changing the ratios of Ni/Mn or Mn/Ga concentrations, which, for specific compositional ranges, can lead to the coincidence between the structural martensitic transformation and the Curie transition of the austenite [14], resulting in a magneto-structural transformation from a ferromagnetic tetragonal martensite to a paramagnetic cubic austenite. This is highlighted in Figs. 2.2-12(a)-(b), where the phase diagram T-c (at. %) as a function of Ni concentration and the typical magnetic susceptibility response in correspondence of the magneto-structural coupling for the $Ni_{2+x}Mn_{1-x}Ga_1$ compound [14] are displayed.

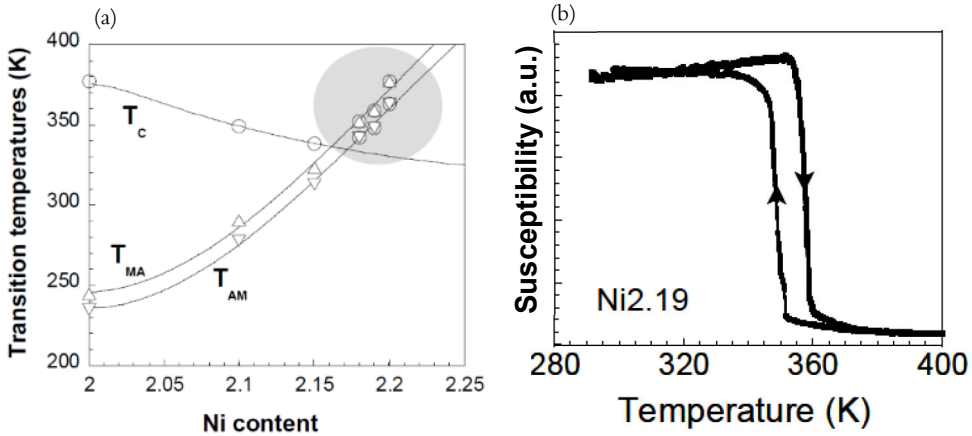


Figure 2.2-12: (a) Phenomenological phase diagram of the Curie transition of the Austenite (T_c) and Martensitic transformation temperatures in heating (T_{MA}) and cooling (T_{AM}) runs as a function of Ni concentration for Ni-Mn-Ga compounds. The grey area highlights the compositional ranges where the structural and magnetic transition temperatures coincide [14]. (b) Example of overlap between the Martensitic and Curie transformations for the specific Ni 2.19 composition [14].

2.2.1 Systems under investigation

In the following, a detailed presentation of the selected Heusler systems is given, including a discussion about the reasons that inspired this choice.

$Ni_{45}Mn_{37}In_{13}Co_5$ Heusler compound is currently one of the most studied and interesting magnetocaloric material, with potential application in the field of magnetic refrigeration technology, since it is characterized by a large inverse magnetocaloric effect around room temperature, where, as above-mentioned, a first-order martensitic transformation takes place, between a ferromagnetic cubic austenite and a weak-magnetic (paramagnetic or anti-ferromagnetic), low symmetry, martensitic phase, on cooling (and vice-versa in heating). Indeed, it has been reported by J. Liu *et al.* [16] and T. Gottschall *et al.* [98] of adiabatic temperature changes of $\Delta T_{ad} = -6.2$ K and -8 K, for the two effective compositions $Ni_{45.2}Mn_{36.7}In_{13}Co_{5.1}$ and $Ni_{45.7}Mn_{36.6}In_{13.5}Co_{4.2}$, respectively, under a moderate magnetic field of 1.9 T, which are remarkable large values for a rare-earth free material. However, these compounds show large thermal hysteresis, ranging from 10 till 20 K, depending on synthesis procedure and specific composition, which implies detrimental energy losses

during the martensitic transformation and irreversibility under application and removal of the magnetic field. In fact, the initial large adiabatic temperature changes reduce to a reversible value of only -1.3 K [16] and -3 K [98] under subsequent applications of the magnetic field, for the two corresponding compositions. Accordingly, the reduction of thermal hysteresis is the primary but still challenging requirement, for the efficient application of the first order magnetocaloric materials in magnetic refrigeration cycles. The reversibility of any caloric effect relies on the competition between the width of the thermal hysteresis and the sensitivity of the transition temperatures to the applied field [99]. Many works have been devoted to the study of the thermodynamic aspects governing the formation of the martensite phase, in order to figure out the mechanism causing and influencing the hysteresis [24,30,79,80,82,94,100], and to delineate some strategies to overcome or partially reduce the hysteresis problem [64,101,102]. Among them, rather than an external manipulation of the hysteresis width, it has been proposed to take advantage of the minor hysteresis loops, in which the transformation between martensite and austenite (major loop) is not completed. In fact, for sufficiently large shift of the transition temperature with magnetic field (high $\frac{dT_t}{\mu_0 dH}$), it is possible to obtain a reversible MCE under cycling, within a temperature range bounded by the forward transition temperature in zero field and the reverse transition temperature at applied magnetic field, in inverse magnetocaloric materials [64,98,99]. Another strategy, that, instead, allows to directly reduce the thermal hysteresis, consists in the simultaneous application of multi external stimuli, i.e. hydrostatic pressure, magnetic field, mechanical loading, in order to combine and exploit the multi-caloric response, such as the barocaloric, elastocaloric and magnetocaloric effects, of the multi-ferroic materials, namely $Gd_5Si_2Ge_2$ [102], $La(Fe, Si)_{13}H_x$ [103], $Fe_{49}Rh_{51}$ [54], and the family of Ni-Mn-In Heusler compounds [104]. Interestingly, it has been demonstrated, for the metamagnetic Ni-Mn-In-Co compound, which exhibits a conventional barocaloric effect and an inverse magnetocaloric effect, that by magnetizing at atmospheric pressure and demagnetizing at applied pressure, the effective hysteresis can be drastically reduced [16]. Finally, according to the geometrically non-linear theory of martensite [24], a significant drop of the thermal hysteresis, during the martensitic transformation, may be achieved by the optimization of the phase compatibility, at the interface between austenite and martensite phases. This can be essentially realized by tuning the composition, in order to minimize the lattice mismatch, due to the symmetry decrease between the two phases, and/or through microstructural engineering, such as optimal grain size and reduction of internal stresses and constraints, such as grain boundaries, dislocations, secondary phase

formation, point defects, which obstacle the growth and shrinkage of the martensite variants [19,24,27,94].

In fact, the propagation of the martensite phase is hindered by extrinsic microstructural energy barriers at the meso-scale, that may be pre-existing or created by the martensitic transformation itself. Consequently, the manipulation of the thermal hysteresis can be achieved by controlling the microstructure and morphology themselves, using specific thermo-mechanical processes [93].

Based on the latter method, in the current PhD research activity, it has been chosen to use the ball-milling technique and subsequent annealing treatments aimed at modifying the morphology and microstructure of the initial bulk compound, and investigating the evolution and change of the magneto-structural properties, as a function of particle's size, shape and microstructural defects. The study, indeed, could provide an insight on the dependence of the thermal hysteresis on the extrinsic microstructural features in metamagnetic Ni-Mn-In-Co compounds, highlighting the differences with respect to the bulk and coarse-grained material.

$Ni_{50}Mn_{25}Ga_{25}$ Heusler compound, instead, has attracted a lot of attention for the magnetic shape memory (MSM) effect, and the huge magnetic-field induced strains (MFIS), since their discovery by Ullakko *et al.* [105], two decades ago. The MFIS effect can be achieved by magnetic field induced reorientation of martensitic variants, through twin boundary motion, or by a magnetic field induced martensitic transformation (MFIT), and it depends on the crystal structure of the martensite [14]. The largest strains (up to 10%) have been found in near stoichiometric Ni-Mn-Ga compositions, showing modulated 10M and 14M structures, making these compounds interesting and promising for applications, like magneto-mechanically controlled actuators or dampers [10,11,14,17]. In order to find out the maximum MFIT effect, a great effort has been spent in exploring the peculiar phase diagram and the multi-functional properties, of this magnetic shape memory compound, by changing the composition. Interestingly, due to the high tunability of the magnetic and martensitic transition temperatures with slight compositional changes, it has been found that, for specific Ni and Mn concentration ranges, in Ni-rich $Ni_{50+x}Mn_{25-x}Ga_{25}$ compositions and Mn-rich $Ni_{50}Mn_{25+x}Ga_{25-x}$ compositions, respectively, it is possible to merge together the martensitic transformation and the Curie transition of the austenite, resulting in a strong magneto-structural coupling and transformation from a low temperature ferromagnetic martensite to a high temperature paramagnetic austenite, as, for instance, in $Ni_{50}Mn_{30}Ga_{20}$ compound [14,75]. Conversely to the case of the metamagnetic Ni-Mn-In-Co system, the ferro-elastic and ferromagnetic properties in $Ni_{50}Mn_{30}Ga_{20}$ Heusler compound are

coupled positively, resulting in a direct magnetocaloric effect and a positive adiabatic temperature change, by applying an external magnetic field [15]. However, the elevate transformation temperature prevents, in this case, to exploit the direct MCE for room-temperature magnetic refrigeration. In the attempt to decrease the transformations temperatures, still maintaining the coupling, it has been reported by D. Zhao *et al.* [15] and S. Stadler *et al.* [106], that by substituting small amount of Mn with Cu, in $Ni_{50}Mn_{25-x}Cu_xGa_{25}$ ($x = 5.5, 6, 6.5 \text{ at. \%}$), the martensitic transformation temperature (T_M) and the Curie transition temperature (T_C) can be concurrently increased and decreased, respectively, in such a way they overlap, close to room-temperature. For the peculiar Temperature (K)-Composition (at.%) phase diagram and high tunability of magneto-thermal, magneto-elastic and magneto-caloric properties, the two compounds $Ni_{50}Mn_{30}Ga_{20}$ and $Ni_{50}Mn_{18.5}Cu_{6.5}Ga_{20}$ have been selected as benchmark materials to investigate also at the nanoscale, in the shape of nano/submicron particles, prepared by the ball-milling technique. In addition to the already mentioned magnetic refrigeration and actuator applications, ferromagnetic nanoparticles of $Ni_{50}Mn_{18.5}Cu_{6.5}Ga_{25}$ could show new promising potentialities in biomedicine, such as for self-regulated magnetic hyperthermia treatment.

2.3 MAGNETIC HYPERTHERMIA

Among the biomedical applications, the magnetic hyperthermia represents one of the most on-going studied cancer therapies [32], which consists in the destruction of the cancerous cells, more sensitive to the increase of temperature than the healthy ones, by the heat dissipated from the magnetic nanoparticles subjected to an alternating magnetic field. The heating effect is generated by the magnetic losses due to different processes of magnetization reversal, which strongly depend on the physical properties of the particles, such as mean particle size, shape, crystallinity, and on the applied magnetic field characteristics (i.e., amplitude and frequency) [107]. Different types of hyperthermia have been investigated and already adopted for the clinical use, but they are commonly based on the whole-body treatment, which potentially can cause damages also in healthy tissue. Alternatively, the magnetically mediated hyperthermia emerges as a non-invasive and controllable procedure, offering different targeting methods of the magnetic nanoparticles, such as the arterial injection, direct injection into the tumor, in situ implant formation (in-situ sol-gel transition), active

targeting by functionalizing nanoparticles with the targeting ligands [108]. After exposure of the tumour to an alternating field, the advantage is to have a localized heat generation by magnetic relaxation mechanisms [109]. To guarantee the effectiveness of this therapy, the increase of temperature and the time of exposure to the magnetic field must be closely monitored, since temperatures higher than 42°C, which are required for the tumour cells treatment, can, on the other hand, apport permanent damages also in the healthy ones. In this perspective, the use of ferromagnetic nanoparticles undergoing the Curie transition temperature to the paramagnetic (weakly magnetic) state within the therapeutic temperature range 42–45°C is highly desirable and of great scientific and technological interest [110]. In fact, these particles could act like a self-controller, generating heat only when below the therapeutic temperature and avoiding excessive overheating, from which the name of self-regulated magnetic hyperthermia nanoparticles.

The main recent published works focus on the study and the use (in water, in cells and in *vivo*) of Fe, Co and iron oxide particles [107,109,111–113] and only a few ones suggest also the potentiality of different types of material, such as Ni-Cu, Ni-Pd, or Ni-Si alloys [110]. In this context, the Heusler nanoparticles of Ni-Mn-Cu-Ga compound could appear as a novel and potentially interesting material to be investigated since these compounds fulfil the two main requirements for such application: a high and abrupt magnetization change close to the human-body T, and a magneto-structural transition from a high moment to low/null moment phase, inducing the switch-off of the effect, at a slightly higher T, e.g., 42–45°C [107,109,110].

Prior their actual exploitation for biomedical purposes a lot of work is still required, such as testing and modelling the magnetic behaviour of the nanoparticles as a function of shape, size, concentration, and solubility in the liquid medium (water).

This motivates our research on the recovery and tunability of the T_C and magnetic properties at the nanoscale for the promising candidate Ni-Mn-Cu-Ga Heusler compound. As shown in section 4.4.3, it will be first assessed the effectiveness and feasibility of the top-down ball-milling method to obtain Heusler nanoparticles, and subsequently highlighted the influence of the size-dependent effect and atomic order degree on the magneto-structural behaviour and magnetic hyperthermia power.

3 EXPERIMENTAL TECHNIQUES

3.1 SAMPLE PREPARATION

The materials presented in this thesis have been prepared in the bulk and powder form, both in the laboratories of the Functional Material Group, at the Technical University of Darmstadt (TU Darmstadt, Germany) and in the laboratories of the Group of Magnetism, at the institute IMEM-CNR of Parma (Italy).

3.1.1 Arc-Melting furnace

The bulk materials described in Chapter 4 have been synthesized using the Arc-melting technique, in the form of button-like ingots and mass of 12-15 g. This is a wide used method for the preparation of intermetallic compounds, both on the industrial and laboratory scale, and it is based on the electric arc, generated by two electrodes, at high potential difference, in an inert gas (*Ar*) filled chamber, to heat and melt the single elements, forming an alloy. The tungsten tip, controllable from outside, acts as first electrode, while the water-cooled copper plate, in whose crucibles the elements are put, acts as the second-one electrode, as can be seen from the image reported in Fig. 3.1-1(a).

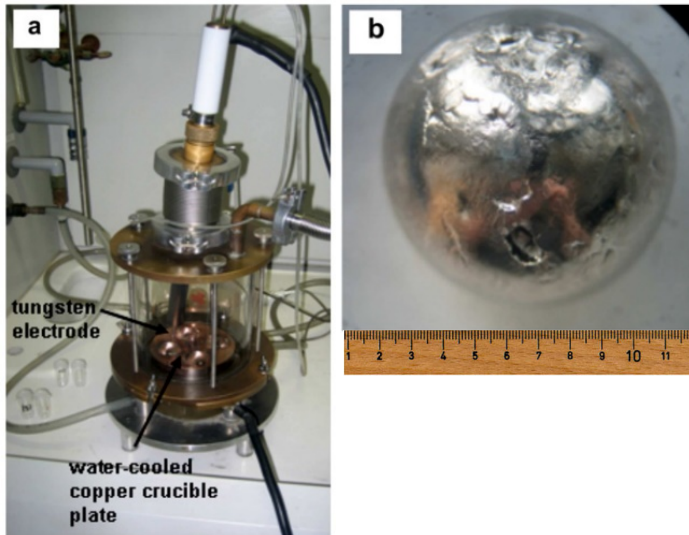


Figure 3.1-1: (a) Photograph of an arc-melter equipped with a tungsten electrode and a water-cooled copper crucible plate; (b) example of a polycrystalline Heusler ingot obtained after arc-melting (Images taken from Ref [9]).

The base elements used, Ni, Mn, Cu, Ga, In, Co, (depending on the composition), of high purity ($> 99.95\%$), were carefully cleaned with isopropanol, to avoid impurity contamination, cut and then weighted in the ratios of the desired stoichiometry. A particular cleaning procedure was adopted for Mn chips, whose surface was highly oxidized: they were arc-melted 3–4 times, in order to evaporate all the oxides, and, finally, obtain a single cleaned Mn ingot, which was, then, cut and added to the others elements of the alloy. In order to compensate for the Mn evaporation losses, the most volatile element, and keep the final composition as close as possible to the nominal one, an excess of Mn, equal to 1.5–3at%, was processed. All the elements were placed on the Cu crucible of the arc-melter and the melting procedure was conducted in a cleaned chamber filled with *Ar* (pre-evacuated and flushed several times, prior each procedure). The process was repeated 3/4 times, turning upside down the as-cast ingot each time, in order to uniformly melt it. An example of the resulting arc-melted Heusler ingot is shown in Fig. 3.1-1(b). After the melting procedure, a heat treatment, in a quartz tube, under protective Argon atmosphere, was performed, to enhance chemical homogeneity and attain the Heusler crystal structure. The ingots were wrapped in Ta foil to prevent oxidation, put it in a quartz tube and, after pumping and flushing in Ar several times, were annealed in a resistance furnace, in under-pressure of Ar. The thermal treatment was followed by a quenching in water. For

each sample, the temperature and duration of the thermal treatment were selected according to the usual annealing conditions, reported in literature, on the basis of the peculiar phase diagram of the compound, and they will be exposed in Chapter 4.

3.1.2 Ball-milling technique

The mechanical attrition or ball-milling technique is one of the possible top-down strategies to prepare nanoparticles, and consists in the gradual particle size reduction, down to the nano-meter scale, through repeated energetic collisions, between the starting coarse-grained powders and the moving balls, in a vial [114]. It is a widespread, cost-effective and reproducible method to prepare nanoparticles/nanostructures, with various shape and dimensionality [48] and it is employed to synthesize different kind of materials, including metals, alloys, organics and ceramics [47]. The mechanism of fracturing and grain refinement is a cold severe plastic deformation process, and, according to Fecht *et al.* [115] and Witkin and Lavernia [116], it can be described in three stages: initially, the deformation is localized in shear bands consisting of an array of high-density dislocations. At a certain strain level, these dislocations annihilate and recombine to form small-angle grain-boundaries, within the individual grains. Finally, the generated sub-grains are subjected to random orientation compared to the adjacent ones, implying grain rotation and formation of crystallite of small size (down to the nano-meter scale) [117]. Fig. 3.1-2 represents the schematic view of the mechanism involved during ball-milling to produce nano-sized grains.

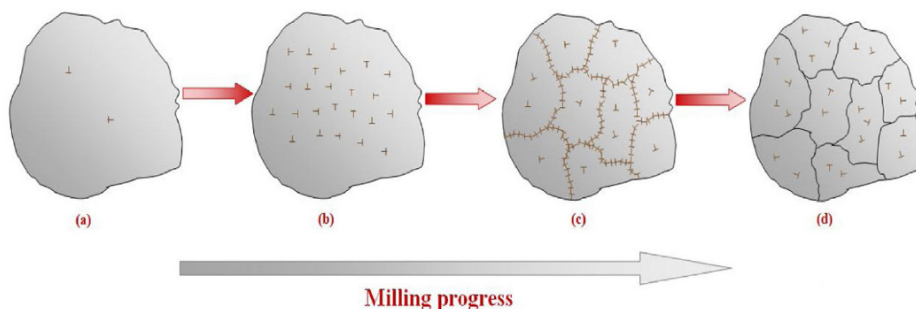


Figure 3.1-2: Schematic picture of the severe plastic deformation process, leading to the formation of nano-sized grains, during the ball-milling procedure [117].

Several different factors influence the milling process and must be optimized, in order to obtain the desired particle morphology and/or microstructure. Some of the most important parameters, that determine the final constitution of the powders, are listed below:

- the type of ball-mill
- the size and material of the grinding media (balls and jars)
- the ball-to-powder weight ratio
- the milling velocity
- the milling time
- the extent of filling the milling vial
- the milling atmosphere
- the use and amount of a process control agent.

It is worth noting that, during the ball-milling process, besides the fracturing, also the cold-welding, between the particles, takes place continuously, and must be balanced, in order to avoid suppression of particle's reduction. Indeed, by increasing the surface to volume ratio, the particles become more reactive, and, favoured by the significant local increase of temperature (even $> 1000^{\circ}\text{C}$, [114]), due to the heat dissipation as the milling proceeds, they have the strong tendency to agglomerate, being always in contact with each other, forming large micron-sized particles, and to adhere to the grinding media, i.e. vial and balls [118]. This is observed especially when ductile materials are milled, such as *fcc* metals and alloys [118], among which the Heusler compounds. In order to minimize the excessive cold-welding, and increase the fracturing rate, it is often introduced into the vial a suitable organic material, referred to as a process control agent or surfactant (surface-active agent), that, being adsorbed onto the surface, hinders the clean metal-to-metal contact and modifies the deformation mode of the particles.

In this PhD activity, each Heusler system was subjected to different ball-milling techniques, namely the planetary ball-milling, the vibration high-energy ball-milling and the shaker cryo-mill, and different conditions, i.e., dry, wet or with the surfactant-assistance, in order to analyse the effect of each method, and adjust the milling parameters, to avoid overheating and agglomeration, and obtain dispersed nano/submicron particles.

The planetary ball-milling is a device consisting of one or more vials, rotating around their own axes, arranged on a support disk, rotating rapidly in the opposite direction. The centrifugal and Coriolis forces drive the impacts among the grinding balls and

the material to be ground, resulting in comminution of the particles [119], as represented in Fig. 3.1-3(a). The technique allows the selection of the rotational speed, the number of milling cycles, the effective milling time and milling rest, and the possibility to mill in gaseous atmosphere (dry conditions) or with a liquid medium (wet conditions).

A Fritsch Pulverisette 7 (Fig. 3.1-3(b)) Planetary ball-mill was employed at the laboratory of Mechano-Chemical synthesis, of institute IMEM-CNR (Parma). It consisted of two working stations, with jars of useful capacity of 20 ml, and both jars and balls made of Agate or Zirconia. The jars could not be sealed, therefore the milling process was conducted directly inside a N_2 -filled glovebox, adding, in some cases, a liquid milling medium (isopropanol or n-heptane) in the vial, in order to avoid overheating and enhance particles' dispersion.

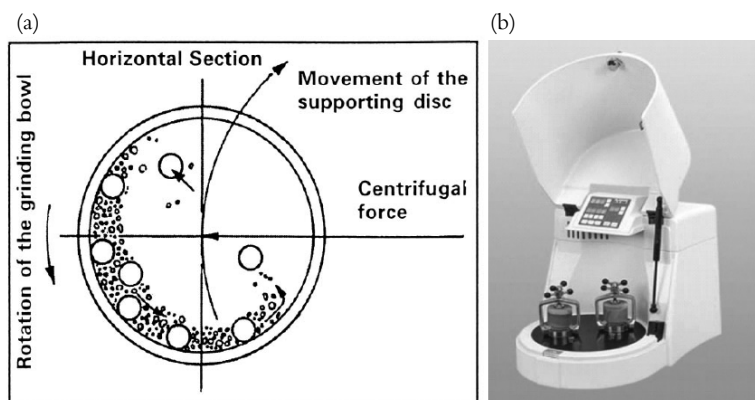


Figure 3.1-3: (a) Schematic representation of the ball motion and grinding process inside a planetary ball-mill [119]; (b) picture of the planetary ball-milling Fritsch Pulverisette 7.

The vibration ball-milling, employed at the technicum laboratory of the Functional Materials Group in Darmstadt, was a SPEX-8000 laboratory miller, that, in comparison to the Planetary ball-mill, generates a higher frequency of impacts and it can be considered as a higher energy ball-mill. Therefore, throughout the PhD thesis, it has been referred to as the high-energy ball-milling. It consisted of one vial of stainless steel of 50 ml capacity, containing grinding balls, of the same material, and the powder sample, that, secured in a clamp, swung energetically back-and-forth several thousand times per minute (about 1200 rpm), combined with lateral

movements of the ends of the vial. Because of the amplitude and speed of the clamp motion, it resulted in a high ball velocity and a great force of the ball's impact [119]. Differently from the planetary ball-milling, the maximum speed velocity could not be variated and only the effective milling time was set up. Moreover, the ball-milling was performed only in dry conditions, after sealing the jar in inert Ar atmosphere, inside a glovebox. In fig. 3.1-4, it is provided a picture of SPEX 8000 mixer/mill and a schematic process of particle refinement during the vibration ball-milling.



Figure 3.1-4: Example of a SPEX 8000 mixer/mill and schematic representation of the movement of the jar and consequently final result on the powders [120].

The cryo-milling or ball-milling at cryogenic temperature, employed at the technicum laboratory of the Functional Materials Group in Darmstadt, was a Retsch shaker cryo-mill, consisted of one jar, tightly clamped horizontally, performing radial oscillations at a frequency up to 30 Hz, while cooled with liquid nitrogen, from the integrated cooling system, before and during the grinding process [121] (Fig.3.1-5). The jar was made of stainless steel, with useful capacity up to 20 ml, and contained a single ball of 20mm of diameter, of stainless steel as well, and the powder sample, filled inside a glove-box, in order to seal it under protective Ar atmosphere. The ball-milling at cryogenic temperature combines the conventional mechanical attrition, due to the inertial impacts of the balls, with the advantage of the extremely low temperature, that increases brittleness and fracturing rate over cold-welding. Indeed, with respect to the planetary ball-mill or vibration high-energy ball-milling, in which

the temperature rise is an unavoidable problem, the extremely low milling temperature in cryo-milling suppresses the recovery and recrystallization processes, leading to finer grain structures and more rapid grain refinement [122].



Figure 3.1-5: Example of a Retsch shaker Cryo-mill connected to the liquid nitrogen dewar [121].

The strategy of the surfactant assisted ball-milling was trying in the planetary ball-mills, as an alternative to the dry and wet (liquid) conditions, adding to the fraction charge of particles, a suitable amount of oleic acid as surfactant, in weight percent (wt.%) with respect to the total powder mass, and n-heptane, as solvent. In general, any surfactant is characterized by an anionic, cationic, zwitterionic or non-ionic hydrophilic head, that is adsorbed onto the particle's surface, and a hydrophobic tail (generally derived from a hydrocarbon) that stretches away from the surface [118,123]. The high surface free energy of the particles is reduced by the organic layers of the surfactant molecules, thus preventing them from aggregation. The nature and amount of the surfactant tremendously affect the physical and chemical properties of the obtained particles. Normally, a large amount of surfactant may cover the whole surface area of the particles and impart more fracturing than cold-welding. However, the lubricating effect lowers the friction coefficient between the colliding balls and particles, which tend to deform and flatten, and, hence, it delays to longer milling times the fracturing, with the negative drawback of possible contamination from surfactant decomposition. Hence, the effectiveness of the surfactant-assisted ball-milling depend on the nature of the surfactant itself (chemical and thermal stability), on the inherent ductility and brittleness of the powders to be milled, on the milling duration and on the milling energy [118].

3.2 STRUCTURAL AND MORPHOLOGICAL CHARACTERIZATIONS

The samples obtained using the above-mentioned techniques were characterized with respect to their crystal structure, morphology, composition and microstructure, using the facilities of both the Functional Materials Group at TU Darmstadt, the laboratories at the institute IMEM-CNR of Parma and of the Chemistry and Physics departments, at the University of Parma.

3.2.1 Structural analysis

The crystallographic structure of the powder samples was analysed by means of X-ray powder diffraction, after sieving to select uniform particle size. Three different instrumentations were used. At TU Darmstadt, it was used a STADI P machine from STOE in transmission mode and θ - 2θ Bragg-Brentano geometry, with a Mo $K\alpha_1$ radiation source, to carry out the room-temperature measurements. The scanned angular range was fixed between 5° and 50° , with step-size of 0.01° . Moreover, Temperature-dependent XRD measurements were performed, between 20–450 K, using Mo $K\alpha$ radiation in transmission geometry on a custom-built setup with a Mythen2 R 1K detector (Dectris Ltd.). The sample was mixed with NIST 640d standard silicon powder for correcting geometric errors and glued on a graphite foil. The temperature was controlled by means of a closed cycle He-cryo-furnace. At the University of Parma, it was employed a Thermo ARL X'tra diffractometer, based on a vertical θ - θ Bragg-Brentano geometry, using the reflection mode and Cu $K\alpha$ radiation. The angular range was scanned between 24° and 95° , with step-size of 0.05° . The diffraction patterns were investigated by using the software Jana 2006 [124]: with the Le Bail refinement, the diffraction peaks were indexed, and the lattice parameters determined.

3.2.2 Morphological & Compositional analysis

In a SEM-FIB Zeiss Auriga Compact, equipped with an INCA Energy Dispersive X-ray Spectroscopy system, at IMEM-CNR, the microanalysis and the morphological study, of both bulk and powder samples, were carried out, in order to investigate both the chemical composition and homogeneity, and the particle's dimension and shape, after the different ball-milling processes. The bulk pieces were cut, with a diamond saw, in slices with plan-parallel surface and 1 cm length and few millimeter thickness and put directly on the carbon tape. With the EDX analysis, the composition was checked out in several regions of nearly 1.5 mm^2 . The hand-grinded and ball-milled powders, depending on their size and ball-milling method (dry/wet conditions, surfactant assistance), were either placed directly on the carbon tape or on a smooth Aluminum foil, after being dispersed and sonicated in isopropanol. The use of a smooth surface was especially required for the morphological SEM analysis of the smallest particles, that, otherwise, on the heterogeneous carbon tape structure, would be hindered. For the analysis of the global particle size distribution and shape uniformity, the electrons were accelerated with an high voltage (20 kV) and the SEM micrographs were obtained by the secondary electrons (SE), emitted by the near-surface regions of the sample. On the other hand, the detailed investigation of the surface morphology and microstructure was carried out selecting a lower electric voltage (5 kV) and using additional detectors, including the back-scattered electrons detector (BSE) and the filtered in-lens electron detector (In-Lens), in order to achieve a better contrast of the crystal grains and martensite lamellae.

3.2.3 Dynamic Light scattering Analysis

The qualitative evaluation of the presence of nanoparticles, in the batches of powders prepared by ball-milling in wet conditions and/or with surfactant-assistance, was carried out employing the Dynamic Light Scattering technique (DLS), using a Brookhaven Instrument 90 plus, with laser wavelength $\lambda=658 \text{ nm}$, at the Physics department, of the University of Parma. The technique is based on the scattering of a laser light at different intensity, caused by the motion of particles or molecules dispersed in a liquid, and it allows to measure the hydrodynamic radius of the suspended particles. Firstly, the ball-milled particles were dispersed in a solvent, i.e., isopropanol or n-heptane, by ultra-sound sonication; secondly, the supernatant suspension was centrifuged in order to separate the nanoparticles to the bigger ones;

thirdly, 3 ml of the smallest particles' dispersion were introduced in a plastic transparent cuvette and were analysed at room temperature.

3.2.4 Transmission Electron Microscope analysis

The morphological, structural and compositional analyses of the smallest particles, prepared with ball-milling, were investigated by means of Transmission Electron Microscopy, in scanning (STEM) and high-resolution modes (HR-TEM), using a JEOL 2200FS microscope operating at 200 kV, equipped with a EDAX micro-analyser, at IMEM-CNR. Few drops, of a pre-dispersed and sonicated particles' solution, were put on a Cu grid. By the selected area electron diffraction, the crystallinity of the achieved nanostructures was determined, while, from the STEM images, their shape and dimension were detected.

3.3 MAGNETIC CHARACTERIZATION

The magnetic characterization of both bulk and powder samples was carried out using the instrumentations of the Group of Magnetism, at IMEM-CNR and at the Physics department, of the University of Parma.

3.3.1 Thermo-Magnetic analysis

In a home-made low-field AC susceptometer, of the Group of Magnetism, at IMEM-CNR (Parma), the magnetic susceptibility, of both bulk and powder samples, was measured as a function of temperature, in heating and cooling branches, under a magnetic field of few Oersted (5-15 Oe), in order to detect the magnetic Curie transition and the magneto-structural martensitic transformation. The schematic design of a homemade AC Susceptometer is illustrated in Fig. 3.3-1: it consists generally of an input coil, a solenoid which generates an small alternating magnetic field, two pick-up coils, wound electrically in series opposition, which register the

induced voltage in the specimen, proportional to $-\frac{dM}{dt}$, and a compensation coil, that precisely balances the sensing unit in the ac susceptometer. The electro-motive force (emf) induced across ideal pick-up coils (i.e., wound with the same number of turns and in identical geometries), is zero in the absence of a sample. Inserting a magnetic sample, centred in one of the secondary coils, results in the generation of a non-zero signal, that is directly proportional to the AC susceptibility, $\chi = \chi' - j\chi''$, of the specimen [125]. In order to measure separately both the real or in-phase component χ' , and imaginary or out-of-phase component χ'' , a lock-in amplifier is used, which requires a reference signal at the same frequency and in phase with the current from the ac current source. The output is a magnified dc voltage proportional to its synchronous ac input signal, which can be detected and analysed on a computer software [126].

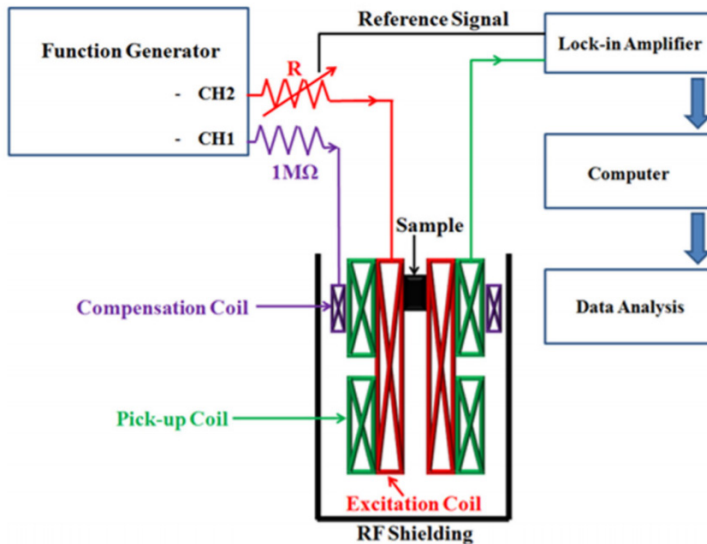


Figure 3.3-1: Schematic representation of a homemade AC susceptometer to measure the magnetic susceptibility as a function of temperature [127].

The sample space in the susceptometer described here was constituted by an over-wrap glass container and was connected to a vacuum rotary pump, enabling a medium vacuum (2×10^{-2} mbar at room temperature) to be achieved. For the measurement, the mass of the specimen was selected of around 20 mg and the rod, to whose bottom

end the specimen was attached, was immersed in liquid nitrogen, in order to start the measurement from cryogenic temperature. The temperature was increased by setting a constant sweep rate ($\frac{dT}{dt}$) of 0.10 V/min, till the maximum temperature value, required for the completion and observation of the magnetic Curie transition. In return, the minimum temperature reached was around room-temperature or slightly lower, due to the free cooling conditions in Argon. During the experiment, the vacuum was maintained in the chamber of the sample till the temperature of 273 K was reached; then it was switched to the over-wrap and the inert Ar gas was flushed on the sample, in order to guarantee a good thermal convection, but the thermal isolation with the external environment.

3.3.2 Extraction Magnetometer

The magnetization measurements as a function of temperature, and at fixed external magnetic field, were performed in the laboratory of Magnetometry, at the Physics department, of the University of Parma, using an Extraction magnetometer, whose picture is shown in Fig. 3.3-2. It consists of an electromagnet, which can generate up to 2 T, and a rod, with the sample encapsulated and connected to the bottom end, that is vertically inserted in the region of uniform magnetic field and, thanks to an electric motor, can be automatically extracted (~ 1 s) from the region, where two pairs of pick-up coils register the induced voltage, whose integration is proportional to the magnetic moment of the specimen. The samples, both in the bulk and powder form, were chosen of mass around 20-40 mg and were measured both at 10 mT and 1 T, selecting heating and cooling ramps, at constant sweep rate $\frac{dT}{dt}$ of 2 K min⁻¹, in order to ensure equilibrium conditions and to correctly study the magnetization behaviour and the thermal hysteresis, across the martensitic transformation. The measurements were conducted in a variable temperature range, between 80 K and 350 K, using a cryostat, cooled with liquid nitrogen, and were performed following the protocol of zero-field cooling, below the martensitic finish temperature M_f , field-warming up to 350 K and field-cooling, afterwards, or, alternatively, zero field heating, up to the maximum temperature of 350 K, field-cooling, till completion of the forward transformation and then field-warming.

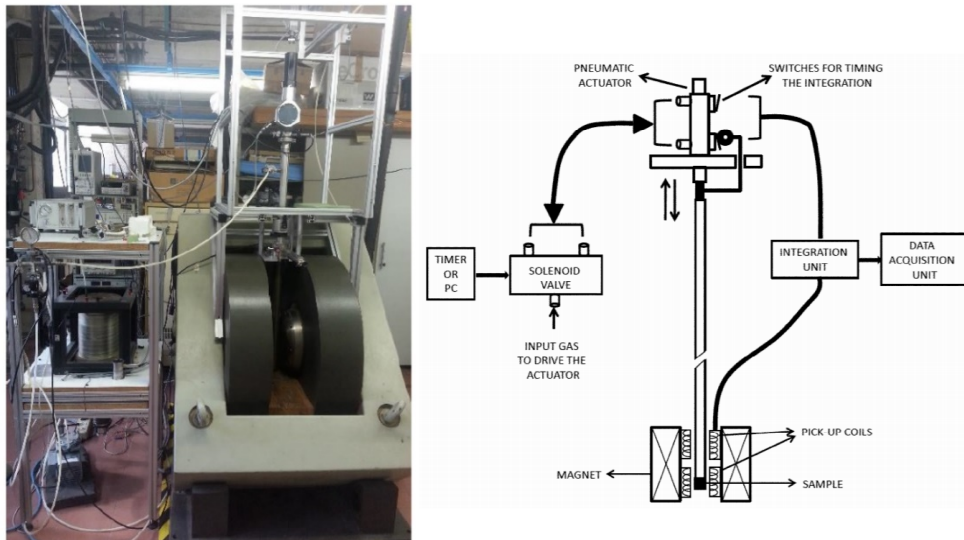


Figure 3.3-2: On the left, picture of the Extraction Magnetometer employed for the measurements and, on the right, schematic illustration of the fundamental parts and working principle of the instrument [128].

3.3.3 Vibrating sample Magnetometer

At TU Darmstadt, a vibrating sample magnetometer, from LakeShore, was used to characterize the magnetization as a function of temperature, in low (5 mT) and high (1 T) magnetic field of bulk and powder samples. It generally consists of an electromagnet, that generates a uniform magnetic field in the sample space, and a vertical rod, connected to a vibration head, holding the sample at the bottom end. Due to the vibration of the magnetic sample inside the uniform region, a variation of the external magnetic field is created in the pick-up coils, placed nearby, inducing a sinusoidal voltage. The amplitude of the ac voltage is proportional to the sample magnetic moment and measured by a lock-in amplifier. For the measurement, a cryostat was installed in order to scan the temperature range, from liquid nitrogen temperature, up to 450 K, at a fixed temperature ramp rate of to 2 K/min.

3.3.4 SQUID Magnetometer

In order to magnetically characterized also small amounts of fine powder and to investigate the magnetic behaviour of some powder batches, down to few Kelvin, a Superconducting Quantum Interference Device (SQUID), of the type Quantum Design MPMS-XL5, was used, at the laboratory of Magnetometry, of the Physic department (University of Parma). SQUID magnetometers are typically used to measure tiny magnetic moment thanks to an extremely high sensitivity. It detects the change of magnetic flux, created by mechanically moving the sample through a superconducting pick-up coil, which is then converted to a voltage, proportional to the sample magnetization. In this thesis, iso-field magnetization curves ($M(T)$) as a function of temperature were measured, between 400 K and 6 K, at a constant sweep rate of 2 K min^{-1} , in field cooling and field-cooled-warming procedures, under an applied low (0.5 mT) and high (1 T) magnetic field.

3.4 MECHANICAL COMPRESSIVE TEST

The mechanical response under compression of the bulk Ni-Mn-Cu-Ga and Ni-Mn-In-Co samples was characterized by compressive stress-strain measurements, at room-temperature, using a Instron 5967 Universal Testing Machine, at the Technical University of Darmstadt.

The sample's specimens were prepared in shape of rectangular blocks, having a cross-sectional area of $2.5 \times 2.5 \text{ mm}^2$ and a height of 5 mm, with flat, parallel surfaces, forming 90° angle between each other. The strain was monitored via a strain gauge, attached to compression tools directly next to the sample, while the stress was applied via a 30 kN load cell. The measurements were repeated on three specimens of the same sample to attain a good reliability of the results.

3.5 MAGNETIC HYPERTHERMIA MEASUREMENTS

The magnetic hyperthermia measurements were carried out on post-milling annealed micrometric and sub-micrometric particles of Ni-Mn-Cu-Ga, as it will be described

in Chapter 4, using a DM100 Series laboratory instrumentation of the nB nanoScale Biomagnetics.

The setup consists of a coil producing an alternating magnetic field, with a variable frequency, ranging from 149.5 to 429 kHz, and a magnetic field amplitude up to 300 G. A glass cuvette ($V=1\text{mL}$) containing a solution of the magnetic particles is introduced into the copper coil, which is cooled by circulating water. The system is thermally insulated with a vacuum jacket of 10^{-6} mbar by a turbomolecular vacuum pump. The temperature increase of the sample is generated by the dissipation as heat of the energy absorbed through the magnetic coupling between the external magnetic field and the magnetic moment of the particles. It is probed with an optical-fibre thermometer and recorded every 0.7 s.

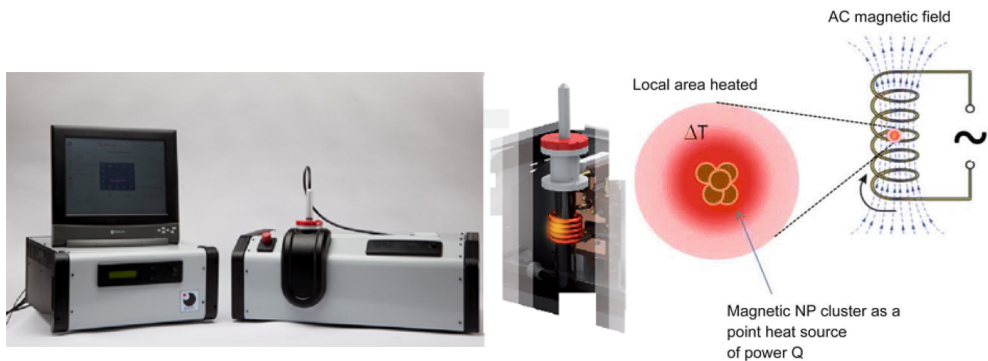


Figure 3.5-1: Example of nB DM 100 Series setup for magnetic hyperthermia laboratory measurements. On the righthand, insertion of the magnetic nanoparticles in the region of the alternating magnetic field (coil), thus generating heat dissipation and local increase of temperature.

4 RESULTS

This Chapter is organized in different sub-chapters to illustrate the experimental results obtained during the preparation and characterization of the bulk materials, and, subsequently, of the achieved powder samples, after hand-grinding and several adopted ball-milling techniques. The starting bulk materials are examined in respect to their composition, magneto-thermal and magneto-structural properties. The hand-grinded powders are analysed from both the structural and magnetic point of view, before and after the application of annealing treatments, to study the effects of size reduction, lattice defects, and assess the recovery of phase transformations as compared to the bulk. This serves as reference for the subsequent investigation of ball-milling and annealing treatments effects on micro- or sub-micrometric ball-milled particles. In distinct sub-chapters, for each Heusler compound, the different selected ball-milling methodologies are presented, and their effects described, with a systematic analysis of morphology, microstructure, structure, and magnetic behaviour of the achieved particles. Then a study on the optimization of the annealing conditions to promote and assess the recovery of the magnetic and magneto-structural phase transitions is reported. The resulting magneto-thermal properties are compared between the different batches of short or long-milled particles and correlated to the peculiar morphological and microstructural features. This is aimed at identifying and, possibly, understanding the extrinsic driving mechanisms and the size-dependent effects on the coupled magneto-structural or metamagnetic martensitic transformation.

4.1 ANALYSIS OF BULK MATERIALS

The bulk Heusler compounds were prepared by Arc-melting technique, as explained in Chapter 3 sect. 3.1.1, in the following amount and nominal compositions: one ingot of $Ni_{45}Mn_{37}In_{13}Co_5$ of 15 g mass, one ingot of $Ni_{50}Mn_{30}Ga_{20}$ of 13 g mass and one ingot of $Ni_{50}Mn_{18.5}Cu_{6.5}Ga_{25}$ of 12.5 g mass. The ingot of Ni-Mn-In-Co compound was subjected to an annealing treatment of homogenization at temperature of 900°C, for a duration of 24 h, based on the work

of T. Gottschall in Ref. [57], while the ingots of Ni-Mn-Ga and Ni-Mn-Cu-Ga compounds were heat treated at 850°C for 72 h, according to the literature papers of F. Albertini *et al.* [14,129] and S. Stadler *et al.* [106]. For the purpose of the PhD research activity, an additional bulk sample of Ni-Mn-In-Co, with nominal composition $Ni_{46}Mn_{37}In_{13}Co_4$, was employed, courtesy of MUSP (Machine Tools and Production Systems Laboratory, Piacenza, Italy), whose specific synthesis procedure is extensively described in Ref. [3]. In Tab. 4.1-1, the nominal and effective compositions of the bulk materials are listed, together with the specifications of Mn-excess processed and thermal treatment applied, for each arc-melted sample.

Nominal Composition Bulk compound	Effective Composition (EDX Analysis)	<i>e/a</i> number	Mn- excess	Thermal Treatment
$Ni_{45}Mn_{37}In_{13}Co_5$	$Ni_{44.5}Mn_{37.9}In_{12.6}Co_5$	7.928	+ 3 wt. %	24h- 900°C+WQ
$Ni_{46}Mn_{37}In_{13}Co_4$	$Ni_{45.7}Mn_{36.9}In_{13.2}Co_{4.2}$	7.927	Ref. [3]	Ref. [3]
$Ni_{50}Mn_{30}Ga_{20}$	$Ni_{49.4}Mn_{30.3}Ga_{20.3}$	7.670	+ 3 wt. %	72h- 850°C+WQ
$Ni_{50}Mn_{18.5}Cu_{6.5}Ga_{25}$	$Ni_{49.7}Mn_{18.7}Cu_{6.4}Ga_{25.2}$	7.739	+ 1.5 wt. %	72 h- 850°C+WQ

Table 4.1-1: List of the Heusler compounds prepared and/or used during the ball-milling process, with specifications of nominal and the effective compositions, number of valence electron concentration per atom (*e/a*) and characteristics of preparation, as the Mn excess and thermal treatment.

The bulk Heusler samples were analysed by means of Energy Dispersive X-ray Spectroscopy (EDX Analysis) to estimate the effective final composition (Tab. 4.1-1). From the atomic concentration (at. %) of each element, the valence electron concentration per atom (*e/a*) was calculated, considering that the transition metals Mn, Co, Ni and Cu provide 7,9,10 and 11 valence electrons, respectively, while the main group elements In and Ga have only 3 valence electrons. The effective compositions were calculated by averaging on several regions of the specimen, as described in the Experimental Techniques (sect. 3.2.2) and the obtained standard deviations were comparable to the instrumental error of 1 at. %, for each element, in all the specimens.

The bulk fragments of $Ni_{49.4}Mn_{30.3}Ga_{20.3}$ have shown a temperature dependence of the AC magnetic susceptibility as the one depicted in Fig. 4.1-1. Following the heating run, it is noted the occurrence of the magneto-structural martensitic transformation in proximity of 360-370 K, as indicated by the increase of the magnetic susceptibility (upward red arrow), from the low-temperature, high anisotropic [130] martensitic phase, to the high temperature, lower anisotropic cubic ferromagnetic austenite, which, immediately after, transforms to the paramagnetic state with a drop to zero of the susceptibility signal, due to the vicinity in temperature of the Curie transition.. However, two distinct slopes of the susceptibility on the Curie transition are detected and marked with $T_{C,1}^A$ and $T_{C,2}^A$ in figure, where the second one is coupled with the martensitic transformation, as revealed by the non-coincidence of the heating and cooling branches and appearance of a small thermal hysteresis. The predominant thermal hysteresis is, instead, detected between the forward ($T_{fwd,1}$) and reverse ($T_{rev,1}$) martensitic transformation at temperatures below $T_{C,1}^A$. Hence, the coupling between the structural martensitic and magnetic Curie transitions, which is peculiar of the $Ni_{50}Mn_{30}Ga_{20}$ composition [14,75], is not perfectly matched and homogeneous in the current bulk sample. This can be ascribed to small compositional variations and/or presence of internal microstructural stresses, originated by the thermomechanical history of the sample. This behaviour, in fact, has been also observed and reported in literature by F. Albertini *et al.* [14,129,130] for similar compositions. Hence, with respect to the ideal shape of the TMA plot, with a single hysteretic Martensitic-Curie transition, from a ferromagnetic martensite to a paramagnetic austenite, the real susceptibility plot appears to be an intermediate situation between the schematic behaviours displayed in the upper right part of Figure 4.1-1. The list of transition temperatures, for the bulk sample of $Ni_{49.4}Mn_{30.3}Ga_{20.3}$, is reported in Table 4.1-2.

Bulk sample:	T_{rev} (± 2 K)	T_{fwd} (± 2 K)	T_C^A (± 2 K)	ΔT_{hyst} (± 4 K)
Ni_{49.4}Mn_{30.3}Ga_{20.3}	$T_{rev,1} = 360$	$T_{fwd,1} = 357$	$T_{C,1}^A = 367$	3
	$T_{rev,2} = 375$	$T_{fwd,2} = 372$	$T_{C,2}^A \cong T_{rev,2}$	3

Table 4.1-2: List of the experimental values of the transition temperature, obtained by thermo-magnetic analysis for the bulk sample of $Ni_{49.4}Mn_{30.3}Ga_{20.3}$ Heusler compound.

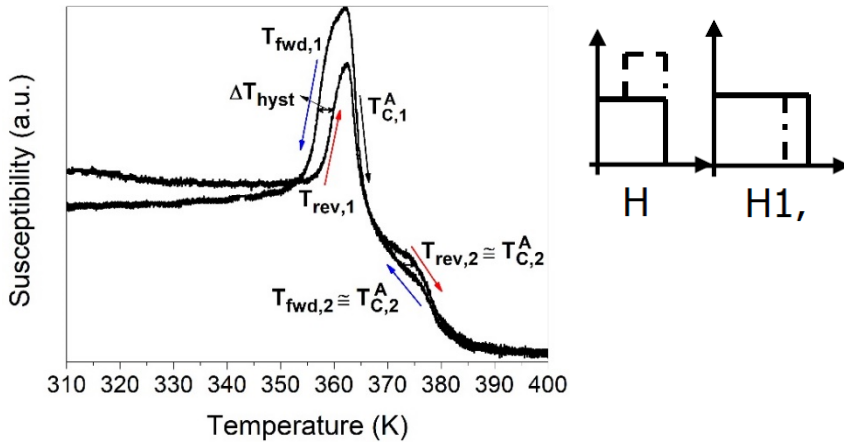


Figure 4.1-1: Temperature dependence of the magnetic susceptibility for the $Ni_{49.4}Mn_{30.3}Ga_{20.3}$ bulk sample, showing the vicinity or coincidence between the martensitic transformation temperatures (T_{rev} , T_{fwd}) and the Curie transition temperature of the austenite (T_C^A). Top-right side: theoretical TMA plots, where the solid and dashed lines stand for the heating and cooling curves, respectively.

The thermomagnetic analysis of the bulk sample $Ni_{49.7}Mn_{18.7}Cu_{6.4}Ga_{25.2}$ has revealed, as expected, the coincidence near room temperature of the structural martensitic transformation and magnetic Curie transition of the austenite [131]. Indeed, by the AC magnetic susceptibility behaviour displayed in Fig. 4.1-2, it can be seen that, starting from an initial ferromagnetic martensitic phase, the sample, upon heating, undergoes a single hysteretic transition, transforming into the paramagnetic austenitic phase, due to the coincidence in temperature with the Curie transition of the austenite. Due to the first-order character of the structural transformation, between the heating and cooling branches it appears a thermal hysteresis. In the top-right hand side of the figure, it has been sketched the ideal thermo-magnetic plot, which is similar to the real one. The thermomagnetic analysis was performed on several different fragments, to check out the chemical homogeneity and hence the uniformity of the magneto-structural behaviour. All the measured fragments showed the same magnetic susceptibility behaviour, with little evidence of secondary phases/inhomogeneities, and small discrepancies, (within the error bars), of the transition temperatures, with each other.

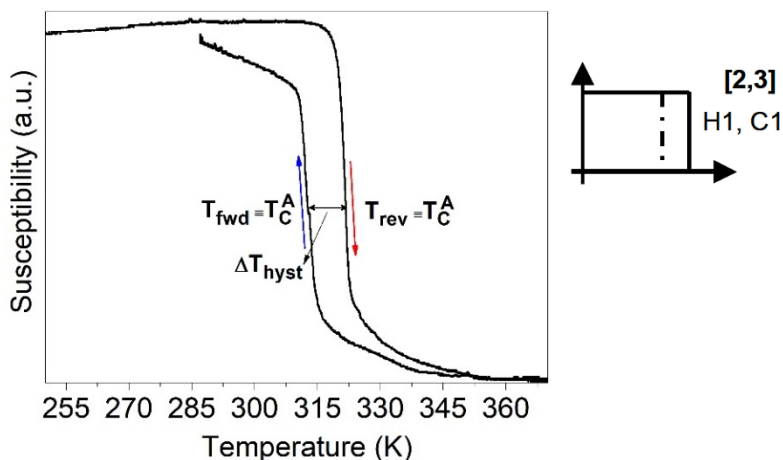


Figure 4.1-2: AC magnetic susceptibility as a function of temperature, for the $Ni_{49.7}Mn_{18.7}Cu_{6.4}Ga_{25.2}$ bulk sample and comparison with the ideal TMA plot (top-right side).

Bulk sample:	A_s (± 2 K)	A_f (± 2 K)	M_s (± 2 K)	M_f (± 2 K)	T_C^A (± 2 K)	ΔT_{hyst} (± 4 K)
Ni_{49.7}Mn_{18.7}Cu_{6.4}Ga_{25.2}	319	324	315	309	322	9

Table 4.1-3: Summary of the experimental values of the martensitic and Curie transition temperatures of the bulk sample of $Ni_{49.7}Mn_{18.7}Cu_{6.4}Ga_{25.2}$.

The other two examined Heusler compounds (Table 4.1-1), with composition $Ni_{44.5}Mn_{37.9}In_{12.6}Co_5$ and $Ni_{45.7}Mn_{36.9}In_{13.2}Co_{4.2}$, presented a sharp metamagnetic martensitic transformation (see section 2.2.1), close to room temperature, well-separated from the Curie transition of the austenite, in agreement to the well-known magneto-structural behaviours reported in published works [95,98,132]. The magnetic susceptibility behaviour of the first Ni-Mn-In-Co compound, prepared by arc-melting, is displayed in Fig. 4.1-4. The measurement shows only the heating branch, in which it is visible an abrupt increase of the magnetic susceptibility, across the reverse martensitic transformation $T_{rev} \approx 277.8$ K, passing from a non-magnetic martensitic phase to a ferromagnetic austenitic phase. On further increasing the temperature, a sharp drop of magnetic susceptibility is detected in correspondence of the Curie transition of the austenite, at $T_C^A \approx 409.6$ K.

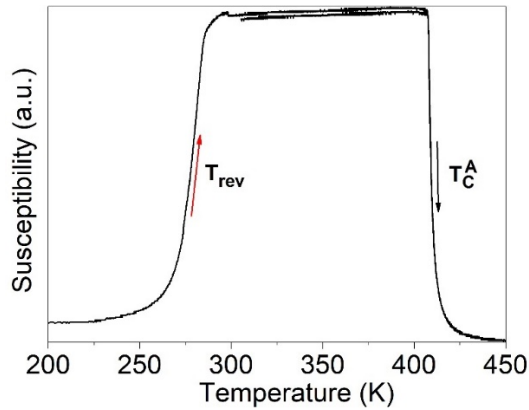


Figure 4.1-3: Low-field AC magnetic susceptibility as a function of temperature for the arc-melted sample of $Ni_{44.5}Mn_{37.9}In_{12.6}Co_5$. The thermomagnetic analysis plot shows the reverse martensitic transformation in heating, from a non-magnetic martensite to a ferromagnetic austenite and, at higher temperature, the Curie transition of the austenite.

In order to detect and study the martensitic transformation during the cooling branch, some specimens of the arc-melted Ni-Mn-In-Co sample were measured in a SQUID magnetometer, down to 10 K, in Field-Cooling and Field-Cooled-Warming procedures, under a magnetic field of 0.5 mT. The low-field magnetization curve $M(T)$ is shown in Fig. 4.1-5. It is visible that at high temperatures the ferromagnetic austenitic phase is stable, while, on decreasing the temperature to the martensite start temperature (M_s), the forward martensitic transformation takes place. This proceeds with formation and movement of the habit planes between parent and product phases, till completion of the martensitic variants' growth through the accessible volume at the martensite finish temperature (M_f). Below this point, a non-magnetic or weak-magnetic martensitic phase is observed. On the reverse process, upon heating, the austenite phase starts to be recovered after sufficient overheating to the austenite start temperature (A_s), though shrinkage of martensitic plates, till completion above the austenite finish temperature (A_f). Because of the energy dissipation during the phase front motion, a thermal hysteresis ΔT_{hyst} accompanies the martensitic transformation, as it is observed as the difference in temperature between the forward and reverse paths, highlighted by the double-sided arrow.

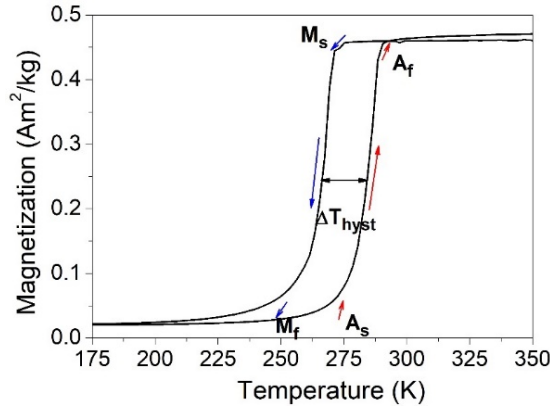


Figure 4.1-4: Magnetization measurement as a function of temperature of $\text{Ni}_{44.5}\text{Mn}_{37.9}\text{In}_{12.6}\text{Co}_5$, under a low magnetic field of 0.5 mT. The $M(T)$ curve shows the metamagnetic martensitic transformation, associated with a thermal hysteresis (ΔT_{hyst}) between the heating and cooling branches.

Different bulk specimens, coming from different slices of the same sample, have been measured by thermo-magnetization and susceptibility measurements. The obtained results have shown some variability in the martensitic transformation temperatures, especially in cooling, larger than 2 K, and, in some cases, also a shift by 6 K to higher temperature of the Curie transition temperature. These differences can be related to the presence of small compositional inhomogeneities and/or different degrees of atomic order inside the bulk material. In the first row of Table 4.1-4 are reported, as an example, the experimental values of the martensitic transformation and Curie transition temperatures obtained for one of the measured bulk fragments.

Bulk samples:	A_s (± 2 K)	A_f (± 2 K)	M_s (± 2 K)	M_f (± 2 K)	T_C^A (± 2 K)	ΔT_{hyst} (± 4 K)
$\text{Ni}_{44.5}\text{Mn}_{37.9}\text{In}_{12.6}\text{Co}_5$	274	294	275	248	407	22
$\text{Ni}_{45.7}\text{Mn}_{36.9}\text{In}_{13.2}\text{Co}_4$	277	294	276	260	393	17

Table 4.1-4: Martensitic transformation temperatures in heating (A_s, A_f) and in cooling (M_s, M_f), thermal hysteresis (ΔT_{hyst}) and Curie transition temperature of the austenite (T_C^A) for the bulk sample of $\text{Ni}_{44.5}\text{Mn}_{37.9}\text{In}_{12.6}\text{Co}_5$ and $\text{Ni}_{45.7}\text{Mn}_{36.9}\text{In}_{13.2}\text{Co}_{4.2}$ compounds.

The second compound, with effective composition $Ni_{45.7}Mn_{36.9}In_{13.2}Co_{4.2}$, synthesized with the method explained in Ref. [3], showed the ac magnetic susceptibility ($\chi_m(T)$) and magnetization ($M(T)$) behaviours, as a function of temperature, similar to the ones above described for $Ni_{44.5}Mn_{37.9}In_{12.6}Co_5$ arc-melted compound. In fig. 4.1-6, it can be seen the large positive change of magnetic susceptibility, between the austenite start A_s and austenite finish A_f temperatures, and, at a higher temperature, the sharp drop to zero, at the Curie transition point of the austenite.

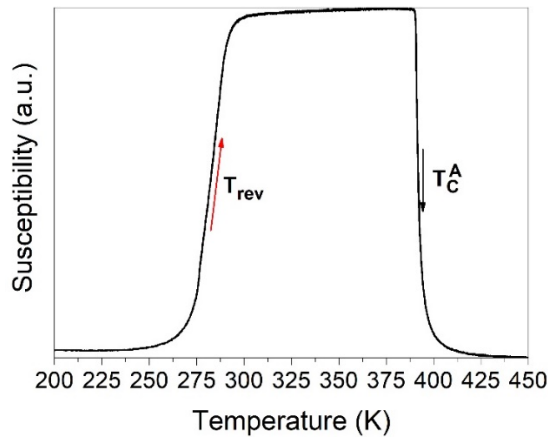


Figure 4.1-5: Magnetic susceptibility as a function of temperature for $Ni_{45.7}Mn_{36.9}In_{13.2}Co_{4.2}$ sample. The plot shows the reverse martensitic transformation below room-temperature, and, at a higher temperature, the Curie transition of the austenite.

As shown in Fig. 4.1-7, the martensite phase starts to form below 270 K and finishes at around 250 K, as indicated by the gradual decrease of the magnetization on cooling down to almost a zero magnetic value, and it is accompanied by a thermal hysteresis between the heating and cooling branches (Table 4.1-4).

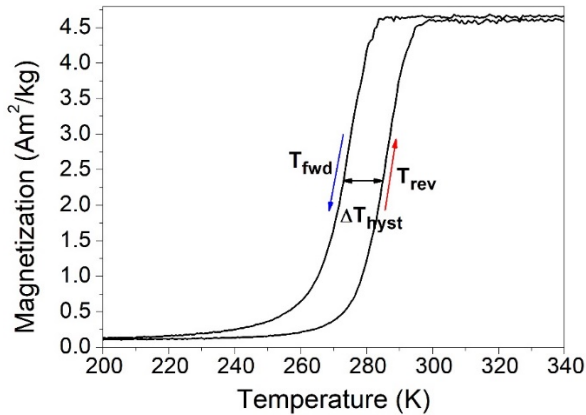


Figure 4.1-6: Temperature-dependent magnetization, at applied magnetic field of 100 Oe, for the $Ni_{45.7}Mn_{36.9}In_{13.2}Co_{4.2}$ bulk sample. The $M(T)$ curve shows a large magnetization change across the metamagnetic martensitic transformation, accompanied by a thermal hysteresis between cooling and heating branches.

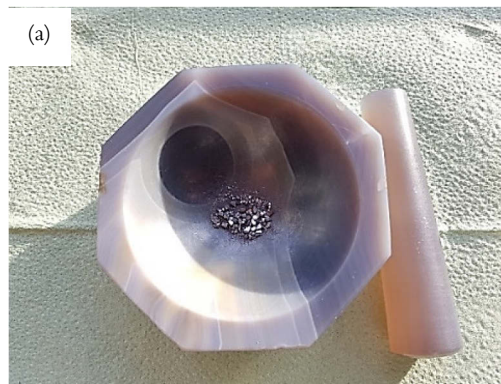
With respect to the other sample of composition $Ni_{44.5}Mn_{37.9}In_{12.6}Co_5$, having only a slight increase (+ 0.01%) of the total valence electron number per atom (e/a), for $Ni_{45.7}Mn_{36.9}In_{13.2}Co_{4.2}$ it was found a significant decrease of the Curie transition temperature ($\sim 17-18$ K below the average Curie transition temperature reported in Tab. 4.1-4) and of the thermal hysteresis (lower than the 39.9 %), without any significant change of the martensitic transformation temperatures. On the one hand, the decrease of stability of the ferromagnetic order in the austenitic phase can be understood by considering the effect of decreasing Co impurities on the Ni sites, carrying a magnetic moment in addition to the Mn ones. Indeed, it has to be noted that the Co atoms contribute to strengthen the ferromagnetism, through the large, positive, magnetic exchange integrals between Co-Co atoms, Co- Mn_Y atoms (Mn atoms on Y-sublattice), Co- Mn_Z atoms (Mn on In-sublattice) and Co-Ni atoms, as reported by P. Entel *et al.* in [90] through theoretical calculations on the magnetic exchange interactions. On the other hand, the magnetic interactions strongly depend on the degree of long-range atomic order achieved after the annealing procedure for homogenization of the sample, and the remanence of some disorder and the random distribution of Mn atoms on both Mn and In sublattices can result in a decrease of the Curie transition temperature. Furthermore, also the overall In content in the Heusler unit cell may play an important role on the final value of the Curie temperature, as shown by D. Salas *et al.* [96] that bulk $Ni_{45}Co_5Mn_{50-x}In_x$ compounds having a larger In concentration present a lower T_C^A . Instead, the decrease

of the thermal hysteresis, without a shift to higher or lower temperatures of the martensitic phase transformation, points out an improvement of phase compatibility in the compound, which can be related to an improved chemical homogeneity and/or favourable microstructure, such as grain size and/or presence of texture (crystallographic preferred orientation), obtained by the different synthesis protocol, consisting in starting from compacted powders [3]. It will be shown that the presence of compositional inhomogeneity and atomic disorder in the bulk has important consequences on the properties of the powders prepared by hand grinding and ball-milling methods.

4.2 ANALYSIS OF THE HAND-GRINDED POWDERS

While only a few bulk fragments were used for the characterization of the magnetic and magneto-structural properties, the larger part of the initial sample was reduced to powders, for the structural characterization, by Powder X-ray diffraction, and for the subsequent ball-milling procedures.

The powders were hand-grinded (HG) in an agate mortar, as depicted in Fig. 4.2-1(a), after removal of the defected surface, to avoid the use of the oxidized and more inhomogeneous parts.



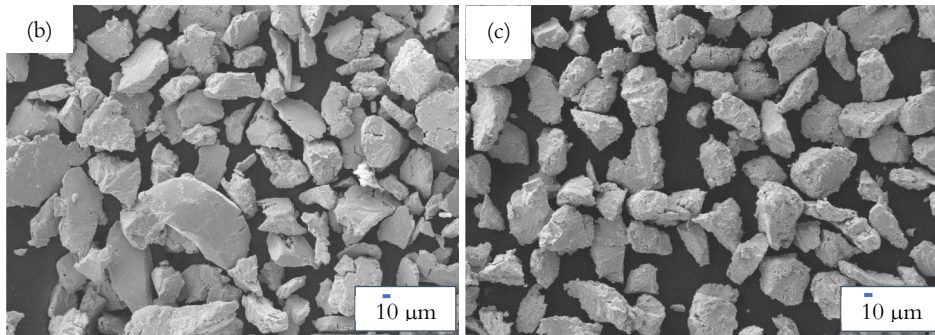


Figure 4.2-1: (a) Picture of fragments of bulk sample to be ground in an agate mortar. (b) and (c) SEM images of the hand-grounded powders of Ni-Mn-Ga and Ni-Mn-In-Co compounds, respectively.

4.2.1 Mechanical Characterization

During the hand grinding process, it was observed a different mechanical response and deformation mechanism between the Ni-Mn-(Cu)-Ga systems and the Ni-Mn-In-Co one. It resulted that the fragments of Ni-Mn-Ga and Ni-Mn-Cu-Ga were more difficult to crush and reduce into powder of micro-meter size as compared to the ones of Ni-Mn-In-Co compound. In fact, as visible in Fig.4.2-1(b), the Ni-Mn-Ga HG particles has the tendency to deform laterally and get thinner, while those of Ni-Mn-In-Co break into chunk and small pieces, as shown in Fig. 4.2-1(c). These phenomena have been ascribed to the peculiar compressive stress-strain behaviours highlighted by the mechanical compressive tests, on the two Heusler materials of Ni-Mn-Cu-Ga and Ni-Mn-In-Co, which will be presented hereafter.

At room temperature, where both the manual crushing procedure and the mechanical tests were carried out, the Ni-Mn-Cu-Ga system is found in the martensitic phase (see Fig. 4.1-5) while the Ni-Mn-In-Co one is in the austenitic phase (see Fig. 4.1-9). This has an important consequence on the mechanisms triggered by the external applied load, as it can be seen by the different obtained stress-strain curves for the two systems, in Figs. 4.2-2(a)-(b), respectively.

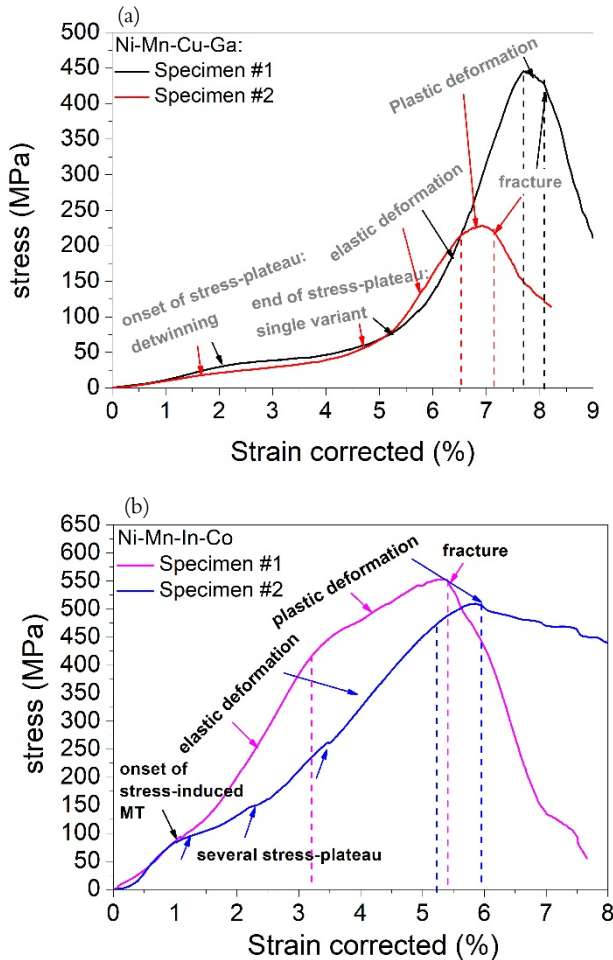


Figure 4.2-2: Stress-strain curves, under compressive load, at room-temperature, (a) for two specimens of Ni-Mn-Cu-Ga and (b) two specimens of Ni-Mn-In-Co bulk samples.

In Fig. 4.2-2(a), for the Ni-Mn-Cu-Ga system, there are reported two curves where the red one is referred to a specimen presenting a significantly larger amount of defects on the surface, as compared to the first specimen (in black line). In both cases, the compressive fracture curve can be divided in four stages: 1) at the beginning of the deformation, a linear monotonic increase of stress with increasing strain is observed till about 1.7% and 2% strain, for the red and black curves, respectively; then a stress-plateau is recognized, till about 4.7% and 5.5% strains; a subsequent further increase of the stress with increasing deformation up to 6.5% and 7.6% is detected; and a final

plastic deformation leading to fracture, after a compressive strain of 7.2% and 8.1%. This deformation mode is typical of the twinned martensitic shape memory materials under compression [133] and it can be described as follows. The initial self-accommodated martensitic phase with twin-related martensitic variants, at the onset of the stress-plateau, undergoes a detwinning process, where the variants aligned in the direction favourable (parallel) to that of the applied compressive load grow at expenses of the other ones, through the twin boundaries motion. At the end of the stress plateau a single martensitic variant is formed. This then starts to deform elastically, in the linear regime, and, after a small plastic deformation, it breaks down. The latter behaviour is more enhanced for specimen 1, showing then a higher elasticity and fracture resistance, which has to be ascribed to the better homogeneity of the surface and lower density of defects.

In Fig. 4.2-2(b), even for the Ni-Mn-In-Co system, there are reported the mechanical responses of two specimens, which, instead, differ in the microstructural texture (grains' crystallographic orientation). In this case, starting to hard and deform elastically the austenitic phase, after increasing the strain up to 1% the specimens undergo the onset of the stress-induced martensitic transformation. However, for the specimen 1 (magenta line), it is not visible a stress-plateau as for specimen 2 (blue line), but rather a steep and linear increase of stress up to 425 MPa with increasing strain to 3.3%. On the other hand, the specimen 2 does not show a single stress-plateau but several partial stress-plateaux, each of them followed by the linear increase, in the elastic regime of stress, over a large strain-range up to nearly 5.5%. Then, while for specimen 1 a plastic deformation between 3.3% and 5.5% strain, followed by a sudden fracture and subsequent linear decrease of stress-strain curve, are observed, for specimen 2, the plastic deformation, recognizable for strain up to 6%, is succeeded by a gradual and slight decrease of stress, for further increasing strain. These different behaviours can be reconducted to a different grain orientation between the two specimens, where for specimen 1 the random distribution of grain orientation results in a higher constrained effect, hindering the stress-induced martensitic transformation and the accommodation of the stresses in an easier way. In specimen 2 the stress-induced MT is more pronounced, but it is not homogeneous in the sample, depending on the local internal resistance to the movement of the phase interface (habit plane) between austenite and martensite, which, in turn, results in a slower nucleation and propagation of the cracks.

On the basis of this analysis, it can be seen that the two Heusler compounds, which are both quite brittle materials, differ in the process of accommodation of strains, and, for instance, for the same strain level of 6%, Ni-Mn-In-Co breaks while Ni-Mn-Cu-Ga shows an elastic deformation, after the detwinning process. The obtained results

are in good agreement with the published experimental data [134–137] and can reasonably explain the above-mentioned observations during the hand grinding process.

4.2.2 $\text{Ni}_{49.4}\text{Mn}_{30.3}\text{Ga}_{20.3}$: a comparison between hand-grinded and bulk samples

In figure 4.2-3, it can be observed the diffraction pattern, collected at room-temperature, for the hand-grinded powders of $\text{Ni}_{49.4}\text{Mn}_{30.3}\text{Ga}_{20.3}$, and the fitting with three different crystal phases. The reflections reveal that, at room temperature, the structure is predominantly tetragonal (*bct*) referred to as the NM martensitic phase (green bar lines), but there is also presence of a small fraction of monoclinic-distorted 7M modulated martensite (orange bar lines), responsible for the gap between the two consecutive peaks of the NM martensite, M(112) and M(200), and an almost negligible percentage of a cubic austenitic phase, whose few and low-intense peaks have been identified as a $L2_1$ superstructure, for the presence of the (111) superlattice reflection (magenta bar lines). The presence and the negligible intensity of the cubic reflections can be related to a residual small fraction of untransformed austenite, below the coupled magneto-structural martensitic transformation temperature, which, on cooling, is expected at around $T_{fwd} \approx 357$ K (see Fig. 4.1-1). The unit cell parameters, of the three refined crystal phases, have been summarized in Table 4.2-1.

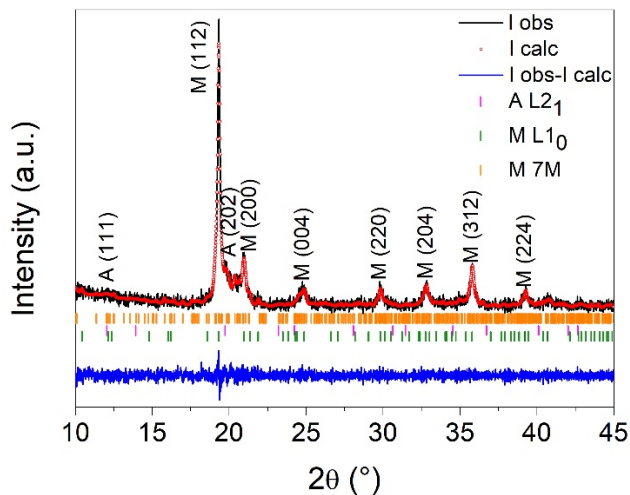


Figure 4.2-3: XRD pattern collected at room temperature for the hand-grinded powder of $Ni_{49.4}Mn_{30.3}Ga_{20.3}$. The observed intensity (black line) is presented together with the calculated one (red circles), while the coloured bar lines identify the Bragg reflections of the fitted crystal phases.

$Ni_{49.4}Mn_{30.3}Ga_{20.3}$ HG powders	Before annealing	@ RT:	
	After ann4h@600°C+WQ @ 400 K:	@ T<100K:	@ T<350 K:
Crystal Phases	A fcc L2₁	M bct L1₀	M 7M modulated
Space group	$Fm\bar{3}m$ (no.225)	$I4/mmm$ (no. 139)	$P2/m(\alpha 0\gamma)00$ (no. 10)
a (Å)	5.849 (0.007)	3.8961 (0.0007)	4.2325 (0.0005)
b (Å)	5.849 (0.007)	3.8961 (0.0007)	5.5215 (0.0005)
c (Å)	5.849 (0.007)	6.584 (0.002)	4.2751 (0.0005)
α (°)	90	90	90
β (°)	90	90	93.35 (0.01)
γ (°)	90	90	90
q (Å ⁻¹)			0.2947 (0.0009) α*

Table 4.2-1: Crystallographic data, obtained by the Le Bail refinement of XRD measurements of hand-grinded powders of $Ni_{49.4}Mn_{30.3}Ga_{20.3}$, before annealing treatment, at room-temperature, where a mixture of all phases has been found out, and after the heat treatment (for 4h at 600°C), where at different temperatures and temperature ranges one or more phases have been detected. The letters 'A' and 'M' stand for Austenite and Martensite phases, respectively.

In order to investigate the possible changes of martensitic transformation behaviour and temperatures with the mechanical stresses induced during hand-grinding, the

thermo-magnetic analysis was performed also on the HG powder. As shown in Fig. 4.2-4 by the temperature-dependent magnetic susceptibility curve in comparison to the bulk's one, the HG powder presented an increase of the sample's fraction transforming with coupled martensitic and Curie transitions at temperature around 375 K. Interestingly, the broadening of this coupled magneto-structural transition is equal to that of the original bulk sample. Hence, the only significant change relies on the increase of the phase fraction transforming at higher temperature, which, possibly, can be connected to the requirement of a larger overheating to overcome the microstructural energy barriers imposed by the grain-size refinement and the introduction of point defects.

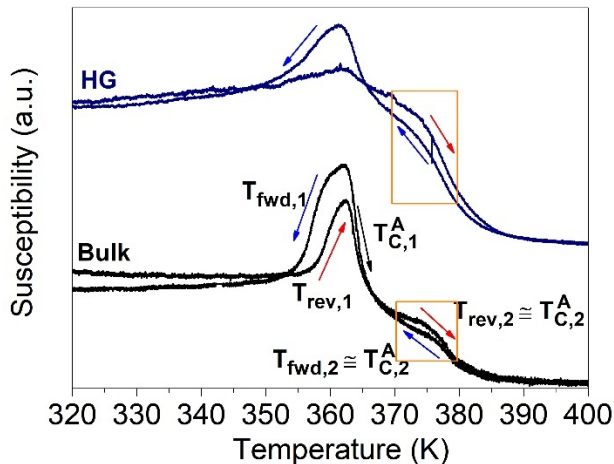


Figure 4.2-4: Comparison between the temperature-dependent magnetic susceptibility of the powders as-hand-grinded (black curve) and the bulk fragment (blue curve) of $\text{Ni}_{49.4}\text{Mn}_{30.3}\text{Ga}_{20.3}$. The region highlighted in orange shows the coupling between the structural martensitic transformation and the magnetic Curie transition of the austenite.

Successively, the powders were subjected to three different heat treatments, in a resistance furnace, inside a quartz tube filled with Ar gas, for releasing the induced lattice deformations and defects, and for studying the best conditions to recover, or even improve, the original magneto-structural properties. Hence, time, temperature and cooling rate of the thermal treatment were selected and varied. The first annealing treatment was performed at $T_{a,1} = 500^\circ\text{C}$ for a duration of $t_{a,1} = 1\text{h}$, followed by water quenching (WQ); the second one, instead, was performed at $T_{a,2} = 600^\circ\text{C}$, for

a longer annealing time of $t_{a,2} = 4\text{h}$, likewise followed by water quenching; the third one was, instead, run at the same temperature of the first annealing $T_{a,1} = T_{a,3} = 500^\circ\text{C}$, for the same duration of the second one $t_{a,2} = t_{a,3} = 4\text{h}$, but followed by a slow cooling rate (SC) in the furnace. In figure 4.2-5, the resulted ac magnetic susceptibility curves, of the powders after the annealing, are shown, as a function of temperature. By comparing the different curves among each other and with respect to the vertical dashed lines, indicating the temperatures at which the separated or coupled martensitic and Curie transitions are observed in the bulk, it is noted that none of the annealed powders present the hysteretic transition around $T_t \approx 375\text{ K}$ (highlighted by the third vertical dashed line), and while for the powders water quenched after the first two annealing treatments, represented with magenta and orange curves, respectively, the Curie and magneto-structural transformations are shifted to lower temperatures and show some inhomogeneity, the powders slowly cooled present a sharper and single Curie transition, at the same temperature of the bulk. Hence, apart from the importance of the annealing temperature for the relaxation process, through atomic diffusion, also the cooling rate plays a fundamental role in determining the degree of microstructural order, thus pointing out that a slow cooling after an annealing at medium temperature of 500°C can improve the magneto-structural properties, with respect to the powders water quenched and to the bulk itself. Moreover, as described by Sánchez-Alarcos *et al.* [92], the shift of the transition temperatures is connected to the different degree of long range $L2_1$ atomic order, that for the slowly cooled samples is expected to be the maximum allowed by the stoichiometry, and, in turn, the Curie transition temperature the highest one, since the sample is as closest as possible to its equilibrium state. In order to evaluate the change of magnetization between bulk and annealed powders, a SQUID magnetometer was employed, to measure the magnetization curves $M(T)$, down to 6.5 K , in an external magnetic field of 1 T . With reference to figure 4.2-6, it is found that the bulk fragment presents the lowest saturation magnetization, of nearly $M_{sat,bulk} = 58\text{ Am}^2/\text{Kg}$, while the highest value of $M_{sat,pwd-wq} = 73\text{ Am}^2/\text{Kg}$ is measured for the powders water-quenched after the annealing at 600°C . This effect is attributed to a homogenization and atomic ordering process, taking place during the annealing of the powders, that can improve the overall magneto-structural behaviour, with respect to an initial bulk sample, that instead contains some compositional variations and/or secondary phases, as revealed by the multiple inflections of the magnetic susceptibility. Moreover, the magnetization difference, between the two batches of annealed powders, can be ascribed to the different atomic occupation of Mn/Ga sites in the lattice cell, giving rise to differences in the interatomic distances between the atoms carrying a magnetic moment (Mn and Ni)

and hence a different amount of anti-ferromagnetic interactions, in the martensitic phase. Interestingly, the obtained results point out that a higher annealing temperature, but still below the transition temperature $L2_1/B2$ of $T_{L2_1/B2} \approx 780^\circ\text{C}$ [92], is required for obtaining a higher final saturation magnetization and recovering the coupled martensitic and Curie transition, in a narrower temperature range with respect to the bulk. On the other hand, a slower cooling rate can enhance the degree of $L2_1$ atomic order and lead to the stabilization of the magneto-structural phase transitions at higher temperatures, as observed in the bulk.

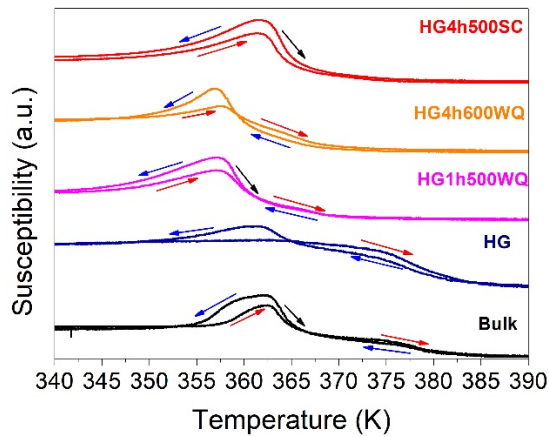


Figure 4.2-5: Effect of annealing treatments on the temperature-dependent magnetic susceptibility of the hand-grinded powders of $\text{Ni}_{49.4}\text{Mn}_{30.3}\text{Ga}_{20.3}$, and comparison with the bulk behaviour.

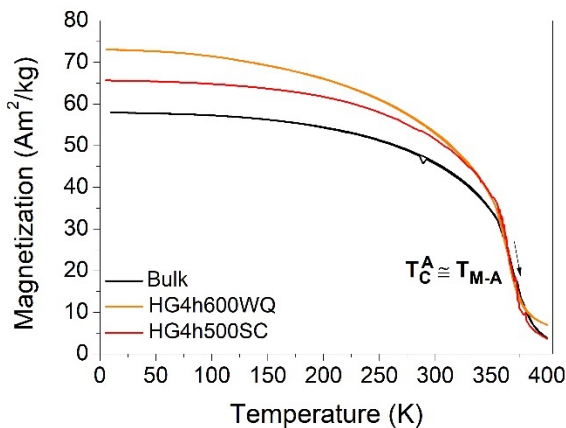


Figure 4.2-6: Magnetization as a function of temperature, under an applied magnetic field of 1T, for the $\text{Ni}_{49.4}\text{Mn}_{30.3}\text{Ga}_{20.3}$ bulk and the post-annealed hand-grinded powders,

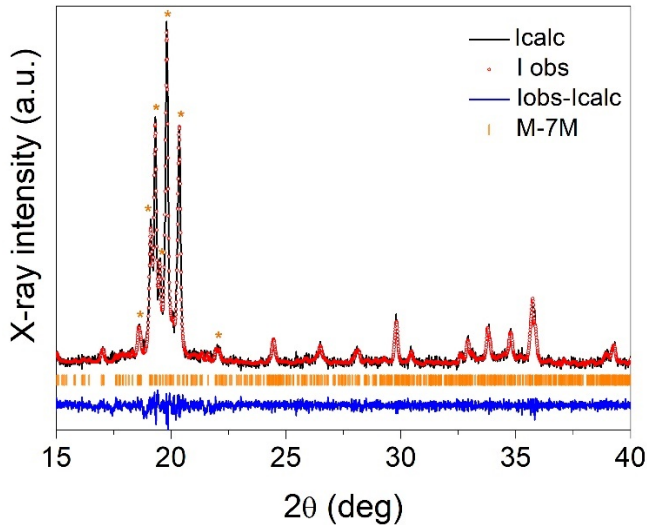


Figure 4.2-7: XRD pattern, collected at room temperature, of the hand-grinded powders, annealed for 4h at 600°C+WQ of $\text{Ni}_{49.4}\text{Mn}_{30.3}\text{Ga}_{20.3}$, showing a modulated 7M martensitic structure.

The structural analysis, by XRD at room-temperature, of the powders annealed for 4h, at 600°C and water quenched afterwards, is reported in Fig. 4.2-7. The diffraction pattern has been refined with a single crystal phase of superstructure $P2/m(\alpha 0 \gamma)00$ referred to as a modulated 7M martensite, with lattice parameters listed in Table 4.2-1. The presence of the sole martensitic phase is expected, since from the susceptibility measurements it has been found that the martensitic finish temperature, on cooling, is around 350 K. It is worth stressing that the thermal treatment has stabilized the modulated 7M martensite, down to 100 K, below which, as it will be shown later by comparing the results of the cryo-milled particles, an inter-martensitic transition leads to the appearance, beside the peaks of the 7M martensite, the additional tetragonal NM martensitic structure. This observation agrees with the results of Çakir *et al.* [138], and Sozinov *et al.* [139], for similar composition and (e/a) number of Ni-Mn-Ga compounds, and it confirms that the $L1_0$ NM structure is the most stable among the martensitic structures. In fact, it can exist both at very low temperatures and at elevated ones, depending on the specific stoichiometric composition, and it is the

only one stable phase under the application of mechanical stresses, as reported in literature [140–142], and, here observed after the hand-grinding process.

4.2.3 $\text{Ni}_{49.7}\text{Mn}_{18.7}\text{Cu}_{6.4}\text{Ga}_{25.2}$: a comparison between hand-grinded and bulk samples

The analysis of the crystal structure, by XRD measurement at room-temperature, for the hand-grinded powders of $\text{Ni}_{49.7}\text{Mn}_{18.7}\text{Cu}_{6.4}\text{Ga}_{25.2}$ is displayed in Fig. 4.2-8. The structure results to be a mixture of a body-centred-tetragonal, referred to the non-modulated martensitic phase ($L1_0$), with also few traces of a monoclinic 7M modulated structure, and a cubic structure, of the austenitic phase, with $L2_1$ atomic order, as recognized by the presence of the A(111) superlattice reflection. In Table 4.2-2, the unit cell parameters for each phase have been summarized. In order to understand the remanence of the austenitic phase, around room-temperature, in the powders after hand crushing, and, hence, to investigate the effect of the mechanical stress on the magneto-thermal behaviour of the martensitic transformation, the thermomagnetic analysis was performed. Indeed, this technique represents a powerful tool to determine the phase homogeneity and/or the presence of secondary magnetic phases, thanks to the detection of the sharpness of the magnetic susceptibility changes or the presence of different inflections and broadening, across the magnetic and magneto-structural phase transformations.

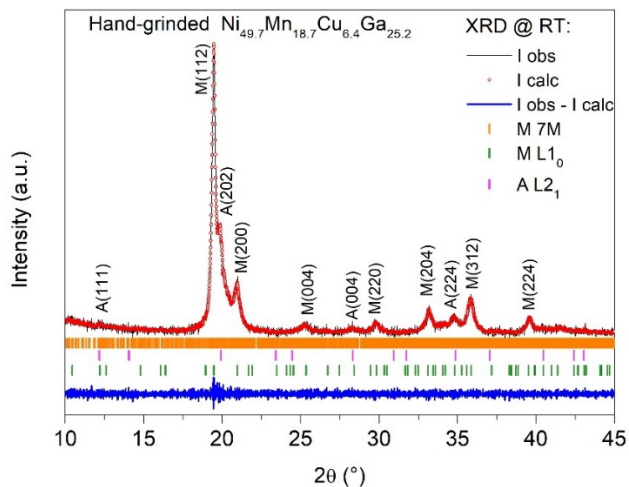


Figure 4.2-8: X-ray diffraction pattern, collected at room temperature, for the hand-grinded powder of $Ni_{49.7}Mn_{18.7}Cu_{6.4}Ga_{25.2}$ compound.

$Ni_{49.7}Mn_{18.7}Cu_{6.4}Ga_{25.2}$ HG powders	Before annealing	@ RT:	
	After ann4h@630°C+WQ @ T≥310 K:	---	@T≤300K:
Crystal Phases	A fcc $L2_1$	M bct $L1_0$	M 7M modulated
Space group	$Fm\bar{3}m$ (no.225)	$I4/mmm$ (no. 123)	$P2/m(\alpha\gamma)00$ (no. 10)
a (Å)	5.8140 (0.0015)	3.901 (0.001)	4.2362 (0.0009)
b (Å)	5.8140 (0.0015)	3.901 (0.001)	5.5211 (0.0020)
c (Å)	5.8140 (0.0015)	6.454 (0.002)	4.3019 (0.0012)
α (°)	90	90	90
β (°)	90	90	92.982 (0.029)
γ (°)	90	90	90
q (Å ⁻¹)			0.2801(0.0016) c^*

Table 4.2-2: List of crystallographic data, obtained by the Le Bail refinement of powder X-rays diffraction measurements for $Ni_{49.7}Mn_{18.7}Cu_{6.4}Ga_{25.2}$ hand-grinded powder, before annealing, where at room-temperature a mixture of the three phases has been found out, and after the annealing treatment, where the phases has been detected in the specified temperature ranges. The letters 'A' and 'M' refer to the Austenite and Martensite phases, respectively.

In Fig. 4.2-9, it is reported the magnetic susceptibility behaviour of the bulk fragment, the hand-grinded powders with coarse particles/grains and the hand-grinded powders

with finer particles/grains. From their mutual comparison, it emerges that the particle-size reduction and the mechanically induced stresses and defects have stabilized the martensitic phase, shifting to a higher temperature the austenite start and austenite finish temperatures. The martensitic finish temperature, instead, remains similar to the one of the bulk: this causes an enlargement of the transformation temperature range. Interestingly, while the coarser powders present different distinct inflections of the magnetic susceptibility, especially on cooling, when the lattice is deformed and the maximum elastic energy is stored for the formation of the twin-related martensitic variants, the finer particles show a smoother magneto-structural transformation behaviour and a narrower thermal hysteresis, even lower than the bulk's one. Moreover, with respect to the bulk fragment, the formation of the first martensitic nuclei, on cooling, takes place at a higher M_s temperature, therefore, with apparently no need of undercooling, as indicated by the proximity of A_f and M_f temperatures. The increase of A_s is ascribed to the necessity of a larger over-heating to promote the recovery of the parent phase through shrinkage of the martensitic domains, which could have been stabilized or pinned by the increase of grain-boundaries and lattice deformations during the mechanical process [143–145]. The increase of transformation broadening points out a heterogeneous/discontinuous transformation behaviour, caused by both the microstructural constraints (caused by grain-refinement) and elastic stored energy [24] and by the separation in multiple non-interacting particles [146]. On the other hand, the increase of defects' concentration, such as grain-boundaries, dislocations and stacking faults, seems to favour the nucleation of the martensite phase, on cooling. However, by decreasing the particle size and hence increasing the surface to volume ratio, it is observed a significant decrease of the saturation magnetization of the martensite, together with a large broadening of the coupled Martensitic-Curie transition, as revealed in Fig.4.2-10, by comparing the high-field $M(T)$ curves of the bulk and hand-grinded fine powders. Hence, the internal disorder, the change of interatomic distances and the predominance of the defected surface over the inner more homogeneous part cause a decrease of the number of Mn atoms coupled ferromagnetically, leading to a gradual suppression of the magneto-structural transformation.

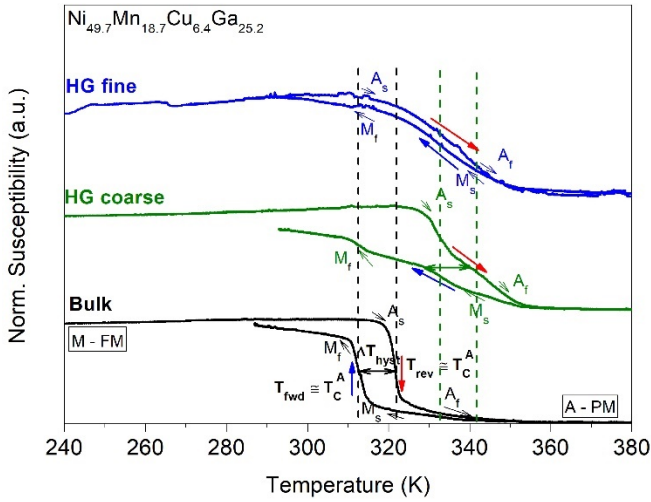


Figure 4.2-9: AC magnetic susceptibility as a function of temperature for the bulk and the hand-grinded powders, with fine and coarser particles, of $\text{Ni}_{49.7}\text{Mn}_{18.7}\text{Cu}_{6.4}\text{Ga}_{25.2}$.

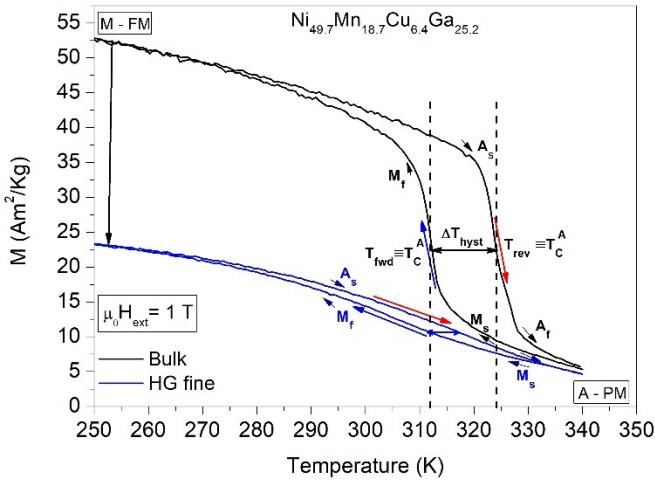


Figure 4.2-10: Magnetization as a function of temperature, at applied magnetic field of 1T, for bulk and hand-grinded fine powder of $\text{Ni}_{49.7}\text{Mn}_{18.7}\text{Cu}_{6.4}\text{Ga}_{25.2}$ compound.

In order to recover the ferromagnetism and a sharp magneto-structural phase transition, two annealing treatments, at temperature of 500°C and 630°C, respectively, and at a fixed annealing time of 4h, were performed, followed by water

quenching. In the following part the two batches will be referred to as HG4h500WQ and HG4h630WQ. Their magnetic susceptibility behaviours are shown in Fig.4.2-11, in comparison to the one of the as-hand-grinded powders (HG) and the starting bulk material. It is observed that the HG4h500WQ and HG4h630WQ powders present a smooth and homogeneous martensitic transformation, that appears to a lower temperature and associated with a smaller thermal hysteresis, with respect to the bulk, as indicated by the horizontal leftward arrows. Moreover, it results that the annealing at temperature of 630°C can better improve the transformation behaviour as compared to an annealing at a lower temperature, since the transformation temperature range is reduced, the phase-homogeneity enhanced, as indicated by the sharpness of the transition, and the transformation temperatures are closer to the bulk's ones.

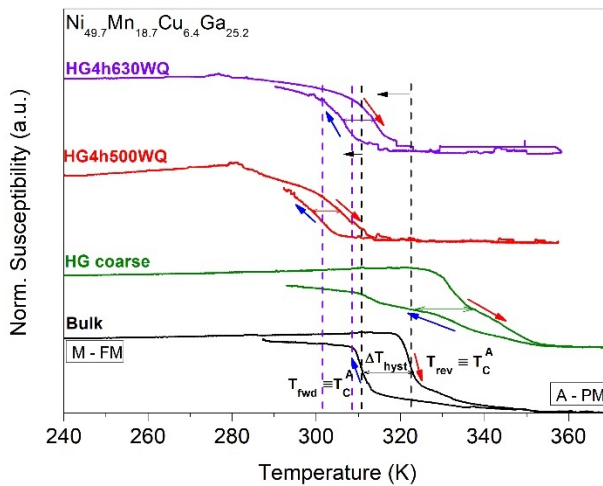


Figure 4.2-11: Comparison between the magnetic susceptibility behaviour, as a function of temperature, of bulk, hand-grinded powder and powders after the specified annealing treatment, for the compound $Ni_{49.7}Mn_{18.7}Cu_{6.4}Ga_{25.2}$.

By considering the high-field magnetization measurements, as a function of temperature, shown in Fig.4.2-12, it can be observed an improvement of the sharpness of the coupled martensitic–Curie transformation for the HG4h630WQ powders, with respect to the bulk, as stressed by the completion in a smaller temperature range of the transformation and a lower magnetic remanence in the paramagnetic state at 340 K, as highlighted in the orange bordered area. Moreover,

the thermal hysteresis is reduced to half of that of the bulk and the coupled magneto-structural transformation is closer to room-temperature, with only a negligible reduction of the saturation magnetization of the ferromagnetic martensitic phase. These phenomena, then, point out the possibility, by decreasing the particles' size and performing optimal thermal treatments at medium temperature, to not only recover the original transformation but even improve the phase homogeneity with respect to the bulk sample. This fact is ascribed to the release of internal defects and microstructural elastic energy barriers, accumulated during the thermo-mechanical history of the sample and possibly to the decrease of gradients of concentration, thus leading to a higher lattice compatibility between neighbouring grains and improvement of the magneto-structural coupling.

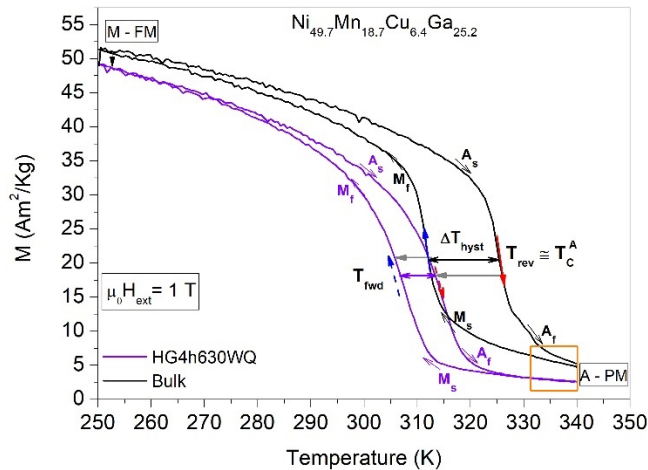


Figure 4.2-12: Temperature-dependence of magnetization for bulk and annealed powders of $Ni_{49.7}Mn_{18.7}Cu_{6.4}Ga_{25.2}$.

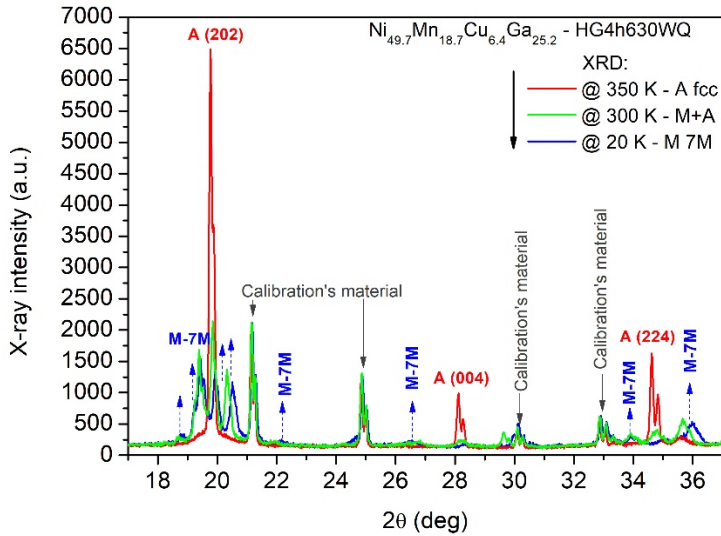


Figure 4.2-13: Evolution of the XRD pattern by decreasing the temperature from 350K to 20K for the post-annealed hand-grinded powders of $\text{Ni}_{49.7}\text{Mn}_{18.7}\text{Cu}_{6.4}\text{Ga}_{25.2}$.

By looking at the temperature-dependent XRD measurements of Fig. 4.2-13, it is possible to observe that also the post-annealed hand-grinded powders of $\text{Ni}_{49.7}\text{Mn}_{18.7}\text{Cu}_{6.4}\text{Ga}_{25.2}$ undergo the structural martensitic transformation from the cubic austenitic phase to the 7M modulated martensitic phase. This occurs at around 310 K, as previously observed from the magnetic measurement (see Fig. 4.2-12). Indeed, at 300 K, the diffraction pattern (in green line) shows the appearance of the peaks of the martensite and a consistent decrease of intensity of the austenitic reflections, with respect to the diffraction pattern at 350 K (red line). Subsequently, during cooling down to 20 K (blue diffraction pattern) the austenitic phase almost vanishes while the reflections of the 7M martensite intensify and shift to higher 2θ positions, for the thermal contraction.

4.2.4 $\text{Ni}_{45}\text{Mn}_{37}\text{In}_{13}\text{Co}_5$: a comparison between hand-grinded and bulk samples

The powder X-Ray diffraction pattern of the hand-grinded $Ni_{44.5}Mn_{37.9}In_{12.6}Co_5$, collected at room-temperature, is displayed in Fig. 4.2-14. By the Le Bail refinement, the structure has been identified as a body-centred-tetragonal belonging to the NM martensitic phase, with a residual trace of the 7M modulated structure and few and low-intense cubic reflections, referred to the austenitic phase, since the (111) superlattice ($L2_1$) peak has been recognized. The lattice parameters, corresponding to the different crystal phases, are reported in Table 4.2-3. In Fig. 4.2-15, it has been enlarged the region between the martensitic peaks M (112) and M (200), in which it is found the maximum deviation of the observed intensity from the calculated one. The presence of a gap, as indicated in figure by the downward arrow, and the almost suppressed peaks of the modulated structure (indicated in orange bar lines), are characteristic features of a defected structure, containing stacking faults and/or twin faults, which result to be very common in the diffraction patterns of cold-worked closed packed metals and alloys, as reported in several published studies [147–149].

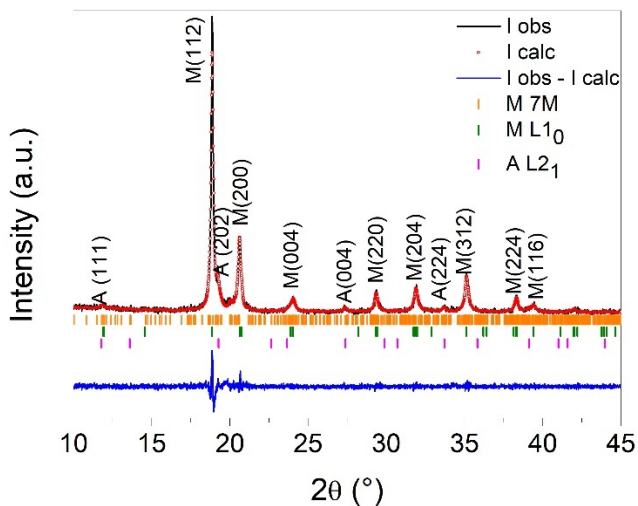


Figure 4.2-14: X-Ray diffraction pattern, collected at room-temperature, of the hand-grinded powder of $Ni_{44.5}Mn_{37.9}In_{12.6}Co_5$ sample.

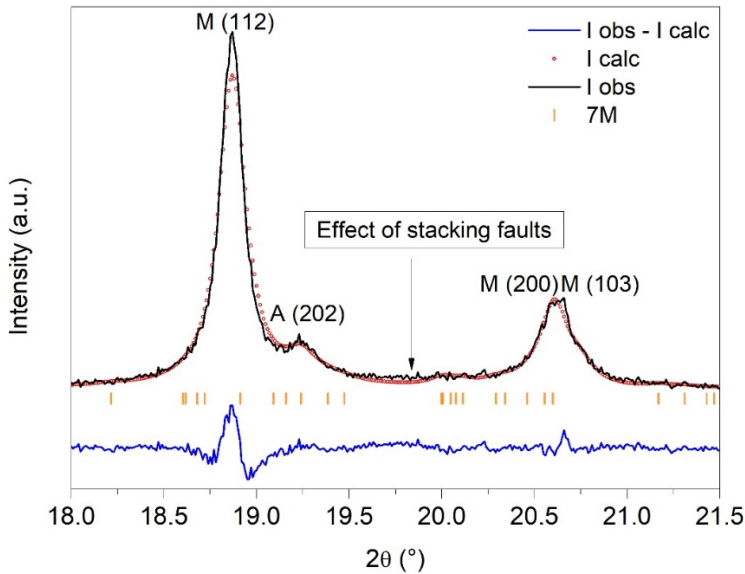


Figure 4.2-15: Enlargement of the X-ray diffraction pattern of Fig. 4.2-19, between the peaks of the martensitic NM structure, $M(112)$ and $M(200)$, showing the effect of the mechanically-induced stacking faults.

$Ni_{44.5}Mn_{37.9}In_{12.6}Co_5$ HG powders	Before annealing	@ RT:	
	After ann30' @850°C+WQ @ T>300 K:	---	@ T<300 K:
Crystal Phases:	Austenite $L2_1$	Martensite $L1_0$	Martensite modulated 7M
Space group:	$Fm\bar{3}m$ (no.225)	$I4/mmm$ (no. 139)	$P2/m(\alpha\gamma)00$ (no. 10)
a (Å)	5.9865 (0.0055)	3.9628 (0.0006)	4.3974 (0.0004)
b (Å)	5.9865 (0.0055)	3.9628 (0.0006)	5.5783 (0.0007)
c (Å)	5.9865 (0.0055)	6.8085 (0.0016)	4.3255 (0.0005)
α (°)	90	90	90
β (°)	90	90	93.64 (0.01)
γ (°)	90	90	90
q (Å ⁻¹)	-	-	0.3428 (0.0007) c^*

Table 4.2-3: Crystallographic data, obtained by the Le Bail refinement of Powder X-Ray diffraction patterns, for the $Ni_{44.5}Mn_{37.9}In_{12.6}Co_5$ hand-grinded powder, before annealing, at room-temperature, where a mixture of all the phases has been detected, and after the annealing (for 30' at 850°C), where for the specified temperature ranges the corresponding phase has been found out.

The effect of the mechanically induced disorder and strain was studied by thermomagnetic analysis, and the differences in the magneto-structural behaviour, with respect to the bulk, were revealed and analysed. In Fig. 4.2-16(a), it is shown that during the first heating run the reverse martensitic transformation of the HG powders does not appear at 275 K as in the bulk, but it is shifted to higher temperatures, close to the Curie transition, especially for the finer particles. Hence, the zero magnetic moment before the increase of magnetic susceptibility points out the presence of martensite stabilized till above room-temperature, in accord to what observed from the XRD pattern. The Curie transition occurs at a slightly lower temperature for the HG fine powder while it remains the same of the bulk for the HG coarse powder. On cooling below the Curie point, it is observed an increase of susceptibility as compared to the heating branch, likely due to the recovery of the ferromagnetic austenite. However, a drastic reduction of the signal is recognized for the smaller HG particles. During the second thermomagnetic measurement, as displayed in Fig. 4.2-16(b), the HG coarse powder shows an increase of susceptibility at low temperature as compared to the bulk. Moreover, the reverse transformation is recovered starting from 275 K, but the susceptibility curve in heating is characterized by two different inflections, leading to a significant shift forward of the austenite finish temperature. The maximum susceptibility of the austenite and the Curie transition temperature remain unaltered with respect to the first run and comparable to the bulk's ones. Instead, for the finer HG particles, the second run has only the effect of recovering a very broad reverse martensitic transformation in heating, characterized by a small susceptibility change between the low and the high-temperature phases. Also, it is worth noting that the magnetic signal below the austenite start temperature has a low but non-zero value.

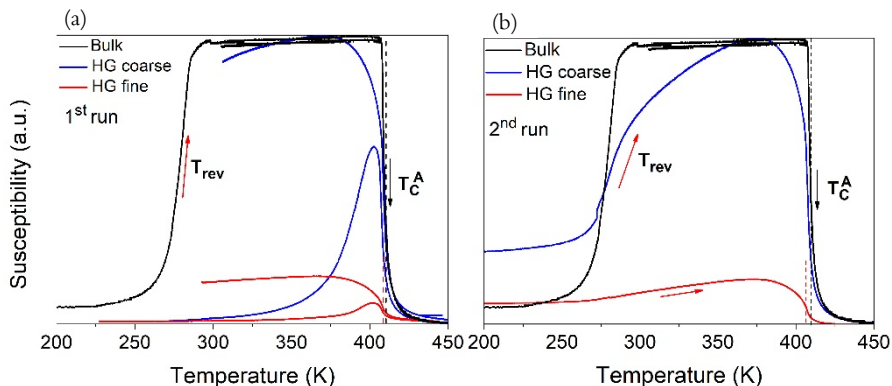


Figure 4.2-16: Magnetic susceptibility as a function of temperature for bulk, hand-grinded coarse and fine powders of $\text{Ni}_{44.5}\text{Mn}_{37.9}\text{In}_{12.6}\text{Co}_5$ during (a) the first and (b) the second thermomagnetic measurement.

Differently from Ni-Mn-Ga Heusler system, where the martensite phase possess a large magneto-crystalline anisotropy, the subclass of Ni-Mn-In and Ni-Mn-In-Co Heusler compounds usually exhibit a weak magnetic martensite, due to the strong competition between antiferromagnetic and ferromagnetic exchange interactions, below the forward martensitic transformation temperature, giving rise to frustrated and complex magnetic interactions [77,91]. By the experimental and theoretical results, different authors have interpreted the magnetic properties of the martensitic phase as super-para-magnetism, super-spin glass behaviour, or superparamagnetic domains embedded in a paramagnetic or anti-ferromagnetic matrix [90,95,97,150–152], stressing that the resulting spin configuration depends on the coupling of the spins to the local strain fields, generated by the atomic disorder of non-stoichiometric Heusler composition, and by the additional lattice strain due to the Co impurities. In light of this phenomenon, two different explanations of the current experimental observations can be formulated. On the one hand, it can be inferred that the addition of a certain number of microstructural defects and lattice deformations, to a pre-existing frustrated magnetic configuration, favours the ferromagnetic coupling in the martensitic state, leading to an increase of the magnetic susceptibility signal. On the other one, since the broadening of the transformation and the increase of the magnetic signal in the low temperature range are much more pronounced in the smaller particles, which contain a higher surface-to-volume ratio, hence, density of defects, the change of the magnetic properties seems to be related to a gradual hindering effect leading to the suppression of the structural martensitic transformation. Likely, as suggested by Bruno *et al.* [94] for Ni-Mn-Sn-Co small-grained ribbons, this is due to the increase of transformation interfaces and energy barriers to overcome, and/or the restricted mobility and volume fractions necessary for the diffusion-less nucleation and propagation of the martensite inside the parent austenite.

In order to solve this dilemma and recover the original sharp metamagnetic martensitic transformation, it was performed a short annealing (30 min) at high temperature (850°C) followed by water quenching. In fig. 4.2-17, the ac magnetic susceptibility measurements, as a function of temperature, are represented and it is shown that the powders after the annealing treatment (dark cyan curve) have recovered a large change of the magnetic susceptibility signal across the reverse martensitic transformation, thanks to the decrease of magnetic signal, in the low-temperature martensitic phase, and, conversely, its increase in the high-temperature

austenitic phase, as compared to the as-hand-grinded powders (in magenta curve). Differently, with respect to the bulk (black curve), it is noticed a significant increase, of roughly 20 K of both the austenite start and austenite finish temperatures, while the Curie transition temperature presents a small decrease of 7 K. These effects have been also observed in literature, by different authors [95,153], as a result of secondary annealing treatments on Ni-Mn-In-Co bulk samples, at temperature above the $L2_1/B2$ ordering temperature, estimated to be at around $T_t^{L2_1-B2} \approx 623-627^\circ\text{C}$ [95,154], and followed by a rapid cooling rate, rather than a lower one. Hence, they are ascribed to microstructural variations, such as the annihilation or the formation of quenched-in vacancies and/or small changes in the atomic positions. Moreover, for the current study, as visible in Fig. 4.2-17, it has been found that by increasing the annealing time to 2 h, at the same fixed annealing temperature of 850°C , the reverse martensitic transformation of the powders slightly decreases of 5 K, with associated an increase of the magnetic susceptibility of the martensite, while the Curie transition temperature increases of 5 K, as compared to the ones of the short-annealed (30 min) powders. Instead, after a longer annealing treatment of 24 h, the reverse martensitic transformation temperature and the magnetic susceptibility change recover the same values observed after the shortest annealing treatment, whereas the Curie transition temperature remains equal to the one of the powders annealed for 2 h. Hence, a non-monotonic trend of the reverse martensitic transformation with the annealing time and a shift to higher temperatures with respect to the bulk have been detected, whereas the final achieved degree of atomic order is close to the initial one and shows a sensible variation only on short annealing duration scales, due to a threshold of vacancy concentration for disorder-order transition assistance [96].

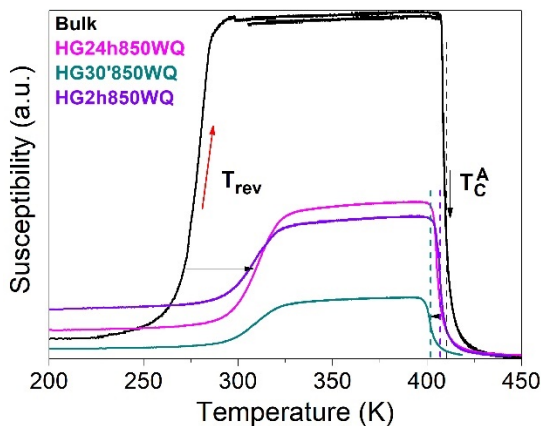


Figure 4.2-17: Temperature-dependence of ac magnetic susceptibility for bulk, hand-grinded powder and post-annealed powders at temperature of 850°C of $\text{Ni}_{44.5}\text{Mn}_{37.9}\text{In}_{12.6}\text{Co}_5$.

By considering the low-field magnetization curves as a function of temperature, reported in Fig. 4.2-18, it is found that, for the post-annealed powders, the martensitic transformation, other than be shifted to a higher temperature, occurs in a broader temperature range and with associated a larger thermal hysteresis, as compared to the bulk. In addition, a slightly higher magnetic signal at low temperatures is observed. This fact, similar to what observed after the hand-grinding process, highlights that even the selected high-temperature annealing procedure(s) can restore the original magneto-structural behaviour.

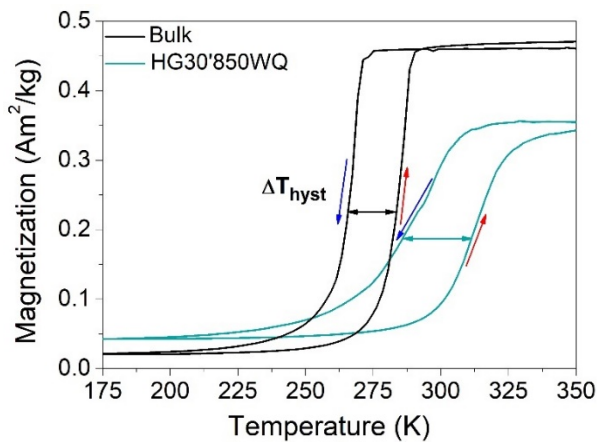


Figure 4.2-18: Temperature-dependent magnetization, under a low magnetic field of 0.5 mT, for bulk (black curve) and post-annealed powders (dark cyan curve) of $\text{Ni}_{44.5}\text{Mn}_{37.9}\text{In}_{12.6}\text{Co}_5$.

Interestingly, with reference to Fig. 4.2-19, an annealing for 2 h at 500°C, below the ordering temperature T^{L2_1-B2} , followed by water quenching, leads to both the increase of the reverse transformation temperature and the slight decrease of the Curie temperature as compared to the bulk in a similar fashion to what previously observed after the heat treatments at high temperature (see Fig. 4.2-17). Conversely to the latter ones, it also leads to the segregation of different magnetic phases, as highlighted by the multiple inflections of the magnetic susceptibility at the Curie transition. By reducing the cooling rate (slow cooling in furnace), instead, the reverse martensitic

transformation is shifted towards lower temperatures, closer to the bulk one. However, independently on the cooling rate, the annealing at 500°C leads to phase segregation phenomenon, as visible in the highlighted areas in correspondence of the Curie transition. A higher phase instability and a lower magnetization change across the martensitic transformation are noticed for the finer particles as compared to the bigger ones.

Therefore, it emerges that the rapid cooling rate, which is supposed to bring about a higher vacancies' concentration, can significantly increase the thermodynamic stability of the martensitic phase, thus shifting the transformation to higher temperatures, and slightly decrease the overall degree of atomic order. The results are in agreement with the literature works on bulk and ribbons samples of the metamagnetic Ni-Mn-In-Co and Ni-Mn-Sn-Co compounds [82,95] and confirm the complex and non-monotonic dependence of the martensitic features on the microstructural and atomic ordering variations.

Finally, the selected annealing temperature below the $L2_1/B2$ ordering temperature has a detrimental effect on the phase stability of this off-stoichiometric compound,

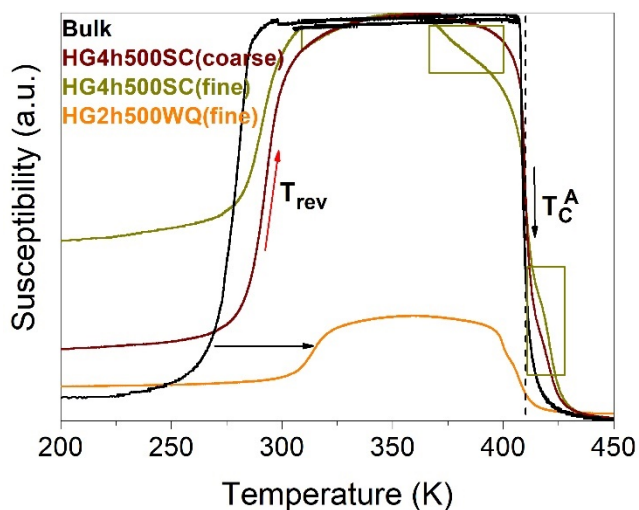


Figure 4.2-19: Thermomagnetic responses of $\text{Ni}_{44.5}\text{Mn}_{37.9}\text{In}_{12.6}\text{Co}_5$ bulk and hand-grinded powders annealed at 500°C, for 2/4h, and then slowly cooled or water quenched. The regions highlighted in cyan show the presence of multiple inflections of the magnetic susceptibility at the Curie transition.

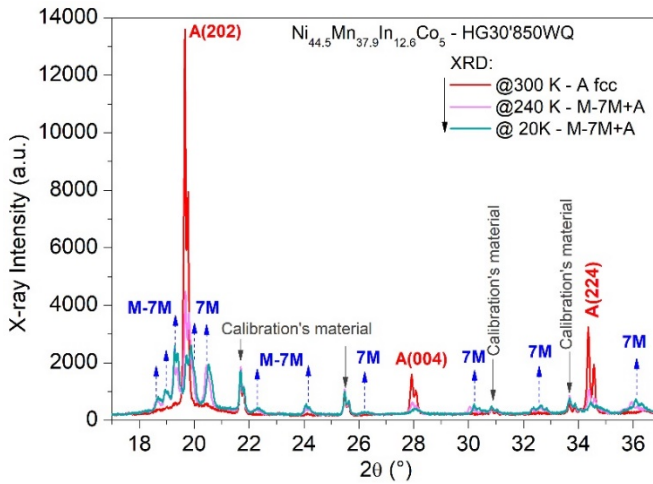


Figure 4.2-20: Evolution of the XRD pattern on decreasing the temperature, from 300 to 20K, for the hand-grinded powders, annealed for 30min at 850°C+WQ, of $\text{Ni}_{44.5}\text{Mn}_{37.9}\text{In}_{12.6}\text{Co}_5$.

The temperature-dependence XRD analysis, of the powders annealed for 30 min at 850°C is shown in Fig. 4.2-20. It is revealed that at room-temperature the structure is fully a cubic austenitic phase (red diffraction pattern). Then, on cooling the temperature just below 300 K, the martensitic transformation takes place and a 240 K it can be noted that the austenitic peaks drastically decrease of intensity and meanwhile the peaks of a 7M modulated martensite appear (green XRD pattern). At 20 K, the transformation is completed, with the increase of intensity of the martensitic reflections (blue line), but a small fraction of untransformed austenite is retained, as recognizable by a non-zero remanence of the fundamental cubic peaks. This fact can then explain the increase of the magnetic signal in the low temperature phase, as due to the residual amount of ferromagnetic austenite.

Similar results were obtained also for the hand-grinded powders of the other Ni-Mn-In-Co system, with the difference that, after the annealing below the T^{L2_1-B2} , no segregation of secondary phases was detected, by the thermo-magnetic analysis, whereas the martensitic transformation temperatures showed a strong dependence on the annealing temperature.

The structural XRD analysis of the $\text{Ni}_{45.7}\text{Mn}_{36.9}\text{In}_{13.2}\text{Co}_{4.2}$ powder is shown in Fig. 4.2-21. It is revealed that at room-temperature, after the hand-crushing, the powders present a well-defined tetragonal NM martensitic structure, with some peaks, of lower intensity, of the cubic austenitic phase, identified with a $L2_1$

superstructure, since the (111) and (311) superlattice reflections have been detected. Moreover, some residual traces of a modulated 7M martensitic structure can be recognized, especially between the austenitic A(202) and martensitic M(200) peaks, but tend to be suppressed by the huge amount of defects and lattice deformations mechanically apported. The crystallographic data obtained with the Le Bail refinement are summarized in Table 4.2-4.

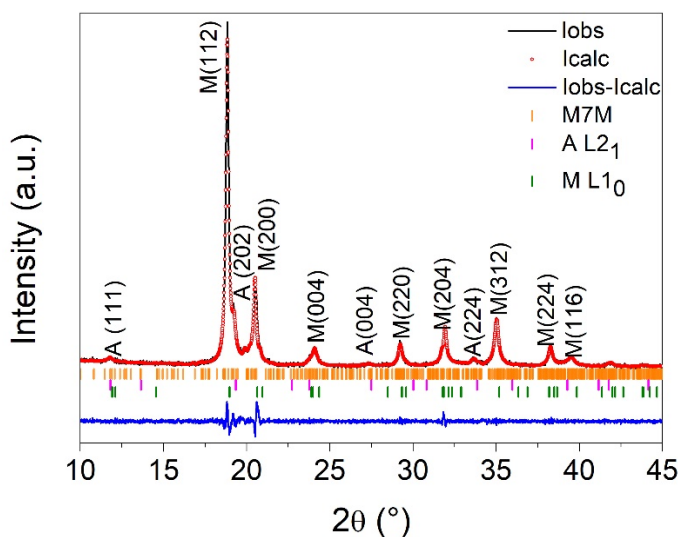


Figure 4.2-21: X-ray diffraction pattern of the hand-grinded powders of $\text{Ni}_{45.7}\text{Mn}_{36.9}\text{In}_{13.2}\text{Co}_{4.2}$ sample, collected at room-temperature, and fitting with the Bragg reflections of the three crystal phases (martensite NM and modulated 7M, and austenite $L2_1$), as reported in legend.

$\text{Ni}_{45.7}\text{Mn}_{36.9}\text{In}_{13.2}\text{Co}_{4.2}$ HG powders:	Before annealing	@ RT:	
	After ann2h@820°C @ T ≥ 300 K:		
Crystal Phases:	Austenite $L2_1$	Martensite $L1_0$	Martensite modulated 7M
Space group:	$Fm\bar{3}m$ (no.225)	$I4/mmm$ (no. 139)	$P2/m(\alpha 0\gamma)00$ (no. 10)
a (Å)	5.971 (0.005)	3.9594 (0.0004)	4.391 (0.003)
b (Å)	5.971 (0.005)	3.9594 (0.0004)	5.568 (0.005)
c (Å)	5.971 (0.005)	6.7237 (0.0012)	4.317 (0.002)
α (°)	90	90	90
β (°)	90	90	93.368 (0.089)
γ (°)	90	90	90

q (\AA^{-1})	-	-	0.3375 (0.0028) c^*
---------------------------	---	---	-----------------------

Table 4.2-4: Crystallographic data, obtained by the Le Bail refinement of Powder X-Ray diffraction patterns of $\text{Ni}_{45.7}\text{Mn}_{36.9}\text{In}_{13.2}\text{Co}_{4.2}$ hand-grinded powder, before annealing, at room-temperature, where a mixture of all the phases has been revealed, and after the annealing treatment (for 2h at 820°C), where in the specified temperature ranges the phases have been observed.

After hand-grinding, the particle size was selected by sieving with different Mesh, such as Mesh 170 to select particles of approximately $d \approx 100 \mu\text{m}$, and Mesh 230 for obtaining particles with dimensions $d < 66 \mu\text{m}$. In Fig.4.2-22, it is reported the behaviour of the magnetic susceptibility as a function of temperature $\chi_m(T)$, for a bulk fragment, the hand-grinded coarse-grained and fine-grained powders, denoted with black, purple and green curves, respectively. From their comparison, it emerges that while the starting bulk material is characterized by a sharp martensitic transformation (here reported only the reverse branch, on heating) with the transformation temperatures A_s and A_f close to each other and a large magnetic susceptibility change between a non-magnetic (antiferromagnetic or paramagnetic) martensite, below A_s , and a high ferromagnetic austenite, above A_f , the prepared hand-grinded powders show a much broader martensitic transformation and a non-null susceptibility signal, in the low temperature phase (upward black arrow, on bottom-left), which are enhanced for the batch of fine-grained particles. The Curie temperature, instead, does not reveal any significant change, with respect to the original one, for the coarse-grained particles, while, instead, a slight decrease of 5 K, for the finest powders.

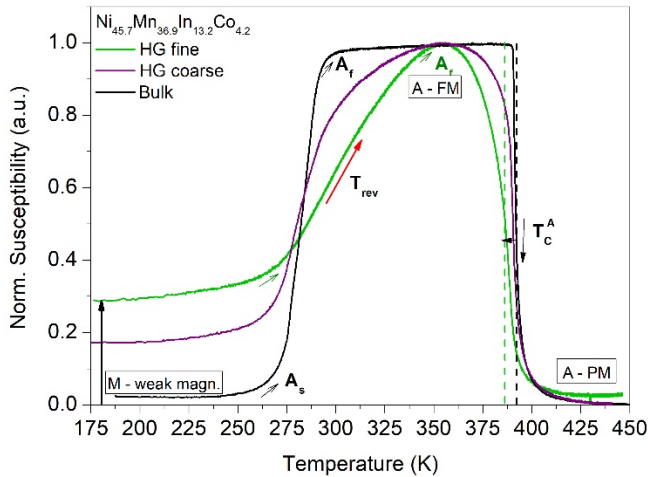


Figure 4.2-22: Low-field ac magnetic susceptibility of bulk fragment (black curve), hand-grinded powder coarse grain (blue curve) and hand-grinded powder fine grain (green curve) of $\text{Ni}_{45.7}\text{Mn}_{36.9}\text{In}_{13.2}\text{Co}_{4.2}$ sample.

The recovery of the initial magneto-structural properties of the bulk (sharpness of the martensitic transformation and the large change of magnetization, between the martensite and austenite phases) in the powders hand-crushed was studied by performing different annealing treatments, both below and above the order-disorder transition temperature of $T^{L2_1-B2} = 627^\circ\text{C}$, and varying the cooling rate (rapid quenching or slow cooling), in order to assess the influence of these parameters on the final martensitic transformation features, of both coarse and fine-grained powders. After the annealing at 500°C for 4 h, followed by a slow cooling, the hand-grinded powders, divided in different batches on the base of the particles' dimensions (Table 4.2-5), have showed the magnetic susceptibility behaviours displayed in Fig. 4.2-23(a), where in black is reported, as reference, the curve of the bulk sample, while in red, green and blue the $\chi_m(T)$ of the coarser particles with $d > 250 \mu\text{m}$, of the particles with dimensions $66 \leq d \leq 89 \mu\text{m}$, and of the smaller ones with $d \leq 66 \mu\text{m}$, respectively. It can be noted that the reverse martensitic transformation occurs at a similar temperature for three different powders batches and it is shifted to a higher temperature as compared to the bulk one. Then, at a temperature well above the austenite finish one, it can be observed a sharp and single magnetic Curie transition, occurring at nearly the same temperature, close to the bulk one. This result stresses an higher homogeneity and stability of this composition against segregation of phases, differently from the other Heusler system, with $\text{Ni}_{44.5}\text{Mn}_{37.9}\text{In}_{12.6}\text{Co}_5$ composition previously discussed. Furthermore, it is interesting to note that by decreasing the

particles' size the magnetic susceptibility signal at low temperature increases. The same trend has been detected also from the high-field magnetization measurements, as a function of temperature, as shown in Fig. 4.2-23(b). Another important result is that, concurrently to the increase of magnetization in the low temperature range, the thermal hysteresis (ΔT_{hyst}) associated with the structural martensitic transformation, gradually increases by decreasing the particle's size, from above 250 μm till below 66 μm (Table 4.2-6). It is worth noticing that the enlargement of the thermal hysteresis is exclusively due to the shift to lower temperature of the forward martensitic transformation (T_{fwd}), on cooling, which, in turn, is caused by the decrease of the martensitic finish temperature (M_f). Conversely, on the heating branch, the reverse martensitic transformation (T_{rev}) of all the batches coincides in temperature and shape, with only a slight righthand shift of the austenite start temperature for the particles' dimension of $89 < d < 125 \mu\text{m}$ (magenta curve). Moreover, with respect to the bulk, apart from the shift to a higher temperature of T_{rev} , it can be noted the decrease of magnetization of the austenitic phase.

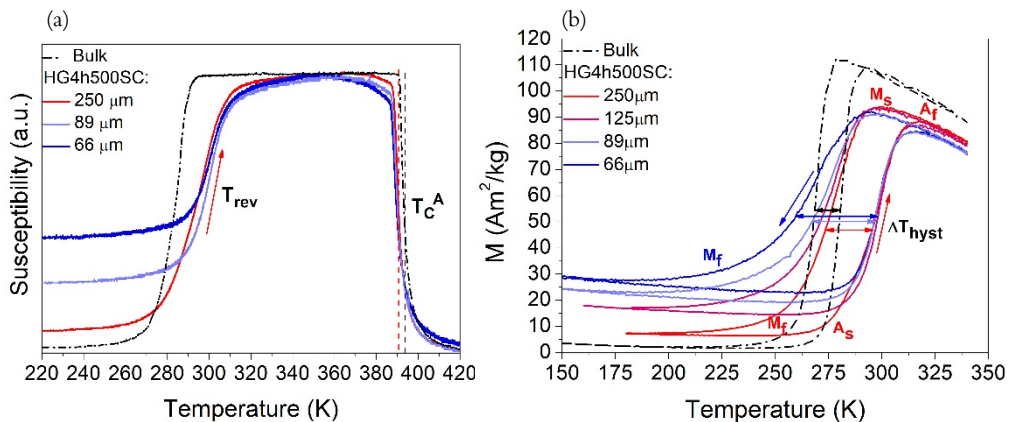


Figure 4.2-23: (a) Thermomagnetic response of $\text{Ni}_{45.7}\text{Mn}_{36.9}\text{In}_{13.2}\text{Co}_{4.2}$ bulk and different batches of hand-grounded powders annealed for 4h at $500^\circ\text{C} + \text{SC}$, having different particle size. (b) High-field magnetization measurements of the same batches, in the temperature interval of the martensitic transformation.

$\text{Ni}_{45.7}\text{Mn}_{36.9}\text{In}_{13.2}\text{Co}_{4.2}$	A_s (± 2 K)	A_f (± 2 K)	M_s (± 2 K)	M_f (± 2 K)	ΔT_{hyst} (± 4 K)	ΔM (± 2 Am^2/kg)	ΔT_{elas} (± 4 K)
HG pwd - ann4h500SC							
$d > 250 \mu\text{m}$	280	312	292	258	21	92	33

89<d<125 μm	287	312	290	254	27	82	31
66<d<89 μm	286	310	290	250	28	75	32
d<66 μm	289	311	290	237	36	71	38

Table 4.2-5: Martensitic transformation temperatures, ranges and magnetization difference of the batches of hand-grinded powders annealed at 500°C, represented in Fig. 4.2-24(b).

By increasing the cooling rate, performing a rapid water-quenching after the annealing treatment at 500°C, for the smaller hand-grinded particles, it has been noted (Fig. 4.2-24(a)) a further increase and a sharpening of the reverse martensitic transformation temperature as compared to the batch of slowly cooled powder, but any change in hysteresis width or magnetization change across the martensitic transformation. Moreover, also the Curie transition temperature of the austenite has remained equal by varying the cooling rate and only slightly lower than the bulk one (Fig. 4.2-24(b)).

Therefore, the magneto-structural properties of the post-annealed powders, especially for the finest ones, have significantly changed and worsened as compared to the original ones of the bulk, because of the increase of the thermal hysteresis and transformation temperature range, and of the drastic decrease of magnetization difference between the two phases. The values of transition temperatures and magnetization change have been listed in Table 4.2-6, for both bulk and powders batches.

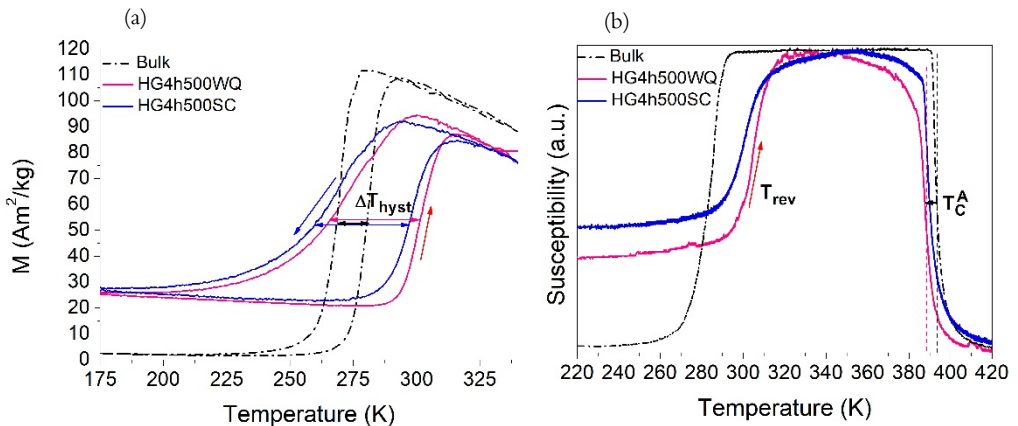


Figure 4.2-24: (a) Comparison between the high-field magnetization curves of the slowly cooled and water quenched powders, after the annealing for 4h at 500°C, and with respect to the starting bulk material of $Ni_{45.7}Mn_{36.9}In_{13.2}Co_{4.2}$ compound. (a) AC magnetic susceptibility as a function of temperature of the corresponding samples.

Sample	A_s (± 2 K)	A_f (± 2 K)	M_s (± 2 K)	M_f (± 2 K)	T_c (± 2 K)	ΔT_{hyst} (± 4 K)	ΔT_{elas} (± 4 K)	ΔM (± 2 Am ² / Kg)	$(T_c - T_0)/T_c$ (± 0.01)
Bulk	277	294	276	260	393	17	9	118	0.27
Hand-grinded powders (d<66 μ m)	253	344	312	212	386	36	95	0.8	0.15
H.G. ann4h@500°C+SC	289	311	290	237	390	36	38	71	0.23
H.G. ann4h@500°C+WQ	294	312	296	238	389	36	37	75	0.22
H.G. ann4h@700°C+SC	279	307	283	235	389	34	38	57	0.24
H.G. ann2h@820°C+SC	272	297	265	228	391	38	31	102	0.28
H.G. ann4h@820°C+SC	273	298	276	218	389	38	41	92	0.26
H.G. ann4h@820°C+WQ	272	305	283	227	384	33	45	94	0.23

Table 4.2-6: List of transition temperatures (Martensitic and Curie) and magnetization change between austenite and martensite phases, derived by the experimental results of the thermo-magnetization and ac magnetic susceptibility measurements of the bulk and powders batches of the $Ni_{45.7}Mn_{36.9}In_{13.2}Co_{4.2}$ system.

In order to explain the increase of magnetization at low temperature as compared to the bulk, and possibly discriminate between a change in the magnetic ordering of the martensitic phase or the occurrence of the martensitic transformation arrest, there have been carried out the temperature dependent XRD measurements, from 340 K down to 20 K, as displayed in Fig. 4.2-25. The diffraction patterns have shown that, on decreasing the temperature, the peaks of the cubic austenitic phase gradually decrease in intensity and meanwhile there appear those of a modulated 7M martensitic structure. However, the fundamental peak of the austenite A(202) is not completely suppressed even at 20 K, thus highlighting that the martensitic transformation is interrupted and a small fraction of austenite is retained at low temperatures. Since the latter is ferromagnetic, its presence can reasonably account for the detection of a higher magnetic moment in the low temperature range as compared to the bulk.

Then, this fact shows that by decreasing the sample size the structural martensitic transformation can be significantly hindered. By the way, recently, different authors [95,151] have pointed out that the so-called kinetic arrest of the martensitic transformation occurs also in Ni-Co-Mn-In bulk compounds, subjected to secondary heat treatments at low temperatures ($T < 400^\circ\text{C}$) or instead thermo-magnetization cycles under application of an increasing magnetic field. Hence, the partial or even complete interruption of the martensitic transformation is not peculiar of only the powder samples, but rather it emerges as a general feature of this compound, due to both presence of internal constraints, such as decrease of volume and increase of microstructural energy barriers, and enhancement of magnetic moment of the austenite phase.

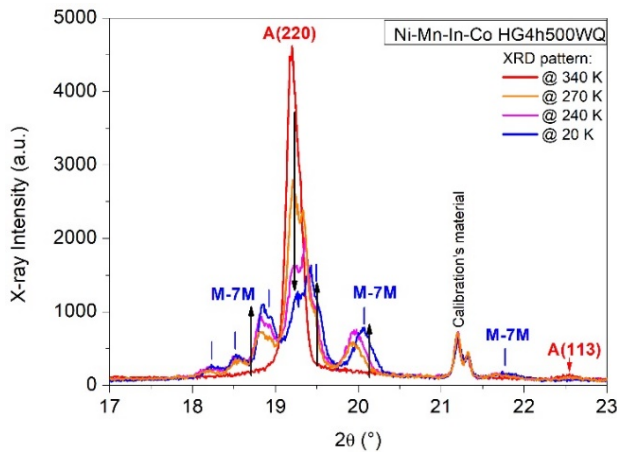


Figure 4.2-25: Evolution of the XRD pattern on decreasing the temperature from 340 K to 20 K for the hand-grinded powder annealed at 500°C and then water quenched of $\text{Ni}_{45.7}\text{Mn}_{36.9}\text{In}_{13.2}\text{Co}_{4.2}$ compound. It is shown that the fundamental austenitic peak (202) decreases in intensity but is not completely suppressed at very low temperatures and it remains together with the reflections of the 7M modulated martensitic structure.

Differently, after selecting an annealing treatment for 2 h at temperature of $T_a = 820^\circ\text{C}$, above the order-disorder transition temperature $T_t^{B2/L2_1} \approx 627^\circ\text{C}$, followed by a slow cooling in furnace, it has been possible to achieve a better recovery of the original configuration. As shown in Figs. 4.2-26(a)-(b) from the magnetic susceptibility and high-field magnetization measurements as a function of temperature, respectively, the austenite start (A_s), austenite finish (A_f), martensite start

(M_s) and Curie transition (T_C^A) temperatures of the post-annealed fine-grained particles are close to the bulk's ones, as well as the magnetic moments of the two phases, even if, below the martensite finish temperature, a higher magnetic signal is retained (Fig.4.2-26(b)). However, notable differences have been revealed in the martensitic transformation behaviour on cooling, as the lefthand shift of the forward martensitic transformation temperature to 20 K lower than the bulk one, due to a drastic decrease of the martensitic finish temperature (M_f), and the significant increase of the thermal hysteresis (ΔT_{hyst}), between the heating and cooling branches. In addition, in Figs. 4.2-26(a)-(b), there have been reported also the measurements of other two powder batches annealed at the same fixed temperature of 820°C, but for a longer annealing time of 4h, followed in one case by the water quenching (dark cyan curve) and in the other one by slow cooling (orange curve).

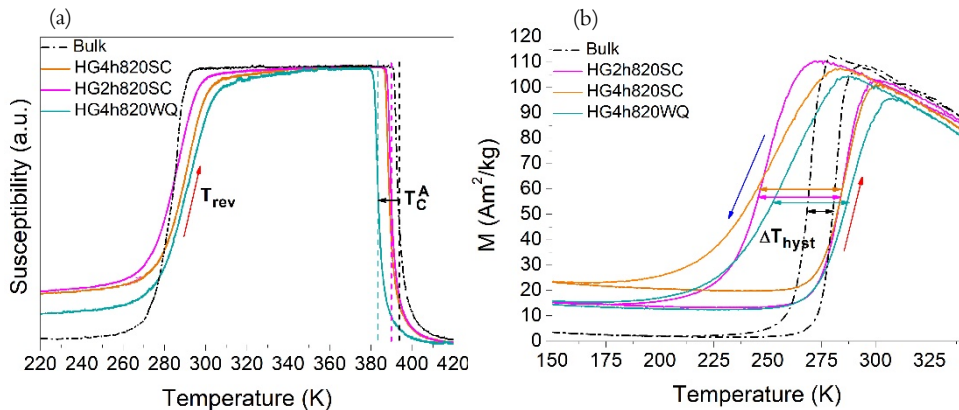


Figure 4.2-26: (a) Thermomagnetic response of $Ni_{45.7}Mn_{36.9}In_{13.2}Co_{4.2}$ bulk and fine-grained hand-grinded powders annealed at 820°C for 2h or 4h, and then slowly cooled or water quenched. (b) High-field magnetization measurements, as a function of temperature, for the same samples, with the same colour legend, as described in figure.

It is shown (Fig. 4.2-26(b)) that the three different batches present almost the same thermal hysteresis, while, instead, an increase of the transformation temperature range, referred to as ΔT_{elas} [82,94] and calculated as $\Delta T_{elas} = \frac{[(A_f - A_s) + (M_s - M_f)]}{2}$ (Table 4.2-6), is observed for the longer annealed powders, due to the shift to a higher temperature of the martensite start temperature (M_s), together with a leftward shift of the martensite finish temperature (M_f) or a rightward shift of the austenite finish

temperature (A_f), for the slowly cooled and water quenched batches, respectively. Moreover, by looking at the magnetic susceptibility measurements of Fig. 4.2-26(a), it is important to notice that the powder water quenched shows a decrease by nearly 10 K of the Curie transition temperature as compared to the original bulk fragment. For the powder annealed for 4h and then slowly cooled, instead, it is observed that, on cooling, concomitantly to the shift to a lower temperature of M_f , there is an increase of magnetic moment in the low temperature range, with respect to the powder annealed for 2 h and slowly cooled (Table 4.2-6).

Besides the already presented annealing treatments, it has been also performed a heat treatment for 4h, at 700°C, followed by slow cooling, in order to understand the role of annealing temperature, by keeping fixed the annealing duration and the cooling rate, in changing the MT features. In Fig. 4.2-27, it is presented a comparison between the M(T) curves of the powder batches annealed at 500°C (blue line), 700°C (green line) and 820°C (orange line). It emerges that the annealing temperature has a significant effect on the martensitic transformation temperatures and magnetic moment of the austenite, leading, respectively, to a decrease and increase by increasing the temperature from 500°C to 820°C (Table 4.2-6). In contrast, the increase of magnetic moment at low temperature (i.e., the amount of retained untransformed austenite) shows a non-monotonic trend, being, among the considered batches, the highest one for the powder annealed at 700°C. The thermal hysteresis, instead, is almost insensitive to the change of annealing conditions. Therefore, this fact points out that a non-trivial variation of retained or thermally induced atomic disorder takes place during the annealing treatment, likely due to a different dependence on annealing time and cooling rate as a function of the selected annealing temperature. The density, type, and distribution of point defects (anti-site defects and vacancies), in turn, have a non-monotonic impact on the martensite phase transformation [96,155].

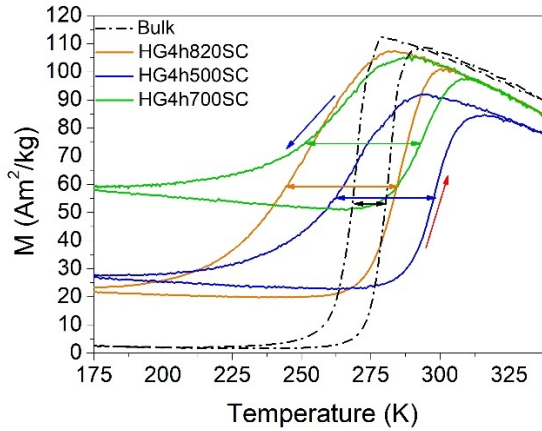


Figure 4.2-27: Magnetization curves as a function of temperature, at applied magnetic field of 1 T, for three batches of hand-grinded powder ($d < 66 \mu\text{m}$) annealed at three different temperatures (500-700-820°C) for same fixed annealing duration and cooling rate, and comparison with the bulk measurement of $\text{Ni}_{45.7}\text{Mn}_{36.9}\text{In}_{13.2}\text{Co}_{4.2}$ compound.

In order to identify some general trends as a function of the degree of atomic order, it has been calculated for each sample (i.e., bulk, hand-grinded and post-annealed powder samples) the corresponding $(T_C - T_0)/T_C$ parameter (see Table 4.2-6), where T_0 is the equilibrium temperature ($T_0 = (M_s + A_f)/2$), and T_C the Curie temperature of the austenite. This parameter is commonly used in literature to assess the change of the overall degree of long-range atomic order in bulk and ribbons of Ni-Mn-In-Co [153] and Ni-Mn-In-Sn [82] compounds, apported by secondary heat treatments, varying the temperature and the cooling rate. In the present case, for the post-annealed hand-grinded powder batches, it has been found out an increase of the mean value of the $(T_C - T_0)/T_C$ parameter by increasing the annealing temperature and selecting a slow cooling rate, which reaches a comparable value to the bulk one, after the short annealing treatment, for 2 or 4 h, at 820°C, followed by slow-cooling, as shown in Fig. 4.2-28(a). Then, in Fig. 4.2-28(b), by plotting the hysteresis values ΔT_{hyst} as a function of $(T_C - T_0)/T_C$, it is possible to observe that there is almost no difference (or only a negligible one, considering the associated error bar) between the as hand-grinded and annealed powder batches, and their hysteresis values turn out to be more than twice the hysteresis width of the bulk, after reduction of the sample size to microparticles with average size $60 \pm 20 \mu\text{m}$. Differently, in Fig. 4.2-28(c), the Curie and martensitic start temperatures have been reported as a function of $(T_C - T_0)/T_C$ parameters, and it is possible to notice a slight linear increase of the former

(T_C) and concomitantly a more evident linear decrease of the latter (M_S) by increasing the $(T_C - T_0)/T_C$ value. These results, together with the above-mentioned observations, highlight, on the one hand, that magneto-thermal and magneto-structural properties as close as possible to the original bulk ones can be better recovered in the hand-grinded powder (with $60 \pm 20 \mu\text{m}$ particle size) after the heat treatment for 2 h, at 820°C , followed by a slow cooling rate, and, on the other one, even though there is a worsening in terms of ΔM or ΔT_{elas} , that by decreasing the value of the order parameter $(T_C - T_0)/T_C$, as for instance by decreasing the annealing temperature and/or applying a rapid cooling rate, it is possible to stabilize the martensitic phase to higher temperatures. This is in good accordance to what reported in literature about the stabilization of the ferromagnetic austenitic phase with enhancement of the degree of atomic order [72,95,153], and reveals the existence of a strong inverse interrelation between the temperature at which the martensite phase starts to nucleate and the overall degree of atomic order and magnetic moment of the parent austenitic phase.

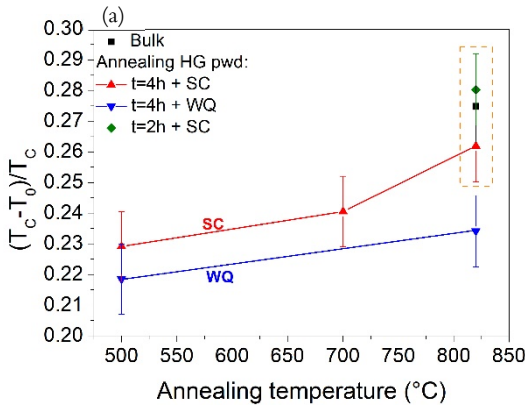
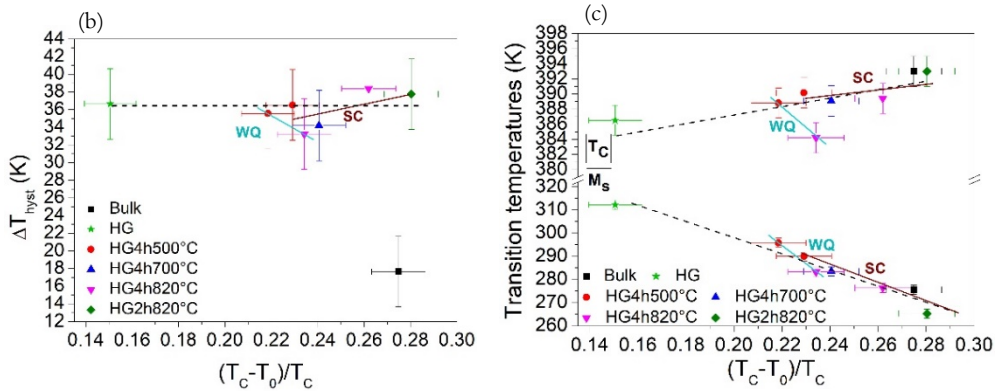


Figure 4.2-28: (a) Annealing temperature-dependence of the $(T_C - T_0)/T_C$ parameter for the water-quenched and slowly-cooled batches of annealed hand-grinded powder and comparison with the value of the bulk sample of $\text{Ni}_{45.7}\text{Mn}_{36.9}\text{In}_{13.2}\text{Co}_{4.2}$ compound. (b) Thermal hysteresis and (c) transition temperatures (Curie and martensite start temperatures) trends of the powder before and after the heat treatments as a function of $(T_C - T_0)/T_C$ parameter and comparison with the corresponding values of the bulk.



Furthermore, the two batches of particles annealed at the different temperatures of 500°C and 820°C, for the same annealing duration of 4 h and slowly cooled afterwards, have been investigated by SEM analysis and in Figs. 4.2-29(a-b) and (c-d) the corresponding SEM images have been reported. It can be noticed that, while there is no difference in particles' shape and/or dimensions, the morphology of the surface is modified by changing the annealing temperature, as visible by comparing Figs. 4.2-29(b)-(d). For the powders annealed at 820°C the surface area is smoother and more homogeneous than the one of the particles annealed at 500°C, where sharp fractures, discontinuities, and steps can be detected. Hence, this evident discrepancy in morphological features of the particles' surface can be associated to the different magnetization of the austenite, which is lower for the particles annealed at a lower temperature, as previously observed from the high-field magnetization measurements (Fig. 4.2-27). Due to the lower available thermal energy upon heating at 500°C as compared to annealing at 820°C, it can be supposed that the atomic mobility is not sufficient to annihilate the point defects and dislocations and promote a complete reconstruction of the surface. Thereby, the retained atomic dangling bonds and microstructural disorder could be responsible for the lowering of Mn atoms, carrying the magnetic moment, which can contribute to the magnetic interactions, thus leading to the decrease of the total saturation magnetization of the austenite.

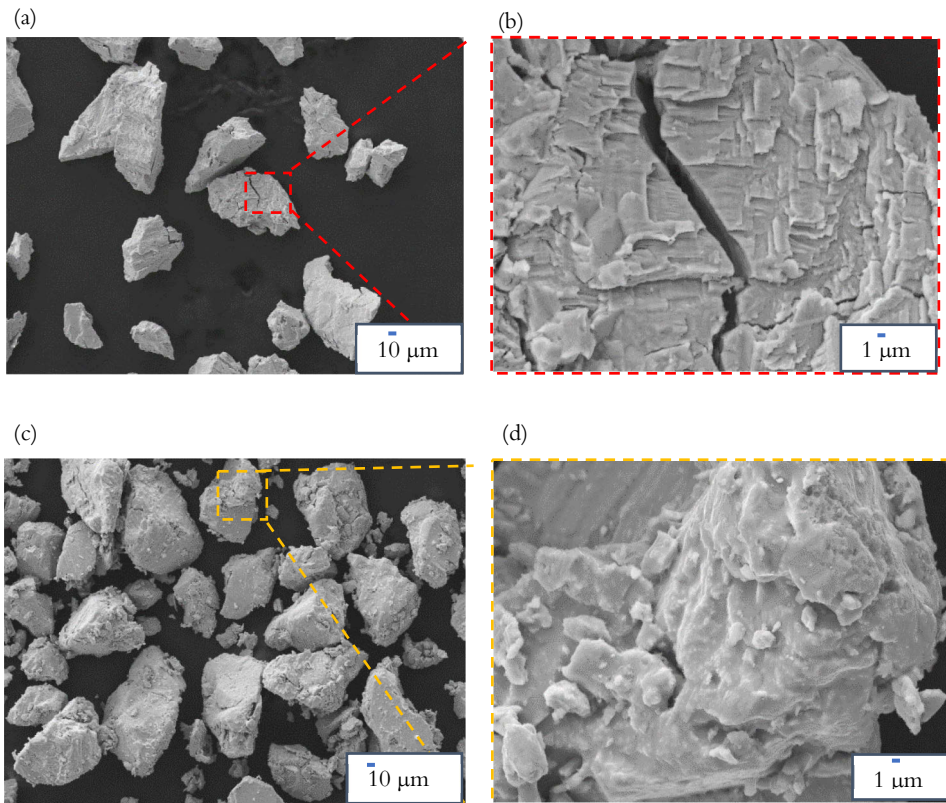


Figure 4.2-29: SEM micrographs of the $Ni_{45.7}Mn_{36.9}In_{13.2}Co_{4.2}$ hand-grinded powders: (a) and (b) after the annealing for 4h at $500^{\circ}C$ (+ slow cooling), at the magnification of 500 X and 5 KX, respectively; (c) and (d) after the annealing for 4h at $820^{\circ}C$ (+slow cooling), at the magnification of 500 X and 5 KX, respectively.

Finally, by combining all the achieved results for the post-annealed hand-grinded powders of $Ni_{45.7}Mn_{36.9}In_{13.2}Co_{4.2}$ compound, the following considerations have been derived. A drastic and irreversible worsening of the magneto-structural properties, in terms of increase of the thermal hysteresis and transformation temperature range and decrease of the magnetization change across the metamagnetic martensitic transformation, is obtained by gradually fracturing and reducing the starting bulk material in form of micro-meter sized particles. The hysteresis width value appears to be predominantly and strictly related to the mean particle size of the powder, since it does not change by applying a thermal treatment after the hand grinding process and by varying the conditions of annealing temperature, time, and cooling rate. Concomitantly to the increase of the thermal hysteresis, it has been

observed an increase of the magnetic moment at low temperatures by reducing the particle size, which depends on the amount of retained untransformed ferromagnetic austenite, as shown by the temperature dependent X-ray diffraction measurements. These features then point out the occurrence of size-dependent phenomena by decreasing the particles' volume, which are likely ascribed to the increase of internal constraints and the difficult propagation, by lattice-shear distortions, of the martensitic phase inside the parent phase [145,156]. In fact, the grain-boundaries and any type of interface become thicker by increasing the surface-to-volume ratio of the particles and act as higher energy barriers against the nucleation and growth of the martensitic phase with respect to the coarser particles with larger available grain's volume [94]. Accordingly, when the grain size is comparable to the characteristic length of deformation mechanism of the martensitic plates (twinning), the grain-boundaries become a source of pinning and strengthening of the austenite, due to the Hall-Petch mechanism of dislocation pileups in small grains [19,145]. Hence, the increase of microplasticity at the phase boundaries leads to a higher frictional work and lower elastic energy storage for the formation and growth of further martensitic plates, resulting in the mechanical stabilization of the austenite [157].

Concerning, instead, the release of mechanically induced stresses and removal of microstructural disorder after the hand grinding process, the annealing treatment at 500°C has resulted to be not effective, as highlighted by the restoration of a lower magnetization of the austenite as compared to the annealing at 820°C. Moreover, it has been observed a shift to higher temperatures of the martensitic transformation temperatures on decreasing the annealing temperature and, for the same fixed annealing temperature (500°C or 820°C) on increasing the cooling rate (water-quenching). Since the powders water quenched end up with a higher concentration of defects, in form of quenched-in vacancies, and/or internal stresses as compared to the slowly cooled ones, the achieved trends highlight that the presence of such local strains and disorder (pre-existing or thermally induced defects), play a fundamental role in creating favourable sites for triggering the martensitic phase transformation, thus decreasing the required undercooling for the heterogeneous martensite nucleation [24]. Therefore, the overall changes in the degree of atomic order, microstructural landscapes, density and width of defects, such as vacancies, anti-phase boundaries, dislocations, during the thermo-mechanical history of the powder, have a strong non-trivial impact on the kinetic and thermodynamic aspects of the martensite phase formation, other than the specific particle size and shape. After taking into account all these factors, the current experimental results have revealed that the best annealing conditions to recover in the hand-grinded powders of $\text{Ni}_{45.7}\text{Mn}_{36.9}\text{In}_{13.2}\text{Co}_{4.2}$, with $d < 66 \mu\text{m}$, a sharp martensitic transition and a large

magnetization change ΔM_{M-A} between the two phases, is a short-duration (2 h) heat treatment at high-temperature (820°C), followed by a slow cooling rate.

4.2.5 Summary of the Hand-grinded powders' preparation

In summary, the process of comminution and grain-refinement apported by the hand grinding process has led, for each Heusler compound, to the stabilization, at room-temperature, of the tetragonal non-modulated martensitic phase, and to a worsening of the martensitic transformation features, with respect to the corresponding starting bulk material. These detrimental effects have been visualized, in the low field magnetic susceptibility and high-field magnetization measurements, as the broadening and the shift to a higher temperature of both the forward and reverse martensitic transformations, accompanied by a decrease of the saturation magnetization of the ferromagnetic phase and a reduction of the magnetization change across the magneto-structural transformation. The latter has been linked to the interruption of the martensitic phase transformation and, hence, to the presence of some fractions of untransformed ferromagnetic austenite at low temperatures, as observed for Ni-Mn-In-Co compounds.

After the relaxation of the mechanical stresses during the annealing treatment, the structural analysis has revealed, for all the examined systems, the appearance of a 7M modulated martensitic structure, on cooling from the high-temperature cubic austenite. This leads to the consideration of a stress-induced origin of the inter-martensitic phase transformation, by temperature and/or mechanical loading, between different martensitic structures (or microstructures), in accord to what has been reported in literature [140,142].

A significant but different influence of the external thermal energy on the restoring of the magneto-structural properties, in the hand-grinded powders, has been observed between the Ni-Mn-Ga/Ni-Mn-Cu-Ga compounds, on the one hand, and the Ni-Mn-In-Co compound, on the other one. Indeed, for the former two systems, presenting a coupled Martensitic-Curie transformation, an annealing treatment at medium temperature (500-600°C) and for a short time (4h) has been sufficient to recover or even improve the magneto-structural properties with respect to the bulk, as for instance, the enhancement of phase homogeneity, reduction of thermal hysteresis, and, in some cases, increase of saturation magnetization.

For Ni-Mn-In-Co, characterized by a metamagnetic martensitic transformation, an optimization of the annealing treatment has been more challenging and, the obtained

results have pointed out the irreversible and drastic worsening of the magnetic and magneto-structural properties by gradually fracturing and reducing the sample size. This fact has been highlighted by the increase of thermal hysteresis and decrease of the magnetization change between the two phases.

From one side, these differences can be connected to the higher Mn-excess and concurrent lower Ni- amount in the off-stoichiometric quaternary Ni-Mn-In-Co compounds as compared to the Ni-Mn-Ga and Ni-Mn-Cu-Ga systems investigated. Consequently, the higher atomic disorder and the alteration of the interatomic Mn-Mn distances can increase the competition between ferro- and antiferromagnetic interactions, which, especially in the martensitic phase, due to the decrease of crystal symmetry from cubic to tetragonal, leads to a complex magnetically ordered state [88,158]. In addition to this, also the type of main-group element X constituting the Ni-Mn-X Heusler compounds, namely In or Ga in the current investigated compositions, and/or the specific atomic substitutions, i.e., small amount of Co in place of Ni atoms, or Cu instead of Mn atoms, have a relevant contribution. Indeed, many published experimental and theoretical results [90,159] have evidenced a higher structural and magnetic stability of the martensitic phase in Ni-Mn-Ga near stoichiometric compounds, as compared to the off-stoichiometric Ni-Mn-In-(Co) ones, where In atoms and Co impurities appear to create local distortions in the Heusler unit cell, for the effect of chemical pressure or atomic volume. The intrinsic atomic disorder and structural-magnetic instability of Ni-Mn-In-Co compositions are also accompanied by a lower fracture resistance against mechanical compressive strengths and plastic deformations with respect to the Ni-Mn-Cu-Ga compounds, as evidenced by the mechanical tests. These phenomena then can account for a higher amount of induced lattice strains and defects by loading/unloading or applying thermal treatments, and the consequent drastic change of the magneto-structural behaviour in Ni-Mn-In-Co Heusler bulk and particles.

Beside the above-described phenomenology, it is still unclear and under investigation the role of particle/grain size on the change and possible tuneability of the phase transformations and magnetic properties.

4.3 BALL-MILLING OF Ni-MN-GA COMPOUND

In this sub-chapter there will be exposed and illustrated the achieved experimental results for Ni-Mn-Ga compound subjected to the cryo-milling and high-energy ball-milling techniques with the aim to obtain micro- or sub-microparticles.

First, the effects of ball-milling on particles' morphology, structural and magnetic properties are presented. Secondly, to assess the possibility to recover the original coupled magneto-structural transformation, the evolution of structure and magneto-thermal properties upon heating is investigated.

The behaviour of the different achieved powders will be compared with each other and with respect to the original bulk and hand-grinded counterparts, to highlight size-dependent phenomena.

4.3.1 High-Energy Ball-milling

In a SPEX-8000 mill (3.1.2), the high-energy ball-milling (HEBM) process was performed on the hand-grinded powder of $\text{Ni}_{49.4}\text{Mn}_{30.3}\text{Ga}_{20.3}$ Heusler compound. Using 4 balls of 12 mm diameter made of stainless steel, the jar of the same material was charged with the powder in proportion of 10:1 ball-to-powder weight ratio and sealed under a protective Ar atmosphere. The milling process was conducted in steps of 30 min milling and 1 h rest, to avoid overheating of the system, up to an overall milling duration of 8 h. In Table 4.3-1, the resulting powder samples and the details of the subsequent applied thermal treatments have been specified.

Sample $\text{Ni}_{49.4}\text{Mn}_{30.3}\text{Ga}_{20.3}$	Milling time (h)	Annealing temperature (°C)	Anneali ng time (h)	Cooling rate	Corresponding name
Hand-grinded (HG)	-	-	-	-	HG
		500-	4	SC	HG4h500SC
		600	-	WQ	HG4h600WQ
High-energy ball milled (HEBM)	0.5	-	-	-	HEBM-0.5h
	1	-	-	-	HEBM-1h
	2	-	-	-	HEBM-2h
	8	-	-	-	HEBM-8h
	300-	1	WQ	8HEBM300WQ	

		400-				8HEBM400WQ	
		500-				8HEBM500WQ	
		790-				8HEBM790WQ	
		1000				8HEBM1000WQ	
Cryo-milled (CM)	1	-	-	-		CM-1h	
	2	-	-	-		CM-2h	
		300-	1	WQ		2CM300WQ	
		400-				2CM400WQ	
		500-	1	4	WQ	SC	2CM
		630-				WQ	500WQ
							2CM
							630WQ
		750-	1	WQ		2CM750WQ	2CM4h
		1000				2CM1000WQ	500SC
							2CM4h
							630WQ

Table 4.3-1: Details of milling procedure and annealing treatments adopted for the hand-grinded and ball-milled powder samples of $Ni_{49.4}Mn_{30.3}Ga_{20.3}$ compound.

The particles HEBM for 2 h (HEBM-2h) and 8 h (HEBM-8h, Table 4.3-1) were investigated by means of SEM analysis to detect differences in size and shape as a function of the milling time. As shown in the SEM images of Fig. 4.3-1(a-b), both the batches are constituted by particles of irregular and chunk morphology, where the effect of the increase of milling time is revealed by the breaking into smaller pieces, from a $45 \pm 10 \mu\text{m}$ to $20 \pm 10 \mu\text{m}$ average length, and the decrease of thickness below or equal to $10 \mu\text{m}$ (Fig. 4.3-1(b)). By comparing these observations with the literature results on ball-milled Ni-Mn-Ga particles, it has been found a significant difference from the claimed nanoparticles achieved by Y. D. Wang *et al.* [43] after subjecting the stoichiometric Ni-Mn-Ga Heusler compound to the same milling technique and milling time.

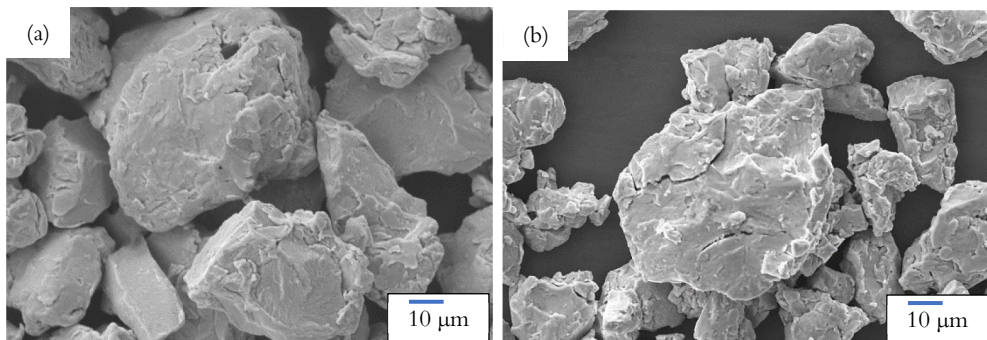


Figure 4.3-1: SEM images of the Ni-Mn-Ga HEBM particles after (a) 2h and (b) 8h of ball-milling process.

By XRD measurements at room-temperature, it has been studied the evolution of the original crystal structure (of the hand-grinded powder) during the HEBM process at different milling times, as reported in Fig. 4.3-2. The starting HG powder presents a predominant tetragonal martensitic structure, as indicated by the corresponding Bragg reflections (vertical black dashed lines) obtained by the Le Bail refinement, and a few traces of a cubic austenitic phase (vertical grey dashed lines). The lattice parameters have been listed in Table 7.1-1 of Appendix. From the diffraction pattern of HEBM-1h powder, it is seen that after 1 h of ball-milling process the initial structure is completely suppressed and peaks in different angular positions have appeared. These are identified with a disordered cubic structure with lattice constant $a=3.672\pm 0.001\text{\AA}$, lower than that of the austenitic phase. Then, after 2 h of HEBM, it is noted a decrease in peak intensity and an increase of peak width. On increasing the milling duration up to 8h, the peak broadening gradually increases for the effect of induced lattice deformations, defects, and grain-size refinement. Indeed, especially for those at the high angle, the reflections are difficult to be recognized and indexed. Moreover, for the fundamental peak at $2\theta=19.3^\circ$ it is observed an asymmetric rightward increase of the width, which, from the Le Bail refinement, appears to be compatible with the presence of a secondary cubic phase, indexed as “A *fcc*”, since it shows the same lattice constant ($a=5.849\pm 0.007\text{\AA}$) of the original austenitic phase. This fact can be understood by considering that part of the energy involved in the milling process is released as thermal energy (heat) which may have promoted in the particles the internal rearrangement or annihilation of dislocations, leading to a partial recovery process [117]. Therefore, it results that the batch of HEBM-8h powder is characterized by particles with a different degree of atomic disorder.

The structural transformation from the *bct* structure to a higher symmetric *fcc* phase during ball-milling, has been observed and reported also by Wang *et al.* [43] and Tian *et al.* [39,41] for Ni-Mn-Ga particles prepared by the high-energy ball milling process, in dry conditions. Hence, this structural evolution can be regarded as a peculiar behaviour of the Ni-Mn-Ga Heusler compound related to the milling energy involved.

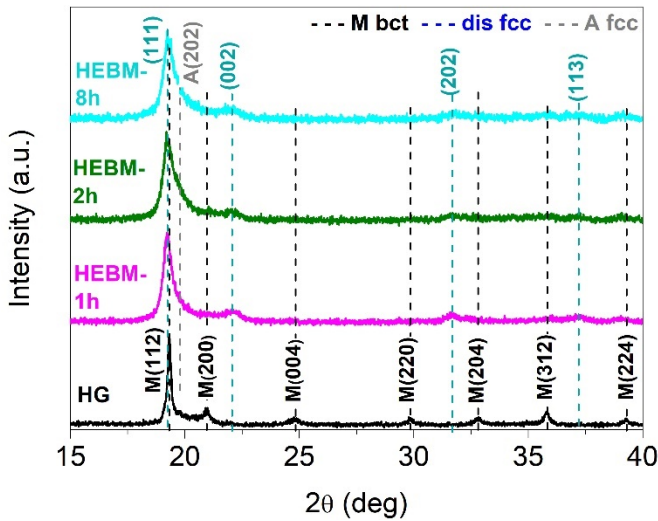


Figure 4.3-2: Room-temperature XRD patterns of Ni-Mn-Ga powders after HEBM process for different times (0.5h-1h-8h) and comparison with the diffraction pattern of the starting HG powder.

The effect related to the introduction of a large quantity of defects and lattice stresses on the magnetic properties of the HEBM particles has been investigated through the thermomagnetic analysis, as shown in Fig. 4.3-3. By looking at the magnetic susceptibility curves as a function of temperature for bulk, HG and HEBM powders samples, it is evident that the original coupled and/or decoupled magneto-structural transitions of the bulk are completely suppressed in the HEBM-8h powder. This fact is ascribable to the high sensitivity of the ferromagnetic order in the Heusler compounds to the configurational order and Mn-Mn interatomic distances, through the oscillatory RKKY exchange interactions, and highlights the drastic destruction of the Heusler phase during a long and high-energetic ball-milling procedure. Instead, by considering the behaviour of the HG powder, it can be understood that the application of an external mechanical stress and the fracturing into smaller pieces lead to an increase of the sample's volume transforming from martensite to austenite on heating (and vice-versa on cooling) in concomitance with the Curie transition of the austenite as compared to the bulk. This results in a single broad and hysteretic magneto-structural transition, in the temperature range 365-385K, similar to the second broad inflection of susceptibility at the Curie transition of the bulk (from 370 to 385 K).

It is worth noticing that similar thermomagnetic responses have been reported also by Albertini *et al.* [14] for bulk and small fragments of $Ni_{50}Mn_{30}Ga_{20}$ and/or

$Ni_{54.5}Mn_{20.5}Ga_{25}$ Heusler compound presenting the concurrence of the martensitic and Curie transitions. In such systems, rather than to the presence of chemical inhomogeneity in the starting bulk material, the observed thermomagnetic behaviour can be ascribed to internal stresses, generated by the thermo-mechanical history, and to their increase by decreasing particle size, giving rise to different paths of structural transformation.

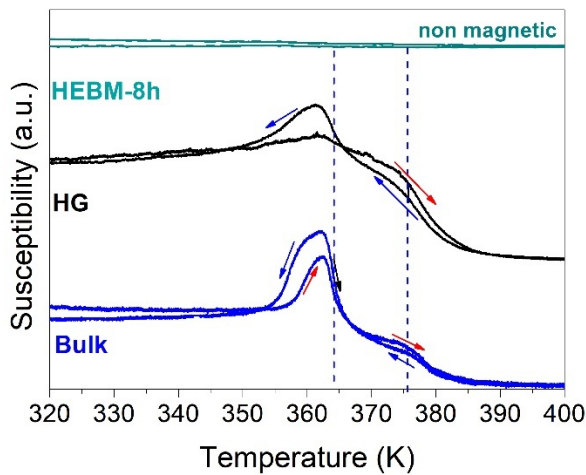


Figure 4.3-3: Comparison between the thermomagnetic responses of bulk, HG and HEBM-8h powder samples of $Ni_{49.4}Mn_{30.3}Ga_{20.3}$ compound.

The recovery of the original phase transitions and magnetic properties in the powder samples has been studied by performing different annealing treatments, for the HG powder, at the fixed time of 4h and at 500°C and 600°C, followed by slow cooling and water quenching. For the HEBM-8h powder, the annealing has been performed at the fixed time of 1h, by varying the temperature from 300°C to 1000°C, followed by water quenching (Table 4.3-1). The same annealing conditions have been applied also to the batch of particles cryo-milled for 2h, as it will be presented in the next section, in order to compare the structural and magneto-thermal evolutions of the two different batches under the same heating procedure.

In Figs. 4.3-4(a)-(b), on the left side, there have been reported the room-temperature XRD measurements and, on the right side, the susceptibility curves as a function of temperature of the corresponding powder batches, after the performed annealing treatments. It has to be noted that the behaviour of the HG powder

annealed at 600°C (HG4h600WQ sample), has been taken as the reference (on the bottom). Starting from the latter, the structural analysis by the Le Bail refinement has revealed a monoclinic-distorted 7M modulated martensitic structure (Table 4.3-2), comparable to the one reported in literature for similar compositions [138]. The thermomagnetic analysis (Fig. 4.3-4(b)), instead, has shown the coupled magneto-structural transition in a lower temperature range and at a lower temperature as compared to the HG powder, and the absence of the two distinct susceptibility behaviours, characterized by different critical (Curie and martensitic) temperatures, of the bulk. This fact points out the effectiveness of the thermal treatment in releasing the internal stresses and improving the phase homogeneity on the powder as compared to the bulk sample. Instead, the decrease of the transformation temperatures can be related to the effect of the quenching, which, differently from the slow cooling rate, prevents to reach the equilibrium atomic order degree allowed by the specific stoichiometry [92]. Concerning the HEBM particles, it emerges that the annealing temperature of 300°C is not sufficient to promote the required atomic mobility since the resulting crystal structure of the 8HEBM300WQ sample is still disordered, as highlighted by the not well-defined diffraction pattern. After the annealing at 400°C, the fundamental reflections of a cubic crystal structure, even though still broad, are recognizable and, from the magnetic point of view, it appears a magnetic Curie transition, spanning on a large temperature interval. Then, it is observed that the subsequent thermal treatment at 500°C has led to an increase of crystallinity of the cubic structure, associable to the recovery, in the HEBM particles, of the austenitic phase, but with retaining of the $B2$ -type disorder in the unit cell, since the superlattice reflections of the $L2_1$ ordered Heusler phase cannot be detected. The corresponding susceptibility behaviour has shown the presence of only a second-order Curie transition, sharper than that of the powder annealed at 400°C and approximately close in temperature to the magneto-structural transition of the reference. In contrast, no traces of the martensitic phase transformation have been detected. Only on further increasing the annealing temperature to 790°C, the diffraction pattern has shown some few traces of a partially recovered modulated 7M martensite at room temperature. Whereas the susceptibility measurement of the 8HEBM790WQ powder has revealed a broad martensitic transformation shifted to lower temperatures with respect to the Curie transition, which occurs at a temperature slightly lower than that of the 8HEBM500WQ sample. Moreover, by increasing the annealing temperature up to 1000°C, it has been noted the occurrence of a structural and magnetic disordering effect, as pointed out by the coexistence at room-temperature of both the non-modulated tetragonal and modulated 7M martensitic structures and the shift to a higher temperature, with a significant increase of broadening, of a not well-defined

magneto-structural transition. Even though for the 8HEBM1000WQ sample is not clearly distinguishable, it will be shown later for the CM-2h powder annealed at 1000°C that the obtained thermomagnetic behaviour is similar to the one of HG powder. This phenomenology stresses the tendency to phase decomposition under heat treatments at excessively high temperatures. In fact, it can be likely supposed that, due to the high atomic mobility at high temperature, the Heusler structure is disordered by the generation of point defects and the changes of configurational order from $L2_1$ to $B2$ -like type, which can be retained after quenching. Such disorder, especially for Mn-rich Ni-Mn-based Heusler compounds, can significantly enhance the intrinsic phase instability and magnetic frustration [91]. Furthermore, at such high annealing temperatures, due to the large surface reactivity of the particles (large surface-to-volume ratio) it is possible to trigger the evaporation of the most volatile Mn element, resulting in compositional variations. Hence, both the chemical inhomogeneity and the quenched-in atomic disorder can drastically affect the interaction between structural, elastic and magnetic degrees of freedom, thus changing the Heusler phase and the martensitic phase transformation in the achieved powder samples.

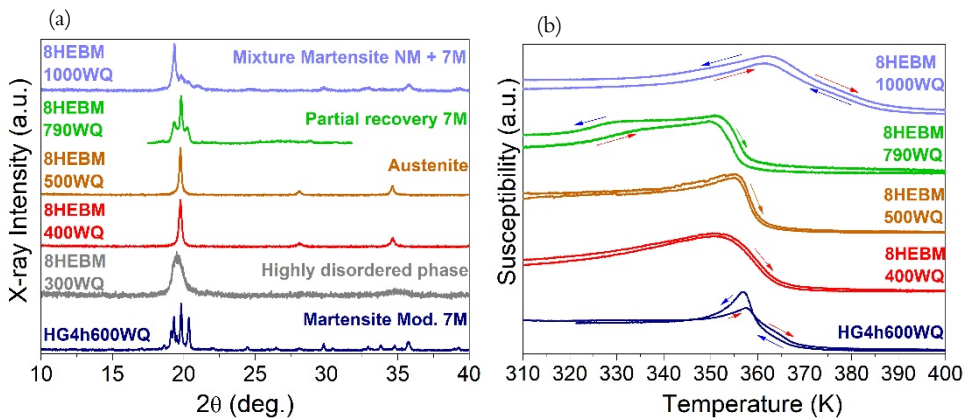


Figure 4.3-4: (a) Evolution with annealing temperature of the room-temperature XRD patterns of Ni-Mn-Ga HEBM-8h powders and comparison with the post-annealed hand-grinded powders (HG4h600WQ). (b) Evolution with annealing temperature of the corresponding magnetic susceptibility behaviours.

4.3.2 Cryo-milling

As above-mentioned, the HG powder of $\text{Ni}_{49.4}\text{Mn}_{30.3}\text{Ga}_{20.3}$ compound was subjected also to the ball-milling process at cryogenic temperatures ($< 123\text{ K}$ (-150°C)), using the cryo-milling technique (Chapter 3.1.2). This, indeed, was expected to impart a faster grain refinement and also less contamination from both milling media and external atmosphere compared to the room-temperature ball-milling [160].

The procedure was conducted in a Retsch Shaker Cryo-mill, using a jar of stainless steel, previously sealed in Ar atmosphere, with one ball of 20 mm diameter and a ball-to-powder weight ratio of 12:1. The vibration frequency was selected to 15 Hz, the whole system was pre-cooled for 10 min with liquid nitrogen's vapour, and then, under a constant LN_2 external flow, the process was conducted up to 2h, alternating 5 min of milling to 2:30 min of rest (at 5 Hz), to avoid overheating during milling. The details of the as-milled and post-milled annealed particles are listed in Table 4.3-1 (sub-section 4.3.1).

The SEM analysis of the particles CM-processed for 2 h (CM-2h) has pointed out a flaky morphology, as shown in Fig. 4.3-5(a), since the particles are characterized by a large length and a small thickness of few microns. Moreover, it has been observed a bimodal size distribution, as highlighted in Fig. 4.3-5(b), due to a large amount of both particles with $30 \pm 10\ \mu\text{m}$ length and bigger ones with $80 \pm 20\ \mu\text{m}$ length.

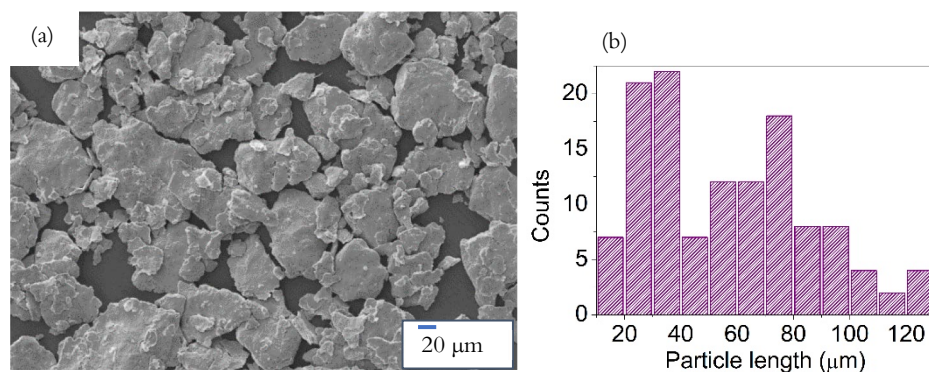


Figure 4.3-5: (a) SEM image of Ni-Mn-Ga particles CM for 2h and (b) corresponding particle size distribution.

In Fig. 4.3-6, there have been reported the room-temperature XRD measurements of the cryo-milled particles after 1h and 2h of milling process, which are compared to the diffraction pattern of the starting HG powder. It can be seen that the original tetragonal non-modulated martensitic structure (*M bct*) is transformed into a disordered *bct* phase for the CM-1h powder since the peaks decrease in intensity and increase in width, showing also an asymmetric broadening. These features are ascribed to the occurrence of grain-refinement and non-uniform lattice deformation. After 2h of CM, instead, the diffraction pattern points out an increase of the asymmetric broadening of the tetragonal reflections and the appearance of new peaks, referred to as a disordered cubic structure (“dis *fcc*”) with a lattice constant $a=3.6745 \pm 0.0003 \text{ \AA}$ lower than the original cubic austenite phase (Table 7.1-1, Appendix). It is then interesting to highlight that the cryo-milling process, being less energetic than the vibrational HEBM [119], for the same fixed milling time, leads to a lower amount of induced defects, lattice deformation and overheating, thus allowing the retaining in the particles of a higher degree of crystallinity. Moreover, it is confirmed, in agreement with the literature results [40,41,43], that the transformation from the *bct* phase to the higher-symmetry *fcc* phase is peculiar of Ni-Mn-Ga compound subjected to the energetic and/or prolonged mechanical milling in dry conditions. In fact, for Ni-Mn-Ga particles ball-milled in a PBM with a liquid milling medium the structural transformation to the cubic phase has not been detected [39].

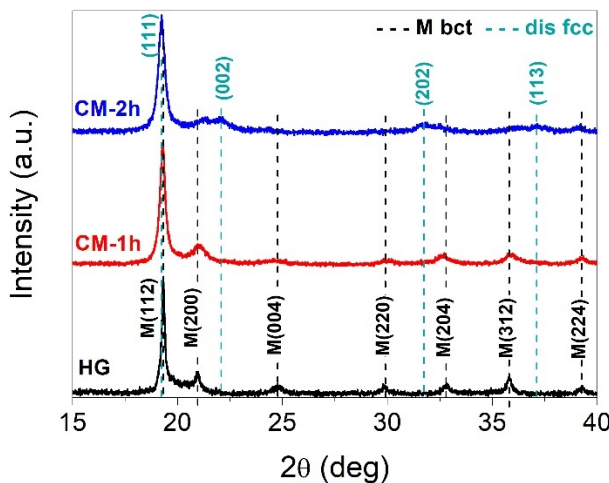


Figure 4.3-6: Room-temperature XRD patterns of hand-grinded powder and after the cryo-milling process for 1h (CM-1h) and 2h (CM-2h) for $\text{Ni}_{49.4}\text{Mn}_{30.3}\text{Ga}_{20.3}$ compound.

The introduction of atomic disorder and the structural change, albeit in minor extent with respect to the HEBM process, has caused the suppression of ferromagnetic order also in the CM-2h particles, as it can be seen by the susceptibility response as a function of temperature in Fig. 4.3-7(b). This fact points out the extreme sensitivity of the magnetic interactions to the structural variations and atomic displacements. Thereby, for the recovery of the original phase transformation, several annealing treatments have been performed, at the fixed time of 1h and at the various temperature from 300°C to 1000°C (Table 4.3-1). In Fig. 4.3-7(a), there are shown the XRD patterns, collected at room-temperature, of the differently annealed powders, compared with those of the reference HG4h600WQ powder (see section 4.2). Figure 4.3-7(b) presents the magnetic susceptibility measurements of the corresponding batches. As mentioned in the previous section, it is important to note that for the HG4h600WQ sample the XRD analysis has revealed the structure of a monoclinic-distorted 7M modulated martensite at room-temperature, with lattice parameters listed in Table 7.1-1 of Appendix. The thermomagnetic analysis, instead, has pointed out the presence of a coupled magneto-structural transformation, from a ferromagnetic high anisotropic martensite to a paramagnetic cubic austenite in the temperature range 360–370 K. Concerning the annealed CM-2h powders, it can be observed that after the heat treatment at 300°C, the structure is still disordered, since only a few and broad peaks can be detected. A gradual increase of peak intensity is observed, instead, on increasing the annealing temperature to 400°C, leading also to the increase of magnetic susceptibility and appearance of a broad Curie transition. With the annealing treatment at temperature between 500°C and 630°C, the restoration of the modulated martensite and associated magneto-structural phase transition takes place, as can be seen in Figs. 4.3-7(a-b). Interestingly, on further increasing the annealing temperature from 750°C up to 1000°C, from the magnetic point of view it emerges a gradual shift towards higher temperature and increase of broadening of the overlapped Martensitic-Curie transition in such a way that it resembles the magneto-structural behaviour of the HG powder. From the structural point of view (Fig. 4.3-7(a)), instead, for the 2CM1000WQ it results the almost suppression of the modulated phase and the appearance of the tetragonal non-modulated martensitic structure. This result is the same obtained for the HEBM-8h particles annealed in the same conditions, hence it is independent on the particle morphology and degree of induced disorder during ball-milling. Rather, it reveals that, similarly to the effect of cold-working during the grinding process, under an excessive high thermal energy the 7M modulated structure becomes unstable and a stress-induced inter-martensitic transformation to the tetragonal structure takes place. Likely, this change is triggered by the induced lattice deformations, dislocations, point

defects, created by a rapid cooling rate (water quenching) from high temperature, which strongly affect the microstructural landscape and thus the growth and accommodation of the martensitic variants as well as the interactions with the ferromagnetic degrees of freedom, due to the peculiar ferro-elastic nature of the martensitic phase [74]. In addition, the suppression of the modulated phase could be also ascribed to configurational disorder in the Heusler phase, to whom the Mn-rich compositions are particularly sensitive [91], since the selected high annealing temperatures of 750°C and 1000°C are close to the transition temperature ($T_t^{L2_1/B2}=780^\circ\text{C}$ [92]) from the ordered $L2_1$ Heusler phase to the disordered $B2$ structure, and after quenching some $B2$ -type disorder could be retained. Accordingly, atomic disorder and internal stresses can modify, without any compositional change, the martensitic phase transformation due to the strong coupling between structural-elastic-thermal-magnetic properties [10].

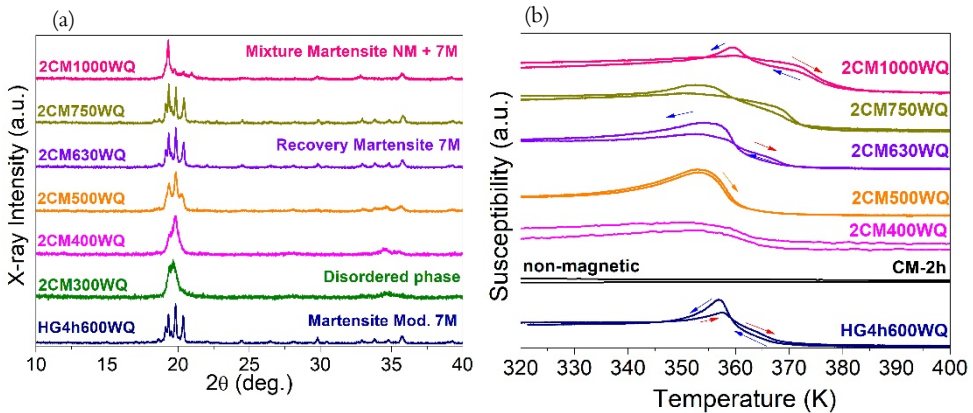


Figure 4.3-7: (a) Evolution of room-temperature XRD spectra for the CM-2h powders of Ni-Mn-Ga as a function of the annealing temperature, and comparison with the post-annealed hand-grinded powders (HG4h600WQ). (b) Thermo-magnetic analysis of the corresponding powders batches.

From low-field ($\mu_0 H_{ext} = 5$ mT) magnetization measurements down to few K, it has been discovered that both bulk and powder samples of $\text{Ni}_{49.4}\text{Mn}_{30.3}\text{Ga}_{20.3}$ compound undergo an inter-martensitic transformation, at a temperature well-below the coupled magneto-structural transition. This has been highlighted in Fig. 4.3-8(a), where, on decreasing temperature below 125 K, it can be noticed that the magnetization of the martensite phase has a drop and between the cooling and heating branches it is opened a thermal hysteresis, which closes in correspondence to the onset

of the magneto-structural transformation, at 360 K, on heating. These features are clearly highlighted in both HEBM particles annealed at 500°C (8HEBM500WQ) and CM particles heat treated at 630°C (2CM630WQ). Therefore, even though the XRD pattern of the former powder has evidenced at room-temperature only the presence of a cubic $B2$ structure of the austenite, the low degree of atomic order does not prevent the formation of the martensitic phase. The observed inter-martensitic transformation is typical of Ni-Mn-Ga Heusler compound with composition similar to the studied one ($e/a=7.64-7.68$) and, as described in [138], takes place on cooling from a 7M modulated structure to a $L1_0$ tetragonal phase and/or a mixture of 7M and $L1_0$ martensitic structures, which are characterized by different magneto-crystalline anisotropy, where the highest one among the martensitic phases is found for the non-modulated phase. The current experimental results validate the hypothesis discussed in literature of the tendency for the $L1_0$ phase to be the ground state. Moreover, it has been shown that for the same composition the tetragonal structure is the most stable one, able to sustain high thermal and mechanical stresses, which points out an intrinsic metastable character of the modulated phase.

With still reference to Fig. 4.3-8(a), it is also worth noticing that both post-annealed HG, CM and HEBM powder batches are characterized by a sharp martensitic transformation, occurring at the same temperature, whereas for the bulk sample there are recognized two different inflections, shifted to slightly higher temperatures, which lead to an increase of broadening. This fact denotes the improvement of homogenization by decreasing the sample size to micro-meter sized particles and applying short heat treatments at medium temperature.

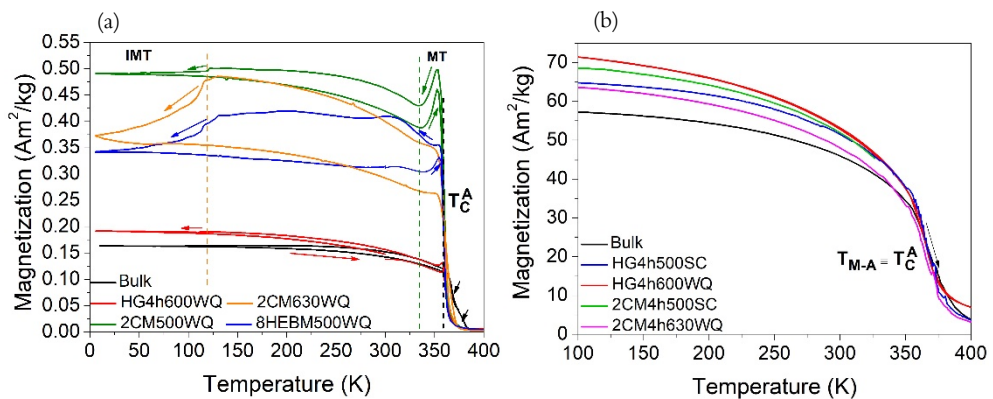


Figure 4.3-8: (a) Low-field Magnetization measurements as a function of temperature for some of the differently annealed CM, HEBM, and HG powders, in comparison to the $M(T)$ of the bulk. (b) High-field temperature-dependent magnetization curves of bulk and post-annealed HG and CM samples.

The improvement of the magneto-structural properties with respect to the initial bulk sample has been achieved for all the hand-grinded and ball-milled particles properly annealed. In fact, by looking at the $M(T)$ measurements at high field ($\mu_0 H_{ext} = 1\text{T}$), in Fig. 4.4-8(b), it is revealed that, at the fixed temperature of 100 K, the saturation magnetization of the martensite can be increased by 20% and 25% of that of the bulk for the 2CM4h500SC and HG4h600WQ powder samples, respectively. Furthermore, it has been noticed that for the CM-2h powder the annealing at 500°C for 4h followed by slow cooling leads to an increase of magnetization as compared to an annealing treatment for 1-4 h, at 630°C, followed by water quenching. On the contrary, for the HG powder, the annealing temperature of 600°C and the water quenching are better conditions to increase the saturation magnetization, as compared to the annealing at 500°C followed by slow cooling. It is worth underlining that recently M. Qian *et al.* [161] have reported on the possibility to enhance the magnetocaloric power with respect to the bulk in off-stoichiometric $Ni_{54.3}Mn_{21.3}Ga_{24.4}$ microparticles, thanks to the reduction of the hysteresis losses, the enlargement of the transformation temperature range and of the saturation magnetization, which are in agreement and, hence, support the current experimental findings.

4.4 BALL-MILLING OF Ni-MN-CU-GA COMPOUND

The second investigated material with the ball-milling technique is the Ni-Mn-Cu-Ga Heusler compound. In this sub-chapter, there will be described the effects of cryo-milling, planetary ball-milling with a solvent and a combination of the two processes with surfactant-assistance, on the reduction of particle size. It will be presented a study on the thermal treatments which are required to recover the austenite and martensite crystal phases and the magneto-thermal properties, in particles subjected to different conditions of milling energy and milling time. Then,

the recovered magneto-structural transformation will be compared to the original bulk's and coarse-grained counterpart's one.

4.4.1 Cryo-milling

The cryo-milling process was conducted on hand-grinded (HG) powder of $\text{Ni}_{49.7}\text{Mn}_{18.7}\text{Cu}_{6.4}\text{Ga}_{25.2}$ compound in the same type of Retsch Shaker Cryo-mill (CM), selecting the same milling parameters of ball-to-powder weight ratio, frequency, intervals of milling and rest, as the ones adopted for the milling procedure of Ni-Mn-Ga compound (see section 4.3.2). The cryo-milling process was run for an overall milling time of 3 h. In Table 4.4-1 the as received and post-annealed CM powders, associated with their corresponding name, are listed.

Sample: $\text{Ni}_{49.7}\text{Mn}_{18.7}\text{Cu}_{6.4}\text{Ga}_{25.2}$	Milling time (h)	Annealing temperature (°C)	Annealing time (h)	Cooling rate	Corresponding name
Hand-grinded (HG)	-	-	-	-	HG
		500-	4	WQ	HG4h500WQ
		630			HG4h630WQ
Cryo-milled (CM)	2	-	-	-	CM-2h
		500	4	WQ	2CM4h500WQ
		630	4	SC	2CM4h630SC
	3	-	-	-	CM-3h
		630	4	WQ	2CM630WQ

Table 4.4-1: Summary of examined HG and CM powders, with specification of the annealing treatments adopted and corresponding batch's name.

The as-received particles (CM-3h) have shown the morphology and size distribution displayed in Figs. 4.4-1(a)-(b), from which it emerges the tendency to deform in elongated and thin flakes, having an average length of $37 \pm 18 \mu\text{m}$ and a thickness of 1-2 μm . Hence, it can be noted a deformation mode similar to the one of Ni-Mn-Ga particles, under the same milling conditions (4.3.2, Fig. 4.3-5(a)), but a resulting more uniform and narrower size distribution, peaked at about 40 μm length.

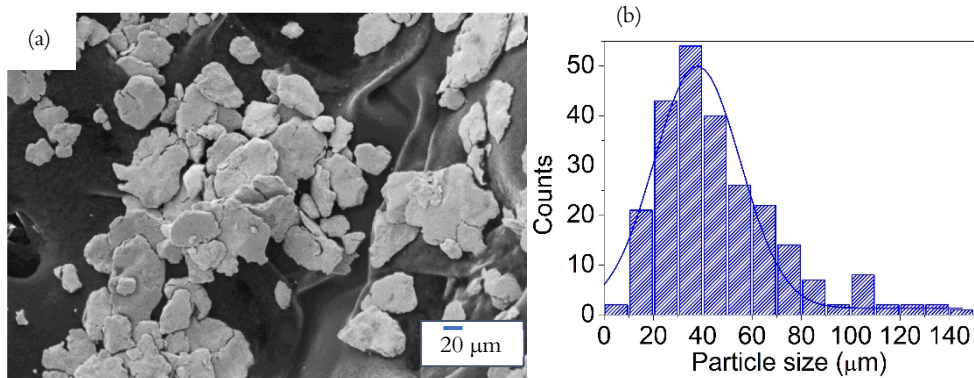


Figure 4.4-1: (a) SEM micrograph of Ni-Mn-Cu-Ga particles CM for 3h and (b) corresponding size distribution.

The structural evolution during the CM process is presented in Fig. 4.4-2, where the XRD measurements collected at room-temperature, for HG, CM-2h and CM-3h powders are compared. First of all, it is shown that the HG powder is characterized by a mixture of tetragonal non-modulated martensite and cubic austenite, whose fundamental reflections have been revealed by the Le Bail refinement (Table 7.2-1, Appendix). Secondly, it is observed that the CM-2h and CM-3h particles show almost the same diffraction pattern, characterized by the suppression of the cubic austenitic reflections and the broadening of the peaks of the original *bct* phase with a non-uniform shift of the fundamental reflections positions. Then, this points out the occurrence of an anisotropic lattice strain during the ball-milling procedure and, possibly, could be related to the oblate shape of the particles (Fig. 4.4-1(a)). It is worth stressing that the preservation of a *bct* structure, although much more disordered than the original martensitic one, is significantly different from the result of the structural transformation to a higher symmetric *fcc* phase obtained for Ni-Mn-Ga CM-2h powder. Therefore, it is revealed that the Ni-Mn-Cu-Ga compound has a higher mechanical stability against prolonged severe plastic deformation. In fact, by published works [137,162], it emerges that the addition of Cu leads to an improvement of mechanical ductility, thanks to the formation of a secondary ductile γ -phase, as compared to the ternary compound. Furthermore, it has been recently reported in literature [131] that, under low-applied mechanical stresses, Ni-Mn-Cu-Ga Heusler compound can be easily textured thanks to the martensitic variants rearrangement, favouring a higher compatibility between grains and hence a higher resistance against defects' propagation and fracture. The combination of these peculiar mechanical and

microstructural features could reasonably account for the current experimental observations under the action of ball-milling.

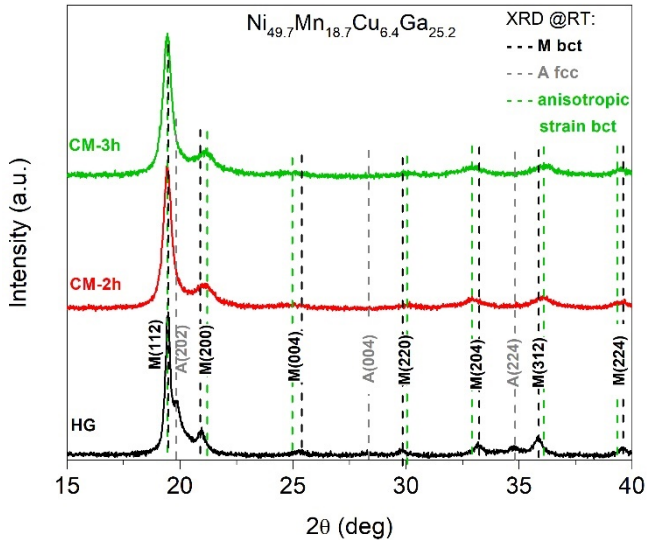


Figure 4.4-2: Room-temperature XRD patterns of hand-grinded and cryo-milled particles (for 2 and 3 hours) of $\text{Ni}_{49.7}\text{Mn}_{18.7}\text{Cu}_{6.4}\text{Ga}_{25.2}$ compound.

The change of the original crystal structure due to the induced atomic disorder and strong lattice strain have caused a drastic suppression of both magneto-structural transformation and ferromagnetic order in the CM powder, as it can be observed in Fig. 4.4-3, by comparing the low-field ($\mu_0 H_{ext} = 10$ mT) $M(T)$ measurements of bulk, HG and CM-3h samples. It is worth noticing that already after the hand grinding process the particles show a reduction of the saturation magnetization of the martensitic phase and the broadening of the coupled magneto-structural transformation, associated with a lower thermal hysteresis between heating and cooling branches. These features are ascribable to the influence of the increase of the surface-to-volume ratio, other than to the introduction and accumulation of stacking faults and point defects as reported in literature [42], which reduces the total number of Mn-Mn atoms coupled ferromagnetically, due to perturbation and/or variations of the interatomic distances and hence sign of the exchange interactions (RKKY). Furthermore, the enlargement of the transition could be related to the fracturing into small non-interacting pieces, which, due to the lack of mechanical coupling,

fundamental for triggering at once the transformation through the volume change of neighbouring parts [146], require a higher external energy (overheating/undercooling) to overcome the internal elastic energy barriers. This leads to a more discontinuous and intermittent transformation behaviour of the non-interacting pieces as compared to a single and large bulk fragment [64,146].

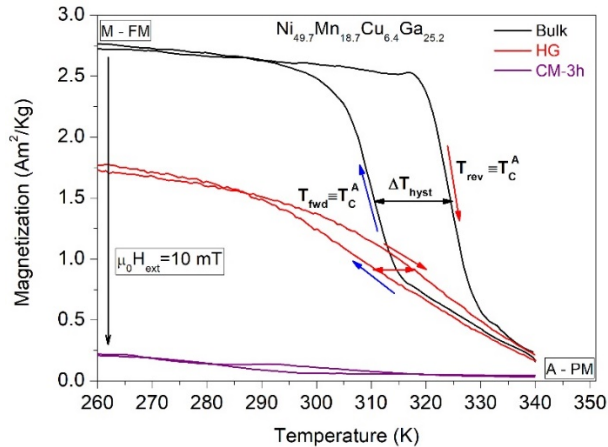


Figure 4.4-3: Low-field magnetization measurements as a function of temperature for bulk, hand-grinded and cryo-milled samples of $\text{Ni}_{49.7}\text{Mn}_{18.7}\text{Cu}_{6.4}\text{Ga}_{25.2}$ compound.

Based on the results Ni-Mn-Ga CM post-annealed particles, also for the Ni-Mn-Cu-Ga CM powders there have been performed the annealing treatments at 500°C and 630°C for 4 h, followed by slow cooling/water quenching (Table 4.4-1). The recovery of the original crystal structure and coupled magneto-structural phase transition has been investigated through high-field temperature-dependent magnetization measurements, as reported in Fig. 4.4-4. It can be seen that all the powder batches, HG, CM-2h and CM-3h, can recover the coupled martensitic-Curie transition, but with notable differences in temperatures, broadening and magnetization change among each other and with respect to the original bulk sample. For the CM-2h powder, it is observed that the annealing at 500°C followed by water quenching leads to a significant shift to lower temperatures of the transformation, both in heating and cooling branches, and to a slight decrease of the saturation magnetization of the martensite as compared to the powder annealed at 630°C and slowly cooled afterwards. The latter shows magneto-structural properties similar to

those of the HG4h630WQ powder and only a slight shift to higher temperatures of the transformation. However, for both the 2CM4h500WQ and 2CM4h630SC samples it is noticed an increase of the transformation temperature range as compared to the annealed hand-grinded powder. This broadening of the transformation is drastically enhanced for the 3CM4h630WQ powder, accompanied also by a significant decrease of magnetization of the martensite. Therefore, these results suggest that for the CM powders milled for more than 2 h the selected annealing conditions are not sufficient for enabling an optimal structural and/or microstructural recovery through annihilation of defects, release of stresses and atomic reordering processes. Further, the enlargement of the phase transformation range seems to be directly connected to the decrease of particle length and thickness, which likely, due to the restricted available volume, can lead to an increase of the elastic energy stored across the transformation. Instead, with respect to the bulk, characterized by a thermal hysteresis of $\Delta T_{hyst} = 13$ K, it is worth noticing that the powder batches show a notable decrease to 5-6 K of the hysteresis width, while the saturation magnetization of the martensite is lowered by only 6.5 %. Moreover, it is observed the almost suppression of magnetization in the paramagnetic state of the austenite, differently from the bulk, thus pointing out the effectiveness of particle size reduction and thermal treatment, for a short duration and at a medium temperature, in improving the sample homogenization. A similar result has been achieved also for bulk samples of $\text{Ni}_{50}\text{Mn}_{19}\text{Cu}_6\text{Ga}_{25}$ compound subjected to compressive stress assisted thermal cycling, as reported in [131], which confirms, on the one hand, the characteristic behaviour of the Ni-Mn-Cu-Ga arc-melted polycrystalline material and, on the other one, leads to the consideration of a possible increase of grains compatibility thanks to the mechanical deformation under grinding and ball-milling.

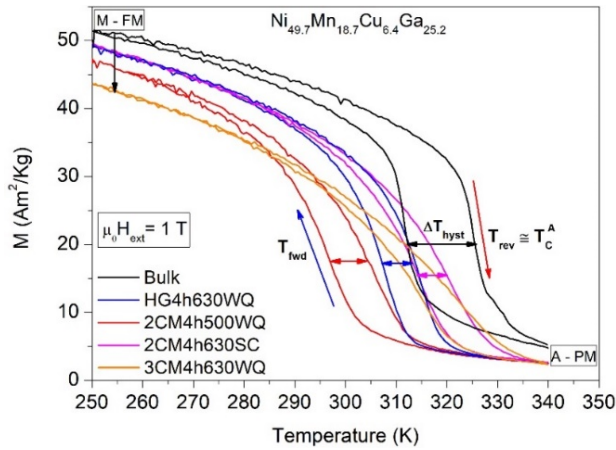


Figure 4.4-4: High-field temperature-dependent magnetization curves for bulk, HG powder and post-annealed batches of CM-2h and CM-3h powders of $\text{Ni}_{49.7}\text{Mn}_{18.7}\text{Cu}_{6.4}\text{Ga}_{25.2}$ compound.

4.4.2 Planetary Ball-milling

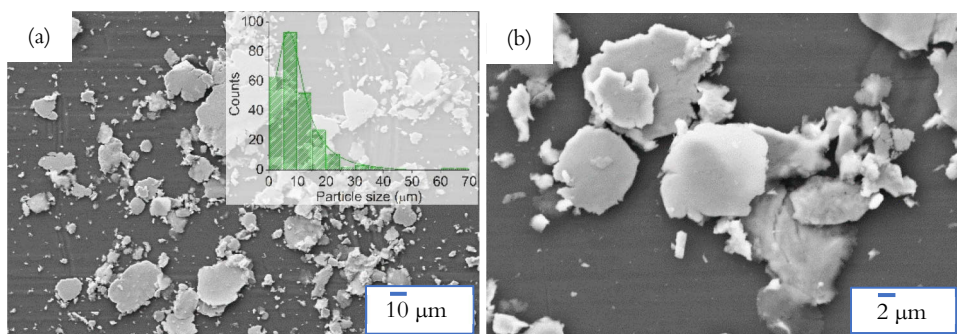
Subsequently, it was tested the planetary ball-milling process in wet conditions, aimed at reducing the particle size towards the nanoscale, avoiding overheating and cold-welding between particles. Hence, in a Fritsch Pulverisette 7, using Zirconia media and spheres of 5 mm diameter, two distinct jars were charged with HG powder and CM-3h powder, respectively, selecting a ball-to-powder ratio of 10:1. While isopropanol, as liquid milling medium, was added in the jar with HG powder, a mixture of Oleic Acid (20 wt. % of the powder) as surfactant, and n-heptane, as solvent, was put in the jar with CM-3h powder, to assess the effectiveness of the two-steps process with surfactant-assistance. The process was run at the rotational speed of 300 rpm, in intervals of 10 min milling and 5 min rest, for several hours. The investigated milled and heat-treated powder batches are summarized in Table 4.4-2.

Sample: $\text{Ni}_{49.7}\text{Mn}_{18.7}\text{Cu}_{6.4}\text{Ga}_{25.2}$	Milling time (h)	Annealing temperature (°C)	Annealing time (h)	Cooling rate	Corresponding name	
Planetary ball-milled with isopropanol (wetPBM)	19	-	-	-	wetPBM-19h	
		750	24	WQ	19wPBM24h750	
		755			SC	WQ
						SC

			35	-	-	-	wetPBM-35h	
				755	22	SC	35wPBM24h755	
							SC	
Cryo- milled (CM)	+	Planetary ball-milled with surfactant- assistance (SAPBM)	3	+	8	-	-	3CM+8SAPBM
					14	755	4	SC

Table 4.4-2: Details of milling process, milling time and thermal treatment selected for the investigated planetary ball-milled powder batches of $\text{Ni}_{49.7}\text{Mn}_{18.7}\text{Cu}_{6.4}\text{Ga}_{25.2}$ compound.

In Figs. 4.4-5, there have been reported the SEM images of the particles PBM with isopropanol for 19 h (a-b) and of the CM-3h particles PBM with surfactant-assistance for 8 h (c-d). It is noted that, as for the CM process, the particles of Ni-Mn-Cu-Ga subjected to the PBM method with a solvent and/or a surfactant present a similar deformation mode, which is characterized by a first elongation into flat and thin flakes and a subsequent fracture into smaller pieces on increasing the milling time. It is recognized that the two-steps method is more effective for achieving a particle size reduction than the prolonged wet PBM process alone starting from coarse HG powder. In fact, while for the batch of wetPBM-19h powder an average particle length of $8 \pm 6 \mu\text{m}$ (Fig. 4.4-5(a)) is obtained, with only a few of sub-micro-meter sized particles (800-900 nm), the majority of the 3CM+8SAPBM particles present a size lower than $2 \mu\text{m}$ (Fig. 4.4-5(c)), with a peak below 500 nm (Fig. 4.4-5(d)). As visible in Fig. 4.4-5(d), these ones form a slurry mixture with the residual surfactant.



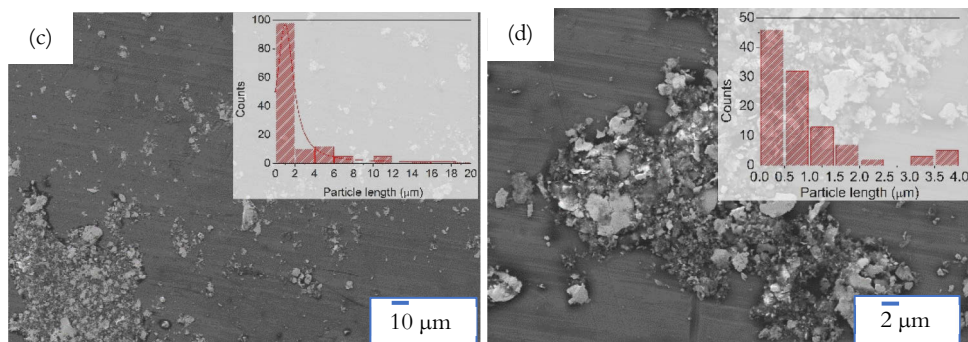


Figure 4.4-5: SEM images showing at two different (increasing) magnifications the morphology of Ni-Mn-Cu-Ga particles (a-b) prepared by wet PBM process for 19 h and (c-d) by the two-steps process with surfactant-assisted PBM for 8 h. Insets: particle size distribution of the corresponding powder batches.

After a milling duration of 35 h, it has been possible to further decrease the thickness of the particles PBM in isopropanol and separate, after a procedure of sonication and centrifugation, the supernatant part of the solution, containing, as a small subgroup of the entire batch, sub-micron meter sized particles. Indeed, the preliminary DLS analysis of this solution has pointed out the presence of nanoparticles with an average hydro-dynamic diameter of 350 nm, as reported by the multimodal size distribution in Fig. 4.4-6. Then, with the TEM analysis, it has been confirmed the achievement of nanoparticles with size of 250–400 nm. These have shown a spatial distribution of elements homogenous among each other, as highlighted by the microanalysis with coloured maps in Fig. 4.4-7. Moreover, the Selected Area Electron Diffraction (SAED) pattern (Fig. 4.4-8) is characterized by continuous rings with evidence of some single spots, hence highlighting that the as-prepared polycrystalline particles are constituted by smaller nanocrystalline units of few tens of nano-meters.

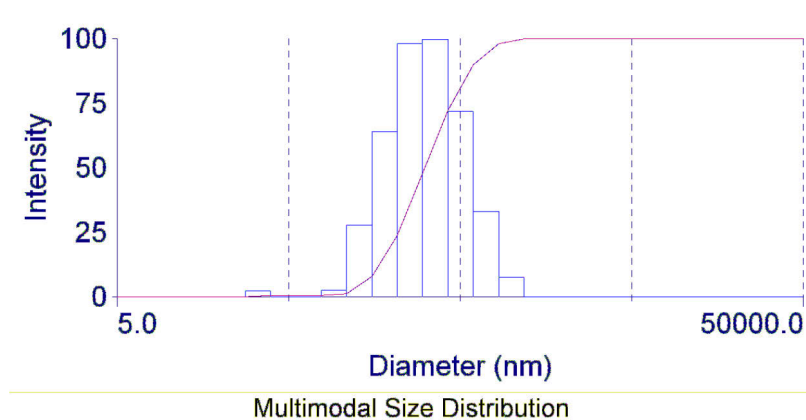


Figure 4.4-6: Multimodal size distribution of hydro-dynamic diameter obtained by Dynamic Light Scattering measurements on Ni-Mn-Cu-Ga particles PBM for 35 h with isopropanol.

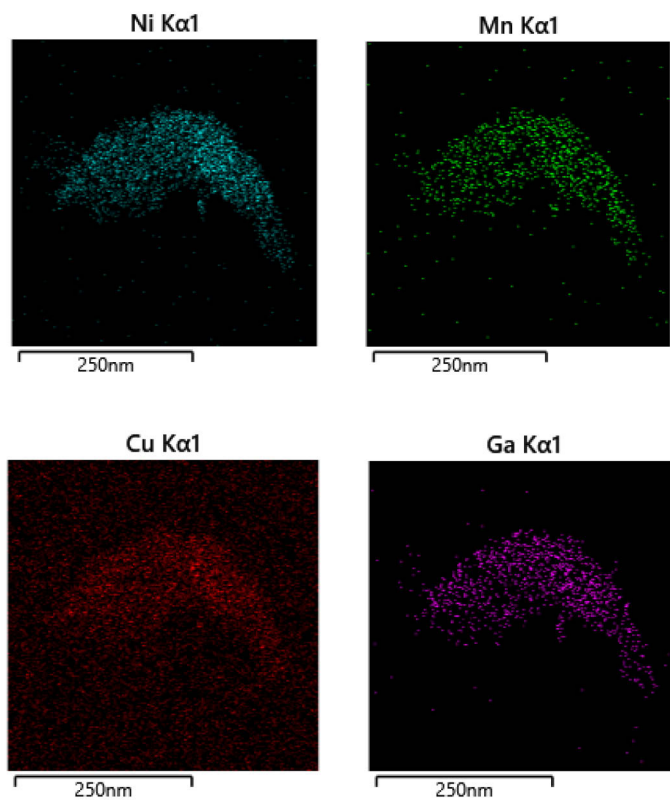


Figure 4.4-7: Compositional maps showing with different colour the spatial distribution of each stoichiometric element in one Ni-Mn-Cu-Ga particle of 250 nm observed with TEM analysis.

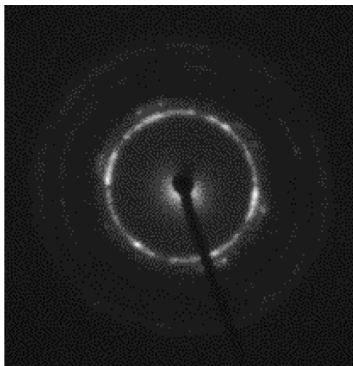


Figure 4.4-8: Example of the obtained Selected Area Electron Diffraction (SAED) pattern, by TEM analysis, for particles of Ni-Mn-Cu-Ga compound of hundreds nano-meters size.

In Fig. 4.4-9, it is shown, instead, the XRD pattern collected at room-temperature of the wetPBM-19h particles, which is compared to the one of the starting HG powder. It emerges that the fundamental peaks of the original tetragonal martensitic structure (Table 7.2-1, Appendix) decrease in intensity and broaden, showing a non-uniform shift of the peak maximum. This behaviour is identical to the one revealed in the diffraction patterns of CM powder (Fig. 4.4-2) and it is linkable to the mechanically induced anisotropic lattice strain, which, in turn, is reflected by the oblate and exfoliated particle shape. Then, it is important to notice that, even for long milling processes of several hours, the Ni-Mn-Cu-Ga particles can show a higher structural stability as compared to the ternary Ni-Mn-Ga compound, other than the possibility to reduce the particle size down to the sub-micrometre scale. These results suggest that a more ductile mechanical deformation and a better accommodation of the stress are realized in the Cu-doped compounds.

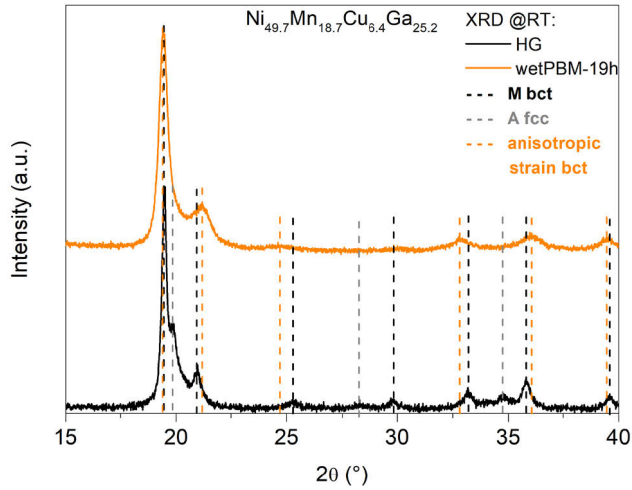


Figure 4.4-9: Room-temperature XRD pattern of Ni-Mn-Cu-Ga wet PBM particles milled for 19 h compared with the one of hand-grinded powder.

Based on the previous results, the recovery of the coupled magneto-structural phase transition has been possible upon optimization of the annealing temperature and time proportionally to the milling time selected. Hence, a long heat treatment for 24 h at the temperature of 750-755°C has been effective to restore the structural and magnetic properties of the wetPBM-19h particles. By looking at Fig. 4.4-10, there have been reported the high-field $M(T)$ curves of the wet PBM particles, water quenched (19wPBM24h750WQ) and slowly cooled (19wPBM24h755SC), after the annealing at 750°C and 755°C, respectively. From their comparison it emerges that the slow cooling rate and a slightly higher annealing temperature led to an increase of the saturation magnetization of the austenite, a shift to higher temperatures of the forward and reverse magneto-structural transformation and only a slight increase by 2 K of the thermal hysteresis. It is interesting to notice that the transformation of 19wPB24h755SC powder is sharper as compared to that of the 2CM4h630SC one (Fig.4.4-4) and the saturation magnetization is increased also with respect to the HG4h630WQ powder one, thus lowered by only 4.8% as compared to the bulk. These peculiar features can be ascribed, on the one hand, to the reduction of microstructural disorder and/or increase of long-range atomic order, thanks to a slow cooling rate rather than a rapid one, and, on the other one, to the onset of recrystallization and grain growth phenomena during long and high-temperature thermal treatments. The formation of new nano-meter sized crystal grains in 19wPBM24h750WQ particles, of 30 μm length and 900 nm thickness, is displayed

in Fig. 4.4-11. It is interesting to observe that, even though the microstructure is not uniformly recrystallized, the martensitic twin-lamellae propagate and self-accommodate throughout the available volume and across the nuclei of new grains.

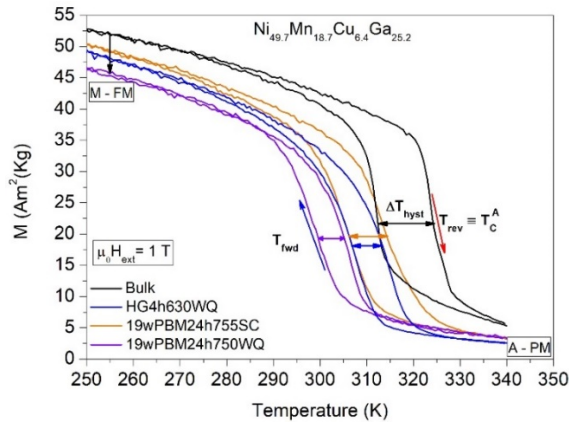


Figure 4.4-10: High-field magnetization measurements of the post-annealed wet PBM particles of Ni-Mn-Cu-Ga, in comparison to that of the post-annealed HG powder and the bulk.

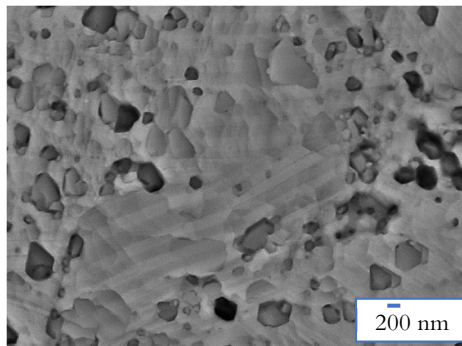


Figure 4.4-11: SEM image showing the beginning of recrystallization nucleation in long heat-treated PBM particles (19wPBM24h750SC) of $\text{Ni}_{49.7}\text{Mn}_{18.7}\text{Cu}_{6.4}\text{Ga}_{25.2}$ compound.

Concerning, instead, the structural analysis, by temperature dependent XRD measurements it has been detected the structural martensitic transformation, from a cubic austenitic phase, characterized by a mixture of $B2/L2_1$ atomic order, due to the low intensity of the superlattice reflections, to a 7M modulated martensitic structure with lattice parameters similar to the ones of the post-annealed hand-grinded

powder (Table 7.2-1, Appendix), on gradually decreasing the temperature below 340 K, as visible in Fig. 4.4-12. Further, it has been noticed that on cooling to 250 K, some low-intense residual traces of the austenite are still detectable, while instead are suppressed at 20 K. The retained fraction of austenite, since is paramagnetic, could reasonably explain the small decrease of saturation magnetization as compared to the bulk.

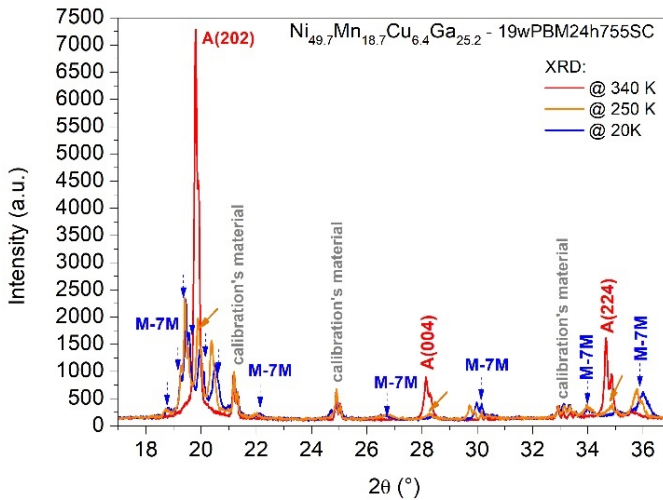


Figure 4.4-12: Evolution as a function of temperature of the XRD patterns for the post-annealed wet PBM particles of $\text{Ni}_{49.7}\text{Mn}_{18.7}\text{Cu}_{6.4}\text{Ga}_{25.2}$ compound.

The heat treatment for 24 h at 755°C, followed by slow cooling, has been applied also to the particles wet PBM for 35 h. Instead, for particles prepared with the two steps method, subjected to 14 h of surfactant-assisted PBM, it has been tried a shorter heat treatment for 4h at 755°C followed by slow cooling (Table 4.4-2). In Fig. 4.4-13, by thermo-magnetization measurements at high field ($\mu_0 H_{ext} = 1$ T), the magneto-structural behaviours of the two batches are presented and compared to the one of HG4h630WQ and bulk samples. It is recognized that the coupled transformation is almost coincident in the three powder batches as well as the hysteresis width and the saturation magnetization of the martensite. In contrast, it emerges an increase of broadening and of magnetic moment at high temperature (340 K) for the PBM processed particles, especially for the 35wPBM24h755SC powder, similar to that of bulk. These results suggest that for long-milled particles the selected

annealing conditions are not sufficient to attain a good degree of chemical and/or microstructural homogenization. Nevertheless, they stress the possibility to recover, even in the smallest sub-micro-meter sized particles, the magneto-structural coupling, and, by reducing the particle size, to improve the irreversible hysteresis losses as compared to the starting bulk sample.

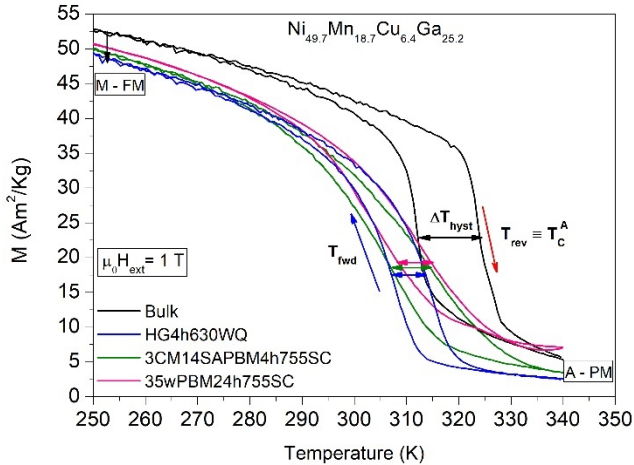


Figure 4.4-13: Magnetization measurements as a function of temperature and at applied magnetic field of 1 T for the post-annealed long-milled particles by PBM process with isopropanol or surfactant-assistance, the hand-grinded powder and the bulk sample of Ni-Mn-Cu-Ga compound.

By SEM analysis, it has been highlighted that, under the performed annealing treatments, both recrystallization and grain-growth phenomena take place, as visible for instance in Figs. 4.4-14(a-b) for 35wPBM24h755SC sample. Moreover, the particles have maintained an elongated and flat morphology and have not shown onset of coalescence or sintering. Thereby, this enables the achievement of dispersed single particles, with recrystallized grains spanning the whole cross-section, where the martensitic variants propagate with straight twin-lamellae of nano-meter sized width (Fig. 4.4-14(b)).

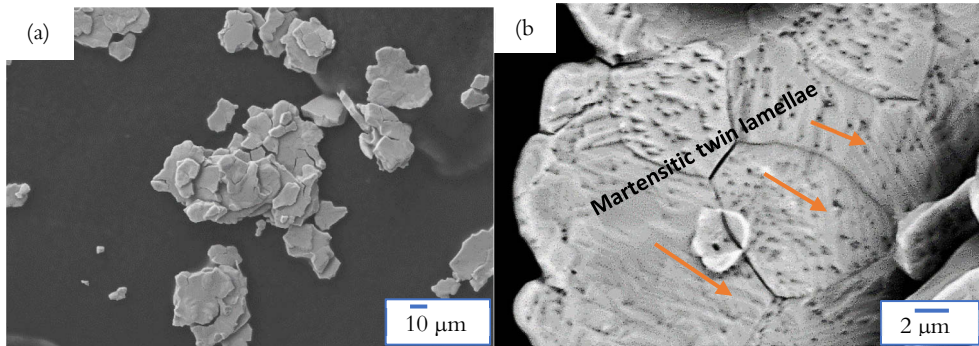
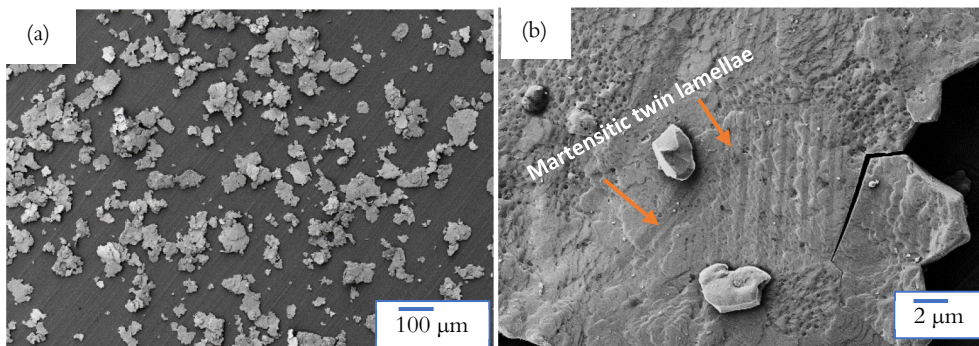


Figure 4.4-14: (a) SEM images showing the morphology of the particles wet PBM for 35h and post-annealed for 24 h at 755°C followed by slow cooling. In (b) there are highlighted the recrystallized grains where the martensitic twin-lamellae can be detected.

Moreover, for the batch of 3CM14SAPBM4h755SC powder, it has been revealed, by SEM analysis, that even after the thermal treatment it is possible to maintain and separate by centrifugation from the biggest ones (Fig. 4.4-15(a-b)), a significant amount of few micro-meter and sub-micro-meter sized particles, with the shown in Figs. 4.4-15(c-e). The sub-micrometric particles present a length in the range of 250-600 nm and a thickness around 100-200 nm.



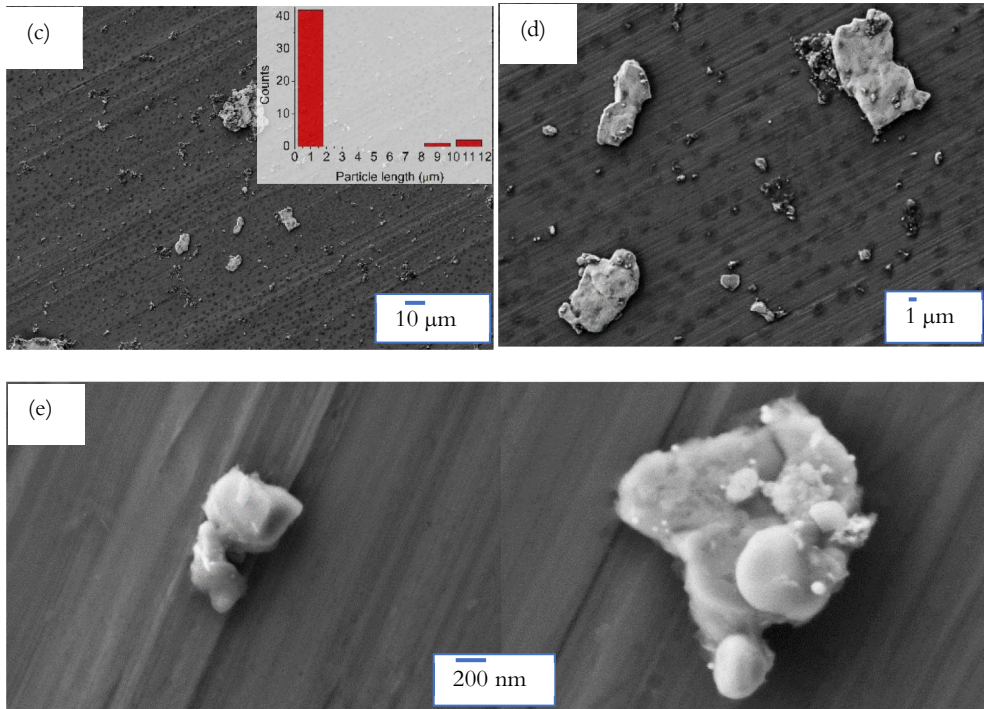


Figure 4.4-15: SEM images showing the morphology of (a-b) the biggest Ni-Mn-Cu-Ga particles of several microns, (c-d) the smaller ones of a few microns, and (e) the smallest ones of hundreds of nanometers, obtained with the surfactant-assisted PBM process and the short annealing treatment at 755°C, followed by slow cooling.

4.4.3 Test of Magnetic Hyperthermia

A magnetic transition in the temperature range 300–328 K, close to the human-being temperature, makes the whole class of magnetocaloric materials a very interesting system for possible exploitation in new-concept biomedical applications [110,163–167]. In particular, the coupled magneto-structural transformation shown by the ferromagnetic Ni-Mn-Cu-Ga Heusler compounds, characterized by an abrupt magnetization change from the ferromagnetic martensite to the paramagnetic austenite, could be exploited in self-regulated magnetic hyperthermia (see sect. 2.3).

In view of this potential application, the Ni-Mn-Cu-Ga powders, particularly those prepared by the two-step process and annealed afterwards (3CM14SAPBM4h755SC powder batch), have been subjected to the magnetic hyperthermia measurements (see sect. 3.5). They were dispersed in 0.5 mL of isopropanol and their concentration was varied from 4 mg/mL to 40 mg/mL, resulting in a mixture of micro-meter ($18 \pm 12 \mu\text{m}$) and sub-micro-meter (100–600 nm) sized particles. Then, they were exposed to an alternating magnetic field of 250 G amplitude and frequency equal to 429 kHz, for 25–30 min.

Figure 4.4-16(a) shows the variation of temperature as a function of time under the applied alternating field, respect to the initial temperature $T_0=23.7^\circ\text{C}$, for the different concentration values of the solution particles + isopropanol. It is seen that, by increasing the concentration, also the initial slope increases and for concentrations above 24 mg/mL, under the same applied radiofrequency field ($A= 250 \text{ G}$; $f=429 \text{ kHz}$), a large increase of temperature is reached. A $\Delta T_{max}= 14.4^\circ\text{C}$ is obtained for the highest concentration of 40 mg/mL in an interval of 25 min (1500 sec). On continuing to measure, it has been observed the appearance of a plateau: this fact is a common feature of all the magnetic hyperthermia measurements and it is mainly ascribable to losses for irradiation, due to the non-optimal isolation of the sample. However, in the present case, it cannot be excluded also a contribution from the self-regulating effect of the particles due to the occurrence of the magneto-structural transformation to the paramagnetic state of the austenite. Indeed, in Fig. 4.4-16(b), the transition is observed at around 311.2 K ($\sim 38^\circ\text{C}$) in heating, equal to the maximum temperature ($T_0 + \Delta T_{max} \approx 38^\circ\text{C}$) reached.

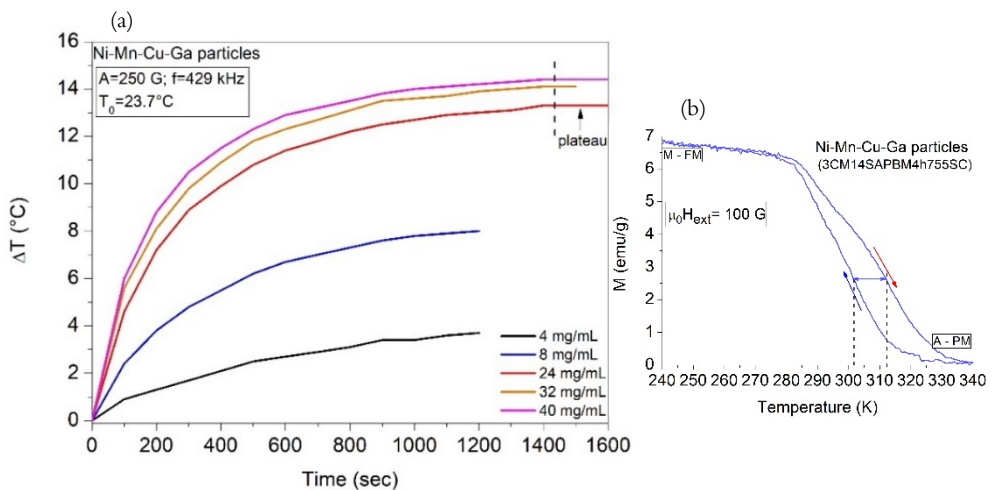


Figure 4.4-16: (a) Variation of temperature as a function of time, under a radiofrequency magnetic field, for solutions of isopropanol and Ni-Mn-Cu-Ga particles (3CM14SAPBM4h755SC powder) at different concentrations. (b) Temperature-dependent magnetization curve, under an applied field of 100 G of the corresponding employed particles.

Thereby, the ferromagnetic particles, undergoing the Curie transition at the temperature equal to the therapeutic one, can potentially act as self-regulators of the magnetic hyperthermia power, which is highly desirable for monitoring the treatment within the tissue [110]. The heating ability is strongly dependent on the particles' properties, such as structure, composition, mean particle size, size distribution and magnetic anisotropy, other than the choice of amplitude and frequency of the alternating field [107,112]. An important parameter that can be derived by the measurements is the Specific Absorption Rate (SAR), defined as the power absorbed per mass of material and measured in W/g [109]:

$$SAR = \frac{C}{m_{sample}} * \frac{dT}{dt}$$

where C is the specific heat capacity of the solvent per unit volume (in this case $C_{isoprop} = 2106.48 \text{ J/KL}$), m_{sample} is the concentration (g/L) of the material, $\frac{dT}{dt}$ the initial slope of the curves $\Delta T(t)$ obtained by taking into account only the first few seconds [112].

In Figs. 4.4-17(a)-(b), the slope of the temperature curves (dT/dt) and the SAR values have been plotted against the concentration of the different solutions, considering the intervals of time of maximum slope of the curve under the exposure to the external alternating field. For the first two samples, associated with the lowest dT/dt values (Fig. 4.4-17(a)), it has been required to consider a longer time interval of 100 sec. By contrast, for the middle concentrations, the maximum temperature variation has been observed after the first 5-6 seconds of exposure, which explains the associated larger error bars, obtained by propagating the experimental errors of $\pm 0.1^\circ\text{C}$ for the temperature (T) and $\pm 0.2 \text{ sec}$ for the time (dt). Interestingly, for the highest concentration, the highest temperature variation has been detected in an interval of 20 sec and it can be seen that the corresponding dT/dt value has a mean value comparable to the first one. The non-uniform behaviour between the solutions makes the evaluation of SAR difficult to derive correctly and reliably, as reflected, in Fig. 4.4-17(b), by the different scattered values, associated with large error bars.

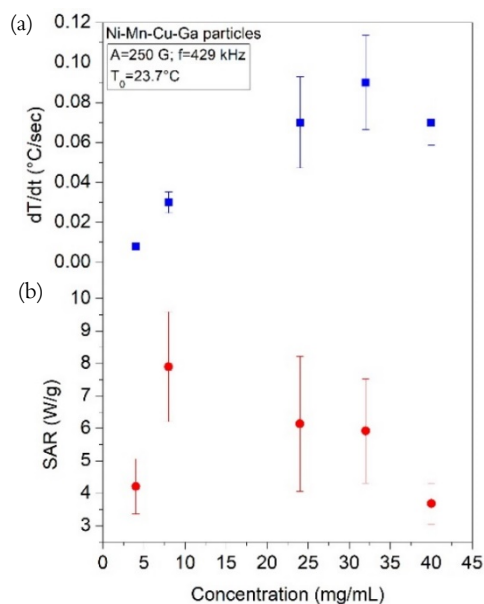


Figure 4.4-17: Concentration-dependence of (a) slope of the $\Delta T(t)$ curves and (b) SAR values after the first 100 and 200 s of exposure to the alternating magnetic field of the solution of Ni-Mn-Cu-Ga particles.

These results can be understood by considering that, due to the tendency of the particles to precipitate on the bottom part of the cuvette, the region of maximum applied field was not coincident with the sample's centre of mass during the measurement, and that, depending on the concentration, different temperature gradients and/or intensity of interactions between particles could have been produced inside the solution. The SAR value is reported in literature to be an independent and absolute parameter, at least in the range of low concentration, i.e., 0.05–1 g/L, and for sufficiently small nanoparticles, e.g., 20–50 nm [109,111,112]. Therefore, in the present case, the increase of concentration (> 4 mg/mL) may have played the fundamental role in triggering inhomogeneities in the heating effect of the particles. To figure out the obtained results, for the solution with the highest concentration of particles, it has been separated the amount of big micro-meter particles, precipitated on the bottom part after the measurement, from the sub-micro/nanoparticles remained suspended on the upper part of the cuvette (supernatant), to weight them and repeat the magnetic hyperthermia measurements independently. It has been found out that the concentration of the smallest particles was only of 2 mg/mL, thus those of the biggest ones equal to 38 mg/mL. In the left-hand side of Fig. 4.4-18,

there have been reported the resulting variations of temperature (ΔT) as a function of time for the separated batches, in comparison to the result of the ensemble (40 mg/mL), while, on the right-hand one, the two corresponding particle size distributions. It is seen that both powder batches present a large size distribution, even though for the big particles it is peaked at $18 \pm 12 \mu\text{m}$ and for the small ones at a size $\leq 200 \text{ nm}$. Moreover, it is observed that the contribution of the latter ones to the total temperature increase is almost negligible, whereas for the bigger particles, in the amount of 38 mg/mL, it is found out a higher and steeper variation of temperature with time, even much pronounced than that of the total ensemble (40 mg/mL). Indeed, the maximum slope of the curve (dT/dt) has been obtained in the first 6 seconds of the measurement, similarly to what observed for concentrations of 24 mg/mL and 32 mg/mL, and, as reported in Fig. 4.4-19(a), it is the highest achieved value among all the measured ones. Further, in Fig. 4.4-19(b), by comparing the SAR parameters of all the batches, it appears that, for the particles' concentration of 38 mg/mL, it can be obtained also the highest SAR, which is close to the mean value of the 8 mg/mL solution. In general, it can be noticed that while the dT/dt seems to increase by increasing the concentration value, the SAR parameter has a non-monotonous variation.

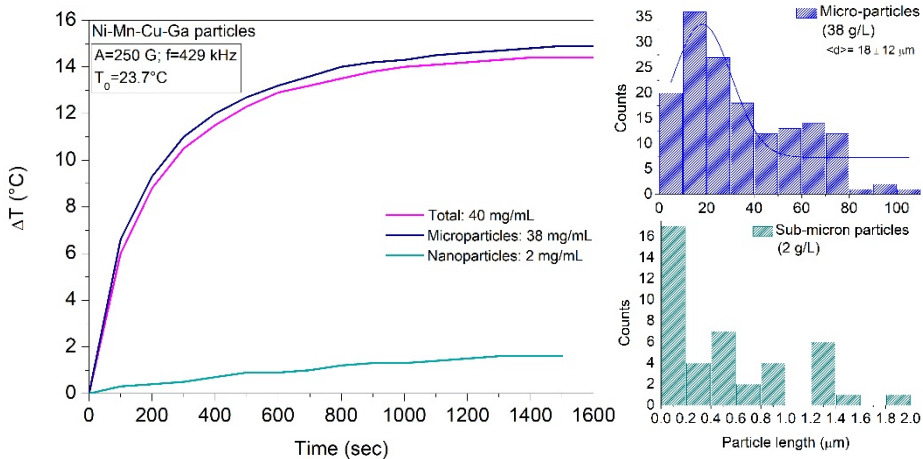


Figure 4.4-18: Temperature variation as a function of time for the separated solutions of microparticles (38 mg/mL) and sub-micro particles (2 mg/mL) and their combination. On the right hand: corresponding particle size distribution.

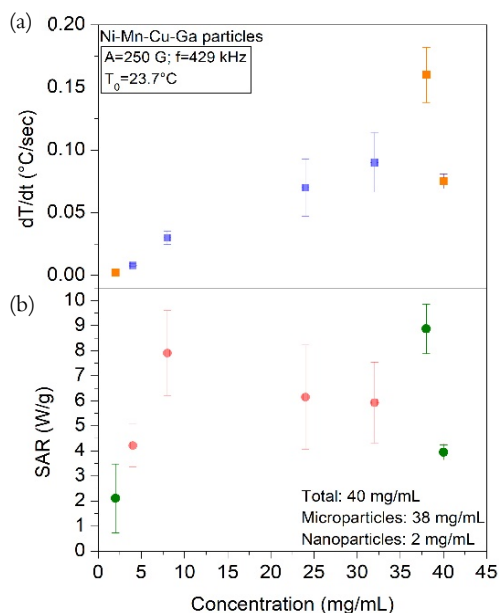


Figure 4.4-19: Concentration-dependence of (a) the slope of the initial increase in temperature and (b) the SAR values of the sample batches reported in Fig. 4.5-18.

It is, then, worth stressing that, based on the particles' morphology (size and shape), different mechanisms of heat dissipation are involved [107]: in fact, the big particles of several hundreds of nano-meters and/or the aggregates formed via strong dipolar interactions generate the heat through the magnetic hysteresis losses, while, usually, the superparamagnetic nanoparticles dissipate the absorbed energy by Néel and Brown relaxations. Much higher specific power absorption (SPA) values are expected for magnetic hysteresis losses [111]. However, following the theoretical and experimental results reported in [168], it emerges that the magnetic hyperthermia responses can drastically change when there is an increase of the magnetic interactions as for instance by increasing the sample concentration, since it can promote the onset of collective-particle behaviour which leads to a competition between the local dipolar field felt by the particles and the amplitude of the applied field. This results in a non-monotonic trend of the SAR maximum values as a function of the sample concentration. This complex scenario of interactions between changes of gradients of concentration and different particles' morphology and relaxation mechanism can plausibly explain the observed non-conventional experimental findings.

In summary, the highlighted trends point out that the heating efficiency strongly depends on the concentration and size of the particles, which require a further optimization in order to achieve SAR values compatible with those reported for NPs of iron oxides in smaller concentrations and subjected to a lower frequency and amplitude of the alternating field. This could be done by first tuning the milling parameters to reduce the size below 100 nm and subsequently optimizing the annealing conditions to promote a better recovery of the magneto-structural phase transition, in terms of a larger magnetization change and a sharper transformation, also in the smallest achieved particles. Nevertheless, this study stresses, as a proof of principle, the potential exploitation of Ni-Mn-Cu-Ga particles with a tailored composition to have the magneto-structural coupling close to the therapeutic temperature as self-regulated magnetic hyperthermia nanoparticles for biomedical applications.

4.5 BALL-MILLING OF NI-MN-IN-CO COMPOUND

After having pointed out the effects of different types of ball-milling on Ni-Mn-Ga/Ni-Mn-Cu-Ga particles' properties, it will be now questioned and investigated, under the same milling conditions, the behaviour of Ni-Mn-In-Co system. First, there will be presented and discussed the results obtained for $Ni_{44.5}Mn_{37.9}In_{12.6}Co_5$ compound during high-energy ball-milling and planetary ball-milling in dry conditions. Then, it will be shown the effect of planetary ball-milling with isopropanol, cryo-milling, and a combination of both procedures for the $Ni_{45.7}Mn_{36.9}In_{13.2}Co_{4.2}$ one. In both cases, after each ball-milling process, there will be shown the effect of different annealing treatments on the recovery of the original Heusler structure and magnetic state and on the morphological/microstructural properties. The magnetic and metamagnetic martensitic phase transitions will be compared with the bulk and coarse-grained particles' ones to highlight differences driven by the size-dependent phenomena.

4.5.1 High-Energy Ball-milling

Using the hand-grinded powders of the sample with effective composition $Ni_{44.5}Mn_{37.9}In_{12.6}Co_5$, in a SPEX-8000 laboratory mill (Chapter 3.1.2), the high-energy ball-milling (HEBM) process was carried out. Similarly to what reported in literature [39,44] and previously adopted for Ni-Mn-Ga system, the ball-to-powder weight ratio was chosen of 10:1 and there were used 4 balls of 12mm diameter, with both jar and balls made of stainless steel. The powders were sealed in the jar under Ar atmosphere, inside a glove box. To avoid overheating of the sample and grinding media, the milling was conducted in intervals of 30 min milling and 1h rest. After an effective milling time of 4h, the milling process was stopped because of the observation of a heavy cold-welding between the particles and a strong adhesion to both balls and jar's walls.

Sample: $Ni_{44.5}Mn_{37.9}In_{12.6}Co_5$	Milling time (h)	Annealing temperature (°C)	Annealing time (h)	Cooling rate	Corresponding Name
Hand-grinded (HG)	-	-	-	-	HG
		850	2	WQ	HG850WQ
High energy Ball-milled (HEBM)	0.5	-	-	-	0.5h-HEBM
		850	2	WQ	0.5hHEBM850WQ
	1	-	-	-	1h-HEBM
	4	-	-	-	4h-HEBM
		500	2	WQ	4hHEBM500WQ
		850	2	WQ	4hHEBM850WQ

Table 4.5-1: Milling procedure, milling time and annealing treatment specifications of the $Ni_{44.5}Mn_{37.9}In_{12.6}Co_5$ powders samples.

The morphology and dimensions of the as-milled HEBM powders after different milling-time (Table 4.5-1) were investigated by means of SEM analysis. In Figs. 4.5-1(a)-(b), it can be seen that the 4h-HEBM particles show a chunk, irregular morphology and a large size-distribution, with an average length of $30 \pm 10 \mu m$ and thickness of $20 \pm 5 \mu m$.

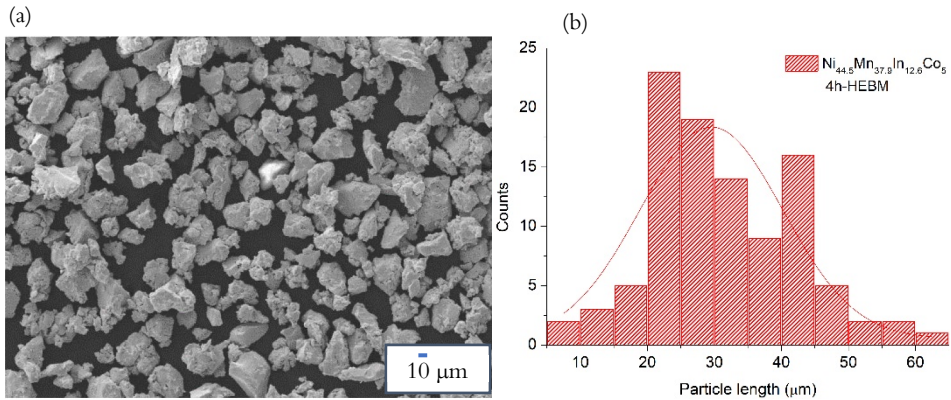


Figure 4.5-1: (a) SEM image of the $\text{Ni}_{44.5}\text{Mn}_{37.9}\text{In}_{12.6}\text{Co}_5$ 4h-HEBM particles and (b) corresponding particle size distribution.

From the XRD analysis at room temperature and subsequent Le Bail refinement, it was investigated the structural evolution of the powders subjected to an increasing milling time. As shown in Fig. 4.5-2, the initial HG powder is characterized by a mixture of tetragonal non-modulated martensite and cubic austenite phases at room-temperature (Table 7.3-1, Appendix). After half an hour of HEBM process, a disordering of the original tetragonal martensitic structure takes place as indicated by the decrease of peaks' intensity and enlargement of their width. The peaks' position, by contrast, does not change as visible by following the vertical dashed coloured lines. After 1h of HEBM the peaks' broadening increases and the reflections, at high 2θ angle, are almost suppressed. Instead, after 4h of HEBM, it can be noted a different shape of the peak at around $2\theta \approx 19^\circ$ and an increase of intensity of some peaks at high-angle, that are linked to an increase of the original cubic fraction. This result is ascribed to the increase of local temperature for the heat dissipation during the long, high-energetic milling process, which is able to promote a partial recovery process, through rearrangement and annihilation of dislocations, and cold-welding between the particles [117]. This phenomenon can explain the presence of different degree of atomic (dis)order between and within the particles of the batch.

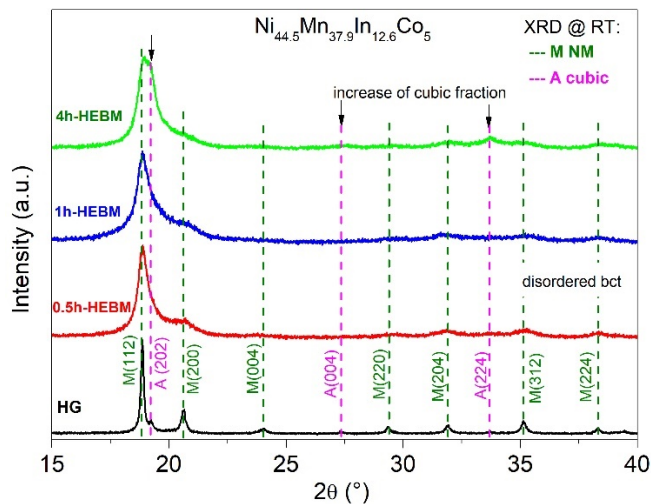


Figure 4.5-2: Comparison between the XRD patterns, collected at room-temperature, of the $\text{Ni}_{44.5}\text{Mn}_{37.9}\text{In}_{12.6}\text{Co}_5$ hand-grinded and high-energy ball-milled (HEBM) powders at increasing milling time.

The high milling energy of the process has played a significant role also on the thermo-magnetic behaviour of the particles. As visible in Fig. 4.5-3, both the ferromagnetic order and the martensitic transformation are suppressed for the 4h-HEBM. This phenomenon is ascribed to the strong sensitivity of the magnetic interactions and martensite phase formation to the atomic disorder and change of interatomic Mn-Mn distances, caused by the induced point defects and lattice deformations. Therefore, to promote the release of mechanical stresses and recover the original magnetic and structural phase, the as-milled particles were heat treated for 2h at the temperatures of 500°C and 850°C, followed by water quenching, in accordance to what previously performed on the HG counterpart (Table 4.5-1). In Fig. 4.5-3, it is revealed that the annealing at low temperature of 500°C, which is below the order-disorder temperature for Ni-Mn-In-Co, as reported in [95,154], gives rise in the 4h-HEBM powder to segregation of secondary phases, as highlighted by the broad Curie transition characterized by two different slopes. By contrast, after the annealing at 850°C, both the 4h- and 0.5h-HEBM powders show a steep second-order magnetic transition, which is shifted to a lower temperature as compared to the one of the HG850WQ powder and it is the sole observed one. In fact, differently from the reference, any other variation of the magnetic susceptibility has been detected down to 100 K for the post-milling annealed powders. Therefore, the original metamagnetic martensitic transformation, which on heating occurs around

room-temperature, is not recovered after short annealing treatments at high temperature, even if the particles have been milled for a short milling time (30 minutes).

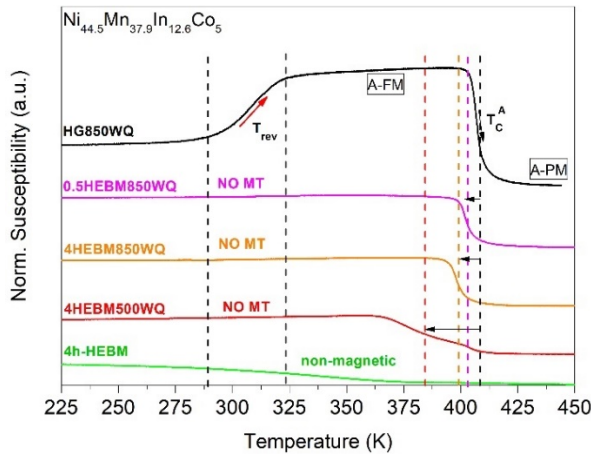


Figure 4.5-3: Temperature-dependent magnetic susceptibility measurements of as-milled and post-annealed 4h- and 0.5h-HEBM powders and post-annealed hand-grinded powders of $\text{Ni}_{44.5}\text{Mn}_{37.9}\text{In}_{12.6}\text{Co}_5$ system.

Since no significant compositional variations were detected between the bulk and the post-annealed powder samples (Table 7.3-2, Appendix), the origin of the different magneto-structural behaviour in the achieved particles could be related to a change of the crystallographic order. Indeed, it has resulted, by X-ray diffraction measurements, that both the 0.5 h and 4hHEBM850WQ samples have crystallized in a cubic $B2$ structure (Table 7.3-1, Appendix), which is more disordered as compared to the $L2_1$ Heusler phase, due to the random distribution of Mn atoms on Mn and In sublattices. Hence, it has emerged that the structural transformation, upon heating, to the $B2$ state is not sufficient for restoring the martensitic transformation, due to the retaining of atomic disorder. This result agrees with what has been observed by V. Sanchez-Alarcos *et al.* [46] for Ni-Mn-In ball-milled particles, annealed at a temperature which does not promote the formation of the Heusler phase. It follows that a long annealing at high temperature is required to permit the restoration of a long-range atomic ordering, and, likely, the metamagnetic martensitic transformation.

4.5.2 Planetary Ball-milling

In light of the necessity to control the milling energy of the process for avoiding an excessive induced disorder and/or cold-welding, it was subsequently employed the planetary ball-milling technique (Chapter 3.1.2), which is more flexible and versatile as compared to the vibration high-energy ball milling, thanks to the possibility of varying the rotational speed and adding a liquid-control agent.

Initially, it has been tested the planetary ball-milling procedure in dry conditions (i.e., in gaseous atmosphere of nitrogen) using the HG powder of $Ni_{44.5}Mn_{37.9}In_{12.6}Co_5$ compound. The results have been reported in sect. 7.3.1 of Appendix. It has been revealed a high phase instability. Then, in order to better correlate the achieved results of phase destruction and decomposition to the applied severe plastic deformation and/or subsequent thermal stresses during annealing, separating the influence of a possible pre-existing phase inhomogeneity of the sample, it has been decided to employ the more stable $Ni_{45.7}Mn_{36.9}In_{13.2}Co_{4.2}$ compound and investigate the effects of both dry and wet milling procedures (Table. 4.5-2).

Sample: $Ni_{45.7}Mn_{36.9}In_{13.2}Co_{4.2}$	Milling time (h)	Annealing temperature (°C)	Annealing time (h)	Cooling rate	Corresponding name
Hand-grinded (HG)	-	-	-	-	HG
		820	2	SC	HG820SC
			4	WQ	HG4h820WQ
Planetary ball-milled with isopropanol (wet PBM)	3	-	-	-	wetPBM-3h
		600	24	WQ	3wPBM24h600WQ
		820	2	SC	3wPBM820SC
			24	WQ	3wPBM24h820WQ
			29		3wPBM29h820WQ
850	4	WQ	3wPBM4h850WQ		
Planetary ball-milled in dry conditions (dry PBM)	3	-	-	-	dryPBM-3h
		600	24	WQ	3dPBM24h600WQ
		820	2	SC	3dPBM820SC
			4	WQ	3dPBM4h820WQ
			24		3dPBM24h820WQ

Table 4.5-2: Milling procedure, annealing conditions and name specifications of the $Ni_{45.7}Mn_{36.9}In_{13.2}Co_{4.2}$ powder samples.

In a planetary ball-mill (PBM) Pulverisette 7, the process was run simultaneously in dry and wet conditions in two distinct Zirconia jars. Hence, in a 10:1 ball-to-powder weight ratio charged jar, it was added isopropanol, as solvent, to control the heat dissipation, enhance particles' dispersion and protect the powder from the external atmosphere. The rotational speed was fixed to 400 rpm and the process was conducted in intervals of 15 min milling and 7 min rest, up to 3 h.

The wet PBM powder has shown a different morphology as compared to the dry PBM one, which is revealed by the SEM images of Figs. 4.5-4(a)-(b). It is noted that the PBM particles in wet conditions (wetPBM-3h, Fig. 4.5-4(b)) are like single, flat and thin flakes, with a few microns or sub-microns length, as revealed by the size-distribution in the inset. The peculiar particles' shape can be inferred to the lubricating effect of the solvent, which lowers the friction coefficient between colliding balls and particles, tending to elongate the latter ones [118]. By contrast, similarly to what obtained for the other Ni-Mn-In-Co compound, after 3h of dry PBM the particles present a roundish shape, with average diameter of $6 \pm 2 \mu\text{m}$ and the strong tendency to cold-welding, leading to large agglomerates.

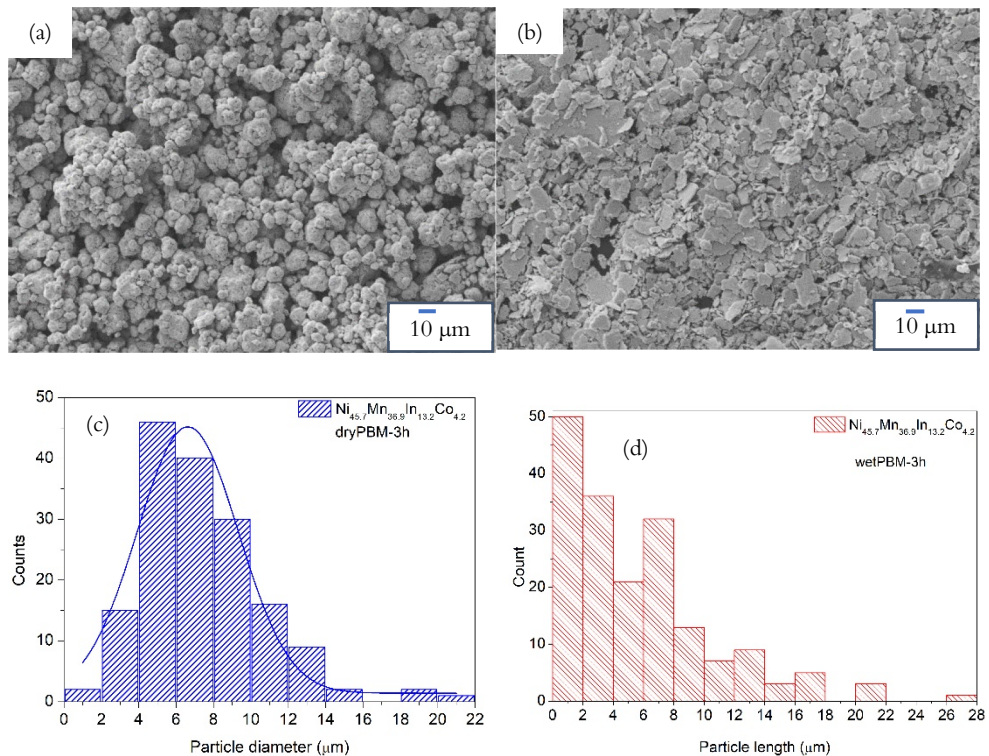


Figure 4.5-4: SEM images of the $Ni_{45.7}Mn_{36.9}In_{13.2}Co_{4.2}$ (a) dryPBM-3h powder and (b) wetPBM-3h powder; (c) and (d) corresponding size distributions.

The effectiveness of isopropanol during the ball-milling process has been proved, with EDX analysis, also by the preservation of the original stoichiometry and the avoidance of oxidation.

The XRD analysis at room temperature has pointed out a different atomic disordering effect of the crystal structure between the dry and wet PBM-3h powders. With reference to Fig. 4.5-5, it is shown that the starting HG powder is characterized by a mixture of martensitic phase, which is predominantly non-modulated tetragonal with a residual trace of 7M modulated structure, and cubic austenitic phase (Table 7.4-1, Appendix). After the wet PBM process, the peaks of the austenite disappear while those of the tetragonal martensite broaden and decrease of intensity. Instead, for the dryPBM-3h powder it is observed the suppression also of the martensitic reflections and the remanence of only the peak at $2\theta=41.8^\circ$, having a larger and non-uniform broadening with respect to the wet PBM powder. Accordingly, the absence of a liquid milling atmosphere leads to a higher frictional force and heating during the energetic collisions with the Zirconia balls, resulting in a higher level of induced lattice strains and defects in the powder particles, at the same fixed milling time of 3 h.

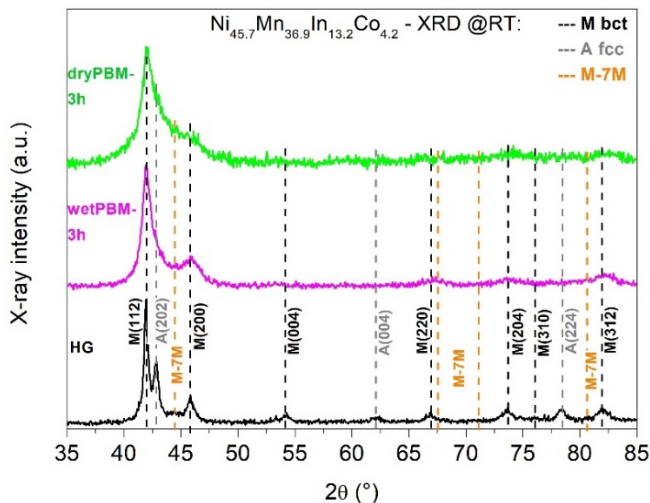


Figure 4.5-5: Room-temperature XRD analysis of the $Ni_{45.7}Mn_{36.9}In_{13.2}Co_{4.2}$ hand-grinded and planetary ball-milled for 3h, in wet (wetPBM-3h) and dry (dryPBM-3h) conditions. The Bragg reflections of the original crystal phases are indicated with the coloured vertical dashed lines.

Nevertheless, a similar drastic change of the original magnetic order of the compound has been observed for both the as-milled wet and dry PBM powders, as shown in Fig. 4.5-6. As for the XRD patterns, the temperature-dependent magnetic susceptibility behaviour of the PBM powders has been compared with the one of the HG sample. It emerges the suppression of both the metamagnetic reverse martensitic transformation on heating and the magnetic Curie transition of the austenite. These effects once again highlight the strong sensitivity of both the ferromagnetic order and the structural martensitic transformation to the induced defects and atomic disorder, which alter the original stacking order, change the interatomic distances between the magnetic species (Mn-Mn) and reduce the total magnetic moment. In particular, the detrimental variations are associated to the increase of surface-to-volume ratio and the accumulation of point defects and antiphase boundaries [42,68].

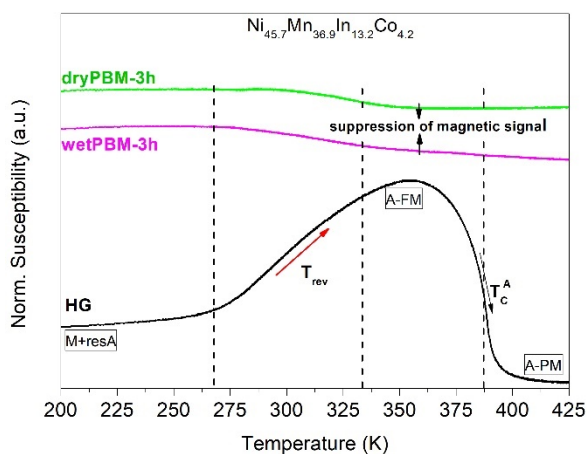


Figure 4.5-6: Low-field magnetic susceptibility curves of the $Ni_{45.7}Mn_{36.9}In_{13.2}Co_{4.2}$ hand-grinded powder and as-PBM powders for 3h, in wet (wetPBM-3h) and dry (dryPBM-3h) conditions.

The recovery of the original phase transformations has been investigated by performing different annealing treatments, at various temperature and/or annealing time, followed by water quenching (Table 4.5-2).

The thermo-magnetic characterization of the post-annealed batches of dryPBM-3h powder (Fig. 4.5-7) has pointed out the same result achieved for the $\text{Ni}_{44.5}\text{Mn}_{37.9}\text{In}_{12.6}\text{Co}_5$ PBM powder annealed for 23 h at 850°C (Fig. 7.3-3, Appendix). Indeed, a long annealing treatment at low temperature of 600°C can only promote a partial recovery of the induced defects and atomic disorder, resulting in appearance of only a broad Curie Transition, shifted at a low temperature as compared to the reference one of HG4h820WQ sample. However, by increasing the annealing temperature to 820°C , the Curie temperature is only slightly rightward shifted and no traces of the martensitic transformation can be detected, at a lower temperature.

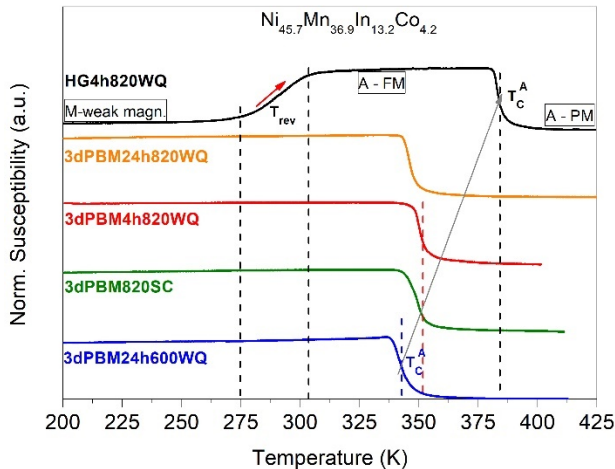


Figure 4.5-7: Effect of the performed annealing treatments on the temperature-dependent magnetic susceptibility measurements of the $\text{Ni}_{45.7}\text{Mn}_{36.9}\text{In}_{13.2}\text{Co}_{4.2}$ dry PBM-3h powder and comparison with the behaviour of the hand-grinded powder annealed for 2h at 820°C and slowly cooled (HG820SC).

By looking at the XRD patterns in Fig. 4.5-8, it is revealed that the 3dPBM24h820WQ powder presents at room-temperature a segregation of different crystal phases, which have been identified as a cubic Heusler austenitic phase, with a certain degree of $L2_1$ atomic order, since the superlattice (111) reflection is recognized, a cubic γ -phase and the manganese dioxide (Table 7.4-1, Appendix). By contrast, the HG820SC powder shows a prevalence of cubic austenite with some traces of a 7M modulated martensite, due to the proximity to room-temperature of the martensitic start temperature. Therefore, the huge difference in Curie transition temperature, between the reference and the 3dPBM24h820WQ powder, relies on

the formation of secondary phases and on the strong influence of the increase of surface-to-volume ratio of the particles (Fig. 7.3-6, Appendix), which unavoidably alter both composition and magnetic/structural stability of the original quaternary Heusler phase.

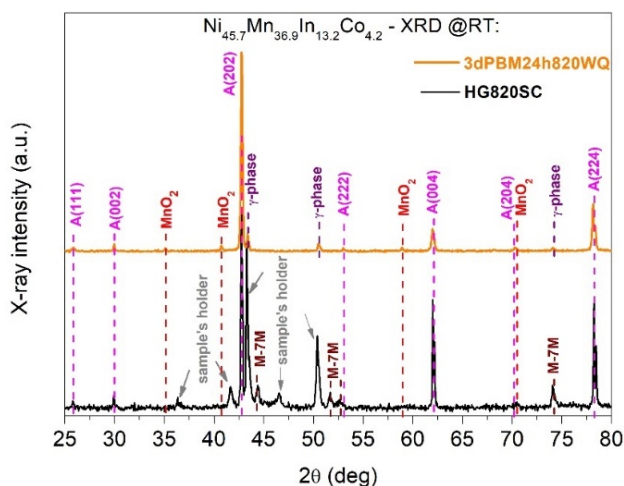


Figure 4.5-8: Comparison between room-temperature XRD patterns of post-annealed hand-grinded (HG820SC) and dry PBM (3dPBM24h820WQ) powders of the $\text{Ni}_{45.7}\text{Mn}_{36.9}\text{In}_{13.2}\text{Co}_{4.2}$ system. The coloured vertical dashed lines indicate the crystal phases obtained by the Le Bail refinement.

For the wet PBM powder, instead, it has been possible to recover the martensitic transformation, other than the Curie transition of the Austenite, by performing thermal treatments at 820°C. Fig. 4.5-9 shows that by increasing the annealing time from 4 h to 29 h, at a fixed annealing temperature of 820°C, a positive inflection of the magnetic susceptibility starts to appear, on heating between 275–300 K (upward red arrow), and gradually increases, with a slight rightward shift of the completion temperature. This feature highlights the occurrence of the reverse martensitic transformation, which is broader as compared to the one of the HG4h820WQ powder. The Curie transition is sharper and shifted to a higher temperature as compared to the one detected after the long annealing (24 h) at medium temperature (600°C), but it remains almost unchanged during the different-duration thermal treatments at the same temperature (820°C). Instead, with respect to the expected Curie transition temperature of the HG4h820WQ sample, it is decreased.

On the one hand, this fact can be related to a different type of atomic ordering of the austenitic phase, such as $B2$ -type instead of $L2_1$, due to the retained disorder generated by the milling process and annealing/quenching procedures, as similarly obtained by W. Ito *et al.* [154] for bulk compounds quenched above rather than below the order-disorder transition temperature ($T_t^{B2/L2_1} = 896$ K), and above-discussed for the post-annealed HEBM and dry PBM powders of $\text{Ni}_{44.5}\text{Mn}_{37.9}\text{In}_{12.6}\text{Co}_5$ compound. On the other one, it can be also ascribed to the formation of manganese oxides, due to the high reactivity to oxygen of the small particles, thus lowering the amount of Mn atoms, carrying the magnetic moment, which contributes to the ferromagnetic interactions.

However, the tendency to oxidation of the wet PBM powder is lower as compared to the dry PBM one, as it has been revealed by SEM and XRD.

Indeed, in the diffraction pattern of 3wPBM24h820WQ sample (Fig. 4.5-10), it can be noted a lower intensity of MnO_2 reflections as compared to the ones observed for the 3dPBM24h820WQ powder (Fig. 4.5-8). Furthermore, no traces of the secondary γ -phase have been highlighted by the Le Bail refinement, but rather it has emerged the presence of a cubic austenite, showing also the superlattice reflections of the Heusler $L2_1$ phase, and an initial formation of martensite at room temperature, presenting few reflections of both tetragonal NM and modulated 7M structures. Differently, the HG820SC powder has revealed a mixture of cubic austenitic phase, with similar degree of atomic order of the 3wPBM24h820WQ sample, and 7M modulated martensitic structure (Table 7.4-1, Appendix).

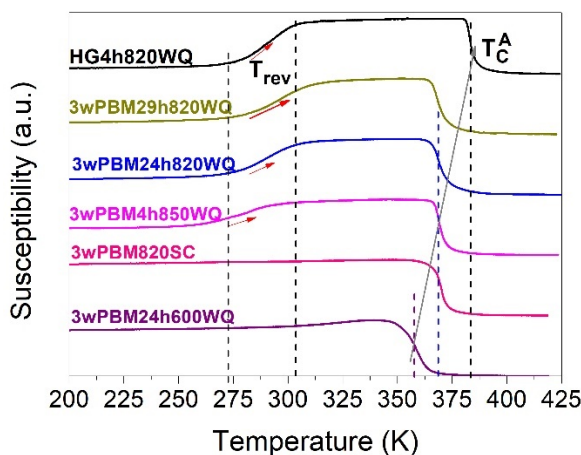


Figure 4.5-9: Evolution during the annealing treatments of the temperature-dependent magnetic susceptibility of the $\text{Ni}_{45.7}\text{Mn}_{36.9}\text{In}_{13.2}\text{Co}_{4.2}$ wet PBM-3h powders and comparison with the post-annealed HG powder's one.

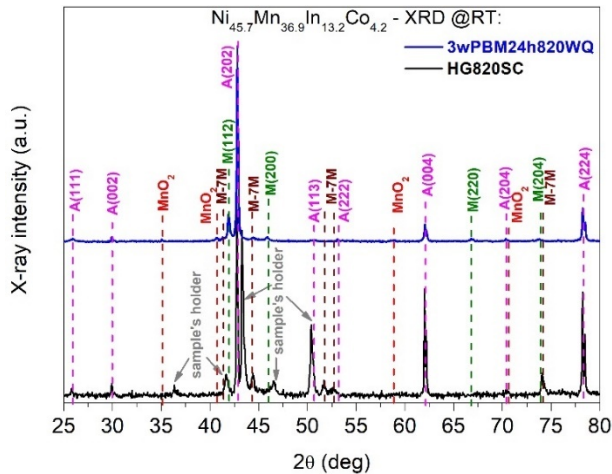


Figure 4.5-10: Room-temperature XRD patterns of post-annealed hand-grinded (HG820SC) and wet PBM (3wPBM24h820WQ) powders of $\text{Ni}_{45.7}\text{Mn}_{36.9}\text{In}_{13.2}\text{Co}_{4.2}$ compound. The coloured vertical dashed lines identify the crystal phases obtained by the Le Bail refinement.

In order to better investigate the martensitic phase transformation and its related properties of the post-annealed powder batches, the high-field magnetization measurements have been carried out, in the temperature region of interest. In Fig. 4.5-11, it is reported the comparison between the $M(T)$ curves of the three batches of wet PBM powder annealed for 4–24–29 h at 820°C and then water quenched, and that of HG powder annealed for 4h at 820°C and slowly cooled afterwards (HG4h820SC), taken as reference. It is evident that the ball-milled powders present notable changes in the transformation behaviour, such as the increase of the thermal hysteresis and transformation broadening, and the decrease of magnetization change between the two phases. Nonetheless, these features evolve as a function of the annealing time and appear to improve by increasing the annealing duration from 4 h to 24 h. For the 3wPBM4h850WQ powder, the martensitic transformation is drastically shifted to lower temperatures, with the opening of a large thermal hysteresis and the interruption of the transformation below 175 K, as highlighted by the high magnetization signal retained at the martensite finish temperature (M_f), giving rise to only a small magnetization difference (ΔM) across the transition (Table 7.4-2,

Appendix). On the contrary, after annealing for 24 h, the transformation temperatures are shifted to higher temperatures, closer to the ones of the reference for what concerns the martensite start and austenite finish temperatures, and, at the same time, both the hysteresis width and the low-temperature magnetic signal are decreased as compared to the short heat treatment. By further increasing the annealing time to 29 h, it is observed a rightward shift of the reverse martensitic transformation temperature and of the martensite start temperature (M_s), while an almost invariance of the M_f temperature and the associated magnetization value. This results in a lower transformation sharpness with respect to the 3wPBM24h820WQ sample. Moreover, it is noted a little decrease of magnetization of the austenite, leading to a smaller ΔM between the low and high temperature phases.

It is worth stressing that a similar transformation interruption has been observed, on cooling below 150 K, also for bulk alloys of $Ni_{45}Co_5Mn_{36.7}In_{13.3}$, subjected to thermo-magnetic cycles under increasing external magnetic fields or to secondary annealing treatments at temperature $T_a \leq 773$ K (500°C), as reported by Ito *et al.* [151] and Bruno *et al.* [95]. The authors have suggested that due to the gradual shift to lower temperatures of the martensite start temperature, the mobility of the parent-martensite phase interface (habit plane) becomes limited, till reaching a critical temperature at which the propagation of the martensite is frozen. The origins of this arrest are still unclear and under debate and both thermodynamic [72,169] and kinetic [151,170] arguments have been invoked to understand this anomaly.

From the current experimental results, it emerges that the recovery of the martensite transformation and the thermodynamic-kinetic aspects of its formation are strictly dependent on the overcoming of the induced internal energy barriers and atomic disorder through the external thermal energy, and, hence, on the microstructural variations and atomic reordering processes apported by the selected annealing conditions. However, the effectiveness of the subsequent thermal treatments in reducing the thermal hysteresis and restoring the original configuration of the bulk, is drastically reduced by decreasing the particles and/or grain size of the powder down to the sub-microscale, thus pointing out the strong size sensitivity of the peculiar metamagnetic martensitic transformation of Ni-Mn-In-Co compound. This hypothesis will be corroborated by comparing the thermo-magnetization measurements and morphological SEM analyses of powders subjected to different ball-milling methods and annealing procedures to enhance size reduction and particles dispersion.

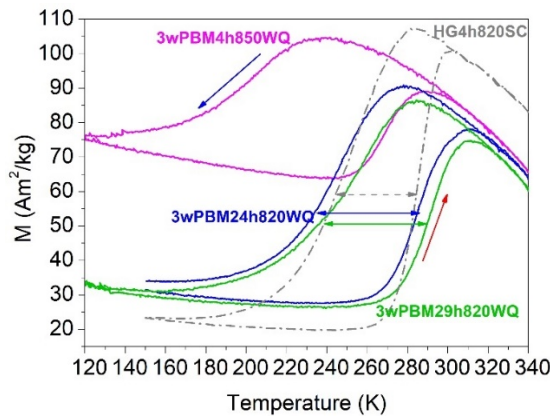


Figure 4.5-11: High-field (1T) magnetization curves as a function of temperature of the $\text{Ni}_{45.7}\text{Mn}_{36.9}\text{In}_{13.2}\text{Co}_{4.2}$ wet PBM powders annealed for 4 h at 850°C and for 24–29 h at 820°C and water quenched, in comparison to the post-annealed hand-grinded HG4h820SC powder.

In Fig. 4.5-12, there are presented the SEM images of the wet PBM powder after the annealing treatments at 600°C, for 24h (a-b) and at 820°C, for 24h (c-d) and for 29h (e-f). It is observed that the particles have nearly the same morphology of the as-milled ones after annealing at medium temperature (Figs. 4.5-12(a-b)), having a flaky shape with a flat surface of average length of 10 μm and a submicrometric or a few microns thickness. By looking at the high magnification image (Fig. 4.5-12(b)), it emerges the presence of a rough surface area, characterized by arrangements of screw and edge dislocations, forming steps and/or sub-grains, at the nanoscale. These mechanisms are typical of the recovery process and occur, upon heating, to decrease the energy stored during the cold-deformation process (crystal defects). Generally, they precede the recrystallization nucleation, which is triggered by a higher atomic mobility and hence higher annealing temperature [171]. In fact, after the annealing treatment for 24 h at 820°C (Figs. 4.5-12(c-d)), the particles show a significant variation in morphology and microstructure, with evidence of recrystallized grains. Although tending to maintain an elongated shape and a mean particle size of $15 \pm 8 \mu\text{m}$ length (inset of Fig. 4.5-12(c)) and a few microns thickness, the particles show a diffuse agglomeration between each other, with also formation of neck junctions (sintering phenomenon). Therefore, under the favourable external thermal energy, the recrystallization nucleation of the particles takes place and is characterized by the formation of equiaxed grains (polygonization) and their subsequent expansion, or “abnormal growth”, at expenses of the neighbouring ones, to minimize the density of grain boundaries and interfaces [171,172]. For the smaller particles it has been

possible to observe a few large grains, spanning the whole particle's thickness (Fig. 4.5-12(d)), differently from the still high density of grain-boundaries and the small grain-size for the larger ones (inset of Fig. 4.5-12(d)). By further increasing the annealing time to 29 h, the grain-growth process is finalized also in the larger and thicker particles, leading to a gradual increase of the grain-size over thickness value (GS/t parameter) [94]. In addition, the almost single-grained particles become more roundish and similar to complex 3D structures of several microns size (Figs. 4.5-12(e-f)). This drastic shape's change is ascribable to the predominant sintering phenomenon, occurring between adjacent particles/grains, leading to a subsequent densification and compaction of the bamboo-like grains. It is worth noticing that the high-temperature thermal treatments have also caused the contamination of the particles with manganese oxides, which are recognized in Figs. 4.5-12(d)-(f) as the trapezoid-like crystals of hundreds of nano-meters size. They are spread all over the surface area, but mainly concentrated near to the edges and bending of the surface.

In view of these morphological and microstructural results, it is possible to match them with and understand the martensitic transformation behaviours observed by the thermo-magnetization measurements (Fig. 4.5-11). Indeed, due to the strong sensitivity to the lattice coherency, microstructural energy barriers and internal stresses [23,31,173], the formation of the martensite cannot be restored after only a partial recovering and reordering of the microstructure and original lattice sites occupation, upon annealing at insufficient temperature (600–700°C). Instead, during the high-temperature (820°C) annealing treatment, the occurrence of the grain-growth process and homogenization between neighbouring grains enables the reduction of microstructurally stored elastic energy and chemical disorder, thus reducing the amount of external energy required to initiate the nucleation of martensite phase (higher M_s temperature) and favouring the transformation in a smaller temperature range (increase of sharpness). However, on the other hand, the excessive duration (29 h) of the high-temperature annealing treatment, together with the selection of a rapid cooling rate, can drastically increase the density of defects, interfaces, and stresses, which alter the formation and propagation of the martensitic variants, resulting in the detrimental increase of transformation broadening. Meanwhile, the hysteresis' width is notably decreased on increasing the annealing duration from 4 h to 24 h and remains almost constant on further increasing the duration to 29 h, showing a negligible dependence on the increase of curvature radius of the particles and/or grain-size. It will be shown later that it is possible to outline a relation between the decrease of the MT's thermal hysteresis and the increase of M_s temperature, for the prepared batches of $\text{Ni}_{45.7}\text{Mn}_{36.9}\text{In}_{13.2}\text{Co}_{4.2}$ compound.

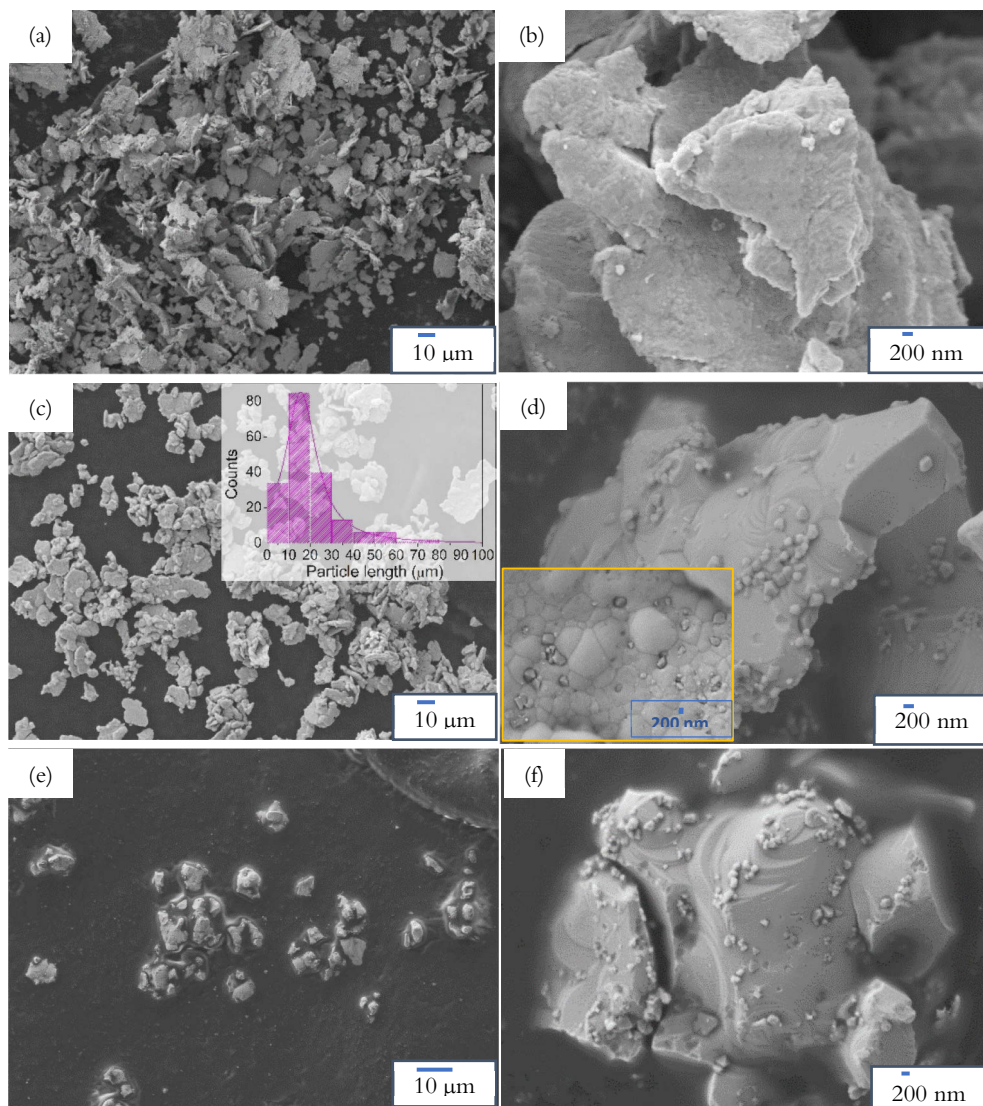


Figure 4.5-12: SEM micrographs, at two different magnifications, of the the $\text{Ni}_{45.7}\text{Mn}_{36.9}\text{In}_{13.2}\text{Co}_{4.2}$ wet PBM particles: (a) and (b) after the annealing for 24h at 600°C; (c) and (d) after the annealing for 24h at 820°C; (e) and (f) after the annealing for 29h at 820°C.

However, the change of ΔT_{hyst} is difficult to be predicted, since it shows a non-monotonic, non-trivial dependence on both microstructural and atomic ordering variations. Overall, from the current experimental results, it is understood that the ball-milling procedure can create a high disordering effect, not only for the

introduction of point defects but also for the reduction of grain-size. Accordingly, a high thermal stimulus for a sufficient long annealing time has to be supplied to allow, through the atomic mobility, the achievement of a high chemical homogeneity and atomic order, in order to recover the original Heusler phase. This fact seems to suggest that the chemical inhomogeneity, due for instance to compositional gradients, is mainly localized at the grain boundaries and its effect becomes relevant on reducing the grain-size of the starting bulk material and, hence, on increasing the interfacial energy term over the volume one. Together with the atomic displacements from the correct occupation sites in the cell, the presence of secondary phases and/or compositional inhomogeneity change the local lattice parameters and prevent the necessary lattice compatibility to promote the formation of the parent-martensite phase interface and the development of twin-related martensitic variants. In this support, it has been shown by J. Liu *et al.* [174] and W. Ito *et al.* [152] that along the grain boundaries precipitates of the Co-rich γ -phase are commonly observed in Ni-Mn-In-Co post-annealed ribbons and arc-melted bulk alloys. Moreover, depending on the peculiar composition of the compound, namely the concentration of Co-impurities, it is possible to reduce the thermal hysteresis of the martensitic transformation and concomitantly increase the magnetization change in the ribbons, by properly increasing the annealing temperature and time, similarly to what has been achieved in the current investigation.

4.5.2.1 Annealing with Alumina powder

Another important obtained experimental outcome is the dependence of the martensitic transformation recovery on the presence of external constraints during the annealing treatment, preventing the agglomeration between particles. In fact, the particles have been annealed in the same conditions of temperature (820°C), time (24 h) and cooling rate (water quenching) already tested, but with the addition of commercial Alumina powder (5-30 μm size) to avoid the sintering and analyse the effect of this condition on the resulting magnetic and magneto-structural properties.

From the SEM analysis (Fig. 4.5-13), it has emerged that the applied method was effective in preventing the agglomeration between the Ni-Mn-In-Co particles. These appear as single flakes (Fig. 4.5-13(a), in brighter colour respect to the Alumina powder) and show the onset of recrystallization and grain-growth phenomena (Fig. 4.5-13(b)) as the ones annealed without Alumina (Figs. 4.5-12(c-d)). However, a completely different martensitic transformation behaviour has been detected by the

magnetic susceptibility and thermo-magnetization measurements, as reported in Figs. 4.5-14(a)-(b).

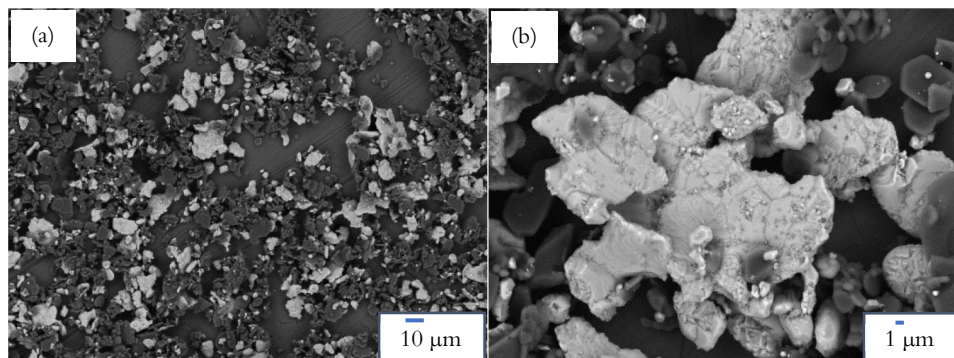


Figure 4.5-13: (a) and (b) SEM-BSE images, at two different magnifications, of the $Ni_{45.7}Mn_{36.9}In_{13.2}Co_{4.2}$ wet PBM powder (brighter colour) mixed with Alumina powder (darker colour) and annealed for 24h at 820°C.

In Fig. 4.5-14(a), for the powder annealed with Alumina, it is noticed a negligible magnetic susceptibility variation, spanning over a broad temperature range, in correspondence of the reverse martensitic transformation, which for the wet PBM powder annealed without Alumina is much sharper and well-defined. Moreover, the Curie transition presents two slightly different slopes, even if it occurs at nearly the same temperature in the two powder batches. Hence a lower degree of compositional phase homogeneity is attained after the annealing in presence of Alumina. Furthermore, by looking at Fig. 4.5-14(b), it is highlighted an almost flattened $M(T)$ curve at 1 T, presenting a significant lower magnetization value of the austenite as compared to the curves of HG820SC and 3wPBM24h820WQ samples. The very low magnetization change across the transformation temperature range points out that, on average, only a small austenitic fraction undergoes the diffusionless martensitic transformation, with formation of phase boundaries (habit planes) and arrangement of different oriented twin-related martensitic variants [175].

Accordingly, for the batch of wet PBM powder annealed in absence of Alumina, the higher ferromagnetic signal of the austenite and the well-defined change of magnetization between the high-temperature and low-temperature phases highlight the presence of a higher coherency and coupling between the structural and magnetic

domains during the martensitic transformation, likely due to fewer internal constraints acting as pinning forces.

The combination of the obtained magneto-structural and morphological results permits to understand and assert that the occurrence of agglomeration and/or sintering between particles during the annealing treatment is a fundamental requirement for restoring an optimal phase homogeneity and a martensitic transformation behaviour comparable to the original one (HG4h820WQ). This phenomenon is strictly connected to the increase of volume over the defected and oxidized particles' surface, the annihilation of point defects and dislocations, and the enlargement of coherent crystal grains through the whole particle's cross-section.

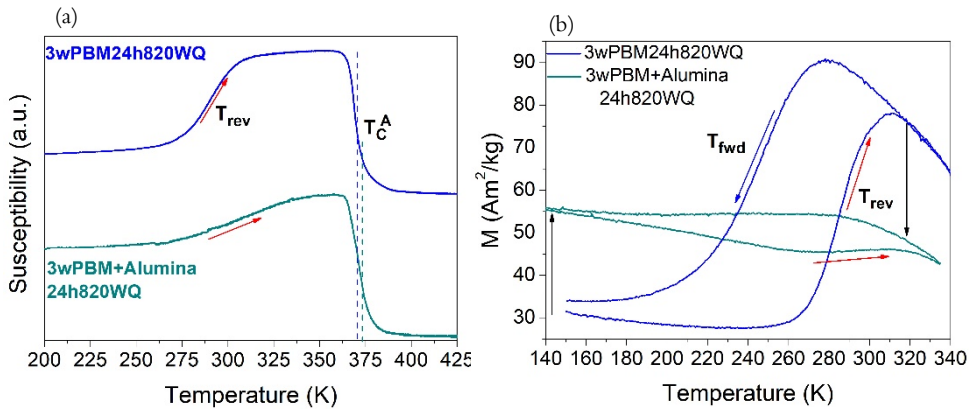


Figure 4.5-14: Temperature-dependent (a) magnetic susceptibility measurements and (b) high-field magnetization curves of the wet PBM particles annealed with or without Alumina powder and comparison with the post-annealed hand-grinded powder of $\text{Ni}_{45.7}\text{Mn}_{36.9}\text{In}_{13.2}\text{Co}_{4.2}$ compound.

4.5.3 Cryo-milling

After the tests of the planetary ball-milling with a solvent to enhance particle dispersion and decrease the particle size down to the sub-microscale, for the $\text{Ni}_{45.7}\text{Mn}_{36.9}\text{In}_{13.2}\text{Co}_{4.2}$ HG powder it has been investigated also the effect of milling at cryogenic temperatures following the same procedure and selecting the same milling parameters used for Ni-Mn-Ga (sub-chapter 4.3.2) and Ni-Mn-Cu-Ga compounds (sub-chapter 4.4.1). The process was run till an overall effective milling time of 4h40min. In Table 4.5-3, the samples hereafter investigated have been

reporting, with the specifications of milling time, annealing conditions, and corresponding names.

Sample: $Ni_{45.7}Mn_{36.9}In_{13.2}Co_{4.2}$	Milling time (h)	Annealing temperature (°C)	Annealing time (h)	Cooling rate	Corresponding name		
Hand-grinded (HG)	-	-	-	-	HG		
			820	2	SC	HG820SC	
				4	WQ	HG4h820WQ	
Cryo-milled (CM)	2	-	-	-	CM-2h		
			620	96	WQ	2CM96h620WQ	
			755	24		2CM24h755WQ	
			820	1		2CM1h820WQ	
				4		2CM4h820WQ	
				24		2CM24h820WQ	
				29		2CM29h820WQ	
			3	-	-	-	CM-3h
			700	24	WQ	3CM24h700WQ	
			755			3CM24h755WQ	
			820	24		3CM24h820WQ	
				29		3CM29h820WQ	
			4.40'	-	-	-	CM-4h40'

Table 4.5-3: Milling procedure, annealing conditions, and corresponding names of the $Ni_{45.7}Mn_{36.9}In_{13.2}Co_{4.2}$ powder batches object of investigation in the current sub-section (4.5.3).

In Figs. 4.5-15(a)-(b), the SEM image and the size distribution of the powder cryo-milled for 3 h (CM-3h) reveal an irregular shape, which is chunky for the bigger particles and flaky for the smaller ones and a large size distribution, mainly peaked at around few microns, with also a discrete amount in the range of 5-20 μm , and fewer one for $d > 25 \mu\text{m}$. These results are consistently different from the Gaussian size distribution, with regular and roundish particles' shape of the dry PBM powder or the homogeneous batch of thin and flat micrometric/sub-micrometric particles of the wet PBM powder (Fig. 4.5-4).

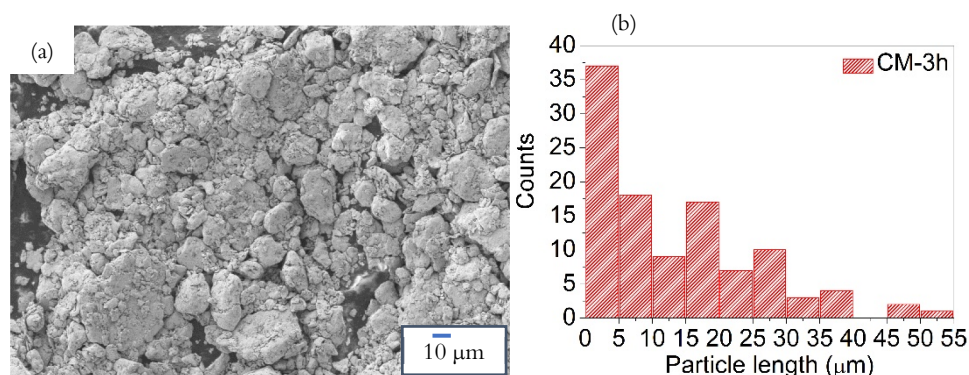


Figure 4.5-15: (a) SEM image and (b) corresponding size distribution of the powder cryo-milled for 3h of the $\text{Ni}_{45.7}\text{Mn}_{36.9}\text{In}_{13.2}\text{Co}_{4.2}$ compound.

By looking at the room-temperature XRD patterns of Fig. 4.5-16, it is possible to visualize the effect of increasing milling time on the crystal structure. The peaks of the HG powder, referred to a tetragonal martensitic phase mixed with small traces of the cubic *fcc* austenite (Table 7.4-1, Appendix), start to broaden and decrease of intensity after 2 h of CM process (CM-2h). The peak broadening increases and becomes asymmetric for the CM-3h powder, due to the higher concentration of induced defects' and, possibly, to the occurrence of an anisotropic lattice strain during the mechanical compressive strength. After 4 h and 40' of milling, the original crystal structure is destroyed by the disordering and the grain-size reduction processes, as revealed by the almost suppression of the high-angle reflections and the enhancement of broadening of the reflections at lower angles, leading to a significant peak shape's change.

By comparing the CM-3h diffraction pattern with those of Fig. 4.5-5, it emerges that the disordering effect caused by the CM process is similar to that of the wet PBM one, therefore the energy involved (friction and overheating) during cryo-milling is lower than those during the dry PBM method at room-temperature. However, the achieved results strongly depend on the milling duration and on the ratio between dimensions of colliding balls and material to grind. In fact, even after the milling at cryogenic temperatures, among the batch of the longest-milled particles, it has been observed an incipit of agglomeration (Fig. 7.4-1, Appendix).

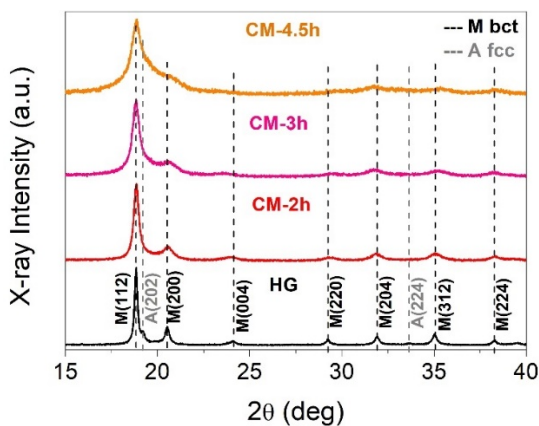


Figure 4.5-16: Evolution of room-temperature X-ray diffraction patterns during cryo-milling (CM) for different milling times and comparison with the diffraction pattern of the starting hand-grinded powder of the $\text{Ni}_{45.7}\text{Mn}_{36.9}\text{In}_{13.2}\text{Co}_{4.2}$ system.

From the susceptibility and magnetometric measurements (Fig. 4.5-17(a)-(b)), it has been revealed that the ferromagnetic order and the martensitic phase transformation (MT) of the powder samples gradually disappear by increasing the amount of disorder and decreasing the particles' size. Indeed, while for the HG powder, it was possible to reveal the change of susceptibility corresponding to the martensitic transformation, although it spanned over a large temperature range, for the CM-2h powder any clear evidence, or only a weak one of the magneto-structural transformation, both in heating and cooling branches was detected. Furthermore, a broad transition, associated with a negligible susceptibility change was observed at a temperature 20 K lower than the Curie transition of the HG powder.

By combining the magnetic with the structural results, it is understood that the tetragonal phase observed from the XRD measurement for the CM-2h sample is different from the tetragonal martensitic phase of the HG powder, since it does not show neither the recovery of the high-magnetic austenite in heating neither the martensitic transformation on cooling. This fact is ascribable to the formation of an amorphous phase by increasing the milling time, as revealed by the peak broadening, which is characterized by the gradual suppression of magnetic moment with the increase of internal strains and defects, as also recently pointed out in literature [176,177].

Concerning the $M(T)$ curve at low temperatures (Fig. 4.5-17(b)), it is observed the increase of magnetic signal below 200 K. This is a common feature of the metamagnetic Ni-Mn-In-Co compounds, both in bulk (single crystals/polycrystals)

[97,150] and ribbons form [11,174] which is related to the coexistence of ferromagnetic and antiferromagnetic interactions, evolving in super-spin glass behaviour on cooling below a critical temperature [77,90,178]. However, in this case, the induced deformation tend to decrease the total magnetic moment of the ferromagnetic clusters [176].

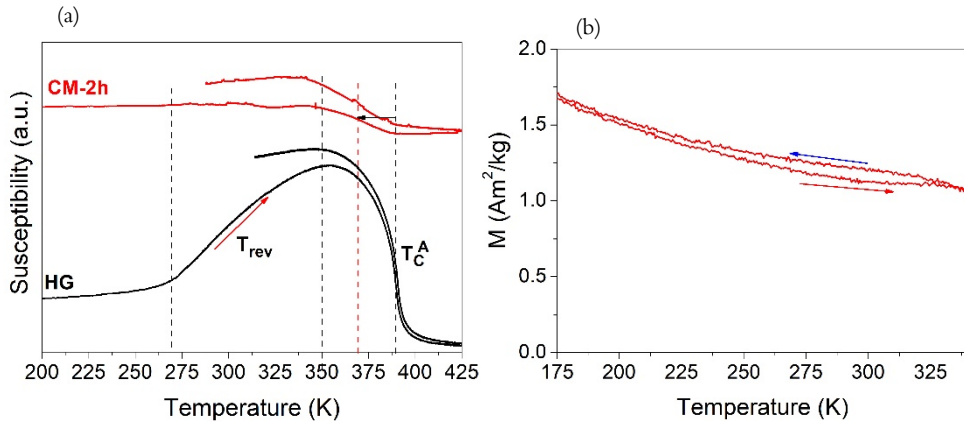


Figure 4.5-17: (a) Magnetic susceptibility measurement as a function of temperature for the hand-grinded (HG) and 2 h cryo-milled powders of $Ni_{45.7}Mn_{36.9}In_{13.2}Co_{4.2}$ system. (b) M - T curve at 1 T of the CM-2h powder.

The study of the magnetic and magneto-structural properties recovery in CM-2h and CM-3h powders has been carried out by testing several different annealing conditions of temperature and time (Table 4.5-3), aimed at investigating their effect and optimizing them. In Figs. 4.5-18(a) the thermo-magnetic response of the post-annealed batches of CM-2h powder is presented and compared with the one of hand-grinded powder annealed for 2h at 820°C and slowly cooled (presenting the behaviour as close as possible to the bulk). It can be seen that an annealing at 620°C, near to the order-disorder transition temperature of the bulk ($T_t^{B2/L2_1} = 896$ K = 623°C) is insufficient to restore the martensitic transformation and only a broad Curie transition shifted at a temperature 30 K lower than the expected is detected. Hence, independently on the long annealing time (96 h) and on the fact that the particles have been milled for only 2 h, the performed heat treatment is not suitable to annihilate the induced defects and restore the initial atomic order. A sharper Curie transition is recovered for the 2CM24h700WQ powder, by increasing the annealing

temperature to 700°C. The martensitic transformation, instead, starts to be retrieved after the heat treatment at 755°C for 24 h, followed by water quenching. In addition, the Curie transition temperature is slightly increased. However, by selecting a slow cooling rate (2CM24h755SC) rather than a rapid one (2CM24h755WQ), the martensitic transformation is suppressed, while the Curie transition is shifted to a temperature 15 K higher. By looking at Fig. 4.5-18(b), it is interesting to notice that the M(T) behaviour of the 2CM24h755WQ sample is almost coincident in cooling to that of the HG4h820WQ powder, associated with also a similar value of magnetic moment at low temperatures. On heating, instead, it emerges a higher broadening of the transition, due to the higher value of the austenite finish temperature (Table 7.4-2, Appendix). Moreover, the saturation magnetization of the austenite is reduced leading to a smaller magnetization change between the two phases.

By increasing the annealing temperature to 820°C, after few hours (1-4 h) of heat treatment, in Fig. 4.5-18(a), it is observed a rightward shift of the Curie transition temperature with respect to the 2CM24h755WQ powder, but only a negligible susceptibility variation in correspondence of the reverse martensitic transformation, which appears at a lower temperature. In fact, the high-field M(T) measurements (Fig. 4.5-18(b)) points out the occurrence of only a partial martensitic phase transformation, starting at temperatures far below the expected ones, both on cooling and heating branches, and characterized by a significant large thermal hysteresis (ΔT_{hyst}) (Table 7.2-2, Appendix). It is important to observe that the saturation magnetization of the austenite increases in samples presenting a lower martensite start temperature, similarly to the behaviour observed for the wet PBM powder annealed for 4 h at 820°C (Fig. 4.5-11). This, in turn, is inversely related to the duration of the annealing treatment, for the fixed annealing temperature of 820°C. On increasing the annealing time to 24 h at the fixed annealing temperature 820°C, it can be noted a significant increase of the Curie transition temperature and of A_f and M_s temperatures (Fig. 4.5-18(a)). However, the MT is remarkably worsened as compared to the to the powder annealed for the same time at a lower temperature (755°C), in terms of the increase of transformation broadening and the decrease of magnetization change. By contrast, the thermal hysteresis is reduced and appears to be similar to that of the HG4h820WQ powder. On further increasing the annealing time to 29 h at the same fixed temperature of 820°C, an inverse trend of the MT features is recognized, as the decrease of martensitic transformation temperatures, increase of saturation magnetization of the austenite and of the retained magnetic signal below the M_f temperature (Fig.4.5-18(b)). On the contrary, the Curie transition of the austenite appears at nearly the same temperature of the annealed HG powder (Fig. 4.5-18(b)).

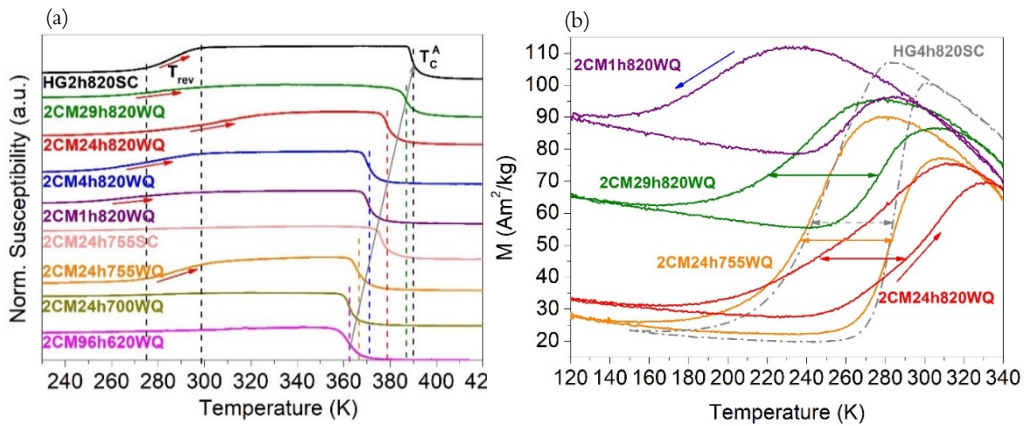


Figure 4.5-18: (a) Temperature-dependent magnetic susceptibility for differently annealed batches of CM-2h powder and comparison with the thermomagnetic behaviour of the HG820SC powder, of $Ni_{45.7}Mn_{36.9}In_{13.2}Co_{4.2}$ compound. (b) High-field magnetization measurements of the batches showing the recovery of the martensitic transformation, and comparison with the bulk and HG820SC samples.

This non-monotonic trend of the martensitic transformation features reveals a strong sensitivity to the atomic reordering processes and the amount and distribution of thermal defects, apported by the high atomic mobility during long heat treatments at high temperature. Indeed, they can likely interact in a non-trivial way with the kinetic and thermodynamic aspects of the martensite phase formation.

By considering the actual average compositions of the examined powder batches, obtained by the EDX analysis (Table 7.4-3, Appendix), it can be observed some variability in the concentration of each element with respect to the expected values of the initial bulk composition. In particular, it is noted that the 2CM24h755WQ, 2CM1h820WQ and 2CM4h820WQ powders, which present a Curie transition temperature lower than that of the 2CM24h820WQ and 2CM29h820WQ samples, are also those showing the lowest average concentration of In element and its highest associated standard deviation (obtained by measuring different regions of several particles), thus denoting a higher chemical inhomogeneity. In general, the four samples annealed at the same temperature of 820°C for different times (1-4-24-29 h), show a gradual increase of the average concentration of Ni and In atoms and conversely a decrease of that of Mn atoms, accompanied by a general decrease of the associated standard deviations. This fact can be likely ascribed to the effect of atomic diffusion and/or morphological changes, as it will be discussed later.

Likely, also these compositional variations among the powder batches may explain the observed changes in martensitic transformation temperatures, thermal hysteresis

and magnetization value of the austenite. In fact, the magnetic and structural properties of the Heusler compounds are strongly sensitive to the chemical disorder and change of atomic rearrangement in the unit cell, especially for Mn atoms, which carry the magnetic moment.

Likewise, in Fig. 4.5-19(a)-(b), there are shown the magnetic susceptibility and the high-field (1 T) magnetization curves as a function of temperature for the CM-3h powder batches after the different annealing treatments (Table 4.5-3), in comparison to the behaviour of the HG4h820WQ sample. For this powder, a more difficult recovery of the martensitic phase transformation is revealed, since, by increasing the temperature above 700°C, neither the annealing at 755°C nor that at 820°C, for the long duration of 24 h, are effective in restoring the expected magnetic and magneto-structural transitions. For the 3CM24h820WQ sample, it is possible to notice in Fig. 4.5-19(b) only a partial martensitic transformation, which is characterized by a notable broadening over a large temperature range and a negligible magnetization change between the high-temperature and low-temperature phases. For the 3CM29h820WQ powder batch, instead, the change of magnetic signal across the martensitic transformation is more evident, even though the transformation broadening is worse than the HG4h820SC powder. Moreover, it has been noted that a subgroup of the 3CM29h820WQ powder batch, with particle size below 66 μm (3CM24h820WQ-d<66 μm), shows an enhancement of broadening (Fig. 4.5-19(b)). By contrast, the Curie transition temperature remains the same of the bigger particles (3CM24h820WQ-d> 200 μm) (Fig. 4.5-19(a)).

As for the post-annealed CM-2h powder, the Curie transition temperature shows an increase and hence a sensitivity to the annealing temperature. Instead, differently from the previous batch, the increase of annealing duration to 29 h has a positive effect on the transformation sharpness, keeping unvaried the T_C^A value, at a temperature well below the expected one.

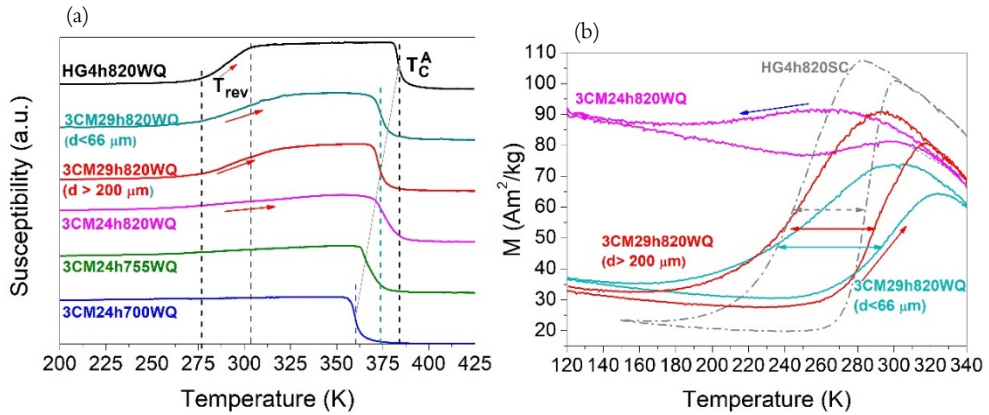


Figure 4.5-19: (a) Magnetic susceptibility response as a function of temperature for the differently annealed batches of CM-3h powder and comparison with the thermomagnetic response of the HG820SC sample, of $\text{Ni}_{45.7}\text{Mn}_{36.9}\text{In}_{13.2}\text{Co}_{4.2}$ compound. (b) High-field magnetization measurements of the batches showing the recovery of the martensitic transformation, and comparison with the bulk and HG820SC samples.

The original bulk configuration is drastically worsened after the ball-milling process and the significant differences in the martensitic transformation behaviour and magnetic properties, even after changing and adjusting the annealing temperature and time, have pointed out the unavoidable limitations in the recovery process upon heating for both the PBM and CM particles. In addition, such challenges are gradually enhanced for particles ball-milled at increasing milling time and/or milling energy, hence presenting a higher density of defects and a lower particle size.

In order to better assess the origin of the transformation broadening (ΔT_{elas}) and possibly relate it to microstructural variations, it has been analysed by high-magnification SEM images the morphology of the particles after each different annealing treatment.

In Figs. 4.5-20 and 4.5-21 there are shown the SEM micrographs of some of the annealed CM-2h and CM-3h powder batches, respectively. As revealed in Fig. 4.5-20(a), it is noticed that the CM-2h particles after the long (96 h) annealing at 600°C maintain the peculiar irregular shape and non-uniform size distribution of the as-prepared ones. Moreover, by zooming on the particles' surface (Fig. 4.5-20(a-2)), it is possible to recognize low-angle grain-boundaries, leading to formation of small sub-grains, brought about the thermally induced rearrangement of dislocations during the recovery process [172]. On increasing the annealing temperature to 755°C, for a

duration of 24 h, the obtained particles (Fig. 4.5-20(b)) present a smoother surface area and a more roundish shape, showing (in the inset) a narrow size distribution peaked at around $15 \pm 8 \mu\text{m}$ length and a thickness of few microns. Furthermore in Fig. 4.5-20(b-2), it can be observed the subdivision in multiple micrometric equiaxed grains characteristic of the recrystallization phenomenon [171]. A significant change in particles' morphology, instead, has occurred after the annealing for 1 h at 820°C , as shown in Figs. 4.5-20(c). In fact, the small particles are agglomerated with the bigger ones and the grains are more roundish. After 24 h at 820°C (Figs. 4.5-20(d)), the grains are larger and the recrystallized structures strongly sintered between them, through the formation of triple junctions. This fact gives rise to chains of agglomerates, of variable length (several tens of microns) and thickness ($2\text{-}10 \mu\text{m}$), rather than a batch of single, non-interacting particles. For the CM-3h particles subjected to the same heat treatment, in Figs.4.5-21(a) it is instead observed the formation of big and thick sintered agglomerates of several tens of microns, which remain separated between them. It is interesting to notice that, even though the recrystallization process has taken place, the recrystallized grains are still small (a few microns of sub-microns size), with sharp facets and voids of various size within and inter-grains, leading to multiple interacting interfaces (Fig. 4.5-21(a-2)). In general, it emerges a more complex microstructure as compared to the one of the 2CM24h820WQ powder. On increasing the annealing time up to 29 h, keeping fixed the temperature to 820°C , the sintering phenomenon is enhanced, resulting, for the CM-2h particles, to an increase of volume and surface bending, due to a higher compaction and the grains' reorientation (Figs. 4.5-20(e)), while, for the CM-3h ones, to the formation of close-packet, foam-like structures. Some of these latter present dimensions below about $66 \mu\text{m}$ (Figs. 4.5-21(b)) and show the coalescence and growth of the grains in the outer part, leading to a decrease of grain-boundaries and surface's smoothening, whereas the heterogenous multiple formation/rearrangement of triple junctions along the thickness prevents the grains' expansion throughout the whole particle's cross-section. This phenomenon is well highlighted in Fig. 4.5-21(b-2), where it is recognizable the assembling of many 3D crystal grains, with different orientation, dimensions, and pores' concentration, resulting in complex porous architectures. Some other of these foam-like structures, instead, reach several hundreds of microns size (Figs. 4.5-21(c)) and are characterized by a tangle of neck junctions of $5\text{-}10 \mu\text{m}$ thickness and a broad distribution of grains, where the martensitic twin lamellae propagate (Fig. 4.3-27(c-2)). The development of this peculiar microstructure, not observed for the wetPBM-3h and CM-2h annealed particles, can be attributed to the presence, in the as-milled CM-3h powder batch, of a higher amount of small particles (micrometric or sub-micrometric) having

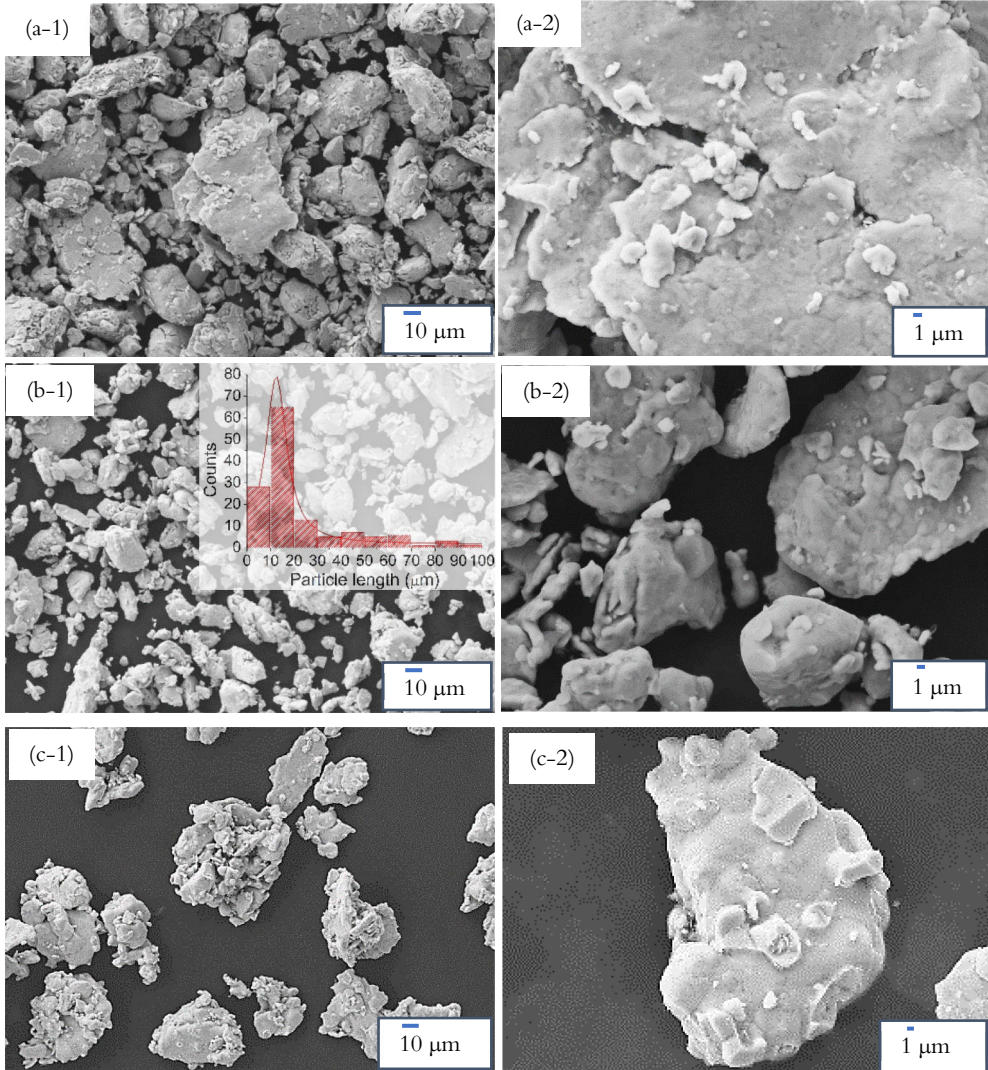
a large surface's bending, hence a small curvature radius, which could have favoured and promoted the avalanche sintering reaction during annealing [179].

Overall, with respect to the batches of wetPBM-3h particles annealed for 24-29 h at 820°C, it emerges that the annealed CM-2h and CM-3h ones are bigger and thicker, and do not show the strong tendency to oxidation.

In relation to the above-discussed martensitic transformation behaviour, it can be supposed that the increase of transformation broadening observed for the CM-2h after the annealing for 24 h at 820°C rather than at a lower temperature is determined by the presence of a larger number of potential transformation interfaces, created by the contact between sintered particles/grains of different size and/or crystallographic orientation. Likely, this phenomenon increases the amount of elastic energy stored in the microstructure, thus requiring a higher undercooling (overheating) to be overcome. A further important result emerging from the comparison between the SEM images of the 2CM24h820WQ (Fig. 4.5-20(d-1)) and 2CM24h755WQ (Fig. 4.5-20(b-1)) powders and their corresponding transformation behaviours (Fig. 4.5-18(b)) is that the grain growth process, occurring during the heat treatment at the higher temperature, is beneficial for decreasing thermal hysteresis of the martensitic transformation (ΔT_{hyst} , Table 7.4-2, Appendix). In fact, the smaller is the grain-size, the stronger is the pinning effect at the grain-boundaries for the phase-interfaces propagation, degrading a larger part of the driving force into frictional work, dissipated as heat, as reported in literature [157]. On the other hand, after the longest annealing treatment, the observed significant increase of volume and variability of bending between adjacent grains can have influenced the change of the martensitic transformation (interruption and shift to lower temperatures) and the increase of the Curie transition temperature. As it will be discussed later (4.5.4), the magneto-structural features of the metamagnetic martensitic transformation can be strongly affected by the morphological variations, atomic reordering processes and lattice incompatibilities, which strengthen the mechanical and ferromagnetic stability of the austenitic phase.

For the 3CM29h820WQ powder, instead, the improvement in the recovery of a large magnetization change across the martensitic phase transformation as compared to the shorter-annealed powder (Fig. 4.5-19(b)) is ascribed to the beneficial effect of the grain-growth process. Further, the lower transformation temperature range detected for the larger sintered pieces with respect to the smaller and separated ones points out that the thermoelastic stress-coupling between the adjacent neck-junctions helps in triggering at once the martensitic phase transformation. Moreover, it can be supposed that the increase of sintered volume over the more defected and

discontinuous surface could account for a strengthening of the Mn-Mn exchange interactions resulting in a total increase of magnetization of the austenite.



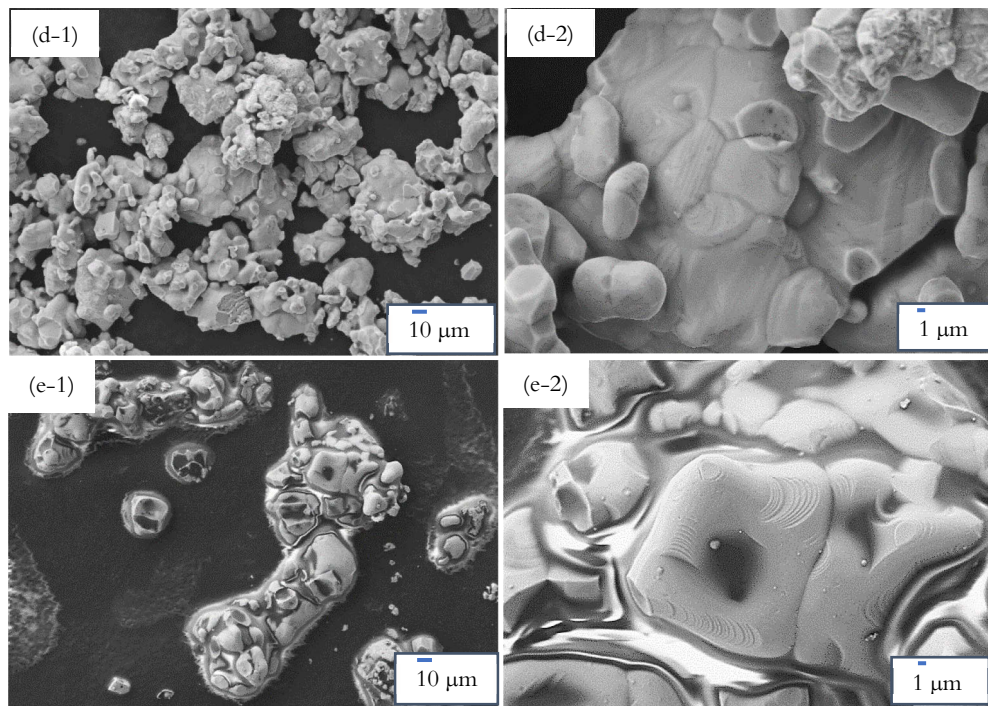
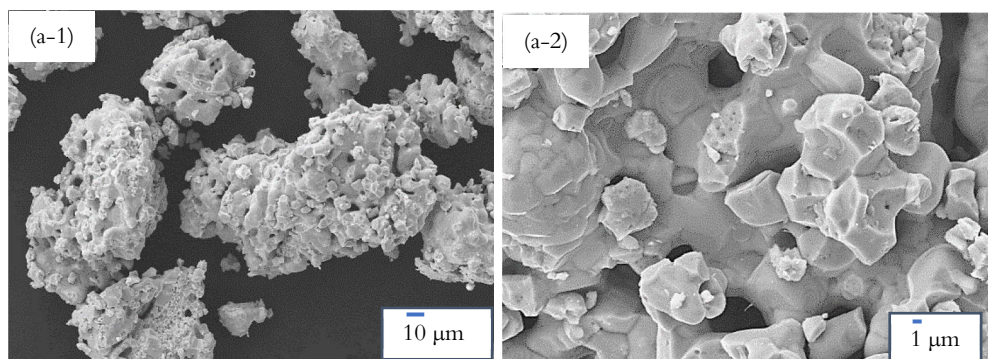


Figure 4.5-20: SEM micrographs, at two different magnifications, of the $\text{Ni}_{45.7}\text{Mn}_{36.9}\text{In}_{13.2}\text{Co}_{4.2}$ CM-2h powders after annealing: (a-1)-(a-2) for 96 h at 620°C; (b-1)-(b-2) for 24 h at 755°C; (c-1)-(c-2) for 1 h at 820°C; (d-1)-(d-2) for 24 h at 820°C; (e-1)-(e-2) for 29 h at 820°C.



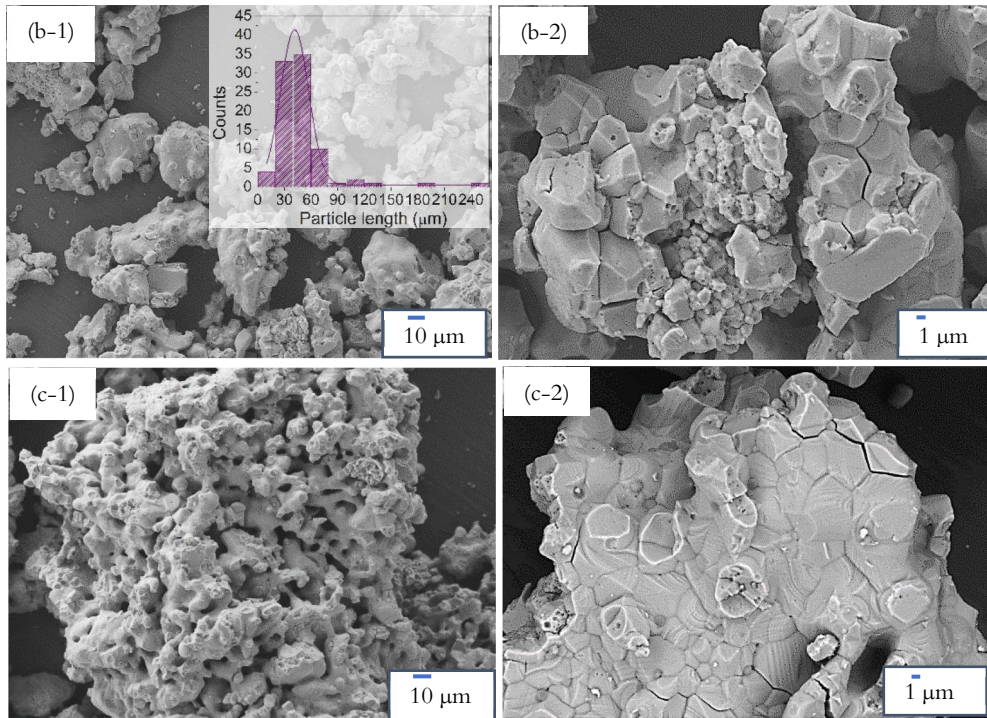


Figure 4.5-21: SEM micrographs, at two different (increasing) magnifications, of the $Ni_{45.7}Mn_{36.9}In_{13.2}Co_{4.2}$ CM-3h powder batches after the annealing: (a-1)–(a-2) for 24 h at 820°C; (b-1)–(b-2) for 29 h at 820°C (particles with $d < 66 \mu\text{m}$) and (c-1)–(c-2) for 29 h at 820°C ($d > 200 \mu\text{m}$).

Generally, the analysis of the SEM images of the annealed particles, combined with the results of their magneto-structural properties, suggests that during the annealing treatment the particles must undergo a full recrystallization and grain-growth processes in order to restore the martensitic phase transformation. However, the high thermal energy required to overcome the energy barriers not only promotes the annihilation of the defects but also gives rise to the solid-state reactions and volume-mass transport, which completely alter the morphology of the powders.

4.5.3.1 Annealing with Alumina powder

Aimed at understanding the role of the sintering phenomenon in restoring the metamagnetic martensitic transformation of the CM particles, it has been tried to

anneal them at the same already-tested conditions of temperature (820°C) and time (24 h), keeping them separated by using commercial Alumina powder, equivalently to what above-described for the wetPBM-3h particles (4.5.3.1).

In Fig. 4.5-22(a-b) it is reported the SEM images of the CM-2h powder after the annealing mixed with Alumina (darker powder), from which, at the first glance, it emerges the avoidance of sintering and the desired separation between particles. Furthermore, by zooming on the particles' surface (Fig. 4.5-22(b)), there can be noted the division in grains through high-angle grain-boundaries, but also a certain superficial roughness, caused by grooves, kinks and steps of growth. Presumably, the formers are due to dislocations loops and/or clusters of interstitial defects [144] and predominantly they are found on the surface area of the bigger and thicker particles, whereas the thinner and smaller ones present a smoother and more homogeneous microstructure. This fact highlights a strong dependence of the recovery process rate on the surface-to-volume ratio of the particles, likely due to the different density of defects and surface energy. Moreover, the significant differences observed between the powder shown in Figs. 4.5-22(a-b) and that annealed in absence of Alumina (Figs. 4.5-20(e-f)) point out that the morphological and microstructural evolution during the heat treatment is strongly affected by the presence of external constraints. A similar scenario has been found out also for the CM-3h powder mixed with Alumina and then annealed for 24 h at 820°C (Figs. 7.4-2 and 7.4-3, Appendix).

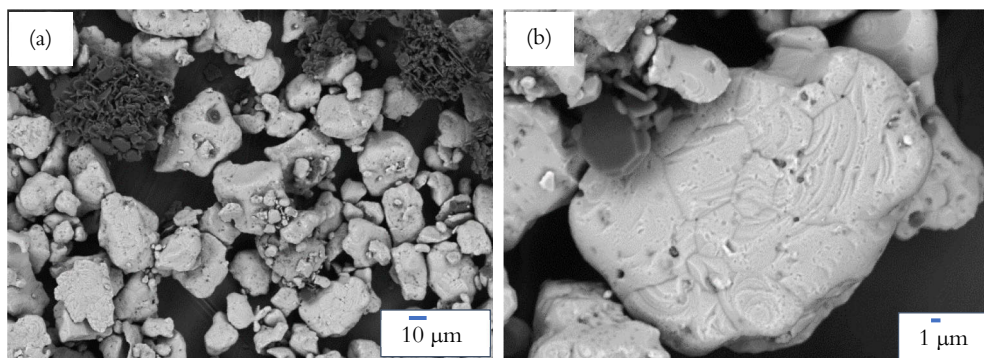


Figure 4.5-22: (a) and (b) SEM images, at two different (increasing) magnifications, showing the morphology of the CM-2h powder of $\text{Ni}_{45.7}\text{Mn}_{36.9}\text{In}_{13.2}\text{Co}_{4.2}$, mixed with Alumina (darker colour) and annealed for 24h at 820°C.

The subsequent thermomagnetic analysis of the post-annealed, non-agglomerated CM-2h particles has revealed a drastic change of the magneto-structural behaviour as compared to the expected one. As shown in Fig. 4.5-23, for the powder annealed with Alumina no evident traces of the reverse martensitic transformation (on heating) can be detected and a broader Curie transition with respect to the batch of powder annealed without Alumina is observed. Nevertheless, the Curie temperatures are close to each other, thus suggesting the presence of a comparable degree of atomic order in the two batches. This fact, then, points out that the attained mixture of ordering types ($B2/L2_1$) is not playing the fundamental role in triggering the recovery of the martensite phase formation, which, rather, seems to be much more dependent on morphological and microstructural features, such as particles' thickness and grains' homogenization.

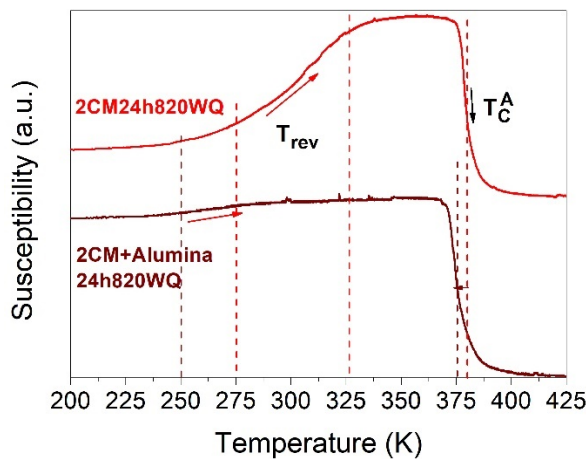


Figure 4.5-23: Comparison between the thermomagnetic responses of the batches of CM-2h powder, annealed in absence or presence of Alumina to avoid sintering, and of the post-annealed hand-grinded powder of $\text{Ni}_{45.7}\text{Mn}_{36.9}\text{In}_{13.2}\text{Co}_{4.2}$ compound.

In light of the achieved results, it can be speculated that the occurrence of sintering between the particles is not a collateral effect of the high-temperature annealing treatment, but, rather, an important requirement to permit, through the surface and volume mass diffusion, a faster and more effective annihilation and rearrangement of defects and dislocations. Thereby, this process can speed up the fulfilment of recrystallization and grain-growth phenomena, allowing a favourable

microstructure for the formation of the martensite phase. In this respect, it has been noticed a notable dependence of the kinetics of the recovery process, and, thus, of the martensitic transformation's restoration, on the shape of the as-milled particles. Indeed, the particles presenting a larger length over thickness ratio, namely a flaky shape, such as the wet PBM powder, have shown, under the same annealing conditions with Alumina, a much more efficient enlargement and smoothing of grains in three directions as compared to the other CM powder batches. These features can be considered as necessary, but not sufficient, conditions to recognize some traces of the martensitic transformation. Then, it is understood that the optimal recovery of the martensitic transformation is strictly related to the occurrence of a minimum coupling between the particles and the reduction of interfacial and internal incompatibilities.

4.5.3.2 Secondary annealing treatments

A secondary heat treatment for 4h at 500°C followed by a slow cooling rate has been performed on the 2CM24h820WQ and 3CM29h820WQ powders, after selecting the particle size below about 66 μm . This further treatment was aimed at investigating the possibility to release internal stresses, due to the quenched-in disorder, and reduce the transformation temperature range.

However, in Figs. 4.5-24(a-b); 4.5-25(a-b), the obtained thermomagnetic and temperature-dependent magnetization curves of the two batches do not reveal any significant variation in the transformation temperature range as compared to that prior to the second heat treatment (also visible by comparing the ΔT_{elas} values before and after the secondary heat treatment listed in Table 7.4-2 of Appendix). By contrast, it emerges an increase of the Curie transition temperature of the austenite (T_C^A) (Figs. 4.5-24(a); 4.5-25(a)), an increase of the magnetic moment of the austenite (Figs. 4.5-24(b); 4.5-25(b)) and of the thermal hysteresis, accompanied by an increase of the magnetic moment in correspondence of M_f temperature.

It is worth noticing that, while for the 2CM24h820WQ+ann4h500SC sample the reverse martensitic transformation is almost coincident with that of the 2CM24h820WQ batch (Fig. 4.5-24(b)), for the 3CM29h820WQ+ann4h500SC sample it is noticed the shift to lower temperatures of both the reverse and forward martensitic transformation (Fig. 4.5-25(b)).

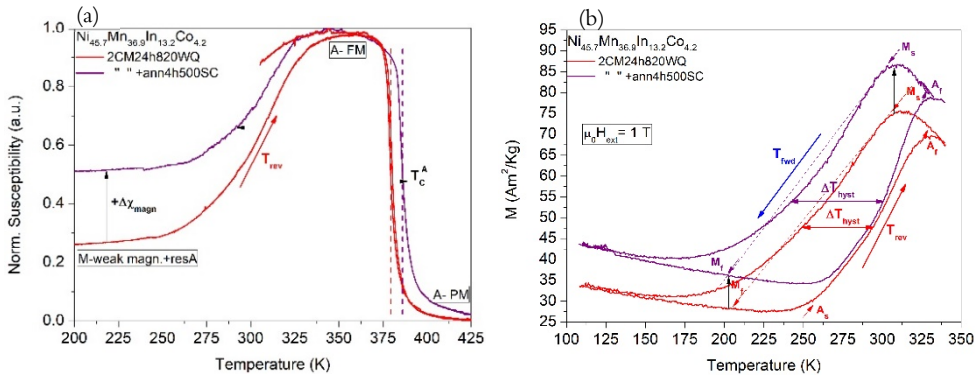


Figure 4.5-24: (a) AC magnetic susceptibility response and (b) high-field magnetization measurement as a function of temperature for the 2CM24h820WQ and 2CM24h820WQ+ann4h500SC powder batches of $Ni_{45.7}Mn_{36.9}In_{13.2}Co_{4.2}$ compound.

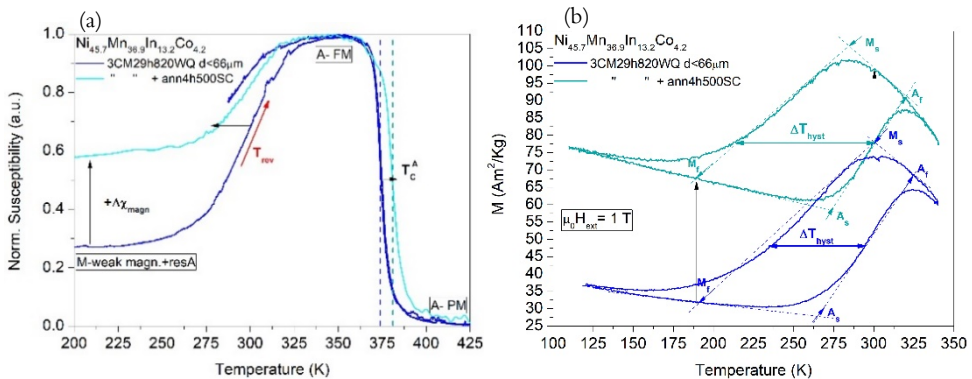


Figure 4.5-25: (a) ac magnetic susceptibility response and (b) high-field magnetization measurement as a function of temperature for the 3CM29h820WQ and 3CM29h820WQ+ann4h500SC powder samples of $Ni_{45.7}Mn_{36.9}In_{13.2}Co_{4.2}$ compound.

In order to recognize a possible correlation between the shift to lower temperatures of the martensitic start temperature (M_S) and the presence of peculiar microstructural features/variations of the particles, a further SEM analysis has been carried out, using the InLens detector and the low voltage of 5kV to better highlight the superficial characteristics.

The SEM images in Figs. 4.5-26(a-b-c) and (d-e-f), referred to the 2CM24h820WQ and the 2CM24h820WQ+ann4h500SC powder batches, respectively, show in both samples the growth of bamboo-like grains and the propagation of the martensitic twin lamellae within the grains and, in some cases,

across the neighbouring ones. By comparing, horizontally, the images at the same magnification (Figs. 4.5-26(a)-(d)), it results that the particles of the latter batch present a lower concentration of grain-boundaries and concomitantly longer martensitic stripes, following the surface's bending, with an average thickness of 2-5 μm . Moreover, as visible in Figs. 4.5-26 (b)-(e), it is interesting to note that the alternation of darker and brighter lamellae is continuous and homogeneous throughout the cross-sectional area and along the terrace planes of growth, leading to the appearance of peculiar features at the interfaces (surface's bending, steps and disconnections of the microstructure) such as the zigzag patterns. These occur only in correspondence of compatible connections and accommodation of the different oriented twin-related martensitic variants, which depend on the specific geometric conditions and bending stresses, as underlined by R. Chulist *et al.* [180] in the study of twin-boundaries accommodation and refinement at inclined interfaces of bent Ni-Mn-Ga single crystals. In addition, it has to be considered that also the structural and microstructural imperfections as well as the presence of compositional inhomogeneity play a fundamental role in the mechanism of propagation of the martensitic phase. In fact, in correspondence of a higher surface roughness, as the presence of pores, presumably caused by interstitial defects, dislocations loops or evaporation losses of the most volatile Mn and In elements (Fig. 4.5-26(c)), the mobility of twin boundaries is hindered and only few martensitic lamellae at the nanoscale are detectable. These defects seem to originate from the long and high-temperature annealing treatment combined to the rapid cooling rate [96,143,144], and lead to lattice stress and disorder acting as pinning centres for the nucleation of the martensite. The latter, in fact, requires a high coherency and lattice compatibility for the formation and mobility of the habit planes between parent and product phases [175,181]. Similar voids have been detected also in particles of the 2CM29h820WQ powder. By contrast, the short annealing at temperature below the order-disorder transition temperature, followed by a slow cooling rate, has been effective in removing the majority of these voids, other than promoting the coarsening of the twin boundaries (at the meso- and microscale rather than at the nanoscale) on smoother and larger grains (Fig. 4.5-26(f)). Also, it can be noted a peculiar new feature at the nanoscale for this powder batch, in the form of nano-meter sized embryos. However, with only the SEM analysis performed, it cannot be understood the origin and not even the possible effect on the martensitic transformation.

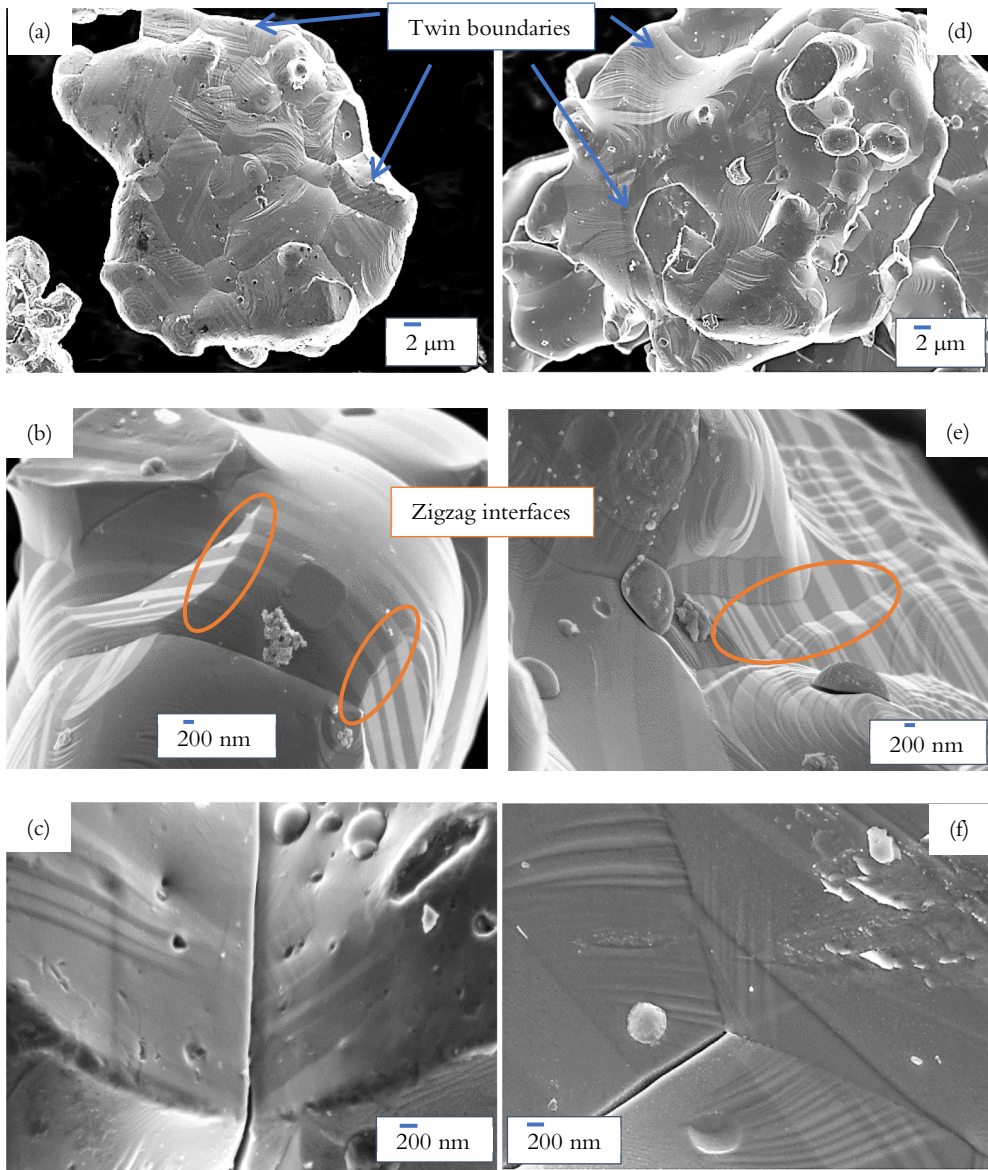


Figure 4.5-26: SEM images, at three different (increasing) magnifications, of the (a-b-c) 2CM24h820WQ powder batch and (d-e-f) the same batch after the short heat treatment at 500°C followed by slow cooling (2CM24h820WQ+ann4h500SC powder batch), of $\text{Ni}_{45.7}\text{Mn}_{36.9}\text{In}_{13.2}\text{Co}_{4.2}$ compound.

In light of this analysis, for providing a plausible interpretation of the increase of the hysteresis width, it is speculated that possibly the coarsening of twin boundaries, occurring to reduce the overall twin boundary energy [78,175], could in turn imply a higher frictional work for the collective rearrangement of the branched microstructure along the observed bending and grain-growth' steps of the surface. But it seems more reasonable to suppose that the change of the martensitic transformation temperatures and parameters is strictly dependent on the increase of long-range order of the austenite, achieved through the slow cooling rate, causing, via the increase of ferromagnetic order, a strengthening of the austenite at the expenses of the martensitic phase stability.

By comparing the SEM images of the 3CM29h820WQ powder (Fig. 4.5-21(c-d)) to those of the 3CM29h820WQ+ann4h500SC (Fig. 4.5-27(a-b)), it is possible to distinguish the presence of a certain graininess, as a sort of micro and nanoprecipitates, on the surface area of the latter sample. The EDX analysis has pointed out only a higher spatial compositional inhomogeneity for Mn (± 1.5 at.%) and In (± 1.2 at.%) elements as compared to the Ni (± 1 at.%) and Co (± 0.3 at.%) ones, which, however, is a common finding in the measured compositions of the annealed CM and wet PBM powders (see Table 7.4-3, Appendix). Therefore, with the sole compositional analysis the nature of the revealed microstructural difference cannot be clearly understood. Differently from the 2CM24h820WQ and the 2CM24h820WQ+ann4h500SC samples, the twin boundaries of the martensitic microstructure cannot be visualized since, as observed from the $M(T)$ measurements, the M_s is shifted to a temperature lower than RT.

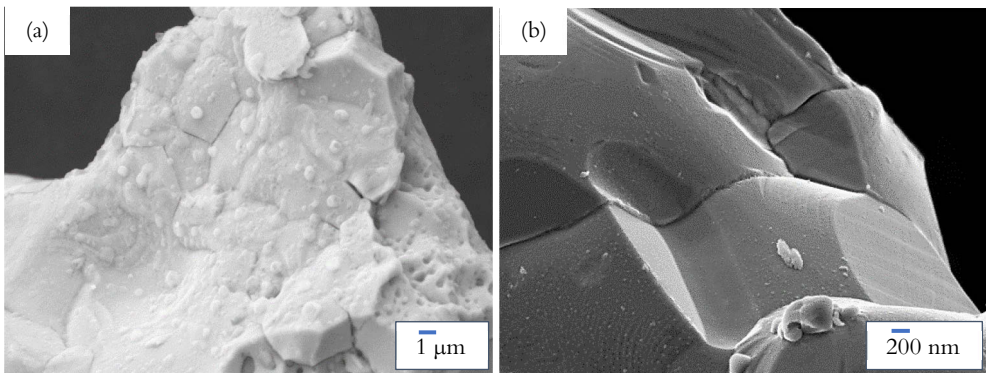


Figure 4.5-27: SEM micrographs showing the surface area (a) with SE detector at 15 kV, and (b) with InLens detector at 5kV, of two particles of the 3CM29h820WQ+ann4h500SC powder batch of $Ni_{45.7}Mn_{36.9}In_{13.2}Co_{4.2}$ compound.

It follows that, possibly, the notable differences in magnetic properties between the 3CM29h820WQ and 3CM29h820WQ+ann4h500SC powders (Figs. 4.5-25(a-b)) may be explained by taking into account also the onset of some compositional inhomogeneity, at a scale well below the spatial resolution of SEM-EDX analysis, other than the decrease of concentration of quenched-in vacancies and/or changes of configurational order, triggered by the selected annealing conditions.

Overall, the morphological analysis has pointed out the difficulty of identifying a single and well-defined microstructural feature that could uniformly explain the change of martensitic transformation characteristics. Such changes are most likely to be ascribed to the occurrence of different degrees of homogenization among the achieved batches of annealed powders. Nevertheless, by the SEM analysis it has been proved that the restoration of the MT is strictly interconnected to the processes of recovery, recrystallization, and grain-growth, taking place during the post-milling annealing treatments at high temperature and long time, which have to be adjusted for the different batches on the base of the milling time and energy. Further, it has emerged that an elongated and thin particle shape is more favourable for a faster recovery of the Heusler phase at a lower annealing temperature and/or time, avoiding the occurrence of sintering.

However, if on the one hand the presence of crystallographic imperfections, internal stresses and the increase of the interfacial energy over the volume term alter both the thermal hysteresis and the elastic energy storage, on the other one the martensitic transformation temperatures show an inverse dependence on the Curie transition temperature, thus decreasing when the ferromagnetic stability of the austenite increases. Therefore, rather than on peculiar compositional or microstructural features, at the micro and sub-micro-meter scale the thermal hysteresis of the particles is strictly connected to the surface-to-volume ratio and the degree of long-range $L2_1$ atomic order.

4.5.4 Summary of results for cryo-milled and wet planetary ball-milled powders

A systematic investigation of the evolution as a function of the annealing conditions of the characteristic martensitic parameters (ΔT_{elas} , ΔT_{hyst} , ΔM , T_{fwd} , M_S), Curie transition temperature (T_C^A) and ratio between the difference in the austenite Curie temperature and MT temperatures and the austenite Curie temperature ($\frac{(T_C - T_0)}{T_C}$) –(Table 7.4-2, Appendix)–, is illustrated and discussed hereafter.

With reference to Figs. 4.5-28(a)-(b), it can be observed the resulting trends for the Curie transition temperature as a function of the annealing temperature (left hand side) and for both the Curie transition and martensitic start temperatures as a function of the annealing time (right hand side). Hence, from Fig. 4.5-28(a), it emerges for both the CM and wet PBM powder batches a notable positive change in the Curie transition temperature only after an annealing treatment at a temperature above 725°C. This change can be ascribed to the onset of the structural transformation from a complete disordered $B2$ structure to a gradual recovery of the Heusler phase, with consequent enhancement of the long-range $L2_1$ atomic order [46].

By looking at Fig. 4.5-28(b), it is evident that the Curie transition temperature of the CM-2h powder is extremely sensitive to the increase of annealing time and presents a monotonic, non-linear increase in all the interval of time, with a more notable increase between 24–29 h. Whereas, for the wetPBM-3h the Curie temperature T_C^A does not reveal any significant dependence on the increase of annealing duration. For the CM-3h powder, instead, with the available data, it can be observed only a slight decrease between 24–29 h. For the same fixed annealing time of 24 h, it is interesting to note the vicinity of T_C^A values for the 3wPBM24h820WQ and 2CM24h755WQ samples and for the 2CM24h820WQ and 3CM24h820WQ powders. After 29 h of heat treatment at 820°C, instead, it is observed that the 3CM29h820WQ powder presents the same Curie temperature of the 3wPBM29h820WQ one.

The M_S temperature, instead, shows a steep linear increase for the CM-2h powder till 24 h of annealing at 820°C, after which a trend-inversion is observed. In contrast, the wetPBM-3h powder has a more gradual but constant increase in the range of 4–29 h of heat treatment at 820°C. Interestingly, for the CM-3h powder, in correspondence to the decrease of Curie temperature, between 24–29 h, an increase of M_S temperature is detected, as opposed to the behaviour of the CM-2h powder.

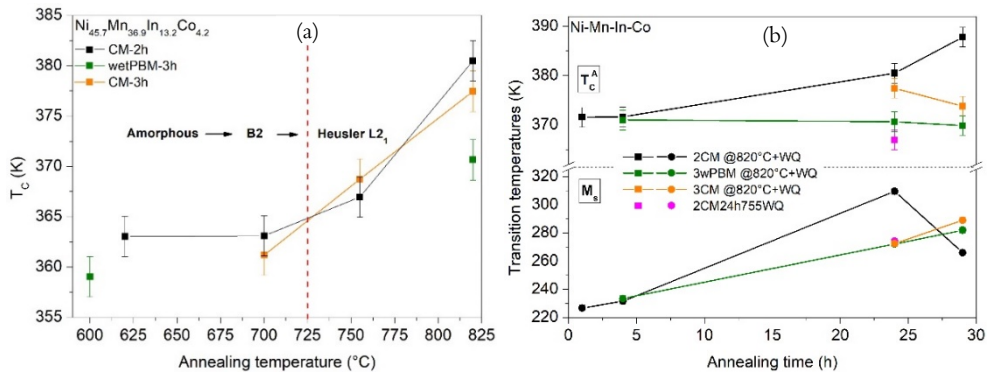


Figure 4.5-28: Phenomenological trends of (a) Curie transition temperature as a function of the annealing temperature and (b) Curie and martensite start temperatures as a function of annealing time, for the CM and wet PBM powders of $\text{Ni}_{45.7}\text{Mn}_{36.9}\text{In}_{13.2}\text{Co}_{4.2}$ compound.

As highlighted in Figs. 4.5-29(a)-(b), also the maximum magnetization value of the austenite at the martensitic start temperature ($M(M_s)$) and the hysteresis width (ΔT_{hyst}) across the transformation, for the CM-2h powder, have a strong dependence on the annealing time, showing a linear decrease up to 24 h and a subsequent abrupt increase for a longer annealing of 29 h at 820°C. Differently, for the other two batches, the identification of some trends is not straightforward. Nevertheless, it has been noticed as a common feature, in the case of increasing the annealing time at the fixed annealing temperature of 820°C, that as long as the M_s increases the thermal hysteresis and the saturation magnetization of the austenite decrease.

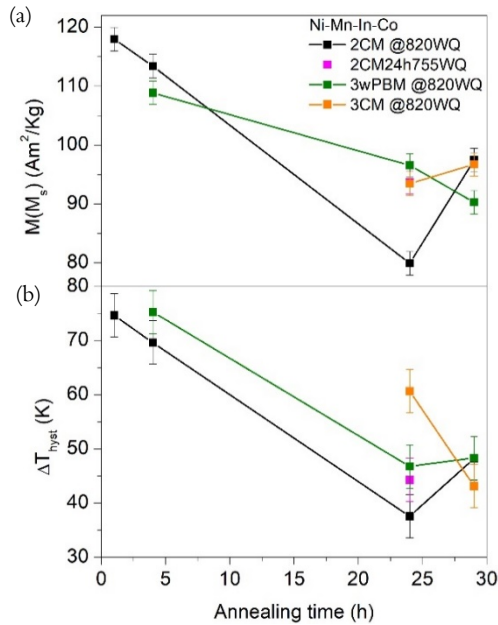


Figure 4.5-29: Dependence on the annealing temperature of (a) the magnetization of the austenite at the martensitic start temperature ($M(M_s)$) and (b) the thermal hysteresis across the martensitic transformation for the CM and wet PBM powder batches of $\text{Ni}_{45.7}\text{Mn}_{36.9}\text{In}_{13.2}\text{Co}_{4.2}$ compound.

From the thermomagnetic results of the different annealed CM-2h powder batches (Fig. 4.5-18(a)), it has been also possible to highlight the dependence of both the transformation temperature range in heating ($A_f - A_s$) and the percentage of magnetic susceptibility change across the reverse martensitic transformation on the increase of annealing temperature, as reported in Fig. 4.5-30. It is worth stressing that the temperature difference ($A_f - A_s$) has been taken as an indicator of the amount of elastic energy storage during the martensitic transformation, in accordance to what reported in literature [82,94,95], while the susceptibility change (%) as a probe for qualitatively determining the fraction of transformed austenitic phase.

It is evident that for temperatures below 725°C , a large elastic energy storage and a low variation of the magnetic susceptibility signal are detected, pointing out an almost suppressed (unrecovered) martensitic transformation. This behaviour is ascribable to the difficulty to form and move the austenite-martensite phase interface (habit-plane) in presence of configurational and lattice disorder, caused by an incomplete reordering and defects' annihilation process (as previously revealed by the SEM images) under a low thermal energy supply. Likely, this can promote only the structural

transformation from an amorphous to a *bcc* structure. Therefore, it is only after annealing at temperature above 750°C that it is possible to recover the martensitic transformation, thanks to a gradual restoration of the long-range $L2_1$ atomic order. It is interesting to observe that for the powder annealed for 24 h at 755°C the susceptibility change is maximum while the elastic energy stored minimum. On further increasing the annealing temperature to 820°C, for the same fixed annealing duration of 24 h, the transformation behaviour worsens, as highlighted by the significant increase of $(A_f - A_s)$, hence decrease of transformation sharpness and the slight reduction of susceptibility change. This is in contrast with the trend observed for T_C , where its value increases by increasing the annealing temperature (Fig. 4.5-28(a)).

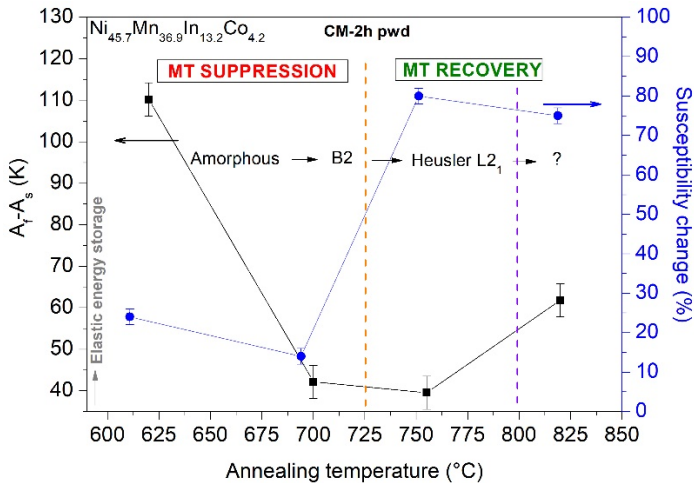


Figure 4.5-30: Dependence of the martensitic transformation temperature range ($A_f - A_s$) on heating and of the normalized susceptibility change on the annealing temperature, for the CM-2h powder batches of $\text{Ni}_{45.7}\text{Mn}_{36.9}\text{In}_{13.2}\text{Co}_{4.2}$ compound.

The combination of all the exposed results for the CM and wet PBM powders leads to the following considerations. The Curie transition temperature and the martensitic transformations features are strongly dependent on the annealing conditions, but they follow two distinct, or even opposite, trends with the annealing time for a fixed annealing temperature ($T > 750^\circ\text{C}$). Hence, the heat treatments can apport significant microstructural, morphological, and atomic ordering variations,

affecting the stabilization of the martensite, which is non-trivially controlled by the restoration of atomic order and the increase of ferromagnetism of the austenite. In this respect, the detected positive change of T_C by increasing the annealing temperature agrees with what has been reported in literature by D. Salas *et al.* [96] for secondary annealing treatments performed on Ni-Mn-In-Co bulk alloys. Following the authors' argument, this fact can be connected to the higher concentration of thermal vacancies, which, enabling the few atomic jumps between Mn and In sublattices, could accelerate the ordering kinetics during quenching, leading to an increase of the $L2_1$ -like ordering.

However, it can be likely supposed that, in the current study, a higher amount of retained disorder such as quenched-in vacancies may have been obtained for the fine particles, due to the faster heat-exchange as compared to the bulk pieces, and, in turn, this may have caused some complex and non-predictable changes of the degree of atomic order.

In order to extrapolate a general picture of the behaviour of the examined powder batches in relation to the degree of atomic order, it has been calculated the corresponding $\frac{(T_C-T_0)}{T_C}$ parameter (Table 7.4-2, Appendix), where T_C is the Curie transition of the austenite and T_0 the equilibrium temperature between austenite and martensite phases, defined as $T_0 = \frac{A_f+M_s}{2}$. Indeed, many authors [72,82,153,155] have reported of a direct proportionality of this parameter with the degree of $L2_1$ atomic order and they have employed it to draw and discuss the trends of the martensitic transformation characteristics for bulks and ribbons Ni-Mn-(Co)-In and Ni-Mn-(Co)-Sn Heusler compounds, annealed in different conditions.

Since the magnetic exchange interactions (FM/AFM) are strongly influenced by the configurational order and by the Mn-Mn interatomic distances through the RKKY-type oscillatory coupling, an increase or decrease of the degree of order changes the distribution of Mn atoms in the unit cell and the stability of the ferromagnetic austenite phase. This in turn affects the temperatures and magnetic properties of the martensitic phase, due to the diffusion-less character of the transformation.

In Fig. 4.5-31, by reporting the values of $\frac{(T_C-T_0)}{T_C}$ parameter as a function of the annealing time, it has been possible to find out same results for the batches of CM and wet PBM powders presenting similar morphological/microstructural features, such as the GS/t ratio, the particle shape and/or the degree of sintering between particles. Thereby, there have been drawn four areas, characterized by different colours, to separate the batches with comparable $\frac{(T_C-T_0)}{T_C}$ parameters, which have also shown similarities in their magneto-structural martensitic behaviours. For

comparison, there have been also added the $\frac{(T_C-T_0)}{T_C}$ parameters corresponding to the HG2h820SC, HG4h820SC and HG4h820WQ samples (Table 4.2-6).

Interestingly, it can be noted that the trends of $\frac{(T_C-T_0)}{T_C}$ with the annealing time, fixing the annealing temperature of 820°C, for the CM and PBM powder batches follow a dependence similar to that of the thermal hysteresis (Fig. 4.5-29(b)). The highest achieved $\frac{(T_C-T_0)}{T_C}$ values, in the range of 0.28-0.32, are referred to the batches annealed for a short time, which have shown significant differences with respect to the expect transformation behaviour, as for instance the shift to lower temperatures of M_s (Fig. 4.5-28(b)) and the interruption of MT below 150 K. The lowest $\frac{(T_C-T_0)}{T_C}$ values, 0.14-0.18, are, instead, associated to the 2CM24h820WQ and 3CM29h820WQ (with $d < 66 \mu\text{m}$) samples, which have presented the largest broadening of MT, but also the lowest values of thermal hysteresis. The middle narrow interval 0.18-0.22 of $\frac{(T_C-T_0)}{T_C}$ corresponds to the powders that reveal the best recovery of the martensitic transformation, in terms of the largest net magnetization change ΔM across the transformation, the lowest ΔT_{elas} and forward and reverse martensitic temperatures as close as possible to the HG4h820WQ powder. It is important to notice that large values of $\frac{(T_C-T_0)}{T_C}$ have been found for both the HG820SC and 2CM29h820WQ samples, present similar T_C^A , M_s and A_f temperatures (Table 7.4-2, Appendix).

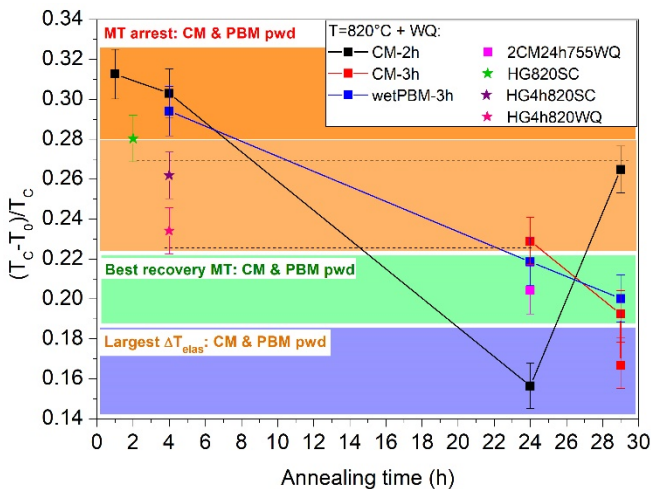


Figure 4.5-31: Dependence of the normalized temperature difference ($\frac{T_C-T_0}{T_C}$) on the annealing duration for CM-2h, CM-3h, wetPBM-3h and HG powders annealed at 820°C and/or 755°C, of $Ni_{45.7}Mn_{36.9}In_{13.2}Co_{4.2}$ compound.

To better understand the relation between similar $\frac{(T_C-T_0)}{T_C}$ parameters and the corresponding transformation behaviours of the powder batches, there have been drawn the graphs of Figs. 4.5-32(a-b)-(c-d).

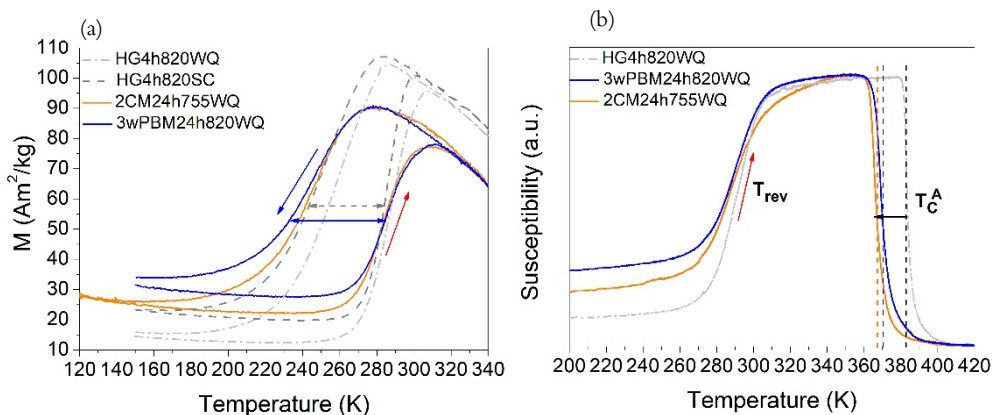
In Fig. 4.5-32(a), it is noted that the 2CM24h755WQ and 3wPBM24h820WQ powders present an almost identical M(T) curve, with the difference of a slightly larger thermal hysteresis and magnetic moment at low temperature for the latter one. Moreover, in Fig. 4.5-32(b), it emerges that the Curie transition temperature has a comparable value between the two samples. With respect to the HG4h820WQ and HG4h820SC powders, it is observed a similarity in the martensitic transition temperatures, especially for M_s and A_s , even though the $\frac{(T_C-T_0)}{T_C}$ values and Curie temperatures are lower (Table 7.4-2, Appendix). It is worth stressing that also from the morphological point of view the 2CM24h755WQ and 3wPBM24h820WQ powders have shown a notable correspondence, as for instance in particle size distribution and grain microstructure. Then, it is supposed that the slightly lower thermal hysteresis for the 3wPBM24h820WQ powder is linked to the lower average particle length and thickness, in analogy to what has been observed for the HG powders, annealed for 4 h at 500°C, by decreasing the particle size (see Fig. 4.2-24(b) and Table 4.2-5).

In Figs. 4.5-32(c)-(d), instead, there are reported the M(T) curves of the three types of ball-milled powders after the same annealing treatment for 29 h, at 820°C, followed by water quenching. It is noticed that the behaviour of the 3CM29h820WQ powder is identical to that of the 3wPBM29h820WQ one, with the only evidence for the latter powder of a decrease of both the saturation magnetization and Curie temperature of the austenite. In contrast, the 2CM29h820WQ powder shows a significant shift forward of the Curie temperature and conversely a decrease of the martensitic transformation temperatures, which is also accompanied by an enlargement of the hysteresis width and a notable increase of the magnetic moment at the martensitic finish temperature. Such magneto-structural behaviour differs significantly to that of the HG4h820SC powder, even though the two powder batches have shown nearly the same value of $\frac{(T_C-T_0)}{T_C}$ parameter (Fig. 4.5-32(d)).

Therefore, it follows that for the post-milling annealed powders the increase of $\frac{(T_C - T_0)}{T_C}$ parameter is not related to the recovery of the martensitic transformation as close as possible to that of the coarse-grained and bulk counterparts, but only to a gradual restoration of the Curie temperature. However, for the powders associated with a $\frac{(T_C - T_0)}{T_C}$ parameter (0.28-0.32) much higher than the bulk (0.27), both the martensitic and Curie transformation temperatures have appeared significantly decreased, thus reflecting a non-direct and non-monotonic dependence on the degree of $L2_1$ atomic order.

Furthermore, with reference to Fig. 4.5-32(c), it is worth noting that for the three powders annealed for 29 h at 820°C the martensitic transformation both in heating and cooling branch appears less sharp than that of the powders annealed for a lower annealing time (24 h instead of 29 h) and/or at a lower annealing temperature (755°C rather than 820°C) (Fig. 4.5-32(a)). Since they all have shown the formation of bamboo-like grains due to the sintering phenomenon, the increase of transformation broadening could be ascribed to the specific microstructural change. Indeed, most probably, the increase of surface bending may have caused the increase of elastic strain energy and lattice stress for the twinning mechanism [180].

In addition, the same value of thermal hysteresis observed for the particles of 3CM29h820WQ and 3wPBM29h820WQ powders could be ascribed to the similar size (of few microns) and shape of the constituent grains, even though the overall particle morphology is substantially different (porous and multi-grains structures of 200 μm length for the former batch; single-crystalline particles of 5 ± 4 μm length and 2 μm thickness, for the latter one).



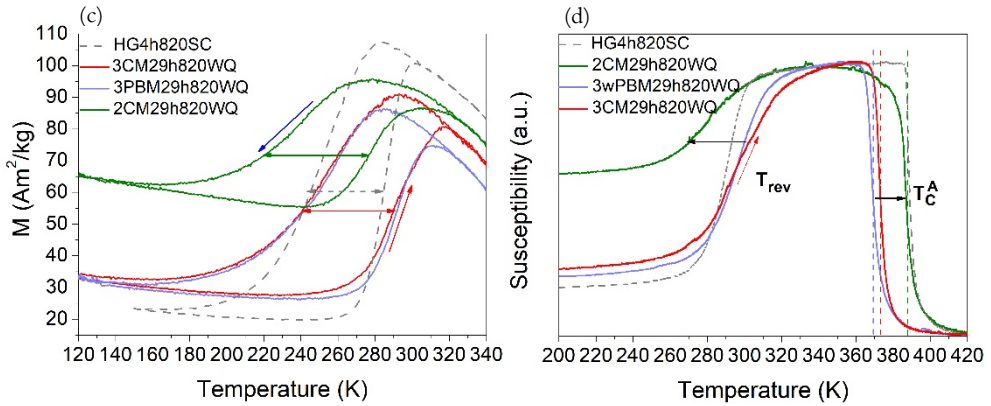


Figure 4.5-32: Temperature-dependence of (a) magnetization (at applied magnetic field of 1 T) and (b) magnetic susceptibility measurements of the post-annealed CM and PBM powders presenting a $\frac{(T_C - T_0)}{T_C}$ value of 0.21–0.22 close to the one of hand-grinded powder annealed at 820°C and then water-quenched (HG4h820WQ). Comparison between (c) the $M(T)$ and (d) $\chi_m(T)$ curves of the 2CM29h820WQ powder and the two batches offhand-grinded powders annealed at 820°C and then slowly cooled, showing similar $\frac{(T_C - T_0)}{T_C}$ parameter of 0.26–0.28.

The combination of all the exposed results, for bulk and post-annealed HG, CM and wet PBM powders, has led to the identification of some general trends, as summarized in Figs. 4.5-33(a-b). It emerges that the martensitic start temperature (M_S) has a linear decrease with the $\frac{(T_C - T_0)}{T_C}$ parameter, for both the post-annealed ball-milled and HG powders (Fig. 4.5-33(a)). By plotting the thermal hysteresis (ΔT_{hyst}) versus M_S , for the post-annealed CM-2h powders it can be noted a linear decreasing trend. The post-annealed HG ones, instead, show a nearly constant value of $\Delta T_{hyst} = 36 \pm 5$ K. Nevertheless, all the types of ball-milled powders, presenting a M_S temperature between 365–310 K, show approximately the same thermal hysteresis of 46 ± 5 K. Besides, this constancy is observed also in the range 0.15–0.29 of the $\frac{(T_C - T_0)}{T_C}$ parameter. By contrast, for higher values of this parameter, the thermal hysteresis has a notable increase.

These results confirm that the recovery and the change of the martensitic characteristics are strongly governed by the microstructural and atomic ordering variations. Moreover, when the martensitic transformation is shifted to lower temperatures the propagation of the martensitic phase becomes more difficult, leading to both the increase of hysteresis losses and the “kinetic arrest” below 150 K. This

phenomenon is also typical for bulk Ni-Mn-In-Co compounds, as reported in literature under the name of “freezing behaviour”, but it is still unclear the origin of such a low mobility of the habit planes [95,151,169,170].

Overall, it has been pointed out that, regardless of their morphology after the annealing treatments, the ball-milled particles, which recover the martensitic transformation at temperatures close to the expected ones, present the same thermal hysteresis. The best recovery has been observed for those powders characterized by a $\frac{(T_C-T_0)}{T_C}$ parameter in the narrow range of 0.20-0.22.

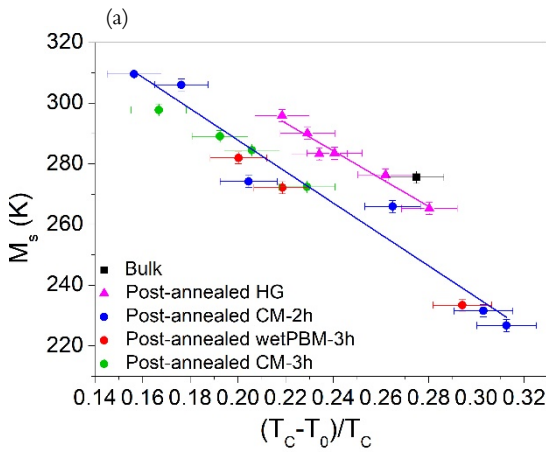
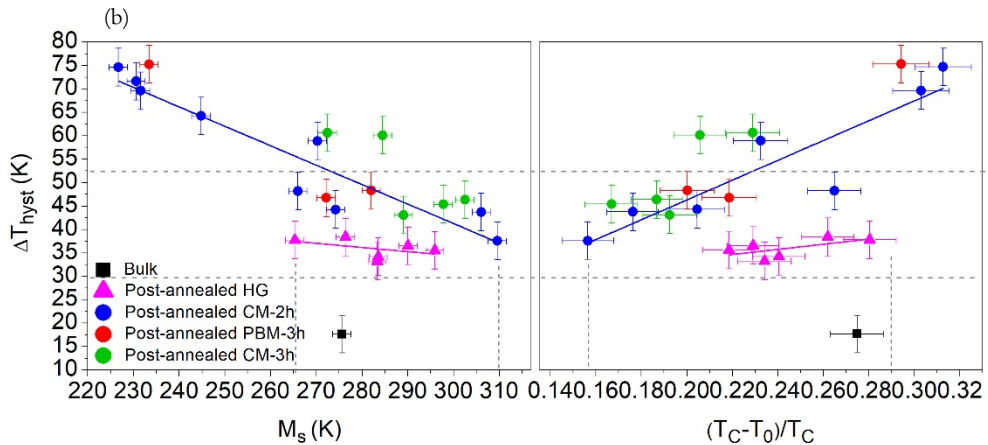


Figure 4.5-33: (a) $\frac{(T_C-T_0)}{T_C}$ -dependence of the martensite start temperature (M_s), for bulk, post-annealed HG, CM and wet PBM powder samples of $Ni_{45.7}Mn_{36.9}In_{13.2}Co_{4.2}$ compound. (b) Thermal hysteresis as a function of M_s and $\frac{(T_C-T_0)}{T_C}$.



To confirm the presence of austenite at low temperatures for the particles presenting the transformation arrest, temperature dependent XRD measurements

have been carried out, collecting them at 340 K, 240 K, 100 K and 20 K, for the 2CM24h7455WQ, 2CM1h820WQ and 2CM29h820WQ samples.

In Fig. 4.5-34, it is visualized that well above room-temperature the XRD patterns of all the batches show the characteristic fundamental reflection A(202) of the cubic *fcc* austenitic structure, with lattice constant $a = 0.59979 \pm 0.00008$ nm. By decreasing the temperature, the intensity of the austenitic peak decreases for the 2CM24h755WQ and 2CM29h820WQ samples, especially for the former one, and meanwhile new peaks appear at both sides of the fundamental cubic reflection, due to the occurrence of the martensitic transformation. The reflections of the martensitic phase have been identified with the monoclinic distorted 7M modulated structure. For the 2CM1h820WQ, due to the lower M_s temperature, the new reflections are visible only on further decreasing the temperature to 100 K, at which, for the other two batches, the amount of austenitic phase decreases and conversely the intensity of the martensitic 7M reflections increases. Moreover, it can be noted a rightward shift of the peak at $2\theta = 20^\circ$, due to the thermal contraction of the cell. On cooling the temperature down to 20 K, the diffraction patterns do not show any significant variation with respect to those at 100 K, for all the powder batches. Hence, the martensitic transformation is stopped close to 100 K. However, for the 2CM24h755WQ powder the martensitic reflections are well-distinguishable from the austenitic peak, which is almost suppressed, thus denoting that only a small trace of untransformed cubic austenite is retained at low temperatures. By contrast, for the other two samples, the austenitic reflections are still intense, while those of the martensite remain low, especially for the powder annealed for a short time.

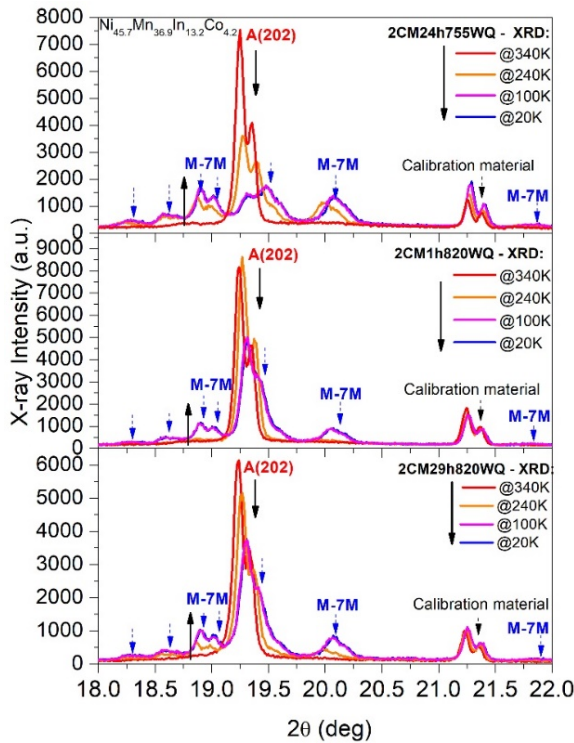


Figure 4.5-34: Evolution of the XRD patterns on decreasing the temperature from 340 K to 20 K for the three differently annealed batches of CM-2h powder of $\text{Ni}_{45.7}\text{Mn}_{36.9}\text{In}_{13.2}\text{Co}_{4.2}$ compound.

This result clearly points out that a higher fraction of the parent phase is not transformed even at very low temperatures in the 2CM29h820WQ and 2CM1h820WQ samples, which then can be correlated to the higher ferromagnetic signal detected in the thermo-magnetization measurements.

In order to highlight possible differences in the degree of atomic order responsible for the shift to lower temperatures of the M_S , it has been compared the normalized intensity of the three XRD patterns, collected at 300 K, in the 2θ range where the $L2_1$ superstructure reflections A(111) and A(113) usually appear. As shown in Fig. 4.5-35, the superlattice A(111) peak is detectable for all the batches around $2\theta = 11.75^\circ$, while the A(113) one, at $2\theta = 22.6^\circ$, has a negligible intensity. Interestingly, by comparing the peak intensity $I(111)$ normalized to the $I(202)$, it has emerged only a slightly higher value for the 2CM29h820WQ powder (0.0398) as compared to the ones of 2CM24h755WQ (0.0337) and 2CM1h820WQ (0.03210) samples.

Therefore, on the basis of these results, it is difficult to clearly recognize substantial differences in the degree of atomic order, at least between the 2CM24h755WQ and 2CM1h820WQ samples, which have also shown only a slight variation in the Curie transition temperature.

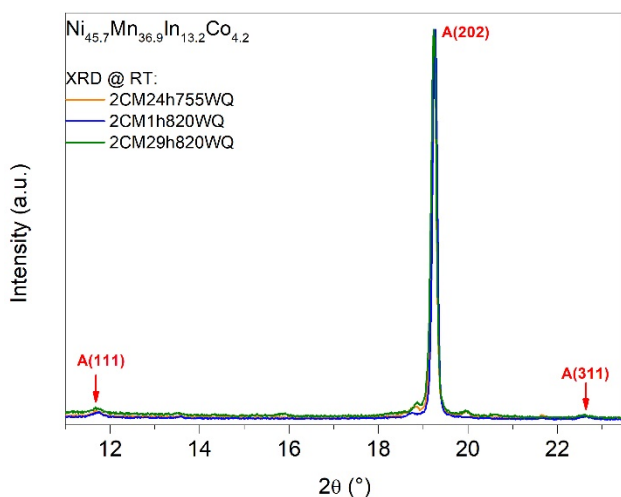


Figure 4.5-35: (a) and (b) Comparison between the XRD patterns collected at 340 K of the three differently annealed batches of CM-2h powder of $\text{Ni}_{45.7}\text{Mn}_{36.9}\text{In}_{13.2}\text{Co}_{4.2}$, over two different 2θ ranges.

4.5.5 A two-steps process: Cryo-milling + wet Planetary ball-milling

The possibility to achieve nanoparticles of Ni-Mn-In-Co compound by using the top-down ball-milling technique has been assessed also investigating the effect of combining a first short cryo-milling process with a subsequent longer planetary ball-milling one.

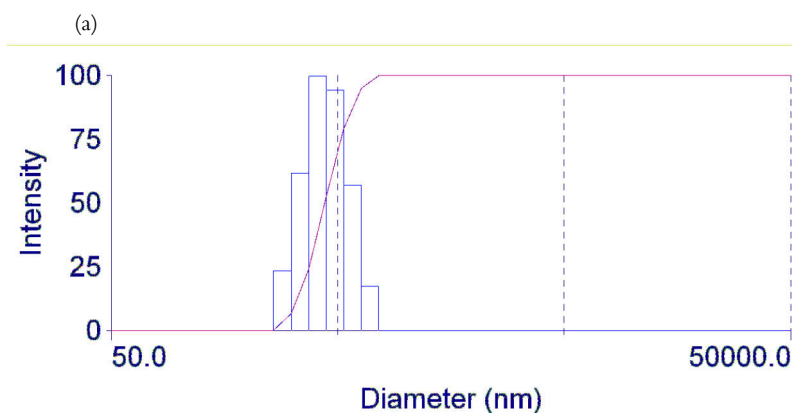
Therefore, the powder of $\text{Ni}_{45.7}\text{Mn}_{36.9}\text{In}_{13.2}\text{Co}_{4.2}$ compound, subjected to 3 h of CM process (4.5.3), were transferred in a jar of Zirconia to perform the PBM process (4.5.2), selecting a 10:1 ball-to-powder weight ratio and adding isopropanol as the liquid milling medium, to avoid agglomeration between particles and

overheating of the system. The procedure was conducted at the rotational speed of 300 rpm, in intervals of 10 min milling and 5 min rest, for a total effective milling time of 35 h (Table 4.5-4).

Sample: $\text{Ni}_{45.7}\text{Mn}_{36.9}\text{In}_{13.2}\text{Co}_{4.2}$		Milling time (h)	Annealing temperature (°C)	Annealin g time (h)	Cooling rate	Corresponding name
Cryo- milled (CM)	+ Planetary ball-milled with isopropanol (wet PBM)	3 + 19	- 820	- 24	- WQ	19wPBM(3CM) 19wPBM(3CM)24 h820WQ
		35	-	-		35wPBM(3CM)

Table 4.5-4: Details of the milling procedure, annealing conditions and corresponding name of the two-steps processed powder of $\text{Ni}_{45.7}\text{Mn}_{36.9}\text{In}_{13.2}\text{Co}_{4.2}$ compound.

The as-received solutions of 19wPBM(3CM) and 35wPBM(3CM) powders were subjected to sonication and centrifugation, in order to separate the suspension from the remanent part, containing the bigger particles. Then, by means of DLS measurements (3.2.3), it was qualitatively assessed the presence of nano-meter sized particles in the suspension. The investigations highlighted the presence of particles with size below 500 nm in both the batches, as shown in Figs. 4.5-36(a)-(b).



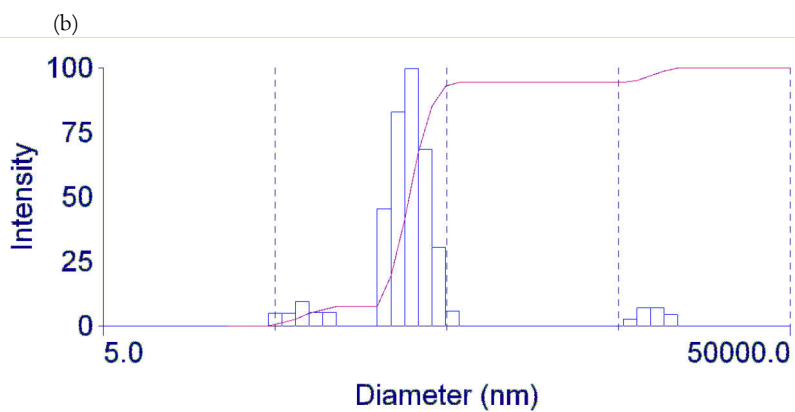


Figure 4.5-36: Multimodal size distribution of the (a) 19wPBM(3CM) and (b) 35wPBM(3CM) powder batches of $\text{Ni}_{45.7}\text{Mn}_{36.9}\text{In}_{13.2}\text{Co}_{4.2}$ compound, obtained by DLS analysis.

Hence, by TEM analysis (3.2.4), it was studied the effective particles' dimensions and chemical composition of the 35wPBM(3CM) sample. As shown in Figs. 4.5-37(a-d), the particles of the suspension have an irregular shape and a size ranging from several hundreds to several tens of nano-meters. Moreover, the obtained selected area electron diffraction (SAED) pattern, shown in Fig. 4.5-38, points out the presence of both continuous rings and single spots, which reveals that the particles of hundreds of nano-meters are clusters, whose units are single-crystals of few nano-meters. The microanalysis, instead, has denoted that the stoichiometric elements have a different spatial distribution in the particles, as for instance recognizable by comparing the colour maps of Fig. 4.5-39, which refer to the chemical distribution of each type of atoms in the particle of Fig. 4.5-37(a). It can be seen that none of the elements between Ni, Mn, Co and In is homogeneously distributed and further they present a different spatial distribution. This is clearly visible for Ni and Mn atoms which are accumulated in correspondence of the brighter areas of Fig. 4.5-37(a), while In atoms are almost totally lacking in regions where the concentration of the other three elements, especially of Ni and Mn atoms, is high. In contrast, the Co atoms appear more homogeneously distributed. Similar results have been obtained also for other examined particles. Therefore, these outcomes reveal, as a general feature, the existence of chemical inhomogeneity at the nanoscale, which, likely, derives directly from the method of preparation and homogenization of the starting bulk material. It is important to stress that this fact agrees with the compositional results, by EDX analysis, of the CM-2h annealed powders. Thereby, it is supposed that by decreasing

the particle size, on increasing the milling duration, the effect of chemical inhomogeneity, existing at the nanoscale, arises and plays a fundamental role, together with the induced atomic disorder, in changing the lattice parameters and the phase transitions' mechanism. A way to reduce the gradients of concentration and overcome the microstructural barriers is through the atomic diffusion and redistribution, which, indeed, can justify the need to perform long annealing treatments at high temperature for recovering the Heusler phase.

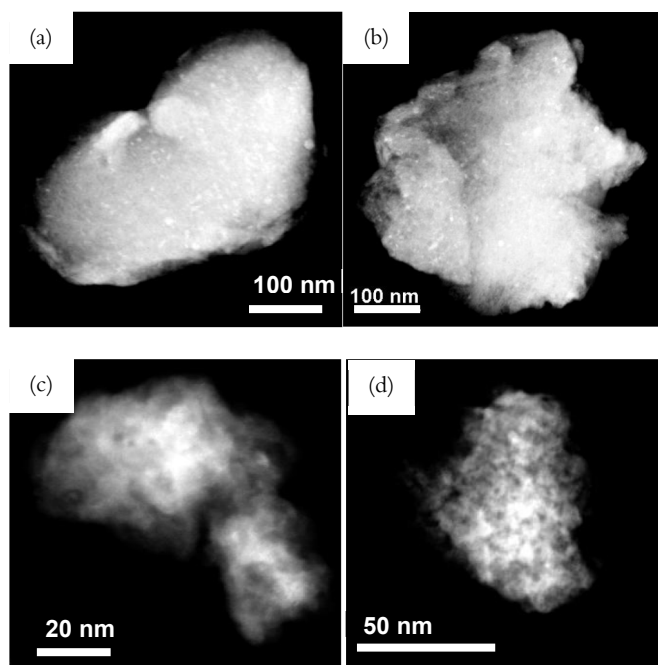


Figure 4.5-37: TEM images of the centrifuged particles of the batch of $\text{Ni}_{45.7}\text{Mn}_{36.9}\text{In}_{13.2}\text{Co}_{4.2}$ CM-3h powder planetary ball-milled with isopropanol for 35h, showing a size of 400-500 nm in (a-b) or smaller, of 30-90 nm, in (c-d).

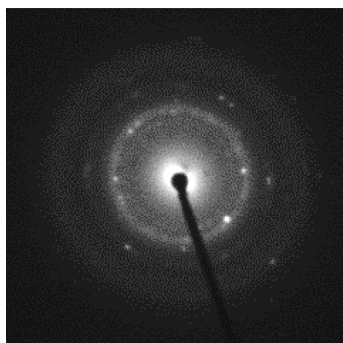


Figure 4.5-38: SAED pattern of one as-milled centrifuged particle of the batch of $Ni_{45.7}Mn_{36.9}In_{13.2}Co_{4.2}$ powder PBM for 35h with isopropanol, showing rings and spots.

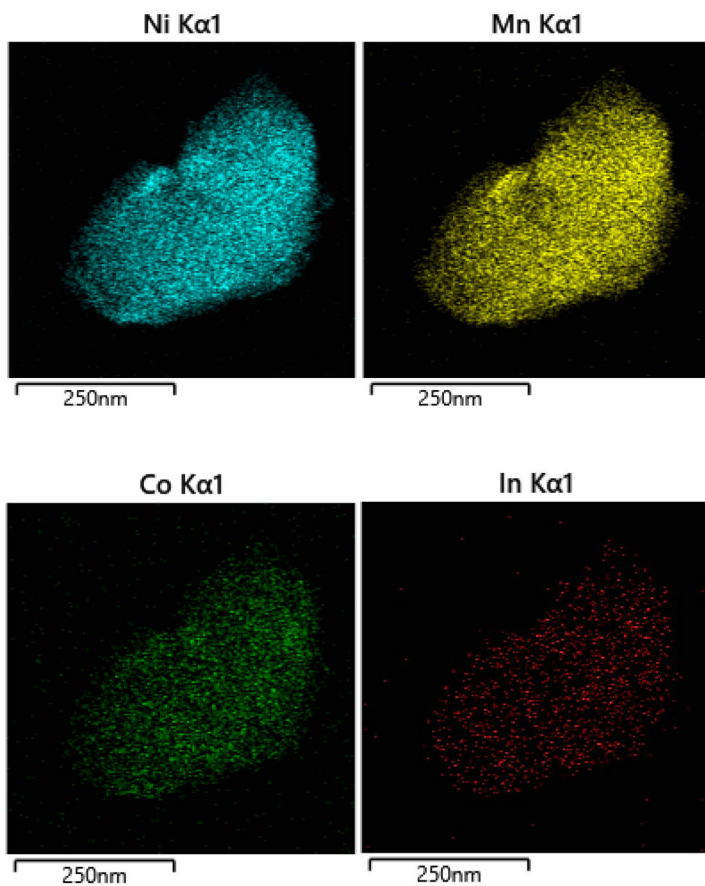
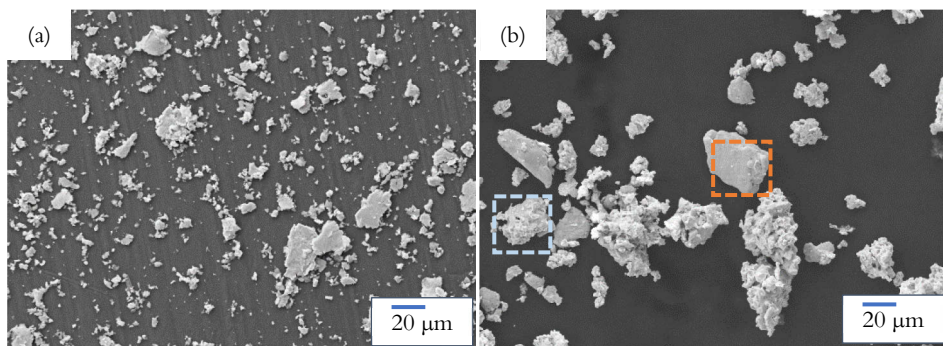


Figure 4.5-39: Compositional maps showing with different colour the distribution of each element, namely Ni, Mn, In, Co, of the phase in the particle shown in Fig. 4.3-45(a).

For the 19wPBM(3CM) powder, the recovery of the original composition, Curie and martensitic phase transitions has been investigated by performing the heat treatment at 820°C for 24 h followed by water quenching (Table 4.5-4), as performed for the other CM and wet PBM powder batches of $\text{Ni}_{45.7}\text{Mn}_{36.9}\text{In}_{13.2}\text{Co}_{4.2}$. In Figs. 4.5-40(a)-(b), there are compared the SEM images of the as-milled particles, on the left, and of the post-annealed ones, on the right. It is evidenced that the morphology of the particles is changed after the annealing, basically due to the occurrence of agglomeration, sintering and grain-growth phenomena, which prevent the separation between particles and the achievement of a quantity of sub-micron and nano-meter sized particles, instead obtained in the as-milled batch. Moreover, by zooming on the post-annealed 19wPBM(3CM)24h820WQ particles, as shown in Figs. 4.5-40(c)-(d), it is possible to distinguish between different degrees of recovered and recrystallized microstructures, depending on the specific particle size and shape. It is supposed that the smallest ones, presenting a higher surface-to-volume ratio, have reasonably a higher driving force (superficial energy) for the annihilation of point defects and dislocations rearrangement as compared to the thicker ones. This leads to a faster recovery process and then to a strong solid-state reaction, leading to coalescence of many submicron meter grains as visible in Fig. 4.5-40(c), by increasing the annealing time. Instead, for larger micro-meter sized particles, the grains contain a higher concentration of dislocations resulting in a rough and inhomogeneous surface area, as shown in Fig. 4.5-40(d).



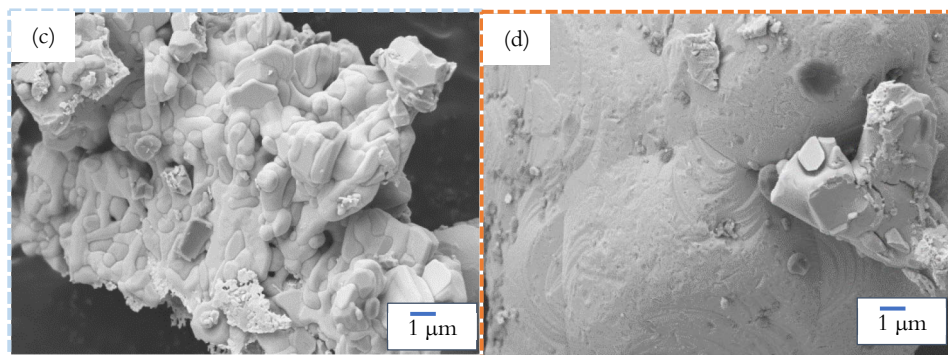


Figure 4.5-40: SEM images of (a) the as-milled 19wPBM(3CM) particles and (b) after the annealing for 24h at 820°C. (c) and (d) zoom on two different morphology and microstructure identified among the batch of post-annealed particles.

Accordingly, the attained non-optimal recovery and homogenization processes can explain and support the results of the thermomagnetic analysis. As visible in Fig. 4.5-41, for the 19wPBM(3CM)24h820WQ sample no traces of the reverse martensitic transformation on heating and only a Curie transition occurring in a broad temperature range can be detected. For comparison, there have been reported also the achieved curves of the batches of CM-3h powder annealed at the same temperature and time conditions with (3CM+Alumina24h820WQ) or without Alumina (3CM24h820WQ), or heat treated at a lower temperature (3CM24h755WQ) or for a longer time (3CM29h820WQ). The best recovery in terms of sharpness of both the martensitic transformation and the magnetic Curie transition is observed only after annealing for 29 h at 820°C.

Therefore, it exists a strong interrelation between the higher amount of disorder and particle size reduction, due to the increase of milling time, and the requirement of an annealing treatment for a duration longer than one day, at a temperature above or equal to 820°C, and in absence of external constraints.

These experimental results imply that for the quaternary Ni-Mn-In-Co compound, at least with the top-down method of ball-milling technique and subsequent thermal treatments, is tricky or even impossible to control the preparation of monodisperse nanoparticles with homogeneous composition and possibility to recover the expected magnetic and magneto-structural properties. On the contrary, these latter appear to be already drastically and irreversibly worsened with respect to the bulk and coarser-grained counterparts' ones in ball-milled particles at the micro and sub-microscale.

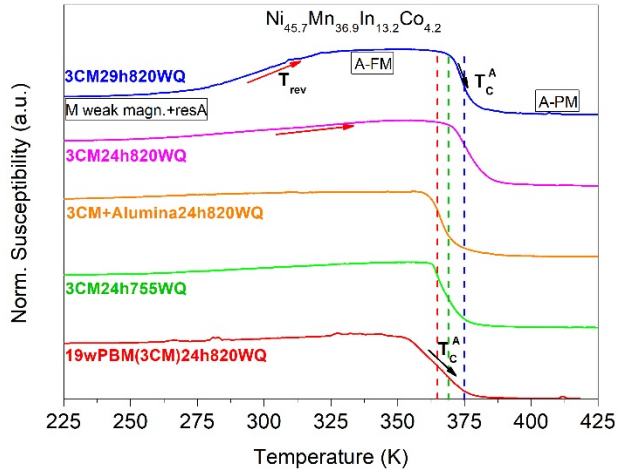


Figure 4.5-41: Comparison between the magnetic susceptibility measurements as a function of temperature for the annealed two-steps processed powder (19wPBM(3CM)24h820WQ) and the batches of CM-3h particles annealed in different conditions of temperature and/or time.

5 SUMMARY & COMPARISON OF THE MAIN RESULTS

In this chapter there are derived some general considerations on the properties of the particles obtained by the ball-milling techniques, with a cross-comparison of the behaviour of each investigated Heusler compound, under the same milling parameters and the applied thermal treatments to recover the magneto-structural phase transition.

The whole investigation on the hand-grinded and ball-milled particles has pointed out, as a general consideration, that Ni-Mn-In-Co Heusler compound presents a significantly different response to the mechanical stresses and induced plastic deformations as compared to the Ni-Mn-Ga and Ni-Mn-Cu-Ga ones. This has led to a different morphological and structural evolution of the achieved particles.

The former compound exhibits a very poor compressive strength and the onset of large plastic deformations leading to a rapid fracturing of the bulk fragments into (tendentially) isotropic and small micro-meter sized pieces, by hand grinding and ball-milling, at cryo-genic temperatures and/or in dry conditions.

Differently, Ni-Mn-(Cu)-Ga compounds can tolerate higher strains and deform elastically thanks to a better accommodation of the stresses through the martensitic variants' reorientation.

It results that after the same fixed milling parameters, as for instance 3 h of cryo-milling process, the particles of Ni-Mn-In-Co have a lower mean particle size and a high tendency to agglomerate, while the Ni-Mn-Cu-Ga ones show a higher length-over-thickness ratio due to the exfoliation-like deformation, a final more uniform and narrow size distribution, and any evidence of particles' aggregation even during long dry milling processes.

Accordingly, on increasing the milling time, the atomic disordering process and the cold-welding are the key-issues governing the final morphology, structure, and microstructure of the Ni-Mn-In-Co particles.

The amorphization of these particles can be avoided, for instance, by adding a solvent as liquid milling medium and selecting a moderate milling energy (10:1 ball-to-powder weight ratio; 300 rpm rotational speed) during the milling process in a planetary ball-mill. On the contrary, in order to increase the fracture rate and overcome the tendency of the Ni-Mn-Ga and Ni-Mn-Cu-Ga particles to deform laterally, an increase of the milling energy is required, such as a longer milling time

and/or higher rotational speed. Interestingly, it has been observed that the addition of a surfactant (oleic acid) other than a solvent during the planetary ball-milling process at moderate rotational speed can speed up the particle size reduction towards the sub-micro/nanoscale, maintaining them dispersed.

Apart from the differences in morphology and mechanical deformation processes, the structural and magnetic characterizations of the hand-grinded and as-milled particles of Ni-Mn-In-Co, Ni-Mn-Ga and Ni-Mn-Cu-Ga have highlighted some common, specific features of the martensitic phase structure.

For instance, it has been observed that the martensitic phase exists in the tetragonal non-modulated structure under the application of mechanical stress, while it presents the characteristic 7M modulated phase after the application of a suitable thermal treatment. The treatment must be performed at a tailored temperature to release the internal mechanical stresses, without creating additional configurational disorder or triggering the phase segregation phenomenon. This is, in fact, typical of the off-stoichiometric Heusler compositions containing excess of Mn atoms and/or Co impurities, and it is strongly dependent on the introduction of further lattice disorder, as in the case of heat treatment at high temperatures followed by water quenching.

Another similarity observed between the three different compounds, after the hand grinding process, is that the achieved powders show an increase of transformation broadening and a drastic decrease of magnetization of the ferromagnetic phase with respect to the starting bulk sample. Such behaviour highlights the strong sensitivity of the magnetic interactions to the change of interatomic distances, increase of the internal stresses and surface-to-volume ratio of the particles.

However, a notable different atomic reordering process and recovery of the martensitic transformation and associated magneto-structural properties upon heating characterize and distinguish the two typologies of examined Ni-Mn-based Heusler compounds.

For the Ni-Mn-In-Co composition, the reduction of particle size has a strong negative impact on the martensitic transformation behaviour, already after decreasing the particle dimensions below about 200 μm . This size reduction leads indeed to a gradual increase of the hysteresis width, in concomitance with the interruption of the forward transformation on cooling branch, which is highly enhanced for smaller particles of few tens of microns. The significant shift to lower temperatures of the martensitic finish temperature, while the martensite start temperature and the reverse transformation remain almost coincident with those of the coarser particles annealed

in the same conditions, points out that the reduction of particle's volume plays a fundamental role.

By taking into account what reported in literature for other shape memory materials undergoing the martensitic transformation, it can be plausibly supposed that also for Ni-Mn-In-Co microparticles the reduction of particle size gives rise to a more difficult accommodation of the elastic strain energy during the collective lattice shear-deformations, and to a hindered mobility of the habit planes at the grain-boundaries, for the increase of microplasticity and energy barriers in small grains/particles.

Nevertheless, for the cryo-milled and planetary ball-milled powders, the study on the effect of different annealing treatments has permitted to highlight that a higher surface-to-volume ratio of the particles, due to a more elongated shape, a smaller size or a lower degree of sintering, can lead to the nucleation of the martensitic phase at a higher temperature. This is accompanied by a decrease of the hysteresis width and an increase of the magnetization change, as compared to the bigger particles, even though the latter show a higher saturation magnetization of the austenite.

To explain such behaviour, on the one hand, it could be suggested that in this way the grains can span across the entire particle thickness (larger grain-size over thickness ratio), thus reducing the density of grain-boundaries acting as microstructural energy barriers, and possibly maintaining compatible geometrical relations between them, such as the grain orientation and the bending stress, allowing a lower twinning stress at the interfaces for the propagation of the martensitic variants. On the other hand, instead, it appears to be strictly connected to the decrease of magnetization and Curie transition temperature of the austenite

The decrease of magnetization of the austenite has been observed not only for particles presenting a lower thickness hence an increased fraction taken by the surface and interfaces as compared to the bigger and sintered ones, but also for particles having a higher density of defects retained from the rapid cooling rate with respect to the slowly cooled ones, without any significant morphological variation.

Since the total magnetic moment is strongly dependent on the amount and distribution of the magnetic Mn atoms, any alteration of their interatomic distances drastically changes the sign of magnetic interactions and, in turn, the magnetic entropy term of the total entropy difference between the two phases, which determines changes in the driving force of the thermo-elastic martensitic transformation ($\Delta G = T\Delta S$). However, also for the non-sintered and separated particles, after the long annealing treatment at high temperature with Alumina powder, it has not been possible to obtain the recovery of the martensitic phase transformation and of the magnetization change, independently on the attained value of the Curie transition temperature.

Remarkably, the SEM analysis has pointed out a rougher surface for the roundish and thicker particles as compared to the thinner ones, highlighting a completely different rate of microstructural recovery and recrystallization processes upon the same annealing conditions, also with respect to the particles annealed in absence of external constraints.

Thereby, the sintering phenomenon can drive more efficiently the defects' annihilation, grains' homogenization, and the attainment of morphological/microstructural features (such as the elongation and the increase of grain-size over thickness ratio) favourable for the nucleation and growth of the martensitic phase. However, its kinetics and final effect on the particles' properties are difficult to be controlled and predicted, since they are related to the specific curvature radius, size, and accumulated lattice disorder of the as-milled particles, which require, proportionally to the milling duration, higher annealing temperature and longer annealing time to enable the growth of stress-free grains.

For the outlined complex and contradictory interdependence of the martensitic transformation restoration on multiple extrinsic factors, related to particle morphology and thermal-activated phenomena, the ball-milling technique with subsequent thermal treatments do not allow a simultaneous and independent control on particle size and recovery of the martensitic and magnetic transitions in Ni-Mn-In-Co particles, especially for the long-milled and smallest ones.

Therefore, a reasonable compromise between recovery and particle size has been possible only for the cryo-milled and planetary ball-milled (with isopropanol) particles, processed for few hours (2-3 h), showing, after optimized annealing conditions, a length of $20 \pm 10 \mu\text{m}$ and a thickness of $6 \pm 4 \mu\text{m}$.

The irreversible worsening of the multifunctional properties of the original Ni-Mn-In-Co bulk and the strong dependence on size, microstructural, and atomic ordering variations point out that the magneto-structural martensitic transformation is highly metastable and can be readily deteriorated by changing the thermo-mechanical history and the morphological configuration of the bulk.

Conversely, for Ni-Mn-Ga and Ni-Mn-Cu-Ga compounds, presenting a direct coupling between ferromagnetic and ferro-elastic domains in the low symmetry martensitic phase, the magneto-structural martensitic transformation can be recovered and tuned in temperature in post-annealed ball-milled particles. Moreover, the transformation can be improved with respect to the starting bulk material in terms of thermal hysteresis' decrease, enhancement of sharpness and height of the magnetization change. This phenomenology, hence, suggests the beneficial effect of particle and grain size reduction to attain a better phase homogeneity after annealing treatments at tailored temperature and time.

Remarkably, for Ni-Mn-Cu-Ga particles, it has been proved that even after long milling procedures (14–35 h), with solvent and/or surfactant-assistance, it is possible to optimize the magneto-structural recovery by adjusting the annealing conditions, such as increasing the temperature from 630°C to 755°C, and/or the time from 4 to 24 h, followed by slow cooling rate.

Interestingly, it has been observed that, upon these thermal treatments, the recrystallization and grain-growth processes take place, and the flaky-morphology of the particles is maintained, thus allowing the achievement of single flat and thin particles, at both the micro- and sub-micrometre scale, with equiaxed grains spanning the whole cross-section.

Likely, the large grain size over thickness ratio and the similar and almost flattened shape of neighbouring grains may improve the lattice coherency and the geometrical compatibility between grains for the formation of the martensitic phase, differently from the case of Ni-Mn-In-Co sintered particles, characterized by significant bending stresses, disconnections, and microstructural heterogeneity.

This fact makes easier, with a lower heat dissipation, the propagation of the twin-related martensitic variants throughout the available volume. In this respect, it is worth noticing that the martensitic twin lamellae, recognized on the surface of post-annealed hand-grinded and ball-milled Ni-Mn-Cu-Ga particles, present a straight and continuous propagation throughout the available volume with constant width of tens of nanometres.

This size is much lower than that of the alternated variants fringes, revealed on cryo-milled powders of Ni-Mn-In-Co, of hundreds or several hundreds of nano-meters, tending to branch at the interfaces, deform, and change direction between neighbouring bamboo-like grains.

Accordingly, it is speculated that the highlighted different microstructural features could suggest, at a first sight, a different energy barrier associated with the formation and motion of the habit planes and twin boundaries, thus intrinsic different irreversible hysteretic losses during the formation of the martensite inside the parent phase, from the atomic to the mesoscopic scale, between the two compounds.

Usually, such behaviour depends on the intrinsic lattice parameters of the austenite and martensite, but, in the present case, the volume variations between the two phases obtained for the three examined compounds are comparable with each other.

It is then supposed that the extrinsic changes of microstructural landscape and formation of structural defects apported by the application of mechanical and thermal stresses have determined and emphasized the notably different transformation behaviours. In fact, on the base of the literature data, the better recovery of the martensitic transformation at different length scales and applied external stresses for

the Ni-Mn-Cu-Ga compound can be correlated to the peculiar ferro-elastic properties and low interfacial energy, enabling a high twin boundaries mobility and texturing at low applied stress.

In contrast, for Ni-Mn-In-Co compound, the combination of a high intrinsic phase instability, poor mechanical elasticity, faster and higher defects generation can reasonably account for a higher lattice incompatibility and higher frictional-energy dissipation during collective shear distortions, movement of phase fronts, and multiple phase front interactions.

It follows that the magneto-structural behaviours of the achieved Ni-Mn-Cu-Ga and Ni-Mn-In-Co micro/sub-microparticles can be explained and understood in relation to their original different bulk properties.

6 CONCLUSIONS AND PERSPECTIVES

The research on the preparation of Heusler particles by using different ball-milling techniques has brought about a clear assessment of the potentialities and limitations of the use of this top-down approach for obtaining sub-micro-meter or nano-meter sized particles which recover the bulk's phase transformations and do not change the achieved small size after the subsequent thermal treatments.

1. On the one hand, the a priori control on final particle size distribution and phase preservation has resulted to be challenging due to a complex balance of several milling parameters.
2. On the other one, the properties of the resulting particles and their ability to recover the desired phase transitions upon annealing treatments have shown a strong dependence on the type of Heusler compound.
3. Particularly, it has emerged that the induced deformation modes and atomic disordering processes as well as the optimal annealing conditions required are strictly governed by the intrinsic phase stability, chemical (in)homogeneity, compressive strength and grains coherency of the material employed.

Based on these remarks, for Ni-Mn-Ga and Ni-Mn-Cu-Ga compounds, it has been first demonstrated that an initial high milling energy is a fundamental requirement for efficiently breaking and overcoming the tendency of the starting hand-grinded powder to deform elastically. The best results can be obtained by combining a first cryo-milling process, for few hours, followed by the surfactant-assisted planetary ball-milling, for several hours.

Differently to what reported in literature, it has been observed that the use of the high-energy ball-milling in dry conditions for several hours (8 h) is not an effective method to reduce the particle size, but rather it leads to a higher atomic disorder and possible contamination from the milling media material and/or cold-welding between the particles.

Secondly, it has been verified the possibility to recover, after the ball-milling process, the original structure and the magneto-structural phase transformation. It has been understood the pivotal role of the annealing temperature in triggering the recovery mechanism, but also the importance of adjusting the annealing time, depending on the milling duration, and the cooling rate, depending on the annealing temperature, to allow a complete stresses' release and defects' annihilation.

Thirdly, even for the longest-milled, sub-micrometric particles, it has been successfully optimized the recovery of the coupled magneto-structural transformation and of the large saturation magnetization of the ferromagnetic martensitic phase. Remarkably, it has resulted the possibility to decrease the thermal hysteresis and enhance the phase homogeneity by gradually reducing the size of the bulk into elongated and thin flakes-like particles.

For Ni-Mn-In-Co compound, instead, it has been evidenced a much more complex scenario due to the possibility to obtain smaller particles but also the significant drawbacks of structural instability and drastic worsening of the martensitic transformation features as a function of the induced atomic disorder, grain-size refinement, and increase of the surface-to-volume ratio of the particles.

First, from the point of view of the preparation, it has been understood the fundamental importance of using a liquid milling medium, such as isopropanol, and a moderate milling energy (in terms of rotational speed and ball-to-powder weight ratio) to avoid cold-welding and amorphization, hence controlling the final particle size by adjusting the ball-milling duration.

Secondly, from the structural and magnetic point of view, it has emerged that the recovery is driven by long annealing treatments at high temperature, whose effectiveness, however, is limited and strongly dependent on the amount of lattice disorder and changes of interatomic distances, leading in some cases to the phase segregation phenomenon.

Thirdly, with respect to the Ni-Mn-Ga and Ni-Mn-Cu-Ga particles, it has been revealed that for Ni-Mn-In-Co powder the loss of mechanical coupling between the pieces of the starting bulk sample, the mechanical and thermal-induced microstructural variations, and the decrease of particle volume cause an irreversible drastic worsening of the martensitic phase transformation. These detrimental effects on reducing the particles size are an increase of the hysteresis width, a broadening of the transformation on a large temperature range and a lowering of the magnetization difference between the two phases, due to the retaining of untransformed fraction of austenite at low temperatures.

Nevertheless, even though it is not possible to fully recover the original bulk properties, some important results for the micrometric ball-milled particles have been found out. Together with the reordering and recovery processes upon heating, a minimum size of the particles is required for triggering the restoration of the Heusler phase and the onset of the martensitic transformation. However, the occurrence of sintering does not allow any improvement in the magnetic and martensitic transformation properties as compared to the batches of loose powders, both short-annealed hand-grinded and lower-temperature heat treated ball-milled ones. Rather,

it appears that the increase of volume of the sintered particles and/or the increase of long-range ferromagnetic order, apported by a slow cooling rate, led to an enhancement of magnetization of the austenite and, conversely, a decrease of the martensite nucleation temperature. The latter phenomenon has been observed in concomitance with an increase of the thermal hysteresis and the interruption of the forward transformation below 160 K, resulting in a smaller magnetization change at the transformation.

Finally, the formation of complex 3D structures, characterized by pores, multiple competing grains, bamboo-like junctions, and high bending stresses have a strong negative impact on the formation of the martensitic phase, likely due to the increase of microstructural elastic energy stored to be overcome, giving rise to a larger transformation broadening.

The current experimental findings have a broad scientific interest in the research field of multifunctional Ni-Mn-based Heusler compounds, since they provide a new preparation route to obtain magnetic micro- and sub-micrometric particles using the ball-milling techniques. In addition, these findings highlight the role of size-dependent effects on the magnetic and martensitic phase transformations of the two benchmark compositions of this class of materials, Ni-Mn-(Cu)-Ga and Ni-Mn-In-Co.

The novelty of this study arises from the fact that it has been possible to show and hence clarify the significant differences in mechanical deformation modes, disordering processes, recovery mechanisms, and structural stability, that characterize and distinguish Ni-Mn-Ga, Ni-Mn-Cu-Ga and Ni-Mn-In-Co compounds, from the macro- to the sub-micrometre scale. This achievement is particularly important in view of their design and the full exploitation of their multifunctionalities for the technological applications.

The current study points out that Ni-Mn-Ga and Ni-Mn-Cu-Ga compounds can be effectively prepared and optimized in form of magnetocaloric micro or sub-microparticles. As compared to the bulk, these particles show indeed a lowering of the irreversible hysteresis losses and the tunability of the coupled magneto-structural transformation nearer to room-temperature, thus making them promising for energy-conversion applications, such as room-temperature solid-state cooling devices. Additionally, from the preliminary characterization carried out, it has been shown that Ni-Mn-Cu-Ga sub-micrometric particles have a great potential for application in the field of biomedicine as self-regulated magnetic hyperthermia nanoparticles, thanks to the vicinity of the first-order magneto-structural transition to the therapeutic temperatures (42°C). In this perspective, further tests with surfactant-assisted planetary ball-milling, as for instance by increasing the milling time and

milling energy, would be required to obtain a smaller mean particle size below 100 nm and to improve, by optimizing the annealing treatments, the sharpness and the associated magnetization change of the coupled magneto-structural transformation.

On the other side, the worsening of the magneto-structural properties of the Ni-Mn-In-Co hand-grinded and ball-milled particles with respect to the bulk have evidenced poor mechanical properties, high intrinsic phase instability, strong metastability/variability of the metamagnetic martensitic transformation, leading to a step forward towards a better understanding of this compound at different length scales.

In addition to confirming the extreme and non-trivial dependence of the martensitic transformation on the microstructural and atomic ordering variations as recently pointed out in literature for the bulk samples, it has been shown that the size-dependent effects appear as an additional degree of freedom to change the critical temperatures and the magnetic properties across the martensitic transformation.

The present study demonstrates that at the micro- and sub-microscale, for the annealed ball-milled particles, the recovery of the martensitic transformation is determined by the full recrystallization of the microstructure and restoration of a certain degree of atomic order. Further, the stabilization of the martensitic phase is inversely related to the increase of long-range ferromagnetic order of the parent austenitic phase. In this respect, it has emerged that the particles water-quenched after suitable annealing treatments and presenting elongated shape and low degree of agglomeration could potentially show a sharper martensitic transformation, at temperatures closer to the original ones, and associated with a lower thermal hysteresis and larger magnetization change, as compared to the roundish sintered ones or those slowly cooled.

In conclusion, we think that the highlighted experimental results could be of large interest for the relevant technological implications in materials science, and we hope they would shed a new light in the comprehension of the martensitic behaviour and related multifunctional properties of the Ni-Mn-based Heusler compounds.

7 APPENDIX

7.1 $\text{Ni}_{49.4}\text{Mn}_{30.3}\text{Ga}_{20.3}$ COMPOUND

XRD @RT	Crystal phases	Cell parameters			
HG	Martensite NM	a=3.8961	b=3.8961	c=6.584	$\alpha = \beta =$
	<i>bct</i>	$\pm 0.0007 \text{ \AA}$	$\pm 0.0007 \text{ \AA}$	$\pm 0.002 \text{ \AA}$	$\gamma = 90^\circ$
	Austenite <i>fcc</i>	a=5.849	b=5.849	c=5.849	$\alpha = \beta =$
	($L2_1$)	$\pm 0.007 \text{ \AA}$	$\pm 0.007 \text{ \AA}$	$\pm 0.007 \text{ \AA}$	$\gamma = 90^\circ$
HG4h600WQ	Martensite 7M	a=4.2325	b=5.5215	c=4.2751	$\alpha = \gamma = 90^\circ$
	modulated	$\pm 0.0005 \text{ \AA}$	$\pm 0.0005 \text{ \AA}$	$\pm 0.0005 \text{ \AA}$	$\beta = 93.35$ $\pm 0.01^\circ$
	Modulation Vector	$q (\text{\AA}^{-1}) = 0.2947 \pm 0.0009 \text{ } a^*$			

Table 7.1-1: Crystallographic data of the hand-grinded (HG) and post-annealed powders (HG4h600WQ) of $\text{Ni}_{49.4}\text{Mn}_{30.3}\text{Ga}_{20.3}$ compound, obtained by the Le Bail refinement of XRD patterns collected at room-temperature.

7.2 $\text{Ni}_{49.7}\text{Mn}_{18.7}\text{Cu}_{6.4}\text{Ga}_{25.2}$ COMPOUND

XRD @RT	Crystal phases	Cell parameters			
HG	Martensite NM	a=3.901	b=3.901	c=6.454	$\alpha = \beta =$
	<i>bct</i> ($L1_0$)	$\pm 0.001 \text{ \AA}$	$\pm 0.001 \text{ \AA}$	$\pm 0.002 \text{ \AA}$	$\gamma = 90^\circ$
	Austenite <i>fcc</i>	a=5.8140	b=5.8140	c=5.8140	$\alpha = \beta =$
	($L2_1$)	$\pm 0.0015 \text{ \AA}$	$\pm 0.0015 \text{ \AA}$	$\pm 0.0015 \text{ \AA}$	$\gamma = 90^\circ$
HG4h500WQ	Austenite <i>fcc</i>	a=5.8120	b=5.8120	c=5.8120	$\alpha = \beta =$
	($L2_1$)	$\pm 0.0002 \text{ \AA}$	$\pm 0.0002 \text{ \AA}$	$\pm 0.0002 \text{ \AA}$	$\gamma = 90^\circ$
	Martensite 7M	a=4.2406	b=5.5193	c=4.3049	$\alpha = \gamma =$
	modulated	$\pm 0.0006 \text{ \AA}$	$\pm 0.0004 \text{ \AA}$	$\pm 0.0002 \text{ \AA}$	90° $\beta = 93.033$ $\pm 0.008^\circ$
	Modulation vector	$q (\text{\AA}^{-1}) = 0.2770 \pm 0.0005 \text{ } c^*$			

Table 7.2-1: Crystallographic data obtained by the Le Bail refinement of room-temperature XRD patterns of HG and post-annealed powders of $\text{Ni}_{49.7}\text{Mn}_{18.7}\text{Cu}_{6.4}\text{Ga}_{25.2}$ compound.

7.3 $\text{Ni}_{44.5}\text{Mn}_{37.9}\text{In}_{12.6}\text{Co}_5$ COMPOUND

PXRD analysis: $\text{Ni}_{44.5}\text{Mn}_{37.9}\text{In}_{12.6}\text{Co}_5$	Crystal Phases	Lattice parameters		
HG	Martensite NM bct ($I4/mmm$) (@$T \leq 300\text{K}$)	a=3.9628 ± 0.0006 \AA	b=3.9628 ± 0.0006 \AA	c=6.8086 ± 0.0017 \AA
	Austenite cubic $L2_1$ ($Fm\bar{3}m$) (@ $T \geq 300\text{K}$)	a=5.988 ± 0.005 \AA	b=5.988 ± 0.005 \AA	c=5.988 ± 0.005 \AA
HG850WQ	Austenite cubic $L2_1$ ($Fm\bar{3}m$) (@ $T \geq 300\text{K}$)	a=5.9759 ± 0.0004 \AA	b=5.9759 ± 0.0004 \AA	c=5.9759 ± 0.0004 \AA
	Martensite NM bct ($I4/mmm$) (@$T \leq 300\text{K}$)	a=3.9544 ± 0.0055 \AA	b=3.9544 ± 0.0055 \AA	c=6.782 ± 0.013 \AA
	Martensite 7M modulated ($P2/m(\alpha\gamma)00$) (@$T \leq 300\text{K}$)	a=4.3786 ± 0.0005 \AA	b=5.5878 ± 0.0009 \AA	c=4.3158 ± 0.0006 \AA
	β ($^\circ$) q_3 (\AA^{-1})	93.696 ± 0.013 0.3412 ± 0.0005		
4hHEBM850WQ	Austenite cubic $B2$ ($Pm\bar{3}m$)	a=2.9879 ± 0.0003 \AA	b=2.9879 ± 0.0003 \AA	c=2.9879 ± 0.0003 \AA

Table 7.3-1: Summary of the crystal phases and lattice parameters of the $\text{Ni}_{44.5}\text{Mn}_{37.9}\text{In}_{12.6}\text{Co}_5$ HG powder and of the post-annealed HG and 4h-HEBM powders, heat treated for 2h at 850°C, followed by water quenching.

Composition:	Ni (at. %)	Mn (at. %)	In (at. %)	Co (at. %)
Bulk	44.5 \pm 0.2	37.9 \pm 0.3	12.5 \pm 0.1	5 \pm 0.08
HG850WQ	43.9 \pm 0.7	39.9 \pm 0.8	11.2 \pm 0.9	4.9 \pm 0.2
4hHEBM850WQ	44.6 \pm 0.8	38.9 \pm 0.6	11.6 \pm 0.5	4.8 \pm 0.4

Table 7.3-2: Chemical composition of bulk and powders samples of $\text{Ni}_{44.5}\text{Mn}_{37.9}\text{In}_{12.6}\text{Co}_5$ detected by EDX analysis.

7.3.1 Planetary ball-milling

In a Planetary ball-mill Pulverisette 7, the HG powder of $Ni_{44.5}Mn_{37.9}In_{12.6}Co_5$ compound was subjected to a dry milling procedure under a gaseous atmosphere of nitrogen. Inside a jar of Zirconia, there were put 20 Zirconia balls of 5 mm diameter and there was selected a 10:1 ball-to-powder weight ratio. The process was run at the rotational speed of 400 rpm, in intervals of 15 min milling and 7 min rest, up to 12h. Subsequently, the powders were kept under protective Ar atmosphere inside a glove box, to avoid oxidation. The specifications of the milling and annealing conditions selected are listed in Table 7.3-3.

Sample: $Ni_{44.5}Mn_{37.9}In_{12.6}Co_5$	Milling time (h)	Annealing temperature (°C)	Annealing time (h)	Cooling rate	Corresponding Name
Hand-grinded (HG)	-	-	-	-	HG
		850	2	WQ	HG850WQ
Planetary Ball-milled (PBM)	3	-	-	-	3h-PBM
		900	23	WQ	3hPBM23h900W Q
	12	-	-	-	12h-PBM
		850	2	WQ	12hPBM850WQ

Table 7.3-3: Milling procedure and annealing treatment specifications for the HG and ball-milled powders of $Ni_{44.5}Mn_{37.9}In_{12.6}Co_5$ compound.

The morphology of the particles, achieved after 3 h and 12 h of PBM in dry conditions, is shown in the SEM images of Figs. 7.3-1(a)-(b). It is noted that the particle's shape is roundish, and the size is generally smaller than 20 μm , with a large Gaussian size distribution and $9 \pm 5 \mu m$ diameter, after 3h of PBM (Fig. 7.3-1(c)). Instead, after 12h of milling process, the size of the particles further decreases and it is obtained a narrow Lorentzian size distribution (Fig. 7.3-1d)), well-peaked at $3 \pm 1.5 \mu m$ diameter. It is worth stressing that the smallest particles achieved are at the submicron scale, with particle's diameter reaching 850-950 nm, thus stressing the effectiveness of the increase of milling time in reducing the particle size. However, it is observed that the particles have a strong tendency to form agglomerates, which points out the occurrence of overheating and the increase of particles' surface energy. Indeed, beside a high surface-to-volume ratio, it can be noted a highly defected and inhomogeneous surface area, ascribable to the effect of friction between particles and balls or particles themselves.

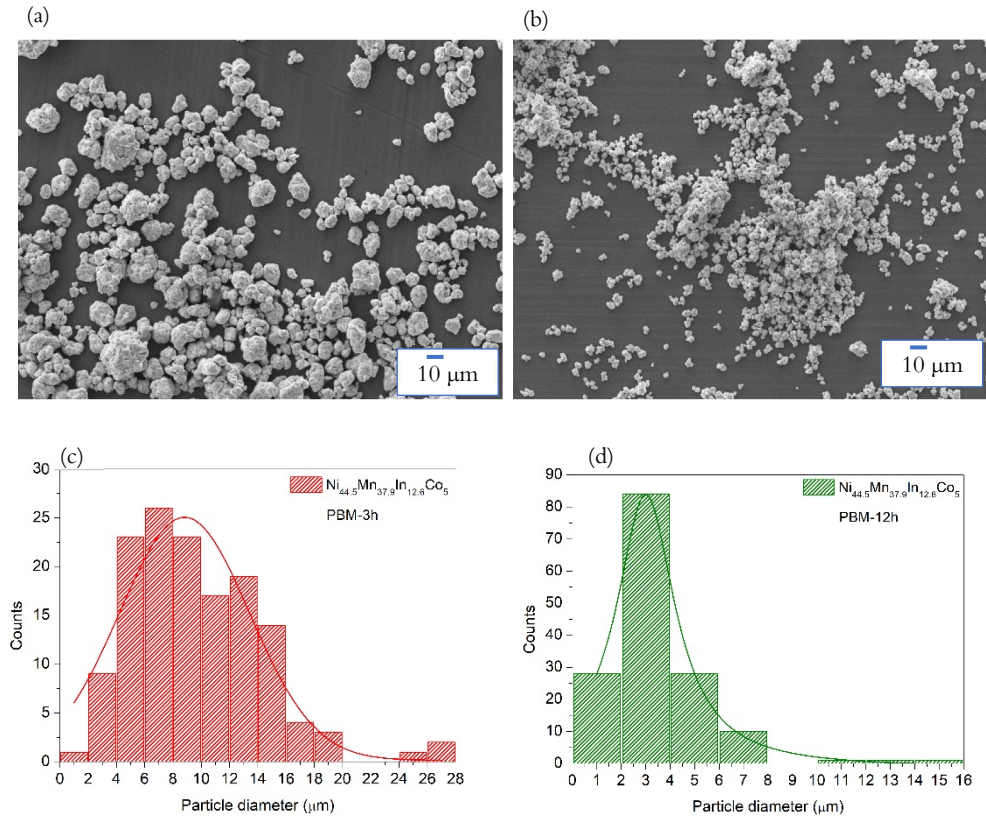


Figure 7.3-1: (a) and (b) SEM images of the $\text{Ni}_{44.5}\text{Mn}_{37.9}\text{In}_{12.6}\text{Co}_5$ PBM powders after 3h and 12h, respectively; (c) and (d) corresponding particle size distributions.

By subsequent EDX and XRD analyses, to check composition and crystal phases, it was revealed a significant contamination from Oxygen, which increased for longer-milled particles batches, having a smaller particle's size. As shown in Fig. 7.3-2, where the XRD patterns collected at room temperature with Cu $K\alpha_1$ radiation are reported, the initial tetragonal martensitic structure of the HG powder undergoes a drastic disordering process during the PBM process. In fact, after 3h of milling the first two fundamentals peaks of the original tetragonal structure appear really broad, while the ones at high 2θ positions are almost suppressed; after PBM of 12h the destruction of the original crystallinity is complete, leading to the appearance of an amorphous structure, where there can be recognized the additional peaks of manganese dioxide.

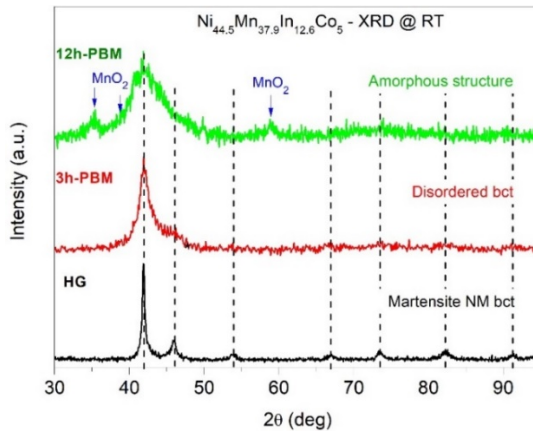


Figure 7.3-2: XRD analysis, at room-temperature, of the hand-grinded (HG), 3h-PBM, and 12h-PBM processed powders of $\text{Ni}_{44.5}\text{Mn}_{37.9}\text{In}_{12.6}\text{Co}_5$, carried out with $\text{Cu K}\alpha_1$ radiation.

In an attempt to recover the initial atomic order and associated magnetic and magneto-structural phase transitions, the 3h-PBM powder was heat treated for 23h at 900°C and water quenched afterwards. This annealed batch has been referred to as 3hPBM23h900WQ (Table 7.3-3) in Fig. 7.3-3, where it can be noted that its magnetic susceptibility behaviour is completely different from the one of the post-annealed hand-grinded powders, named as HG850WQ. Indeed, it emerges that only a magnetic Curie transition is recovered but at a lower temperature, as indicated by the horizontal leftward black arrow. Instead, on heating from 200 K, no other significant susceptibility changes can be detected but only a weak change of inflection in the region highlighted in orange, differently to the behaviour of the HG850WQ powder, showing the occurrence of the reverse martensitic transformation in correspondence of 300–325 K. By a further investigation of the magnetic susceptibility of the 3hPBM23h900WQ sample in the range of low temperatures, it has been found out the result reported in the inset, which reveals the presence of a thermal hysteresis, between the cooling and the heating branches, of notable amplitude of $\Delta T_{\text{hyst}} \approx 80$ K, while the change of magnetic signal across the martensitic transformation is negligible. This fact denotes the hindering of the martensitic phase formation in the ball-milled annealed particles and it has to be analysed together with the decrease of temperature and sharpness of the magnetic Curie transition. Reasonably, a low degree of long-range atomic order and a change of composition may account for these phenomena.

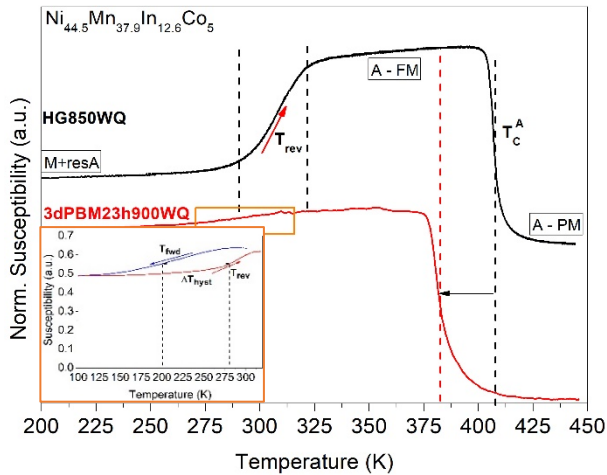


Figure 7.3-3: Thermo-magnetic analysis of the $Ni_{44.5}Mn_{37.9}In_{12.6}Co_5$ 3h-PBM powders after the annealing for 23h at 900°C (followed by water quenching) and of the hand-grinded powders heat treated for 2h at 850°C (+water quenching). Inset: magnetic susceptibility of the former batch, in cooling and heating branches, between 100–320 K.

By the XRD analysis, in fact, it has resulted a negligible amount of $L2_1$ -type atomic order, due to the low intensity of the superlattice reflections, and the presence of the additional peaks of Manganese dioxide (Fig. 7.3-4). However, also for the HG850WQ powder it was not possible to detect well-defined peaks of the Heusler superstructure, thus stressing the unavoidable retaining of certain amount of $B2$ -type atomic disorder after the annealing, which could derive both from the specific thermo-mechanical history of the sample and/or from quenched-in vacancies of the original bulk compound [95]. Nevertheless, the cubic reflections did not change positions between the HG and 3h-PBM annealed powders, suggesting an overall preservation of the phase. By contrast a detrimental phase segregation phenomenon has been highlighted for the 12h-PBM powder after performing a short heat treatment at 850°C. As shown in Fig. 7.3-4, several reflections have been observed and indexed with different phases. Apart from the intense peaks of manganese dioxide, it has been recognized the presence of an Heusler $L2_1$ superstructure, as revealed by the well-defined and intense (111) superlattice reflection, a cubic γ -phase and a tetragonal phase. Hence, the original off-stoichiometric quaternary composition is divided in different phases, such as the nearly stoichiometric ternary $Ni_{50}Mn_{25}In_{25}$ Heusler phase, the binary $Ni_{50}Mn_{50}$ phase and a residual Co-rich phase. This decomposition is well reflected by the magnetic susceptibility behaviour as a function of temperature, shown in Fig. 7.3-5. The 12hPBM850WQ powder is characterized by a first sharp

Curie transition at around 327 K, associated to the Curie transition of the austenite of the $Ni_{50}Mn_{25}In_{25}$ phase, and a second broad magnetic transition shifted to a higher temperature, of 375 K, attributed to the Co-rich γ -phase. The peculiar segregation phenomenon is a common tendency in the off-stoichiometric, Co-doped Ni-Mn-In compositions, as described by different authors in literature, based on both experimental and theoretical evidences [90,91,174].

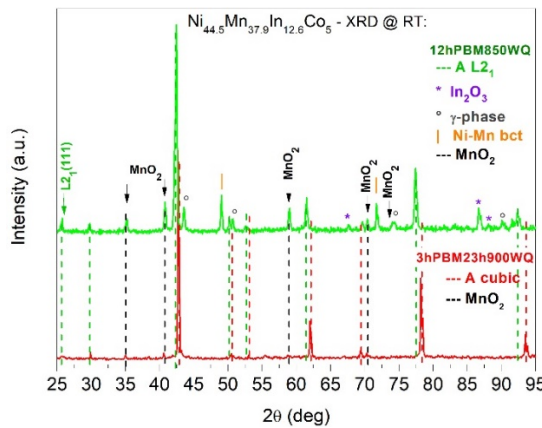


Figure 7.3-4: Room-temperature XRD analysis of the $Ni_{44.5}Mn_{37.9}In_{12.6}Co_5$ 3h- and 12h-PBM powder batches, annealed for 23h at $900^{\circ}C$ (followed by water quenching) and for 2h at $850^{\circ}C$ (followed by water quenching), respectively.

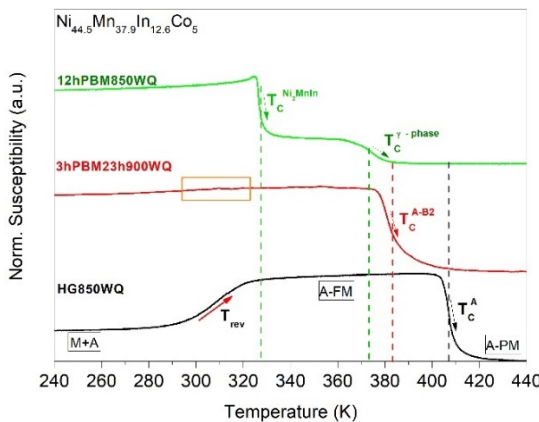


Figure 7.3-5: Magnetic susceptibility response as a function of temperature for the $Ni_{44.5}Mn_{37.9}In_{12.6}Co_5$ hand-grinded powders annealed for 2h at $850^{\circ}C$, the 3h-PBM particles annealed

for 23h at 900°C and the 12h-PBM powders annealed for 2h at 850°C, in black, red and green curves, respectively.

The current experimental results have once more highlighted the necessity to control the milling energy and hence the induced atomic disorder, in order to avoid amorphization, which not only prevents the recovery of the original phase transitions but also leads to decomposition in different crystal phases, during heat treatments at high temperature. Furthermore, the increase of the surface-to-volume ratio has made the particles more reactive to the presence of oxygen, giving rise to growth of crystalline manganese oxides on the surface, and to the thermally activated atomic phenomena such as sintering between particles during the long heat treatment at high temperature (Fig. 7.3-6).

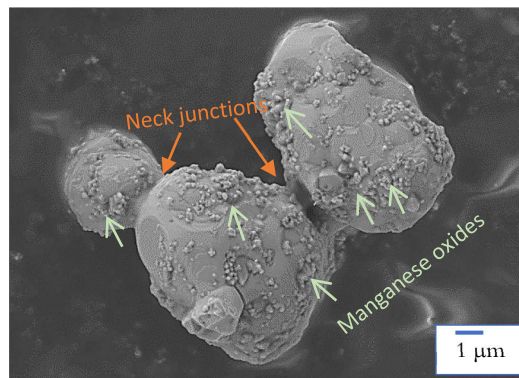


Figure 7.3-6: SEM micrograph showing the morphology of the $Ni_{44.5}Mn_{37.9}In_{12.6}Co_5$ 3h-PBM particles heat treated for 23h at 900°C, where there have been indicated the presence of manganese oxides on the surface and the neck junctions due to sintering between adjacent roundish particles.

7.4 $Ni_{45.7}Mn_{36.9}In_{13.2}Co_{4.2}$ COMPOUND

PXRD @ RT	Crystal Phases	Lattice parameters		
$Ni_{45.7}Mn_{36.9}In_{13.2}Co_{4.2}$				
HG	Martensite NM <i>bct</i> ($L1_0$)	a=3.9594 $\pm 0.0004 \text{ \AA}$	b=3.9594 $\pm 0.0004 \text{ \AA}$	c=6.7237 $\pm 0.0012 \text{ \AA}$

HG820SC	Austenite <i>fcc</i> ($L2_1$)	a=5.971 $\pm 0.005 \text{ \AA}$	b=5.971 $\pm 0.005 \text{ \AA}$	c=5.971 $\pm 0.005 \text{ \AA}$
	Austenite <i>fcc</i> ($L2_1$)	a=5.971 $\pm 0.005 \text{ \AA}$	b=5.971 $\pm 0.005 \text{ \AA}$	c=5.971 $\pm 0.005 \text{ \AA}$
	Martensite 7M mod.	a=4.391 $\pm 0.003 \text{ \AA}$	b=5.568 $\pm 0.005 \text{ \AA}$	c=4.317 $\pm 0.002 \text{ \AA}$
3dPBM24h820WQ	β (°) q_3 (\AA^{-1})	93.368 ± 0.089 0.3375 ± 0.0028		
	Austenite <i>fcc</i> ($L2_1$)	a=5.9939 \AA (0.0001)	b=5.9939 \AA (0.0001)	c=5.9939 \AA (0.0001)
	γ -phase <i>fcc</i>	a=3.6207 \AA (0.0004)	b=3.6207 \AA (0.0004)	c=3.6207 \AA (0.0004)
	MnO_2 <i>fcc</i>	a=4.440 \AA (0.001)	b=4.440 \AA (0.001)	c=4.440 \AA (0.001)
	3wPBM24h820WQ	Austenite <i>fcc</i> ($L2_1$)	a=5.9784 \AA (0.0002)	b=5.9784 \AA (0.0002)
3wPBM24h820WQ	Martensite NM <i>bct</i> ($L1_0$)	a=3.9594 \AA (0.0009)	b=3.9594 \AA (0.0009)	c=6.724 \AA (0.004)
	Martensite 7M mod.	a= 4.3910 \AA (0.0003)	b=5.5843 \AA (0.0003)	c=4.3222 \AA (0.0001)
	β (°) q_3 (\AA^{-1})	93.635 (0.004) 0.34307 (0.00008)		
	MnO_2 <i>fcc</i>	a=4.4236 \AA (0.0013)	b=4.4236 \AA (0.0013)	c=4.4236 \AA (0.0013)

Table 7.4-1: Specifications of crystal phases and corresponding lattice parameters for the batches of $Ni_{45.7}Mn_{36.9}In_{13.2}Co_{4.2}$ HG powder, before and after the annealing for 2h at 820°C, followed by slow cooling, and the dry and wet PBM powders, after the annealing for 24h at 820°C, followed by water quenching.

Sample: $Ni_{45.7}Mn_{36.9}In_{13.2}Co_{4.2}$	A_s (± 2 K)	A_f (± 2 K)	M_s (± 2 K)	M_f (± 2 K)	T_c (± 2 K)	ΔT_{hyst} (± 4 K)	ΔT_{elas} (± 4 K)	ΔM (± 2 Am ² / kg)	$\frac{(T_c - T_0)}{T_c}$ (\pm 0.01)
Bulk	277	294	276	260	393	17	9	118	0.27
HG820SC	272	297	265	228	391	38	31	102	0.28
3wPBM4h820WQ	252	290	233	158	371	75	57	38	0.29
3wPBM24h820WQ	267	307	272	208	371	47	52	68	0.22
3wPBM29h820WQ	274	309	282	205	370	48	56	63	0.20
2CM24h755WQ	267	309	274	214	367	44	51	74	0.20
2CM1h820WQ	240	284	226	148	371	75	61	28	0.31
2CM4h820WQ	247	287	231	163	372	69	54	55	0.30
2CM24h820WQ	258	332	309	205	380	37	89	51	0.16
+ ann4h500SC	274	330	306	211	386	44	76	48	0.17
2CM29h820WQ	255	304	266	197	388	48	59	39	0.26
3CM24h820WQ	253	309	272	169	377	61	80	9	0.23
3CM29h820WQ ($d > 66 \mu m$)	269	315	289	208	374	43	63	69	0.19

3CM29h820WQ ($d < 66 \mu\text{m}$)	264	327	298	202	375	45	79	47	0.17
+ ann4h500SC	274	320	284	189	381	60	71	33	0.21

Table 7.4-2: List of values of transition temperatures, magnetization change and $\frac{(T_C - T_0)}{T_C}$ parameter, obtained by thermo-magnetization and susceptibility measurements, for the batches of post-annealed ball-milled powders, annealed hand-grinded powder and bulk sample of $\text{Ni}_{45.7}\text{Mn}_{36.9}\text{In}_{13.2}\text{Co}_{4.2}$ compound.

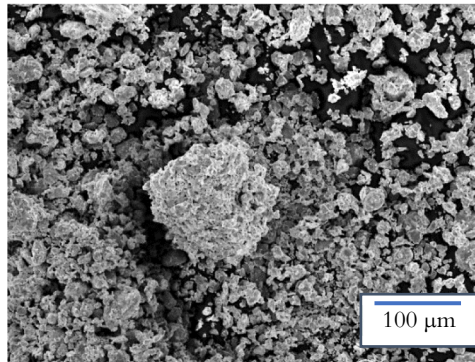


Figure 7.4-1: SEM micrograph of the CM-4h40' powder of $\text{Ni}_{45.7}\text{Mn}_{36.9}\text{In}_{13.2}\text{Co}_{4.2}$ system, showing the formation of agglomerates.

Sample:	Ni (at. %)	Mn (at. %)	In (at. %)	Co (at. %)	
$\text{Ni}_{45.7}\text{Mn}_{36.9}\text{In}_{13.2}\text{Co}_{4.2}$					
Bulk	45.7±0.5	36.9±0.3	13.2±0.2	4.2±0.3	
3wPBM4h820WQ	45.2±1.8	37.1±1.8	13.1±0.9	4.5±0.6	
3wPBM24h820WQ	46.4±0.2	38.2±2.3	11.4±2.1	4±0.5	
2CM24h755WQ	46.3±0.4	36.8±0.8	12.3±1.5	4.5±0.5	
2CM1h820WQ	45.1±0.7	37.6±0.6	12.5±0.8	4.7±0.1	
2CM4h820WQ	Smooth grains	46.7±0.1	35.4±0.5	13.6±0.3	4.2±0.4
	Rough regions	45.3±1.7	38.1±1.7	12.4±1.5	4.2±0.2
	Combination of both	45.7±1.6	37.3±1.8	12.8±1.3	4.2±0.2
2CM24h820WQ	45.6±0.2	37.06±0.57	13.1±0.3	4.2±0.3	
2CM29h820WQ	46.1±0.8	36.4±0.5	13.2±0.3	4.2±0.5	
3CM29h820WQ+ann4h500SC	45.2 ± 1	37.4 ± 1.5	13.2±1.2	4.2±0.3	

Table 7.4-3: Results of compositional EDX analysis for some of the differently annealed batches of wetPBM-3h, CM-2h and CM-3h powders and comparison with the bulk composition of $Ni_{45.7}Mn_{36.9}In_{13.2}Co_{4.2}$ compound.

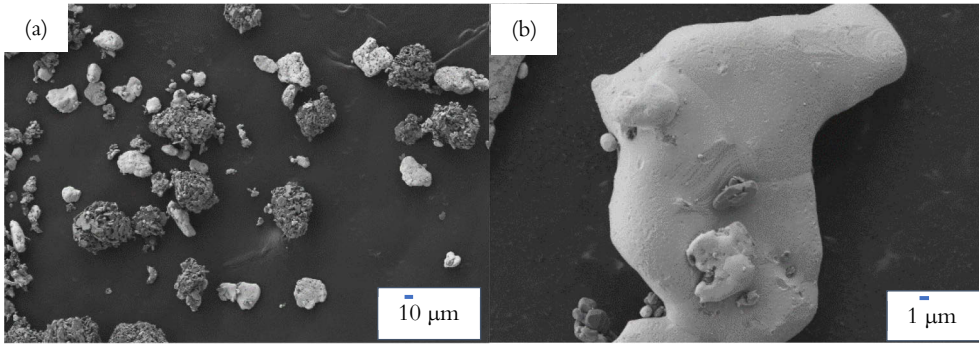


Figure 7.4-2: (a) and (b) SEM images showing at two different (increasing) magnifications the morphology of the CM-3h particles (brighter colour) annealed for 24 h at 820°C with Alumina powder (darker colour) to avoid sintering. In (b) it is possible to notice that the bigger recrystallized particles present a rougher surface area as compared to the smallest and thinner ones.

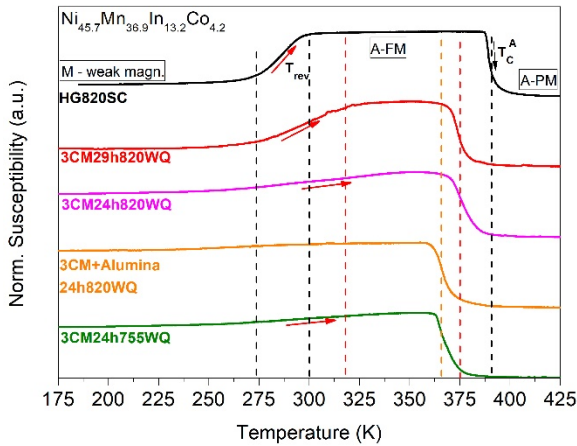


Figure 7.4-3: Thermomagnetic analysis of the CM-3h particles mixed with Alumina powder and annealed for 24 h at 820°C (followed by water quenching) in comparison to the behaviour of the powder annealed in the same conditions but without Alumina or at a different temperature or time. The curve of the HG powder, annealed for 2 h at 820°C and then slowly cooled, is taken as reference.

8 LIST OF PUBLICATIONS

1. *Published Manuscript:*

G. Cavazzini, F. Cugini, M.E. Gruner, C. Bennati, L. Righi, S. Fabbri, F. Albertini, M. Solzi, “**Tuning the magnetic and magnetocaloric properties of austenitic Ni-Mn-(In,Sn) Heuslers**”, *Scripta Materialia* 170 (2019) 48-51

2. *Submitted Manuscript:*

G. Cavazzini, F. Cugini, D. Delmonte, G. Trevisi, L. Nasi, S. Ener, D. Koch, L. Righi, M. Solzi, O. Gutfleisch, and F. Albertini, “**Multifunctional Ni-Mn-Ga and Ni-Mn-Cu-Ga Heusler particles towards the nanoscale by ball-milling technique**”, *Journal of Alloys and Compounds* (2021) No. JALCOM-D-21-00454

3. *Submitted Manuscript:*

S. Fabbri, F. Cugini, F. Orlandi, N. Sarzi Amadè, F. Casoli, D. Calestani, R. Cabassi, G. Cavazzini, L. Righi, M. Solzi, F. Albertini, “**Magnetocaloric properties at the austenitic Curie transition in Cu and Fe substituted Ni-Mn-In Heusler compounds**”, *Journal of Alloys and Compounds* (2020) No. JALCOM-D-20-13250

4. *Manuscript under preparation:*

G. Cavazzini, F. Cugini, D. Delmonte, G. Trevisi, S. Ener, D. Koch, L. Righi, M. Solzi, O. Gutfleisch, and F. Albertini, “**On the recovery and modification of the metamagnetic martensitic transformation in milled Ni-Mn-In-Co microparticles**”

9 BIBLIOGRAPHY

- [1] J.L. Dupont, P. Domanski, P. Lebrun, F. Ziegler, 38th Note on Refrigeration Technologies: The Role of Refrigeration in the Global Economy, 2019.
- [2] D. Salazar-Jaramillo, P. Álvarez-Alonso, P. Lázpita, J.L. Sánchez Llamazares, P. Gorriá, J.A. Blanco, V.A. Chernenko, Magnetocaloric Effect in Specially Designed Materials, in: *Magn. Nanostructured Mater. From Lab to Fab*, 2018. <https://doi.org/10.1016/B978-0-12-813904-2.00007-3>.
- [3] F. Puglielli, V. Mussi, F. Cugini, N. Sarzi Amadè, M. Solzi, C. Bennati, S. Fabbrici, F. Albertini, Scale-Up of Magnetocaloric NiCoMnIn Heuslers by Powder Metallurgy for Room Temperature Magnetic Refrigeration, *Front. Energy Res.* (2020). <https://doi.org/10.3389/fenrg.2019.00150>.
- [4] O. Gutfleisch, M.A. Willard, E. Brück, C.H. Chen, S.G. Sankar, J.P. Liu, Magnetic materials and devices for the 21st century: Stronger, lighter, and more energy efficient, *Adv. Mater.* 23 (2011) 821–842. <https://doi.org/10.1002/adma.201002180>.
- [5] A. Gschneidner, V.K. Pecharsky, A.O. Tsokol, Recent developments in magnetocaloric materials, *Reports Prog. Phys.* (2005). <https://doi.org/10.1088/0034-4885/68/6/R04>.
- [6] V.K. Pecharsky, K.A. Gschneidner, Giant magnetocaloric effect in Gd₅(Si₂Ge₂), *Phys. Rev. Lett.* (1997). <https://doi.org/10.1103/PhysRevLett.78.4494>.
- [7] J.H. Belo, A.L. Pires, J.P. Araújo, A.M. Pereira, Magnetocaloric materials: From micro- to nanoscale, *J. Mater. Res.* (2019). <https://doi.org/10.1557/jmr.2018.352>.
- [8] V. Gschneidner, K. Pecharsky, Thirty years of near room temperature magnetic cooling: Where we are today and future prospects, *Int. J. Refrig.* 31 (2008).
- [9] T. Graf, C. Felser, S.S.P. Parkin, Simple rules for the understanding of Heusler compounds, *Prog. Solid State Chem.* (2011). <https://doi.org/10.1016/j.progsolidstchem.2011.02.001>.
- [10] M. Kohl, M. Gueltig, V. Pinneker, R. Yin, F. Wendler, B. Krevet, Magnetic shape memory microactuators, *Micromachines.* 5 (2014) 1135–1160. <https://doi.org/10.3390/mi5041135>.
- [11] J. Liu, N. Scheerbaum, S. Kauffmann-Weiss, O. Gutfleisch, NiMn-based alloys and composites for magnetically controlled dampers and actuators, *Adv. Eng. Mater.* (2012). <https://doi.org/10.1002/adem.201200038>.
- [12] K. Otsuka, T. Kakeshita, Science and technology of shape-memory alloys: New developments, *MRS Bull.* (2002). <https://doi.org/10.1557/mrs2002.43>.
- [13] L. Mañosa, A. Planes, M. Acet, Advanced materials for solid-state refrigeration, *J. Mater. Chem. A.* (2013). <https://doi.org/10.1039/c3ta01289a>.
- [14] F. Albertini, M. Solzi, A. Paoluzi, L. Righi, Magnetocaloric properties and magnetic anisotropy by tailoring phase transitions in NiMnGa alloys, *Mater. Sci. Forum.* 583 (2008) 169–196. <https://doi.org/10.4028/www.scientific.net/msf.583.169>.

- [15] D. Zhao, T. Castán, A. Planes, Z. Li, W. Sun, J. Liu, Enhanced caloric effect induced by magnetoelastic coupling in NiMnGaCu Heusler alloys: Experimental study and theoretical analysis, *Phys. Rev. B.* 96 (2017). <https://doi.org/10.1103/PhysRevB.96.224105>.
- [16] J. Liu, T. Gottschall, K.P. Skokov, J.D. Moore, O. Gutfleisch, Giant magnetocaloric effect driven by structural transitions, *Nat. Mater.* (2012). <https://doi.org/10.1038/nmat3334>.
- [17] A. Planes, L. Māosa, M. Acet, Magnetocaloric effect and its relation to shape-memory properties in ferromagnetic Heusler alloys, *J. Phys. Condens. Matter.* (2009). <https://doi.org/10.1088/0953-8984/21/23/233201>.
- [18] R. Tickle, R.D. James, Magnetic and magnetomechanical properties of Ni₂MnGa, *J. Magn. Magn. Mater.* (1999). [https://doi.org/10.1016/S0304-8853\(99\)00292-9](https://doi.org/10.1016/S0304-8853(99)00292-9).
- [19] D.C. Dunand, P. Müllner, Size effects on magnetic actuation in Ni-Mn-Ga shape-memory alloys, *Adv. Mater.* 23 (2011) 216–232. <https://doi.org/10.1002/adma.201002753>.
- [20] M.P. Li, Q.P. Sun, Nanoscale phase transition behavior of shape memory alloys — closed form solution of 1D effective modelling, *J. Mech. Phys. Solids.* (2018). <https://doi.org/10.1016/j.jmps.2017.09.008>.
- [21] B. Erkartal, V. Duppel, R. Niemann, L. Schultz, S. Fähler, U. Schürmann, L. Kienle, Structure and composition of magnetocaloric Ni-Mn-In-Co thin films on the nanoscale-A TEM study, *Adv. Eng. Mater.* (2012). <https://doi.org/10.1002/adem.201200072>.
- [22] M.P. Caputo, C. V. Solomon, A facile method for producing porous parts with complex geometries from ferromagnetic Ni-Mn-Ga shape memory alloys, *Mater. Lett.* (2017). <https://doi.org/10.1016/j.matlet.2017.04.112>.
- [23] R. Delville, B. Malard, J. Pilch, P. Sittner, D. Schryvers, Microstructure changes during non-conventional heat treatment of thin Ni-Ti wires by pulsed electric current studied by transmission electron microscopy, *Acta Mater.* (2010). <https://doi.org/10.1016/j.actamat.2010.04.046>.
- [24] O.U. Salman, A. Finel, R. Delville, D. Schryvers, The role of phase compatibility in martensite, in: *J. Appl. Phys.*, 2012. <https://doi.org/10.1063/1.4712629>.
- [25] A. Mostafaei, K.A. Kimes, E.L. Stevens, J. Toman, Y.L. Krimer, K. Ullakko, M. Chmielus, Microstructural evolution and magnetic properties of binder jet additive manufactured Ni-Mn-Ga magnetic shape memory alloy foam, *Acta Mater.* (2017). <https://doi.org/10.1016/j.actamat.2017.04.010>.
- [26] B. Kockar, I. Karaman, J.I. Kim, Y.I. Chumlyakov, J. Sharp, C.J. (Mike. Yu, Thermomechanical cyclic response of an ultrafine-grained NiTi shape memory alloy, *Acta Mater.* (2008). <https://doi.org/10.1016/j.actamat.2008.04.001>.
- [27] B. Malard, J. Pilch, P. Sittner, V. Gartnerova, R. Delville, D. Schryvers, C. Curfs, Microstructure and functional property changes in thin NiTi wires heat treated by electric current - High energy X-ray and tem investigations, *Funct. Mater. Lett.* (2009). <https://doi.org/10.1142/S1793604709000557>.
- [28] P. Ranzieri, S. Fabbri, L. Nasi, L. Righi, F. Casoli, V.A. Chernenko, E. Villa, F. Albertini, Epitaxial Ni-Mn-Ga/MgO(1 0 0) thin films ranging in thickness from 10 to 100 nm, *Acta Mater.* (2013). <https://doi.org/10.1016/j.actamat.2012.09.056>.

- [29] M. Takhsha Ghahfarokhi, F. Casoli, S. Fabbri, L. Nasi, F. Celegato, R. Cabassi, G. Trevisi, G. Bertoni, D. Calestani, P. Tiberto, F. Albertini, Martensite-enabled magnetic flexibility: The effects of post-growth treatments in magnetic-shape-memory Heusler thin films, *Acta Mater.* (2020). <https://doi.org/10.1016/j.actamat.2020.01.049>.
- [30] A.N. Bucsek, G.A. Hudish, G.S. Bigelow, R.D. Noebe, A.P. Stebner, Composition, Compatibility, and the Functional Performances of Ternary NiTiX High-Temperature Shape Memory Alloys, *Shape Mem. Superelasticity.* (2016). <https://doi.org/10.1007/s40830-016-0052-5>.
- [31] R. Ahluwalia, S.S. Quek, D.T. Wu, Simulation of grain size effects in nanocrystalline shape memory alloys, *J. Appl. Phys.* (2015). <https://doi.org/10.1063/1.4923044>.
- [32] A. Akbarzadeh, M. Samiei, S. Davaran, Magnetic nanoparticles: Preparation, physical properties, and applications in biomedicine, *Nanoscale Res. Lett.* (2012). <https://doi.org/10.1186/1556-276X-7-144>.
- [33] C. Wang, L. Basit, Y. Khalavka, Y. Guo, F. Casper, T. Gasi, V. Ksenofontov, B. Balke, G.H. Fecher, C. Sönnichsen, Y.K. Hwu, J.J. Lee, C. Felser, Probing the size effect of Co₂FeGa-SiO₂@C nanocomposite particles prepared by a chemical approach, *Chem. Mater.* (2010). <https://doi.org/10.1021/cm1023579>.
- [34] L. Basit, C. Wang, C.A. Jenkins, B. Balke, V. Ksenofontov, G.H. Fecher, C. Felser, E. Mugnaioli, U. Kolb, S.A. Nepijko, G. Schönhense, M. Klimenkov, Heusler compounds as ternary intermetallic nanoparticles: Co₂FeGa, *J. Phys. D: Appl. Phys.* (2009). <https://doi.org/10.1088/0022-3727/42/8/084018>.
- [35] T. Fichtner, C. Wang, A.A. Levin, G. Kreiner, C.S. Mejia, S. Fabbri, F. Albertini, C. Felser, Effects of annealing on the martensitic transformation of Ni-based ferromagnetic shape memory heusler alloys and nanoparticles, *Metals (Basel)*. (2015). <https://doi.org/10.3390/met5020484>.
- [36] C. Wang, J. Meyer, N. Teichert, A. Auge, E. Rausch, B. Balke, A. Hütten, G.H. Fecher, C. Felser, Heusler nanoparticles for spintronics and ferromagnetic shape memory alloys, *J. Vac. Sci. Technol. B, Nanotechnol. Microelectron. Mater. Process. Meas. Phenom.* (2014). <https://doi.org/10.1116/1.4866418>.
- [37] C.H. Wang, Y.Z. Guo, F. Casper, B. Balke, G.H. Fecher, C. Felser, Y. Hwu, Size correlated long and short range order of ternary Co₂FeGa Heusler nanoparticles, *Appl. Phys. Lett.* (2010). <https://doi.org/10.1063/1.3488805>.
- [38] S. Aksoy, Synthesis and characterization of NiMnIn nanoparticles, *J. Magn. Magn. Mater.* (2015). <https://doi.org/10.1016/j.jmmm.2014.04.003>.
- [39] B. Tian, F. Chen, Y.X. Tong, L. Li, Y.F. Zheng, Y. Liu, Q.Z. Li, Phase transition of Ni-Mn-Ga alloy powders prepared by vibration ball milling, *J. Alloys Compd.* (2011). <https://doi.org/10.1016/j.jallcom.2011.01.104>.
- [40] B. Tian, F. Chen, Y. Liu, Y.F. Zheng, Structural transition and atomic ordering of Ni_{49.8}Mn_{28.5}Ga_{21.7} ferromagnetic shape memory alloy powders prepared by ball milling, *Mater. Lett.* (2008). <https://doi.org/10.1016/j.matlet.2008.01.071>.
- [41] B. Tian, F. Chen, Y.X. Tong, L. Li, Y.F. Zheng, Phase transformation and magnetic property of Ni-Mn-Ga powders prepared by dry ball milling, *J. Mater. Eng. Perform.* (2012). <https://doi.org/10.1007/s11665-012-0365-2>.

- [42] B. Tian, F. Chen, Y. Liu, Y.F. Zheng, Effect of ball milling and post-annealing on magnetic properties of Ni_{49.8}Mn_{28.5}Ga_{21.7} alloy powders, *Intermetallics*. (2008). <https://doi.org/10.1016/j.intermet.2008.08.002>.
- [43] Y.D. Wang, Y. Ren, Z.H. Nie, D.M. Liu, L. Zuo, H. Choo, H. Li, P.K. Liaw, J.Q. Yan, R.J. McQueeney, J.W. Richardson, A. Huq, Structural transition of ferromagnetic Ni₂MnGa nanoparticles, *J. Appl. Phys.* (2007). <https://doi.org/10.1063/1.2713370>.
- [44] A. Aslani, M. Ghahremani, M. Zhang, L.H. Bennett, E. Della Torre, Enhanced Magnetic Properties of Ni₅₁Mn_{33.4}In_{15.6} Heusler Alloy Nanoparticles, *IEEE Trans. Magn.* (2017). <https://doi.org/10.1109/TMAG.2017.2734880>.
- [45] D.M. Liu, Z.H. Nie, Y.D. Wang, Y.D. Liu, G. Wang, Y. Ren, L. Zuo, New sequences of phase transition in Ni-Mn-Ga ferromagnetic shape memory nanoparticles, *Metall. Mater. Trans. A Phys. Metall. Mater. Sci.* (2008). <https://doi.org/10.1007/s11661-007-9435-8>.
- [46] V. Sánchez-Alarcos, V. Recarte, J.I. Pérez-Landazábal, S. Larumbe, R. Caballero-Flores, I. Unzueta, J.A. García, F. Plazaola, J.A. Rodríguez-Velamazán, Mechanically induced disorder and crystallization process in Ni-Mn-In ball-milled alloys, *J. Alloys Compd.* (2016). <https://doi.org/10.1016/j.jallcom.2016.08.068>.
- [47] M. Broseghini, L. Gelisio, M. D’Incau, C.L. Azanza Ricardo, N.M. Pugno, P. Scardi, Modeling of the planetary ball-milling process: The case study of ceramic powders, *J. Eur. Ceram. Soc.* 36 (2016) 2205–2212. <https://doi.org/10.1016/j.jeurceramsoc.2015.09.032>.
- [48] F. Zhou, S.R. Nutt, C.C. Bampton, E.J. Lavernia, Nanostructure in an Al-Mg-Sc Alloy Processed by Low-Energy Ball Milling at Cryogenic Temperature, *Metall. Mater. Trans. A* 34 A (2003).
- [49] V.K. Pecharsky, V.K. Pecharsky, K.A. Gschneidner, K.A. Gschneidner, A.O. Pecharsky, A.M. Tishin, Thermodynamics of the magnetocaloric effect, *Phys. Rev. B - Condens. Matter Mater. Phys.* (2001). <https://doi.org/10.1103/PhysRevB.64.144406>.
- [50] V.K. Pecharsky, K.A. Gschneidner, Magnetocaloric effect and magnetic refrigeration, *J. Magn. Magn. Mater.* (1999). [https://doi.org/10.1016/S0304-8853\(99\)00397-2](https://doi.org/10.1016/S0304-8853(99)00397-2).
- [51] J. Lyubina, Magnetocaloric materials for energy efficient cooling, *J. Phys. D. Appl. Phys.* (2017). <https://doi.org/10.1088/1361-6463/50/5/053002>.
- [52] V.D. Buchelnikov, V. V. Sokolovskiy, Magnetocaloric effect in Ni-Mn-X (X = Ga, In, Sn, Sb) heusler alloys, *Phys. Met. Metallogr.* (2011). <https://doi.org/10.1134/S0031918X11070052>.
- [53] P.J. Von Ranke, N.A. De Oliveira, B.P. Alho, E.J.R. Plaza, V.S.R. De Sousa, L. Caron, M.S. Reis, Understanding the inverse magnetocaloric effect in antiferro-and ferrimagnetic arrangements, *J. Phys. Condens. Matter.* (2009). <https://doi.org/10.1088/0953-8984/21/5/056004>.
- [54] E. Stern-Taulats, T. Castán, A. Planes, L.H. Lewis, R. Barua, S. Pramanick, S. Majumdar, L. Mañosa, Giant multicaloric response of bulk Fe₄₉Rh₅₁, *Phys. Rev. B.* (2017). <https://doi.org/10.1103/PhysRevB.95.104424>.
- [55] C.P. Bean, D.S. Rodbell, Magnetic disorder as a first-order phase transformation, *Phys. Rev.* (1962). <https://doi.org/10.1103/PhysRev.126.104>.

- [56] O. Tegus, G.X. Lin, W. Dagula, B. Fuquan, L. Zhang, E. Brück, F.R. De Boer, K.H.J. Buschow, A model description of the first-order phase transition in MnFeP 1-xAsx, in: *J. Magn. Mater.*, 2005. <https://doi.org/10.1016/j.jmmm.2004.11.325>.
- [57] T. Gottschall, On the magnetocaloric properties of Heusler compounds: Reversible, time- and size-dependent effects of the martensitic phase transition, 2016.
- [58] A. Giguère, M. Foldeaki, B. Ravi Gopal, R. Chahine, T.K. Bose, A. Frydman, J.A. Barclay, Direct measurement of the “giant” adiabatic temperature change in Gd₅Si₂Ge₂, *Phys. Rev. Lett.* (1999). <https://doi.org/10.1103/PhysRevLett.83.2262>.
- [59] F. Casanova, X. Batlle, A. Labarta, J. Marcos, L. Mañosa, A. Planes, Entropy change and magnetocaloric effect in Gd₅(SixGe_{1-x})₄, *Phys. Rev. B - Condens. Matter Mater. Phys.* (2002).
- [60] L. Caron, Z.Q. Ou, T.T. Nguyen, D.T. Cam Thanh, O. Tegus, E. Brück, On the determination of the magnetic entropy change in materials with first-order transitions, *J. Magn. Mater.* (2009). <https://doi.org/10.1016/j.jmmm.2009.06.086>.
- [61] K.A. Gschneidner, V.K. Pecharsky, E. Brück, H.G.M. Duijn, E.M. Levin, Comment on “direct measurement of the ‘giant’ adiabatic temperature change in Gd₅Si₂Ge₂,” *Phys. Rev. Lett.* (2000). <https://doi.org/10.1103/PhysRevLett.85.4190>.
- [62] J.R. Sun, F.X. Hu, B.G. Shen, Comment on “direct measurement of the ‘Giant’ adiabatic temperature change in Gd₅Si₂Ge₂,” *Phys. Rev. Lett.* (2000). <https://doi.org/10.1103/PhysRevLett.85.4191>.
- [63] A.M. Tishin, Y.I. Spichkin, The magnetocaloric effect and its applications, 2016. <https://doi.org/10.1887/0750309229>.
- [64] O. Gutfleisch, T. Gottschall, M. Fries, D. Benke, I. Radulov, K.P. Skokov, H. Wende, M. Gruner, M. Acet, P. Entel, M. Farle, Mastering hysteresis in magnetocaloric materials, *Philos. Trans. R. Soc. A Math. Phys. Eng. Sci.* 374 (2016). <https://doi.org/10.1098/rsta.2015.0308>.
- [65] G. Porcari, F. Cugini, S. Fabbrici, C. Pernechele, F. Albertini, M. Buzzi, M. Mangia, M. Solzi, Convergence of direct and indirect methods in the magnetocaloric study of first order transformations: The case of Ni-Co-Mn-Ga Heusler alloys, *Phys. Rev. B - Condens. Matter Mater. Phys.* (2012). <https://doi.org/10.1103/PhysRevB.86.104432>.
- [66] F. Cugini, G. Porcari, M. Solzi, Non-contact direct measurement of the magnetocaloric effect in thin samples, *Rev. Sci. Instrum.* (2014). <https://doi.org/10.1063/1.4890394>.
- [67] F. Cugini, M. Solzi, On the direct measurement of the adiabatic temperature change of magnetocaloric materials, *J. Appl. Phys.* (2020). <https://doi.org/10.1063/5.0002870>.
- [68] F. Cugini, L. Righi, L. van Eijck, E. Brück, M. Solzi, Cold working consequence on the magnetocaloric effect of Ni₅₀Mn₃₄In₁₆ Heusler alloy, *J. Alloys Compd.* (2018). <https://doi.org/10.1016/j.jallcom.2018.03.293>.
- [69] T. Kihara, Y. Kohama, Y. Hashimoto, S. Katsumoto, M. Tokunaga, Adiabatic measurements of magneto-caloric effects in pulsed high magnetic fields up to 55 T, *Rev. Sci. Instrum.* (2013). <https://doi.org/10.1063/1.4811798>.
- [70] C.J. Palmstrøm, Heusler compounds and spintronics, *Prog. Cryst. Growth Charact. Mater.*

- (2016). <https://doi.org/10.1016/j.pcrysgrow.2016.04.020>.
- [71] S. Singh, L. Caron, S.W. D'Souza, T. Fichtner, G. Porcari, S. Fabbri, C. Shekhar, S. Chadov, M. Solzi, C. Felser, Large Magnetization and Reversible Magnetocaloric Effect at the Second-Order Magnetic Transition in Heusler Materials, *Adv. Mater.* (2016). <https://doi.org/10.1002/adma.201505571>.
- [72] V. Recarte, J.I. Pérez-Landazábal, V. Sánchez-Alarcos, J.A. Rodríguez-Velamazán, Dependence of the martensitic transformation and magnetic transition on the atomic order in Ni-Mn-In metamagnetic shape memory alloys, *Acta Mater.* (2012). <https://doi.org/10.1016/j.actamat.2012.01.020>.
- [73] T. Miyamoto, W. Ito, R.Y. Umetsu, R. Kainuma, T. Kanomata, K. Ishida, Phase stability and magnetic properties of Ni₅₀Mn_{50-x}In_x Heusler-type alloys, *Scr. Mater.* (2010). <https://doi.org/10.1016/j.scriptamat.2009.10.006>.
- [74] M. Acet, L. Mañosa, A. Planes, Magnetic-Field-Induced Effects in Martensitic Heusler-Based Magnetic Shape Memory Alloys, in: *Handb. Magn. Mater.*, 2011. <https://doi.org/10.1016/B978-0-444-53780-5.00004-1>.
- [75] P. Entel, V.D. Buchelnikov, V. V. Khovailo, A.T. Zayak, W.A. Adeagbo, M.E. Gruner, H.C. Herper, E.F. Wassermann, Modelling the phase diagram of magnetic shape memory Heusler alloys, *J. Phys. D. Appl. Phys.* 39 (2006) 865–889. <https://doi.org/10.1088/0022-3727/39/5/S13>.
- [76] L. Righi, F. Albertini, S. Fabbri, A. Paoluzi, Crystal structures of modulated martensitic phases of FSM Heusler alloys, *Mater. Sci. Forum.* (2011). <https://doi.org/10.4028/www.scientific.net/MSF.684.105>.
- [77] P. Entel, M. Siewert, M.E. Gruner, H.C. Herper, D. Comtesse, R. Arróyave, N. Singh, A. Talapatra, V. V. Sokolovskiy, V.D. Buchelnikov, F. Albertini, L. Righi, V.A. Chernenko, Complex magnetic ordering as a driving mechanism of multifunctional properties of Heusler alloys from first principles, *Eur. Phys. J. B.* (2013). <https://doi.org/10.1140/epjb/e2012-30936-9>.
- [78] R. Niemann, U.K. Röäßler, M.E. Gruner, O. Heczko, L. Schultz, S. Fähler, The role of adaptive martensite in magnetic shape memory alloys, *Adv. Eng. Mater.* (2012). <https://doi.org/10.1002/adem.201200058>.
- [79] J. Ortín, A. Planes, Thermodynamic analysis of thermal measurements in thermoelastic martensitic transformations, *Acta Metall.* (1988). [https://doi.org/10.1016/0001-6160\(88\)90291-X](https://doi.org/10.1016/0001-6160(88)90291-X).
- [80] P. Wollants, J.R. Roos, L. Delaey, Thermally- and stress-induced thermoelastic martensitic transformations in the reference frame of equilibrium thermodynamics, *Prog. Mater. Sci.* (1993). [https://doi.org/10.1016/0079-6425\(93\)90005-6](https://doi.org/10.1016/0079-6425(93)90005-6).
- [81] M. Wang, M. Jiang, G. Liao, S. Guo, X. Zhao, Martensitic transformation involved mechanical behaviors and wide hysteresis of NiTiNb shape memory alloys, *Prog. Nat. Sci. Mater. Int.* (2012). <https://doi.org/10.1016/j.pnsc.2012.03.010>.
- [82] N.M. Bruno, C. Yegin, I. Karaman, J.H. Chen, J.H. Ross, J. Liu, J. Li, The effect of heat treatments on Ni₄₃Mn₄₂Co₄Sn₁₁ meta-magnetic shape memory alloys for magnetic refrigeration, *Acta Mater.* (2014). <https://doi.org/10.1016/j.actamat.2014.03.020>.

- [83] L. Righi, F. Albertini, E. Villa, A. Paoluzi, G. Calestani, V. Chernenko, S. Besseghini, C. Ritter, F. Passaretti, Crystal structure of 7M modulated Ni-Mn-Ga martensitic phase, *Acta Mater.* (2008). <https://doi.org/10.1016/j.actamat.2008.05.010>.
- [84] P.J. Webster, K.R.A. Ziebeck, S.L. Town, M.S. Peak, Magnetic order and phase transformation in Ni₂MnGa, *Philos. Mag. B Phys. Condens. Matter; Stat. Mech. Electron. Opt. Magn. Prop.* (1984). <https://doi.org/10.1080/13642817408246515>.
- [85] A.G. Khachatryan, S.M. Shapiro, S. Semenovskaya, Adaptive phase formation in martensitic transformation, *Phys. Rev. B.* (1991). <https://doi.org/10.1103/PhysRevB.43.10832>.
- [86] V. V. Sokolovskiy, V.D. Buchelnikov, S. V. Taskaev, V. V. Khovaylo, M. Ogura, P. Entel, Quaternary Ni-Mn-In-Y Heusler alloys: A way to achieve materials with better magnetocaloric properties?, *J. Phys. D. Appl. Phys.* (2013). <https://doi.org/10.1088/0022-3727/46/30/305003>.
- [87] E. Şaşıoğlu, L.M. Sandratskii, P. Bruno, Role of conduction electrons in mediating exchange interactions in Mn-based Heusler alloys, *Phys. Rev. B - Condens. Matter Mater. Phys.* (2008). <https://doi.org/10.1103/PhysRevB.77.064417>.
- [88] G. Cavazzini, F. Cugini, M.E. Gruner, C. Bennati, L. Righi, S. Fabbri, F. Albertini, M. Solzi, Tuning the magnetic and magnetocaloric properties of austenitic Ni-Mn-(In,Sn)Heuslers, *Scr. Mater.* (2019). <https://doi.org/10.1016/j.scriptamat.2019.05.027>.
- [89] P. Entel, M.E. Gruner, D. Comtesse, M. Wuttig, Interaction of phase transformation and magnetic properties of heusler alloys: A density functional theory study, *JOM.* (2013). <https://doi.org/10.1007/s11837-013-0757-2>.
- [90] P. Entel, M.E. Gruner, S. Fähler, M. Acet, A. Çahır, R. Arróyave, S. Sahoo, T.C. Duong, A. Talapatra, L. Sandratskii, S. Mankowsky, T. Gottschall, O. Gutfleisch, P. Lázpita, V.A. Chernenko, J.M. Barandiaran, V. V. Sokolovskiy, V.D. Buchelnikov, Probing Structural and Magnetic Instabilities and Hysteresis in Heuslers by Density Functional Theory Calculations, *Phys. Status Solidi Basic Res.* (2018). <https://doi.org/10.1002/pssb.201700296>.
- [91] V. V. Sokolovskiy, M.E. Gruner, P. Entel, M. Acet, A. Cakir, D.R. Baigutlin, V.D. Buchelnikov, Segregation tendency of Heusler alloys, *Phys. Rev. Mat.* 3 (2019).
- [92] V. Sánchez-Alarcos, V. Recarte, J.I. Pérez-Landazábal, G.J. Cuello, Correlation between atomic order and the characteristics of the structural and magnetic transformations in Ni-Mn-Ga shape memory alloys, *Acta Mater.* (2007). <https://doi.org/10.1016/j.actamat.2007.03.001>.
- [93] J. López-García, I. Unzueta, V. Sánchez-Alarcos, V. Recarte, J.I. Pérez-Landazábal, J.A. Rodríguez-Velamazán, J.A. García, F. Plazaola, Correlation between defects and magnetostructural properties in Ni-Mn-Sn metamagnetic shape memory alloys, *Intermetallics.* (2018). <https://doi.org/10.1016/j.intermet.2017.12.028>.
- [94] N.M. Bruno, Y.J. Huang, C.L. Dennis, J.G. Li, R.D. Shull, J.H. Ross, Y.I. Chumlyakov, I. Karaman, Effect of grain constraint on the field requirements for magnetocaloric effect in Ni₄₅Co₅Mn₄₀Sn₁₀ melt-spun ribbons, *J. Appl. Phys.* (2016). <https://doi.org/10.1063/1.4960353>.
- [95] N.M. Bruno, D. Salas, S. Wang, I. V. Roshchin, R. Santamarta, R. Arroyave, T. Duong, Y.I. Chumlyakov, I. Karaman, On the microstructural origins of martensitic transformation arrest in a NiCoMnIn magnetic shape memory alloy, *Acta Mater.* (2018).

- <https://doi.org/10.1016/j.actamat.2017.08.037>.
- [96] D. Salas, O. Eliseeva, Y. Wang, T. Duong, Y.I. Chumlyakov, Y. Ren, R. Arroyave, I. Karaman, Effects of composition and crystallographic ordering on the ferromagnetic transition in Ni–Co–Mn–In magnetic shape memory alloys, *Acta Mater.* (2019). <https://doi.org/10.1016/j.actamat.2019.01.008>.
- [97] J.A. Monroe, J.E. Raymond, X. Xu, M. Nagasako, R. Kainuma, Y.I. Chumlyakov, R. Arroyave, I. Karaman, Multiple ferroic glasses via ordering, *Acta Mater.* (2015). <https://doi.org/10.1016/j.actamat.2015.08.049>.
- [98] T. Gottschall, K.P. Skokov, B. Frincu, O. Gutfleisch, Large reversible magnetocaloric effect in Ni-Mn-In-Co, *Appl. Phys. Lett.* (2015). <https://doi.org/10.1063/1.4905371>.
- [99] A. Planes, E. Stern-Taulats, T. Castán, E. Vives, L. Mañosa, A. Saxena, Caloric and Multicaloric Effects in Shape Memory Alloys, in: *Mater. Today Proc.*, 2015. <https://doi.org/10.1016/j.matpr.2015.07.332>.
- [100] J. Cui, Y.S. Chu, O.O. Famodu, Y. Furuya, J. Hattrick-Simpers, R.D. James, A. Ludwig, S. Thienhaus, M. Wuttig, Z. Zhang, I. Takeuchi, Combinatorial search of thermoelastic shape-memory alloys with extremely small hysteresis width, *Nat. Mater.* (2006). <https://doi.org/10.1038/nmat1593>.
- [101] I. Titov, M. Acet, M. Farle, D. González-Alonso, L. Mañosa, A. Planes, T. Krenke, Hysteresis effects in the inverse magnetocaloric effect in martensitic Ni-Mn-In and Ni-Mn-Sn, *J. Appl. Phys.* (2012). <https://doi.org/10.1063/1.4757425>.
- [102] C. Magen, L. Morellon, P.A. Algarabel, M.R. Ibarra, Z. Arnold, J. Kamarad, T.A. Lograsso, D.L. Schlagel, V.K. Pecharsky, A.O. Tsokol, K.A. Gschneidner, Hydrostatic pressure control of the magnetostructural phase transition in Gd₅Si₂Ge₂ single crystals, *Phys. Rev. B - Condens. Matter Mater. Phys.* (2005). <https://doi.org/10.1103/PhysRevB.72.024416>.
- [103] J. Lyubina, K. Nenkov, L. Schultz, O. Gutfleisch, Multiple metamagnetic transitions in the magnetic refrigerant La(Fe,Si)₁₃Hx, *Phys. Rev. Lett.* (2008). <https://doi.org/10.1103/PhysRevLett.101.177203>.
- [104] L. Mañosa, X. Moya, A. Planes, O. Gutfleisch, J. Lyubina, M. Barrio, J.L. Tamarit, S. Aksoy, T. Krenke, M. Acet, Effects of hydrostatic pressure on the magnetism and martensitic transition of Ni-Mn-In magnetic superelastic alloys, *Appl. Phys. Lett.* (2008). <https://doi.org/10.1063/1.2830999>.
- [105] K. Ullakko, J.K. Huang, C. Kantner, R.C. O’Handley, V. V. Kokorin, Large magnetic-field-induced strains in Ni₂MnGa single crystals, *Appl. Phys. Lett.* (1996). <https://doi.org/10.1063/1.117637>.
- [106] S. Stadler, M. Khan, J. Mitchell, N. Ali, A.M. Gomes, I. Dubenko, A.Y. Takeuchi, A.P. Guimarães, Magnetocaloric properties of Ni₂Mn_{1-x}Cu_xGa, *Appl. Phys. Lett.* (2006). <https://doi.org/10.1063/1.2202751>.
- [107] R. Hergt, S. Dutz, R. Müller, M. Zeisberger, Magnetic particle hyperthermia: Nanoparticle magnetism and materials development for cancer therapy, *J. Phys. Condens. Matter.* (2006). <https://doi.org/10.1088/0953-8984/18/38/S26>.
- [108] S. Laurent, S. Dutz, U.O. Häfeli, M. Mahmoudi, Magnetic fluid hyperthermia: Focus on

- superparamagnetic iron oxide nanoparticles, *Adv. Colloid Interface Sci.* (2011). <https://doi.org/10.1016/j.cis.2011.04.003>.
- [109] A. Espinosa, J. Kolosnjaj-Tabi, A. Abou-Hassan, A. Plan Sangnier, A. Curcio, A.K.A. Silva, R. Di Corato, S. Neveu, T. Pellegrino, L.M. Liz-Marzán, C. Wilhelm, Magnetic (Hyper)Thermia or Photothermia? Progressive Comparison of Iron Oxide and Gold Nanoparticles Heating in Water, in Cells, and In Vivo, *Adv. Funct. Mater.* 28 (2018). <https://doi.org/10.1002/adfm.201803660>.
- [110] H.G. Bagaria, J.L. Phillips, D.E. Nikles, D.T. Johnson, Self-regulated magnetic fluid hyperthermia, in: *AICHe Annu. Meet. Conf. Proc.*, 2005.
- [111] M. Campanini, R. Ciprian, E. Bedogni, A. Mega, V. Chiesi, F. Casoli, C. De Julián Fernández, E. Rotunno, F. Rossi, A. Secchi, F. Bigi, G. Salviati, C. Magén, V. Grillo, F. Albertini, Lorentz microscopy sheds light on the role of dipolar interactions in magnetic hyperthermia, *Nanoscale.* (2015). <https://doi.org/10.1039/c5nr00273g>.
- [112] P. Guardia, R. Di Corato, L. Lartigue, C. Wilhelm, A. Espinosa, M. Garcia-Hernandez, F. Gazeau, L. Manna, T. Pellegrino, Water-soluble iron oxide nanocubes with high values of specific absorption rate for cancer cell hyperthermia treatment, *ACS Nano.* (2012). <https://doi.org/10.1021/nn2048137>.
- [113] D. Niculaes, A. Lak, G.C. Anyfantis, S. Marras, O. Laslett, S.K. Avugadda, M. Cassani, D. Serantes, O. Hovorka, R. Chantrell, T. Pellegrino, Asymmetric Assembling of Iron Oxide Nanocubes for Improving Magnetic Hyperthermia Performance, *ACS Nano.* (2017). <https://doi.org/10.1021/acsnano.7b05182>.
- [114] C. Dhand, N. Dwivedi, X.J. Loh, A.N. Jie Ying, N.K. Verma, R.W. Beuerman, R. Lakshminarayanan, S. Ramakrishna, Methods and strategies for the synthesis of diverse nanoparticles and their applications: A comprehensive overview, *RSC Adv.* (2015). <https://doi.org/10.1039/c5ra19388e>.
- [115] H.J. Fecht, E. Hellstern, Z. Fu, W.L. Johnson, Nanocrystalline metals prepared by high-energy ball milling, *Metall. Trans. A.* (1990). <https://doi.org/10.1007/BF02646980>.
- [116] D.B. Witkin, E.J. Lavernia, Synthesis and mechanical behavior of nanostructured materials via cryomilling, *Prog. Mater. Sci.* 51 (2006).
- [117] S.M. Almotairy, A.F. Boostani, M. Hassani, D. Wei, Z.Y. Jiang, Effect of hot isostatic pressing on the mechanical properties of aluminium metal matrix nanocomposites produced by dual speed ball milling, *J. Mater. Res. Technol.* (2020). <https://doi.org/10.1016/j.jmrt.2019.11.043>.
- [118] C. Wen, A. Nouri, Surfactants in Mechanical Alloying/Milling: A Catch-22 Situation, *Crit. Rev. Solid State Mater. Sci.* 39 (2014).
- [119] C. Suryanarayana, Mechanical alloying and milling, CRC Press, 2004. <https://doi.org/10.4150/kpmi.2006.13.5.371>.
- [120] Government Scientific Source, (n.d.). <https://marketing.govsci.com/2019/03/27/the-8000-line-mixer-mill-powerful-high-energy-ball-mills/>.
- [121] No Title, (n.d.). <https://www.retsch.com/products/milling/ball-mills/mixer-mill-cryomill/function-features/>.

- [122] J. Ye, J. He, J.M. Schoenung, Cryomilling for the fabrication of a particulate B4C reinforced Al nanocomposite: Part I. Effects of process conditions on structure, *Metall. Mater. Trans. A Phys. Metall. Mater. Sci.* (2006). <https://doi.org/10.1007/s11661-006-0190-z>.
- [123] M. Ullah, M.E. Ali, S.B.A. Hamid, Surfactant-assisted ball milling: A novel route to novel materials with controlled nanostructure—A review, *Rev. Adv. Mater. Sci.* (2014).
- [124] V. Petříček, M. Dušek, L. Palatinus, Crystallographic computing system JANA2006: General features, *Zeitschrift Fur Krist.* (2014). <https://doi.org/10.1515/zkri-2014-1737>.
- [125] P. Laurent, J.F. Fagnard, B. Vanderheyden, N. Hari Babu, D.A. Cardwell, M. Ausloos, P. Vanderbemden, An ac susceptometer for the characterization of large, bulk superconducting samples, *Meas. Sci. Technol.* (2008). <https://doi.org/10.1088/0957-0233/19/8/085705>.
- [126] M. Nikolo, Superconductivity: A guide to alternating current susceptibility measurements and alternating current susceptometer design, *Am. J. Phys.* (1995). <https://doi.org/10.1119/1.17770>.
- [127] K.L. Chen, J.H. Chen, S.H. Liao, J.J. Chieh, H.E. Horng, L.M. Wang, H.C. Yang, Magnetic clustering effect during the association of biofunctionalized magnetic nanoparticles with biomarkers, *PLoS One.* (2015). <https://doi.org/10.1371/journal.pone.0135290>.
- [128] T.S. Tripathi, G.C. Tewari, A.K. Rastogi, A magnetometer for cryogen-free systems: Extraction and integration method, *Curr. Sci.* (2009).
- [129] F. Albertini, L. Pareti, A. Paoluzi, L. Morellon, P.A. Algarabel, M.R. Ibarra, L. Righi, Composition and temperature dependence of the magnetocrystalline anisotropy in $\text{Ni}_{2+x}\text{Mn}_{1+y}\text{Ga}_{1+z}$ ($x+y+z=0$) heusler alloys, *Appl. Phys. Lett.* (2002). <https://doi.org/10.1063/1.1525071>.
- [130] F. Albertini, L. Morellon, P.A. Algarabel, M.R. Ibarra, L. Pareti, Z. Arnold, E. Al., Magnetoelastic effects and magnetic anisotropy in Ni_2MnGa polycrystals, *J. Appl. Phys.* 89 (2001).
- [131] M. V. McLeod, D. Bayer, Z. Turgut, A.K. Giri, B.S. Majumdar, Significant enhancement of magnetocaloric effect in a NiMnCuGa Heusler alloy through textural modification, *J. Appl. Phys.* (2020). <https://doi.org/10.1063/5.0003366>.
- [132] A. Taubel, T. Gottschall, M. Fries, S. Riegg, C. Soon, K.P. Skokov, O. Gutfleisch, A Comparative Study on the Magnetocaloric Properties of Ni-Mn-X(-Co) Heusler Alloys, *Phys. Status Solidi Basic Res.* (2018). <https://doi.org/10.1002/pssb.201700331>.
- [133] Y. Liu, Z. Xie, Detwinning in shape memory alloy, 2007.
- [134] X.M. Huang, L. Da Wang, H.X. Liu, H. Le Yan, N. Jia, B. Yang, Z. Bin Li, Y.D. Zhang, C. Esling, X. Zhao, L. Zuo, Correlation between microstructure and martensitic transformation, mechanical properties and elastocaloric effect in Ni-Mn-based alloys, *Intermetallics.* (2019). <https://doi.org/10.1016/j.intermet.2019.106579>.
- [135] Y. Feng, H. Chen, F. Xiao, X. Bian, P. Wang, Improvement of mechanical property and large shape recovery of sintered $\text{Ni}_{45}\text{Mn}_{36.6}\text{In}_{13.4}\text{Co}_5$ alloy, *J. Alloys Compd.* (2018). <https://doi.org/10.1016/j.jallcom.2018.06.244>.
- [136] C.-L. Tan, K. Zhang, X.-H. Tian, W. Cai, Magnetic and mechanical properties of Ni-Mn-

- Ga/Fe–Ga ferromagnetic shape memory composite, *Chin. Phys. B.* 24 (2015).
- [137] J. Wang, H. Wang, C. Jiang, Microstructure and mechanical properties of a Ni₃₀Cu₂₀Mn_{41.5}Ga_{8.5} dual-phase shape memory alloy, *Mater. Sci. Eng. A.* (2013). <https://doi.org/10.1016/j.msea.2013.04.111>.
- [138] A. Cakir, L. Righi, F. Albertini, M. Acet, M. Farle, S. Akturk, Extended investigation of intermartensitic transitions in Ni–Mn–Ga magnetic shape memory alloys: A detailed phase diagram determination, *J. Appl. Phys.* 114 (2013).
- [139] A. Sozinov, A.A. Likhachev, N. Lanska, O. Soderberg, K. Ullakko, V.K. Lindroos, Effect of crystal structure on magnetic-field-induced strain in Ni–Mn–Ga, in: *Smart Struct. Mater. 2003 Act. Mater. Behav. Mech.*, 2003. <https://doi.org/10.1117/12.484353>.
- [140] Y. Ge, N. Zárubová, O. Heczko, S.P. Hannula, Stress-induced transition from modulated 14M to non-modulated martensite in Ni–Mn–Ga alloy, *Acta Mater.* (2015). <https://doi.org/10.1016/j.actamat.2015.02.028>.
- [141] S. Roth, U. Gaitzsch, M. Pötschke, L. Schultz, Magneto–mechanical behaviour of textured polycrystals of NiMnGa ferromagnetic shape memory alloys, in: *Adv. Mater. Res.*, 2008. <https://doi.org/10.4028/www.scientific.net/amr.52.29>.
- [142] Y. Liu, I. Karaman, H. Wang, X. Zhang, Two types of martensitic phase transformations in magnetic shape memory alloys by in-situ nanoindentation studies, *Adv. Mater.* (2014). <https://doi.org/10.1002/adma.201400217>.
- [143] A. Mansouri Tehrani, H. Shahrokhshahi, N. Parvin, J. Brgoch, Influencing the martensitic phase transformation in NiTi through point defects, *J. Appl. Phys.* (2015). <https://doi.org/10.1063/1.4923474>.
- [144] T.Y. Hsu, Y. Linfah, The effect of quenched-in vacancies on the martensitic transformation, *J. Mater. Sci.* (1983). <https://doi.org/10.1007/BF00544145>.
- [145] C. Celada-Casero, J. Sietsma, M.J. Santofimia, The role of the austenite grain size in the martensitic transformation in low carbon steels, *Mater. Des.* (2019). <https://doi.org/10.1016/j.matdes.2019.107625>.
- [146] T. Gottschall, D. Benke, M. Fries, A. Taubel, I.A. Radulov, K.P. Skokov, O. Gutfleisch, A Matter of Size and Stress: Understanding the First–Order Transition in Materials for Solid-State Refrigeration, *Adv. Funct. Mater.* (2017). <https://doi.org/10.1002/adfm.201606735>.
- [147] F. Girgisdies, *Peak Profile Analysis in X-ray Powder Diffraction*, (n.d.).
- [148] P. Scardi, M. Leoni, R. Delhez, Line broadening analysis using integral breadth methods: A critical review, *J. Appl. Crystallogr.* (2004). <https://doi.org/10.1107/S0021889804004583>.
- [149] Y. Zhao, J. Zhang, Microstrain and grain-size analysis from diffraction peak width and graphical derivation of high-pressure thermomechanics, *J. Appl. Crystallogr.* (2008). <https://doi.org/10.1107/S0021889808031762>.
- [150] J.I. Pérez-Landazábal, V. Recarte, V. Sánchez-Alarcos, C. Gómez-Polo, E. Cesari, Magnetic properties of the martensitic phase in Ni–Mn–In–Co metamagnetic shape memory alloys, *Appl. Phys. Lett.* (2013). <https://doi.org/10.1063/1.4795716>.

- [151] W. Ito, K. Ito, R.Y. Umetsu, R. Kainuma, K. Koyama, K. Watanabe, A. Fujita, K. Oikawa, K. Ishida, T. Kanomata, Kinetic arrest of martensitic transformation in the NiCoMnIn metamagnetic shape memory alloy, *Appl. Phys. Lett.* (2008). <https://doi.org/10.1063/1.2833699>.
- [152] W. Ito, Y. Imano, R. Kainuma, Y. Sutou, K. Oikawa, K. Ishida, Martensitic and magnetic transformation behaviors in Heusler-type NiMnIn and NiCoMnIn metamagnetic shape memory alloys, in: *Metall. Mater. Trans. A Phys. Metall. Mater. Sci.*, 2007. <https://doi.org/10.1007/s11661-007-9094-9>.
- [153] V. Sánchez-Alarcos, V. Recarte, J.I. Pérez-Landazábal, E. Cesari, J.A. Rodríguez-Velamazán, Long-range atomic order and entropy change at the martensitic transformation in a Ni-Mn-In-Co metamagnetic shape memory alloy, *Entropy*. (2014). <https://doi.org/10.3390/e16052756>.
- [154] W. Ito, M. Nagasako, R.Y. Umetsu, R. Kainuma, T. Kanomata, K. Ishida, Atomic ordering and magnetic properties in the Ni₄₅Co₅Mn_{36.7}In_{13.3} metamagnetic shape memory alloy, *Appl. Phys. Lett.* (2008). <https://doi.org/10.1063/1.3043456>.
- [155] Y. Wang, D. Salas, T.C. Duong, B. Medasani, A. Talapatra, Y. Ren, Y.I. Chumlyakov, I. Karaman, R. Arróyave, On the fast kinetics of B2-L21 ordering in Ni-Co-Mn-In metamagnetic shape memory alloys, *J. Alloys Compd.* (2019). <https://doi.org/10.1016/j.jallcom.2018.12.034>.
- [156] P. La Roca, L. Isola, P. Vermaut, J. Malarria, Relationship between grain size and thermal hysteresis of martensitic transformations in Cu-based shape memory alloys, *Scr. Mater.* (2017). <https://doi.org/10.1016/j.scriptamat.2017.03.016>.
- [157] Y. Chen, C.A. Schuh, Size effects in shape memory alloy microwires, *Acta Mater.* (2011). <https://doi.org/10.1016/j.actamat.2010.09.057>.
- [158] F. Orlandi, S. Fabbri, F. Albertini, P. Manuel, D.D. Khalyavin, L. Righi, Long-range antiferromagnetic interactions in Ni-Co-Mn-Ga metamagnetic Heusler alloys: A two-step ordering studied by neutron diffraction, *Phys. Rev. B.* (2016). <https://doi.org/10.1103/PhysRevB.94.140409>.
- [159] K.R. Priolkar, P.A. Bhoje, D.N. Lobo, S.W. D'Souza, S.R. Barman, A. Chakrabarti, S. Emura, Antiferromagnetic exchange interactions in the Ni₂Mn_{1.4}In_{0.6} ferromagnetic Heusler alloy, *Phys. Rev. B - Condens. Matter Mater. Phys.* (2013). <https://doi.org/10.1103/PhysRevB.87.144412>.
- [160] N. Kumar, K. Biswas, Cryomilling: An environment friendly approach of preparation large quantity ultra refined pure aluminium nanoparticles, *J. Mater. Res. Technol.* (2019). <https://doi.org/10.1016/j.jmrt.2017.05.017>.
- [161] M. Qian, X. Zhang, Z. Jia, X. Wan, L. Geng, Enhanced magnetic refrigeration capacity in Ni-Mn-Ga micro-particles, *Mater. Des.* (2018). <https://doi.org/10.1016/j.matdes.2018.03.062>.
- [162] Y. Xin, Y. Li, Microstructure, mechanical and shape memory properties of polycrystalline Ni-Mn-Ga High temperature shape memory alloys, *Mater. Sci. Eng. A.* (2016). <https://doi.org/10.1016/j.msea.2015.09.123>.
- [163] S. Nasrin, F.U.Z. Chowdhury, S.M. Hoque, Study of hyperthermia temperature of manganese-substituted cobalt nano ferrites prepared by chemical co-precipitation method for biomedical application, *J. Magn. Magn. Mater.* (2019). <https://doi.org/10.1016/j.jmmm.2019.02.010>.

- [164] M. Pavel, A. Stancu, Ferromagnetic nanoparticles dose based on tumor size in magnetic fluid hyperthermia cancer therapy, in: *IEEE Trans. Magn.*, 2009. <https://doi.org/10.1109/TMAG.2009.2031076>.
- [165] A.G. Belous, Synthesis and properties of ferromagnetic nanostructures and their possible use in medicine and microwave engineering, in: *Int. Conf. Oxide Mater. Electron. Eng. - Fabr. Prop. Appl. OMEE 2014 - B. Conf. Proc.*, 2014. <https://doi.org/10.1109/OMEE.2014.6912344>.
- [166] E. Pollert, O. Kaman, P. Veverka, M. Veverka, M. Maryško, K. Zavřeta, M. Kačenka, L. Lukeš, P. Jendelová, P. Kašpar, M. Burian, V. Herynek, Core-shell La_{1-x}Sr_xMnO₃ nanoparticles as colloidal mediators for magnetic fluid hyperthermia, in: *Philos. Trans. R. Soc. A Math. Phys. Eng. Sci.*, 2010. <https://doi.org/10.1098/rsta.2010.0123>.
- [167] E. Fantechi, C. Innocenti, M. Zanardelli, M. Fittipaldi, E. Falvo, M. Carbo, V. Shullani, L. Di Cesare Mannelli, C. Ghelardini, A.M. Ferretti, A. Ponti, C. Sangregorio, P. Ceci, A smart platform for hyperthermia application in cancer treatment: Cobalt-doped ferrite nanoparticles mineralized in human ferritin cages, *ACS Nano*. (2014). <https://doi.org/10.1021/nn500454n>.
- [168] I. Conde-Leboran, D. Baldomir, C. Martinez-Boubeta, O. Chubykalo-Fesenko, M. Del Puerto Morales, G. Salas, D. Cabrera, J. Camarero, F.J. Teran, D. Serantes, A Single Picture Explains Diversity of Hyperthermia Response of Magnetic Nanoparticles, *J. Phys. Chem. C*. (2015). <https://doi.org/10.1021/acs.jpcc.5b02555>.
- [169] R.Y. Umetsu, W. Ito, K. Ito, K. Koyama, A. Fujita, K. Oikawa, T. Kanomata, R. Kainuma, K. Ishida, Anomaly in entropy change between parent and martensite phases in the Ni₅₀Mn₃₄In₁₆ Heusler alloy, *Scr. Mater.* (2009). <https://doi.org/10.1016/j.scriptamat.2008.08.022>.
- [170] W. Ito, R.Y. Umetsu, R. Kainuma, T. Kakeshita, K. Ishida, Heat-induced and isothermal martensitic transformations from kinetically arrested parent phase in NiCoMnIn metamagnetic shape memory alloy, *Scr. Mater.* (2010). <https://doi.org/10.1016/j.scriptamat.2010.03.010>.
- [171] P.R. Rios, F. Siciliano, H.R.Z. Sandim, R.L. Plaut, A.F. Padilha, Nucleation and growth during recrystallization, *Mater. Res.* (2005). <https://doi.org/10.1590/S1516-14392005000300002>.
- [172] I.Z. Awan, A.Q. Khan, Recovery, recrystallization, and grain-growth, *J. Chem. Soc. Pakistan*. (2019). <https://doi.org/10.1016/b978-008044019-4/50024-6>.
- [173] Q. Sun, A. Aslan, M. Li, M. Chen, Effects of grain size on phase transition behavior of nanocrystalline shape memory alloys, *Sci. China Technol. Sci.* (2014). <https://doi.org/10.1007/s11431-014-5505-5>.
- [174] J. Liu, T.G. Woodcock, N. Scheerbaum, O. Gutfleisch, Influence of annealing on magnetic field-induced structural transformation and magnetocaloric effect in Ni-Mn-In-Co ribbons, *Acta Mater.* (2009). <https://doi.org/10.1016/j.actamat.2009.06.054>.
- [175] S. Kaufmann, R. Niemann, T. Thersleff, U.K. Röbber, O. Heczko, J. Buschbeck, B. Holzapfel, L. Schultz, S. Fähler, Modulated martensite: Why it forms and why it deforms easily, *New J. Phys.* (2011). <https://doi.org/10.1088/1367-2630/13/5/053029>.
- [176] J.I. Pérez-Landazábal, V. Sánchez-Alarcos, V. Recarte, O.A. Lambri, F.G. Bonifacich, D.L.R. Khanna, I. Unzueta, J.A. García, F. Plazaola, J. López-García, M.J. Ruiz, J.A. Rodríguez-Velamazán, E. Cesari, Influence of structural defects on the properties of metamagnetic shape

- memory alloys, *Metals* (Basel). (2020). <https://doi.org/10.3390/met10091131>.
- [177] D.L.R. Khanna, V. Sánchez-Alarcos, V. Recarte, J.I. Pérez-Landazábal, Correlation between particle size and magnetic properties in soft-milled Ni₄₅Co₅Mn₃₄In₁₆ powders, *Intermetallics*. (2021). <https://doi.org/10.1016/j.intermet.2020.107076>.
- [178] V.D. Buchelnikov, P. Entel, S. V. Taskaev, V. V. Sokolovskiy, A. Hucht, M. Ogura, H. Akai, M.E. Gruner, S.K. Nayak, Monte Carlo study of the influence of antiferromagnetic exchange interactions on the phase transitions of ferromagnetic Ni-Mn-X alloys (X=In,Sn,Sb), *Phys. Rev. B - Condens. Matter Mater. Phys.* (2008). <https://doi.org/10.1103/PhysRevB.78.184427>.
- [179] S. Jonas, A. Kolezyński, J. Lis, P. Stoch, K. Tkacz-Śmiech, Model studies of microstructure changes in sintering of ceramics, in: *Solid State Phenom.*, 2009. <https://doi.org/10.4028/www.scientific.net/SSP.147-149.890>.
- [180] R. Chulist, L. Straka, H. Seiner, A. Sozinov, N. Schell, T. Tokarski, Branching of {110} twin boundaries in five-layered Ni-Mn-Ga bent single crystals, *Mater. Des.* (2019). <https://doi.org/10.1016/j.matdes.2019.107703>.
- [181] R.C. Pond, X. Ma, Y.W. Chai, J.P. Hirth, Chapter 74 Topological Modelling of Martensitic Transformations, *Dislocations in Solids*. (2007). [https://doi.org/10.1016/S1572-4859\(07\)80006-4](https://doi.org/10.1016/S1572-4859(07)80006-4).

ACKNOWLEDGEMENTS

These three years of Ph.D. research mark an important achievement in my academic activity, personal growth, and self-awareness, and they would not have been equally powerful and crucial for me without the people that I have met and that accompanied me through this challenging but exciting journey.

My sincere thanks to all you guys.

First of all, I would like to acknowledge my supervisor and co-tutors, Prof. Massimo Solzi (SMFI, Unipr), Prof. Oliver Gutfleisch (TU-Darmstadt) and Dr. Franca Albertini (IMEM-CNR), for giving me the extraordinary opportunity to travel and enrich my personal background through many different experiences of work and interpersonal exchange, in Italy, Germany and outside Europe. I thank you for having sustained and supported me in all the circumstances (especially in this terrible year of pandemic!), with great energy and patience.

A very big thanks goes to my supervisor Prof. Massimo Solzi, who, since my Bachelor degree, supports me with great generosity, kindness, and infinite patience, being for all these years my indispensable and inspiring guide, not only from a professional level but also from a personal one.

A special acknowledgement to Dr. Francesco Cugini (SMFI, Unipr) for the constant availability, assistance and the important teachings provided during the session of magneto-metric characterization. Thank you also for the fruitful and passionate scientific discussions and elucidations.

Great thanks to all the members (gone and remained ones) of the MatFun Group at IMEM-CNR Institute of Parma (Dr. Franca Albertini, Dr. Simone Fabbri, Dr. Francesca Casoli, Dr. Riccardo Cabassi, Dr. César de Julian Fernandez, Dr. Milad Takhsa Ghahfarokhi, Dr. Fulvio Bolzoni), who helped me, with advices and technical support, to gain a better knowledge and awareness of the experimental work and the scientific investigation. Special thanks to Dr. Simone Fabbri and the group of MUSP who provided one of the bulk materials investigated in this Ph.D. thesis.

I would like to thank also Dr. Davide Delmonte (IMEM-CNR) for the crucial contribution to my work, thanks to the availability and help in the preparation through the Planetary ball-milling technique (using the precious small Zirconia balls!) of my powder samples.

I am sincerely grateful to Dr. Giovanna Trevisi (IMEM-CNR) for the constant and fundamental support with the SEM analysis of the infinite number of powder samples prepared. Thank you for the useful explanations and suggestions which helped me in improving my research method.

Thanks to Dr. Lucia Nasi (IMEM-CNR) for the useful TEM analysis sessions which enriched my study.

I would like to thank Prof. Lara Righi (SCVSA, Unipr) for the availability to perform X-ray diffraction measurements and the trainings in the analysis and interpretation of the crystallographic data.

Thanks to Dr. Davide Orsi and Dr. Gianfranco Galli (SMFI, Unipr) for the collaboration and important support with the DLS measurements.

Special acknowledgements to Prof. Oliver Gutfleisch and all the members and the visiting researchers, Doctors and Ph.D. students (you are so many!), of the Functional Materials Group at TU-Darmstadt.

Thank you for having welcomed me with beautiful hospitality and kindness during my first stay in 2018 and again with great enthusiasm in 2019. All of you is in my heart, for lots of beautiful and funny moments spent together, the sincere and deep friendship established during the months in Darmstadt and the fruitful exchange of ideas, which have been fundamental to open my mind and grow up.

A very big thanks to Dr. Semih Ener, for the technical support and the scientific supervision, to the Ph.D. student Lukas Pfeuffer for the availability to do the mechanical measurements for me this year and the useful on-line meetings, to Dr. David Koch for the important contribution to my work with the temperature dependent XRD measurements and the very big help in data analysis.

My sincere thanks to Timur Sirman who hosted me during my second visit to Darmstadt, making me feel extremely comfortable and letting me discover the powerful of living and sharing experiences with friends.

I really miss you guys and I miss my life in Darmstadt. Hope we could have the possibility to see each other again in 2021!

Thanks to the Coordinator Prof. Enrico Dalcanale, to all Professors and Students of the PhD course in Material Science and Technology and all Professors of the Physics Unit of the SMFI Department.

Thanks to Fondazione Cariparma for the financial support to my PhD research.

Ora, però, permettetemi di rivolgere i miei più sentiti ringraziamenti alle persone che sono e sono state in questi lunghi anni davvero indispensabili per la mia crescita, nella mia lingua madre!

Questa tesi è dedicata a tutti gli amici riscoperti o conosciuti durante questi ultimi tre anni, perché proprio grazie alla vostra vitale presenza, sostegno e diversità mi sono potuta riscoprire, mettendomi in gioco e smussando i miei spigoli con esperienze che da sola non avrei mai avuto il coraggio di provare e/o affrontare.

Grazie a tutti voi perché siamo riusciti a stare vicini e a farci forza insieme, nonostante questo terribile anno di pandemia.

Tra gli amici dell'Università (e/o dell'entourage), un ringraziamento speciale è rivolto a Ludovica, Claudia, Valentina, Sofia, Alexa, Paolo, Davide, Giuseppe.

Fuori dell'Università, invece, ci tengo a ringraziare Giorgia e Vicky.

Un affettuoso ringraziamento va alla mia cara amica Giulia, che, nonostante la lontananza e il fatto che non ci sentiamo assiduamente, è un punto di riferimento, sempre pronta ad ascoltarmi e a regalarmi una ventata di entusiasmo, positività e dolcezza.

Grazie a Giuditta, alla quale mi lega non solo la parentela ma anche una bella amicizia, rafforzata, proprio come noi, in questi ultimi anni. Ti ringrazio per non arrabbiarti (troppo) per le mie assenze, per la tua intraprendenza e vulcanicità, che rende sempre molto divertente, spensierato e stimolante il tempo trascorso insieme.

Un ringraziamento speciale è rivolto al gruppo delle serate estive in terrazza (inaugurato proprio quest'anno), e di quelle invernali, tisana e chiacchiere, in taverna, animato da Fede, Ric, Filips e la Giga. Quella che si è instaurata e ci lega fortemente è un'amicizia travolgente e prorompente che, in questi due anni che ci conosciamo, mi ha regalato tanta felicità, cambiando la mia vita in meglio, perché carica di affetto, stima reciproca e voglia di conoscersi ed imparare l'uno dall'altra.

Infine, il grazie più importante va ai miei genitori, a mia sorella (la Giga) e a mio fratello, che costituiscono le fondamenta di tutto ciò che sono diventata e sono riuscita a costruire. Questa tesi è prima di tutto dedicata a voi, gli unici che abbiano vissuto interamente insieme a me tutti i momenti belli e radiosi e quelli più difficili e tormentati, riuscendomi sempre a sostenere e a sopportare con incredibile forza e serenità. Grazie Mamma e Papà perché se continuo a crescere e a cercare di migliorarmi buona parte del merito è vostro, per gli insegnamenti datemi, e per l'esempio e la fiducia che mi mostrate. Grazie miei fratellini super in gamba perché il vostro sostegno, la vostra intelligenza e allegria sono indispensabili, mi aiutano a superare le difficoltà e riempiono il quotidiano di tanta felicità e armonia.

Grazie davvero a tutte le persone che, anche se non direttamente citate, contribuiscono a farmi stare bene e ad illuminare il mio cammino.

Greta